Spring 1-1-2016

Thermal Analysis of Hollow Core Ventilated Slab Systems

Benjamin Park
University of Colorado at Boulder, benjamin.park@colorado.edu

THERMAL ANALYSIS OF
HOLLOW CORE VENTILATED SLAB SYSTEMS

by

BENJAMIN PARK

B.A., University of Seoul, 2007

M.S., University of Colorado at Boulder, 2012

A thesis submitted to the

Faculty of the Graduate School of the

University of Colorado in partial fulfillment

Of the requirement for the degree of

Doctor of Philosophy

Department of Civil, Environmental, and Architectural Engineering

2016

The thesis entitled:

Thermal Analysis of Hollow Core Ventilated Slab Systems

written by Benjamin Park

has been approved for the Department of Civil, Environmental, and Architectural Engineering

_____

Moncef Krarti (Committee Chair)

_____

Gregor Henze

_____

John Zhai

_____

Wil Srubar III

_____

Junghyon Mun

Date _____

The final copy of this thesis has been examined by the signatories and we find that both the content and the form meet acceptable presentation standards of scholarly work in the above mentioned discipline.

Park, Benjamin (Ph.D., Architectural Engineering)

Thermal analysis of hollow core ventilated slab systems

A thesis directed by Professor Moncef Krarti, Ph.D., PE, LEED® AP

Abstract

Hollow core ventilated slab systems actively utilize building thermal mass through air channels inside precast floor slabs to meet any heating and cooling requirements. Various configurations of hollow core ventilated slab systems have been employed in northern/western Europe, Australia, and Middle East region. Compared to conventional air systems, hollow core slab systems offer some benefits including better thermal comfort, reduced heating and cooling energy consumption, and improved ventilation control.

Most of the models reported for ventilated slab systems are based on simplified thermal analysis and do not take account the multi-dimensional heat transfer associated with hollow cores with floor slabs. The research study outlined in the PhD dissertation starts by the development of a comprehensive simulation environment to accurately assess the thermal performance of hollow core ventilated slab systems. Specifically, a transient multi-dimensional numerical solution is developed and validated suitable for the thermal analysis of hollow core ventilated slab systems. The simulation environment is then used to perform a series of parametric analyses to evaluate the performance of ventilated slab systems under various design and operating conditions. In particular, the effects on energy efficiency performance of the ventilated slab systems are considered for a wide range of parameters including convective heat transfer inside hollow cores, supply air inlet temperatures, air mass flow rates, hollow core depths, and hollow core diameters. In addition and in order to reduce computational efforts, the use of 2-D model instead of 3-D

analysis is explored and verified to determine the thermal performance of ventilated slab systems.

In addition to heat transfer, moisture condensation within the hollow cores has been investigated to evaluate the potential for water accumulation and mold growth risk. Heat and moisture room model and enthalpy heat exchanger model are implemented and validated. The simulation environment can accurately predict the variations of the humidity ratios of the supply air as well as of the room ambient air. As part of the application of the developed simulation environment, optimum control strategies have been developed for enhancing the performance of ventilated slab systems to heat and cool the commercial buildings. Optimum control settings have identified using Particle Swarm and Genetic Algorithm optimization techniques. A comparative analysis of the energy performance of ventilated slab systems against rooftop systems for an office building is carried out for various climatic conditions. Based on the analysis, a set of design and operation guidelines for the hollow core ventilated slab systems is developed in order to enhance their energy performance for US commercial buildings.

Acknowledgements

First, I would like to thank my family for their endless support and love throughout this endeavor. I am grateful for my education in the Department of Architectural engineering at the University of Seoul, my graduate education in the Building Systems Program at the University of Colorado at Boulder. I would like to thank Moncef Krarti and all faculties at CU for their superb guidance and technical support.

Lastly, to all my friends, I appreciate your encouragement, support, and kind friendship throughout my time in school.

CONTENTS

CHAPTER 1: INTRODUCTION 1

1.1 BACKGROUND 1

1.2 LITERATURE REVIEW 9

1.3 JUSTIFICATION OF THE RESEARCH 16

1.4 RESEARCH OBJECTIVES 20

1.5 ORGANIZATION OF THE THESIS 22

CHAPTER 2: DEVELOPMENT OF THE HOLLOW CORE VENTILATED SLAB SYSTEM MODEL 25

2.1 INTRODUCTION 25

2.2 DEVELOPMENT OF NUMERICAL SOLUTION FOR THE VENTILATED SLAB SYSTEMS 26

2.3 VALIDATION OF A NUMERICAL MODEL 39

2.4 MESH GRID SENSITIVITY 40

2.5 TIMESTEP SENSITIVITY 41

2.6 PARAMETRIC ANALYSIS 42

2.7 SUMMARY AND CONCLUSIONS 49

CHAPTER 3: DEVELOPMENT OF THREE-DIMENSIONAL HEAT TRANSFER FLOOR MODEL 52

3.1 INTRODUCTION 52

3.2 THREE-DIMENSIONAL NUMERICAL SOLUTION 53

3.3 EFFECT OF THE EXTERIOR WALL HEIGHT 56

3.4 EFFECT OF FLOOR SHAPE AND SIZE 58

3.5 SUMMARY AND CONCLUSIONS 72

CHAPTER 4: DEVELOPMENT OF SIMULATION ENVIRONMENT FOR HOLLOW CORE VENTILATED SLAB SYSTEM 74

4.1 DEVELOPMENT OF A SIMULATION ENVIRONMENT 74

4.2 OUTSIDE-FACE HEAT BALANCE 77

4.3 CONDUCTION THROUGH THE WALL 77

4.4 INSIDE-FACE HEAT BALANCE 78

4.5 INDOOR AIR HEAT BALANCE 79

4.6 RC NETWORK FORMULATION 79

4.7 WINDOW HEAT BALANCE MODEL 82

4.8 CONVECTIVE COEFFICIENT CALCULATION 87

4.9 OUTSIDE SURFACE LONGWAVE RADIATION HEAT EXCHANGE 88

4.10 INTERNAL LONGWAVE RADIATION HEAT EXCHANGE 89

4.11 MODEL VERIFICATION 90

4.12 IMPACT OF THERMAL BRIDGE ON PERFORMANCE OF A HOLLOW CORE VENTILATED SLAB 101

4.13 SUMMARY AND CONCLUSIONS 119

CHAPTER 5: DEVELOPMENT OF ENTHALPY HEAT EXCHANGER MODEL 122

5.1 INTRODUCTION 122

5.2 HEAT AND MASS BALANCE MODEL 122

5.3 ENTHALPY HEAT EXCHANGER MODEL 123

5.4 CONDENSATE RATE MODEL 128

5.5 EVAPORATE RATE MODEL 133

5.6 UPDATE HUMIDITY RATIO OF AIR 134
5.7 DESCRIPTION OF THE SIMULATION ENVIRONMENT 136
5.8 MODEL VERIFICATION 137
5.9 SIMULATION RESULTS 141
5.10 ANNUAL SIMULATION RESULTS 156
5.11 SUMMARY AND CONCLUSIONS 159

CHAPTER 6: DEVELOPMENT OF OPTIMAL CONTROL STRATEGY FOR HOLLOW CORE VENTILATED SLAB SYSTEM 162

6.1 INTRODUCTION 162
6.2 MEAN RADIANT TEMPERATURE CALCULATION 163
6.3 THERMAL COMFORT MODEL 170
6.4 OPTIMAL CONTROL STRATEGY 174
6.5 DESCRIPTION OF THE ANALYSIS 181
6.6 SIMULATION RESULTS 186
6.7 SENSITIVITY ANALYSIS FOR THE OFFICE BUILDING 194
6.8 SUMMARY AND CONCLUSIONS 214

CHAPTER 7: CONCLUSIONS AND FUTURE WORK 216

7.1 SUMMARY AND CONCLUSIONS 216
7.2 FUTURE WORK 222

REFERENCE 224

TABLES

Table 3.1: Input parameters used for the analysis 59

Table 3.2: Comparison of exponential curve fit coefficients for 2-D and 3-D floor model with no heat source in Golden, CO 62

Table 3.3: Heat transfer and heat flux for steady-state 1-D, 2-D, and 3-D floor model with no heat source in Golden, CO 62

Table 3.4: Comparison of exponential curve fit coefficients for 2-D and 3-D floor model with 1000 W/m^3 heat source in Golden, CO 65

Table 3.5: Heat transfer and heat flux for steady-state 1-D, 2-D, and 3-D floor model with 1000 W/m^3 heat source in Golden, CO 66

Table 3.6: Comparison of exponential curve fit coefficients for 2-D and 3-D floor model with no heat source in Golden, CO 69

Table 3.7: Heat transfer and heat flux for transient 1-D, 2-D, and 3-D floor model with no heat source in Golden, CO 69

Table 3.8: Comparison of exponential curve fit coefficients for 2D and 3D floor model with 1000 W/m^3 heat source in Golden, CO 71

Table 3.9: Heat transfer and heat flux for transient 1D, 2D, and 3D floor model with 1000 W/m^3 heat source in Golden, CO 72

Table 4.1: MoWiTT coefficients 88

Table 4.2: Roughness multiplier 88

Table 4.3: Description of the building model used for validation 94

Table 4.4: Characteristics of building envelope, internal loads, and the ventilated slab system 102

Table 4.5: Comparison of energy consumption by the ventilated slab system and estimation of

thermal bridging effects during heating season (January 15th to 17th) and cooling season (August 17th to 19th) for 8 meter wide slab in Golden, CO..... 109

Table 4.6: Comparison of energy consumption by the ventilated slab system and estimation of thermal bridging effects during heating season (January 15th to January 17th) and cooling season (August 18th to August 19th) for 8 meter wide slab in Golden, CO 113

Table 5.1: Material properties for a hollow core slab: Lightweight concrete and heavyweight concrete..... 142

Table 5.2: Description of simulation cases..... 142

Table 5.3: Condense water calculated by detailed and simple methods..... 156

Table 6.1: Coefficients A-E for calculating angle factors for a seated person 168

Table 6.2: Comparison of the optimal solution obtained from Matlab global optimization toolbox with brute-force simulation..... 194

FIGURES

Figure 1.1: U.S. Building total primary energy consumption and building share of U.S. primary energy consumption (DOE, 2011) 1

Figure 1.2: Energy end-use splits for the U.S.: (a) residential building and (b) commercial building (DOE, 2011) 2

Figure 1.3: A typical hollow core ventilated slab system (PAROC, 2012) 3

Figure 1.4: Two node state space example with a heat source at node 1 (EnergyPlus, 2013) 17

Figure 1.5: EnergyPlus finite difference node types (Tabares-Velasco, 2012) 18

Figure 2.1: Schematic of the hollow core ventilated slab system 25

Figure 2.2: Control volume for the two-dimensional heat conduction problem with heat generation source 27

Figure 2.3: Selected mesh configuration used for the two-dimensional building model 38

Figure 2.4: The effect of supplying 40°C air through a hollow core ventilated slab 40

Figure 2.5: Impact of the number of nodes of the grid mesh on the prediction accuracy and computational effort 41

Figure 2.6: Impact of the time step on the prediction accuracy and CPU time 42

Figure 2.7: Cross-section view of ventilated slab and wall joint and variables used for parametric analyses 43

Figure 2.8: Average heat transfer rates along the slab surfaces with no insulation as functions of convective coefficient inside a hollow core 44

Figure 2.9: Average heat transfer rates along the slab surfaces with no insulation as functions of convective coefficient on a floor surface 45

Figure 2.10: Average heat transfer rates along the slab surfaces with no insulation as functions of

inlet supply air temperature 46
Figure 2.11: Average heat transfer rates along the slab surfaces with no insulation as functions of air mass flow rate 47
Figure 2.12: Average heat transfer rates along the slab surfaces with no insulation as functions of the depth of hollow cores 48
Figure 2.13: Average heat transfer rates along the slab surfaces with no insulation as functions of hollow cores contact area embedded in fixed concrete slab thickness for two core diameters 49
Figure 3.1: Three-dimensional control volume 54
Figure 3.2: Variation of heat flux along the floor inside surface and heat flux at floor edge for (a) 2D and (b) 3D FDM floor model with various exterior wall heights in Golden, CO..... 57
Figure 3.3: (a) Heat loss vs. perimeter length for uninsulated floors (b) Heat loss per unit area vs. A/P for uninsulated slabs in Golden, CO. 58
Figure 3.4: Section view of multi-dimensional slab and wall joint model: (a) 2-D and (b) 3-D model 59
Figure 3.5: (a) Heat loss vs. perimeter length and (b) Heat loss per unit area vs. A/P for 1-D, 2-D, and 3-D floor model with no heat source in Golden, CO. 61
Figure 3.6: (a) 2-D floor model exponential curve fit and (b) 3-D floor model exponential curve fit with no heat source in Golden, CO. 61
Figure 3.7: (a) Heat loss vs. perimeter length and (b) Heat loss per unit area vs. A/P for 1D, 2D, and 3D floor model with 1000 W/m^3 heat source in Golden, CO. 64
Figure 3.8: (a) 2-D floor model exponential curve fit and (b) 3-D floor model exponential curve fit with 1000 W/m^3 heat source in Golden, CO..... 65
Figure 3.9: Daily outdoor air temperature profile used for dynamic boundary condition..... 67

Figure 3.10: (a) Heat loss vs. perimeter length and (b) Heat loss per unit area vs. A/P for 1-D, 2-D, and 3-D floor model with no heat source in Golden, CO. 68

Figure 3.11: (a) 2-D floor model exponential curve fit and (b) 3-D floor model exponential curve fit with no heat source in Golden, CO. 68

Figure 3.12: (a) Heat loss vs. perimeter length and (b) Heat loss per unit area vs. A/P for 1D, 2D, and 3D floor model with 1000W/m^3 heat source in Golden, CO. 70

Figure 3.13: (a) 2D floor model exponential curve fit and (b) 3D floor model exponential curve fit with 1000 W/m^3 heat source in Golden, CO..... 71

Figure 4.1: Schematic of the FDMRC simulation environment tool..... 74

Figure 4.2: Flow chart of the integrated simulation environment 75

Figure 4.3: Schematic of heat balance calculation procedure..... 76

Figure 4.4: Description of RC thermal network for a single layer exterior wall 80

Figure 4.5: Thermal network for the multi-layer exterior walls and a thermal zone..... 82

Figure 4.6: FDMRC environment validated with EnergyPlus..... 90

Figure 4.7: A section view of the building slab and exterior walls for two thermal zones used for the verification analysis: (a) ventilated heating slab and (b) ventilated cooling slab 91

Figure 4.8: Variable temperature control strategy for the hollow core ventilated slab system 92

Figure 4.9: Outdoor air temperature and exterior incident solar radiation from January 15^{th} to 18^{th} in Golden, CO. 95

Figure 4.10: Outdoor air temperature and exterior incident solar radiation from August 17^{th} to 20^{th} in Golden, CO. 95

Figure 4.11: Histogram of heating energy use for (a) Zone 1 and (b) Zone 2 obtained from EnergyPlus and FDMRC during representative heating season 97

Figure 4.12: Time series mean air temperature and heating energy use comparison between

EnergyPlus and FDMRC: (a) Mean air temperature in Zone 1, (b) Mean air temperature in Zone 2, (c) Heating energy use in Zone 1, and (d) Heating energy use in Zone 2 98
Figure 4.13: Histogram of cooling energy use for (a) Zone 1 and (b) Zone 2 obtained from EnergyPlus and FDMRC during representative cooling season 99
Figure 4.14: Time series mean air temperature and cooling energy use comparison between EnergyPlus and FDMRC: (a) Mean air temperature in Zone 1, (b) Mean air temperature in Zone 2, (c) Cooling energy use in Zone 1, and (d) Cooling energy use in Zone 2 100
Figure 4.15: (a) Insulation in the inner surface of the wall and (b) Insulation in the center plane of the wall 102
Figure 4.16: (a) Zone 1 mean air temperature and (b) Zone 2 mean air temperature obtained from FDMRC-1D and FDMRC-2D during heating season (January 15th to 18th) 105
Figure 4.17: (a) Zone 1 heating energy use and (b) Zone 2 heating energy use obtained from FDMRC-1D and FDMRC-2D during heating season (January 15th to 18th) 106
Figure 4.18: (a) Zone 1 mean air temperature and (b) Zone 2 mean air temperature obtained from FDMRC-1D and FDMRC-2D during cooling season (August 17th to 19th) 107
Figure 4.19: (a) Zone 1 cooling energy use and (b) Zone 2 cooling energy use obtained from FDMRC-1D and FDMRC-2D during cooling season (August 17th to 19th) 108
Figure 4.20: (a) Zone 1 mean air temperature and (b) Zone 2 mean air temperature obtained from FDMRC-1D and FDMRC-2D during heating season (January 15th to 17th) 110
Figure 4.21: (a) Zone 1 heating energy use and (b) Zone 2 heating energy use obtained from FDMRC-1D and FDMRC-2D during heating season (January 15th to 17th) 111
Figure 4.22: (a) Zone 1 mean air temperature and (b) Zone 2 mean air temperature obtained from FDMRC-1D and FDMRC-2D during cooling season (August 17th to 19th) 112
Figure 4.23: (a) Zone 1 cooling energy use and (b) Zone 2 cooling energy use obtained from

FDMRC-1D and FDMRC-2D during cooling season (August 17th to 19th)..... 113
Figure 4.24: Impact of R-value of insulation at slab/wall joint on ventilated slab system energy consumption with various slab width in Golden, CO during (a) Heating and (b) Cooling season..... 115
Figure 4.25: Impact of R-value of insulation at slab/wall joint on ventilated slab system energy consumption with various slab width in Golden, CO during (a) Heating and (b) Cooling season..... 116
Figure 4.26: Impact of R-value of insulation inside exterior wall on ventilated slab system energy consumption with various slab width in Golden, CO during (a) Heating and (b) Cooling season..... 118
Figure 4.27: Impact of R-value of insulation inside exterior wall on ventilated slab system energy consumption with various slab width in Golden, CO during (a) Heating and (b) Cooling season..... 119
Figure 5.1: The process of water condensation (dehumidification) in the idealized case 129
Figure 5.2: Flow chart of the integrated simulation environment including heat and mass air heat balance model and water condensate/evaporate models..... 136
Figure 5.3: Description of room model and temperature and humidity ratio control scheme.... 137
Figure 5.4: Zone air set-point temperature control strategy 138
Figure 5.5: Comparison of results from FDMRC and EnergyPlus for (a) mean air temperature, (b) humidity ratio, and (c) relative humidity ratio obtained during representative days for the cooling season (Aug 16th to 20th) in Golden, CO..... 139
Figure 5.6: Comparison of results from EnergyPlus, FDMRC with sensible heat exchanger model, and FDMRC with enthalpy heat exchanger model obtained during representative days of the heating season..... 140

Figure 5.7: Comparison of results from EnergyPlus, FDMRC with sensible heat exchanger model, and FDMRC with enthalpy heat exchanger model obtained during representative days of the cooling season 141
Figure 5.8: Supply air conditions for various analysis cases 143
Figure 5.9: Time variations of ceiling and core surfaces and dew-point temperatures when the room air temperature is maintained at 25°C for 24 hours with: (a) supply air temperature=18°C and RH = 80% and (b) supply air temperature=18°C and RH=95% ... 144
Figure 5.10: Time variations of the ceiling and core surfaces and dew-point temperatures when the heavyweight slab is precooled during unoccupied period with: (a) supply air temperature=15°C and RH = 80% and (b) supply air temperature=15°C and RH=95% ... 145
Figure 5.11: Time variations of the ceiling and core surfaces and dew-point temperature when the heavyweight slab is precooled during unoccupied period: (a) supply air temperature=15°C and RH = 80% and (b) supply air temperature=15°C and RH=95% 146
Figure 5.12: Time variations of the ceiling and core surfaces and dew-point temperature when the heavyweight slab is precooled during unoccupied period with: (a) supply air temperature=12°C and RH = 80% and (b) supply air temperature=12°C and RH=95% ... 148
Figure 5.13: Time variations of the ceiling and core surfaces and dew-point temperature when the heavyweight slab is precooled during unoccupied period with: (a) supply air temperature=12°C and RH = 80% and (b) supply air temperature=12°C and RH=95% ... 149
Figure 5.14: Time variations of the ceiling and core surfaces and dew-point temperature when the lightweight slab is precooled during unoccupied period with: (a) supply air temperature=15°C and RH = 80% and (b) supply air temperature=15°C and RH=95% 150
Figure 5.15: : Time variations of the ceiling and core surfaces and dew-point temperature when the lightweight slab is precooled during unoccupied period with: (a) supply air

temperature=15°C and RH = 80% and (b) supply air temperature=15°C and RH=95% ... 151
Figure 5.16: : Time variations of the ceiling and core surfaces and dew-point temperature when the lightweight slab is precooled during unoccupied period with: (a) supply air temperature=12°C and RH = 80% and (b) supply air temperature=12°C and RH=95% ... 153
Figure 5.17: : Time variations of the ceiling and core surfaces and dew-point temperature when the lightweight slab is precooled during unoccupied period with: (a) supply air temperature=12°C and RH = 80% and (b) supply air temperature=12°C and RH=95% ... 154
Figure 5.18: Comparison of condensate and evaporate rates as well as the amount of condense water obtained from detailed and simple calculation methods 156
Figure 5.19: Number of hours per year of water condensation occurring inside hollow cores or on ceiling surfaces in three US locations: San Francisco, CA, Port Arthur, TX, and Miami, FL 158
Figure 5.20: Number of hours per year of water condensation occurring inside hollow cores or on ceiling surface in three US locations: San Francisco, CA, Port Arthur, TX, and Miami, FL 159
Figure 6.1: The psychrometric thermal comfort chart from the ANSI/ASHRAE Standard 55.. 163
Figure 6.2: Average values of the angle factor between a siting person and horizontal or vertical rectangle surfaces when the person rotates around a vertical axis (Fanger, 1982) 167
Figure 6.3: Six sides of an enclosure with occupant positioned off-centered. 169
Figure 6.4: An example of Complex method procedure 176
Figure 6.5: An example of particle swarm procedure 180
Figure 6.6: Occupancy and lighting schedule for the commercial building 182
Figure 6.7: The structure of the optimal controller for deterministic simulation 184
Figure 6.8: Computational time required for the optimization process of 1-D and 2-D model . 187

Figure 6.9: Percent difference of cooling energy use between 1-D and 2-D model after optimization process as a function of percent difference of cooling energy use between 1-D and 2-D model for various slab sizes and utility rates 188
Figure 6.10: Reduction from Y- to Δ-network 189
Figure 6.11: Parallel thermal network 190
Figure 6.12: Percent cost difference between 1-D and 2-D numerical model as a function of ratio of heat transfer rate through exterior walls to heat transfer rate through a slab 191
Figure 6.13: Comparison of coefficient of variation (CV) for 1-D model with/without correction 192
Figure 6.14: Comparison of optimization solution obtained from 1-D model with correction and 2-D model 192
Figure 6.15: Energy cost as a function of 6hr interval set-point temperature schedule combination obtained from brute-force simulation 193
Figure 6.16: Exponential penalty function and step penalty function with two weighting factors 195
Figure 6.17: Cost and CPU time with two different penalty function (i.e. exponential function and step function) as a function of time interval 196
Figure 6.18: Cost and CPU time as a function of population size 197
Figure 6.19: Cost as a function of weighting factor of penalty function 198
Figure 6.20: Variation of PMV for two different weighting factors 198
Figure 6.21: Fitness value for each generation of GA 200
Figure 6.22: Set-point schedule of the ventilated slab system operation 201
Figure 6.23: Hourly zone air temperature profiles 201
Figure 6.24: Hourly total cooling energy use profiles 202

Figure 6.25: Hourly PMV profiles 202
Figure 6.26: Comparison of normalized energy cost 203
Figure 6.27: Comparison of normalized energy consumption 203
Figure 6.28: Set-point schedule of the ventilated slab system operation from GA 205
Figure 6.29: Hourly cooling energy use profiles 205
Figure 6.30: Comparison of savings potential of different control strategies 206
Figure 6.31: Percent energy cost savings of precooling vs. conventional control as a function of a hollow core slab thickness: (a) $\mathrm{Ru} = 4$ and (b) $\mathrm{Ru} = 10$ 207
Figure 6.32: Comparison of ceiling/roof surface temperatures of different control strategies with various slab thickness: (a) conventional control and (b) precooling control 208
Figure 6.33: Comparison of savings potential of different utility structures with various slab thickness 210
Figure 6.34: Comparison of ceiling/roof surface temperatures of different control strategies with various slab thickness: (a) conventional control and (b) forced precooling control (21.4°C) 211
Figure 6.35: Comparison of hourly cooling energy use of different control strategies with various slab thickness: (a) 0.12m thick slab, (b) 0.25m thick slab, and (c) 0.50m thick slab 213

CHAPTER 1: INTRODUCTION

1.1 Background

It is reported that the U.S. has seen a significant increase in energy consumption in recent years. The building total primary energy use has increased by 53 percent in 2010 relative to 1980 as shown in Figure 1.1. The portion of primary energy consumption by residential and commercial building has also increased according to building energy data book provided by Department of Energy (DOE). Residential buildings in the U.S consumes 70% more energy than they did 30 years ago (DOE, 2011). The energy consumption by commercial buildings in the U.S. has increased by 111% compared to 1980. In the residential sector, 43% of the total energy consumption is used for space heating and cooling as shown in Figure 1.2 (a). Figure 1.2 (b) shows that 24% of the total energy consumption is used for space heating and cooling in the commercial sector. There has always been thus interest in techniques and technologies to reduce energy consumption for space heating and cooling in the U.S. buildings.

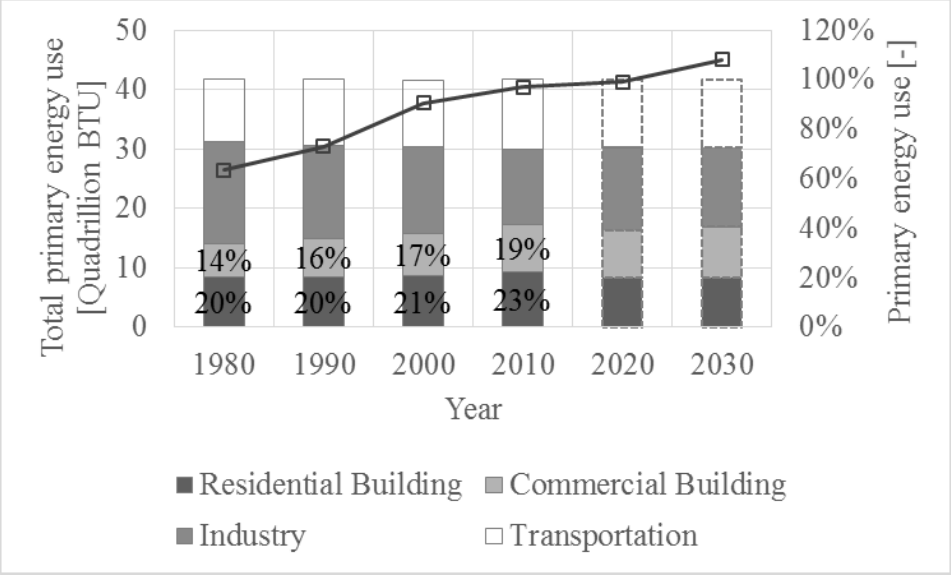

Figure 1.1: U.S. Building total primary energy consumption and building share of U.S. primary energy consumption (DOE, 2011)

(a)

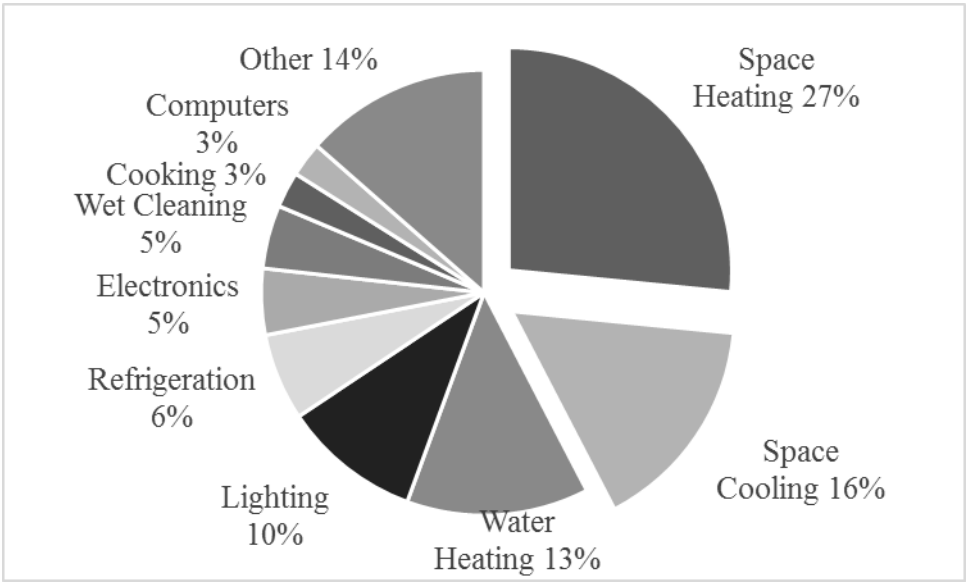

(b)

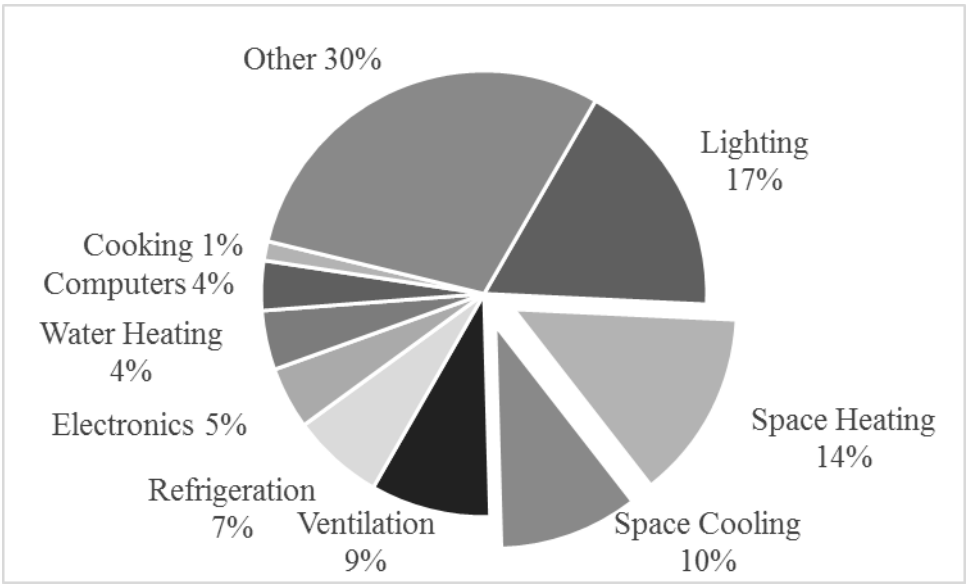

Figure 1.2: Energy end-use splits for the U.S.: (a) residential building and (b) commercial building (DOE, 2011)

The use of building thermal mass is one of the effective techniques to reduce the building energy consumption. Recently, active cooling/heating systems incorporated with building thermal mass are widely used in residential and commercial buildings, which use mechanical means for

coolth/heat collection and transportation. A variety of applications for active cooling/heating systems associated with building mass have been studied. One example of active cooling/heating systems is a hollow core ventilated slab system. The fluid (air) is forced through passages within pre-cast concrete roof/floor slabs. This forced air can enhance the thermal-storage capabilities and the heat removal capabilities of the building's mass. Figure 1.3 shows a typical hollow core ventilated slab system (PAROC, 2012).

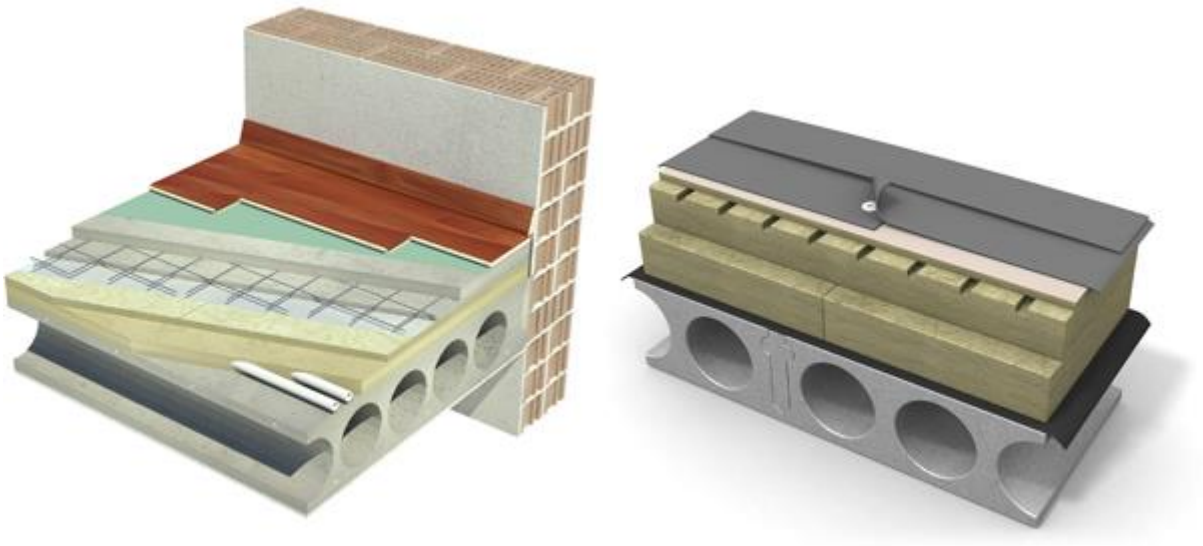

Figure 1.3: A typical hollow core ventilated slab system (PAROC, 2012)

Thermally activated slabs were initially applied to heat buildings in Europe. Moreover, most of the research analyses of thermally activated slabs were conducted in western Europe. In particular, the most successful advanced thermal building slab system is the patented FES-slab (known by the trade name 'TermoDeck' in the United Kingdom) that was first used during the late 1970s in Sweden. It has been estimated that more than 300 TermoDeck buildings have been constructed in Sweden, Norway and United Kingdom (UK) (ASA Consulting, 2006). Specifically, two residential projects have achieved the *Passive House Requirements* and more recently two other residential

projects have been designed to achieve *Miljöbyggnad Guld* criteria in Sweden. In UK, a commercial building was given a BREEAM rating of 87.5% in 2007 which was considered then the highest ever awarded BREEAM rating (Kennet, 2005). By 2008 the FES-slab system had been successfully applied in over 1,500,000 m^2 of projects in Sweden, Norway, UK and Saudi Arabia (ASA Consulting, 2005). The operational experiences of TermoDeck buildings in Scandinavia and UK show heating energy consumption to be 30 to 50 kWh/m^2 per year. This energy use is approximately 40% lower than that observed for buildings with conventional heating and ventilation systems. A merit of the hollow core ventilated slab systems is that it can be combined with several air-conditioning types. In general, the supply air ducts run down to each floor from the air-handling unit, placed on the roof, and then the supply air is feed to horizontal ducts installed in each floor. Small branch ducts introduce the supply air into hollow cores within slab to be supplied to spaces through diffusers. The exhaust air returns to the air-handling unit as is the case for the conventional systems. TermoDeck has reported that the ventilated slab system achieves up to 50% peak electrical power reduction (Willis and Wilkins, 1993; Evans, 1993; Standeven, 1998; Field, 2001). TermoDeck systems installed in Europe and Middle East have achieved 30 to 50% lower cooling energy consumption compared to equally sized conventional air systems. Moreover, it has been noted that ventilated slab systems reduce fans and chillers energy consumption. In hot climates, the reduction in fans and chillers can be up to 50%. Moreover, the suspended ceiling finishes are not necessarily required, and the floor height can be reduced by 15 to 25% which can beneficial in saving construction costs especially for high-rise buildings. Finally, it has been reported that ventilated slab systems provide fairly good thermal comfort to occupants and stable indoor air temperatures throughout the year (Arnold, 1993; Winwood, 1997; Kenneth, 2006).

Park and Krarti (refer to Appendix) assessed the energy performance of the hollow core ventilated

slab system that is proposed for the 3-story office building located in Kochi, India. The climate of Kochi, India is very hot and humid. Two energy models, LEED baseline model and proposed design model, of 3-story office building is created by using EnergyPlus. LEED baseline building model has traditional packaged rooftop air conditioner with DX cooling coil and furnace according to ASHRAE Standard 90.1-2007. The proposed design model equipped with ventilated slab system maintains the inside surface temperature of ceiling 1-2°C lower compared to the LEED baseline model. The lower inside surface temperatures of the proposed design model lead to the reduction of cooling energy consumption during the occupied period. It was concluded that the proposed building energy model with the ventilated slab system consumes 19% less energy compared to the LEED baseline model. Specifically, the ventilated slab system can reduce cooling energy use and fan energy use by 18% and 66%, respectively.

A hollow core ventilated slab system has similar features with radiant slab heating/cooling system since both systems actively utilizes the thermal mass of the building. Unlike water based radiant slab system, ventilated slab system is a fan-assisted, heating, cooling and ventilation system that uses the high thermal mass of structural, hollow core floor slabs through which warmed or cooled fresh air is distributed into the space. To summarize the advantages and disadvantages of the two systems (i.e. radiant slab system and ventilated slab system) are as follows.

Radiant floor heating systems (RFHs) have become popular due to their potential to reduce energy consumption as well as to provide better thermal comfort. Indeed, RFHs can maintain uniform cooling and heating distribution throughout the conditioned spaces. Hydronic panel systems may be connected in series in order to increase their exergetic efficiency. Water based systems such as radiant floor heating and radiant floor cooling are often referred to as low exergy systems since they facilitate heating and cooling at low temperatures close to the ambient environment. Low

temperature differences require that heat transfer takes place over relatively large surfaces as is the case for radiant floor heating systems. The overall efficiency of most energy sources strongly depends on the supply temperature provided by the heating system, the lower the supply temperature, the higher is the system efficiency. For heat pumps, a simple rule of thumb states that lowering the heating system supply temperature by 1°C would yield a reduction of annual energy consumption of approximately 2% (Nielsen, 2012). If the heating system is designed with radiant floor heating operating at a supply temperature on 30°C instead of radiators with a supply temperature on 50°C, an annual energy cost savings of 30–40% can be achieved depending on the heat pump type and other parameters. Indoor air temperature as well as mean radiant temperature can be controlled with the radiant panels, minimizing air motion within air conditioned spaces. Moreover, radiant panel systems have relatively low initial cost compared to conventional air-conditioning systems. They also require less space for mechanical equipment and control devices. This feature is especially valuable in hospital patient rooms, offices, and other applications where space is at a premium. Moreover, RFHs create inhospitable living conditions for house dust mites compared to other heating systems. With radiant systems, noise associated with fan-coil or induction units is eliminated. In addition, peak loads are reduced as a result of thermal energy storage in the panel structure, as well as in the walls and partitions directly exposed to the radiant panels.

Several studies have reported that radiant heating systems can be more energy efficient compared to conventional air systems. Zaheer-uddin and Cho (1999) concluded that radiant floor heating systems can save up to 15 percent of energy usage compared to conventional heating systems. Experimental research analysis (CADDET, 1999) reported that electric radiant panel systems can achieve 33% to 52% of heating energy savings compared to air-to-air heat pump and electric

baseboard heating systems, respectively. Stetui (1999) concluded that radiant systems can save up to 30% of the energy consumption and 27% of the peak demand for US office buildings. Watson and Chapman (2002) reported that radiant systems can benefit from building thermal mass to shift the peak hour and enhance thermal comfort in the space. Zhai et al. (2009) reported that radiant heating systems can achieve significant energy savings when compared to convective air systems at equal indoor thermal comfort and air quality levels. Radiant heating systems require less energy due to the fact that unlike conventional convective air systems, radiant heating systems deliver heat directly to the occupants by radiation; therefore, when heating is required in the conditioned space, the same thermal comfort can be achieved at lower indoor air temperatures. Typically, similar thermal comfort level can be accomplished with 3 to 4˚C lower indoor air temperatures during heating operation. As a result, air infiltration thermal loads can be reduced for radiant panels due to lower temperature difference between indoor and outdoor when compared to conventional air systems.

Moreover, radiant ceiling cooling (RCC) systems are generally used to provide cooling for either residential or office buildings. RCC systems are commonly used in Scandinavian countries, Switzerland, and Germany. Indeed, RCC systems provide energy efficient alternatives to traditional air conditioning systems with improved indoor thermal comfort. There are two primary types of radiant cooling systems with a broad range of technologies. One type consists of radiant cooling slab systems that deliver cooling using elements of the building structure, commonly slab floors. These systems are generally referred to as thermally activated building systems or TABS (Gwerder, 2008). The other type includes radiant cooling systems that deliver cooling through ceiling panels. Radiant cooling slab systems are cheaper than ceiling panel systems and offer the benefits of thermal mass while ceiling panel systems offer faster temperature control and flexibility

due to their low thermal mass level. Radiant ceiling panel systems are typically integrated with suspended acoustical ceilings. The ceiling panels are generally made up of steel or copper pipes with diffusion fins. The materials of panels have high thermal conductivity values but they have low thermal inertia. Various theoretical or experimental results show that radiant ceiling panels can achieve energy savings up to 30% compared to conventional air systems (Laoudi, 2004). Several factors such as design capacities, temperature settings, and locations of the radiant panels affect their energy efficiency as well as their ability to maintain thermal comfort. Properly designed radiant systems can produce long term energy savings of up to 30% (Conroy, 2001).

Due to their high thermal inertia, radiant heating and cooling slab systems are extremely difficult to control and exhibit some risks of condensation especially in the case of rapid increase in relative humidity within the conditioned spaces. For radiant panel cooling systems, dehumidification and panel surface condensation may be of a significant concern under specific operating conditions. In particular, preventing condensation problems can affect the selection of the cooling capacity of a radiant cooling system. The surface temperature should not be allowed to be equal or below the dew point temperature within the space.

When cooling slabs by natural means such as night ventilation is not sufficient, direct cooling using conventional air conditioning systems may be considered to remove indoor heat gains and maintain thermal comfort. For hollow core slab systems, the required capacity and size of the conventional air conditioning systems could be reduced significantly. During cooling operation, hollow core slab systems may store cooling energy during night by taking advantages of external economic factors such as electricity demand limiting tariff options, and provide passive radiative cooling during daytime. Usually, hollow core slab systems have some inherent advantages when compared with conventional air conditioning systems. In particular, thermal comfort can be

maintained using higher average indoor air temperature due to direct radiant heat exchange of occupants' heads with the ceiling. In fact, ventilated slab systems can keep the mean radiant temperature lower compared to other conventional air-based system by controlling the slab surface temperature (slab surface temperature can significantly affects the mean radiant temperature). In addition, thermal comfort levels may be better than those achieved by the conventional air conditioning systems because of the minimization of air movement and surface temperature differences. Moreover, the long air path within the slab hollow cores minimizes the transmission of noise from the central air handling unit. High ventilation rate may be used to improve indoor air quality and may reduce odor related illness (Godish and Spengler, 1996; Mendell, 1993; Menzies and Bourbeau, 1997; Seppänen et al., 1999; Wargocki et al., 2002; Sundell et al., 2011). The reduced demand for ''wet'' air conditioning plant also limits the risk of micro biological contamination such as Legionnaire's disease (Xu et al., 2014). Considerable energy could be saved during the daytime due to options to set higher indoor temperature and to utilize other energy sources such as cool ambient air. Peak load may be reduced because of cool storage within the slab. Thus, the capacity of ventilated slab system could be reduced significantly.

However, hollow core slab systems have also some disadvantages compared to the conventional air conditioning systems. In particular, high ventilation rates inherent to ventilated slab systems require more fan power. Moreover, condensation can occur in the cores since moisture can be introduced into the slab when outdoor air heats the hollow core slab.

1.2 Literature review

Despite the insulation requirements specified by regulations, thermal bridges in the building's envelope remain a weak spot in the constructions. Moreover, in many countries construction practices tend to implement only partially the insulation measures foreseen by regulations. As a

result, thermal losses are in practice greater than those predicted during the design stage.

Deque (2001) modeled 2-dimensional T and L shaped wall intersection structures using Clim 2000. The accuracy of heat losses is increased by up to 7% by taking 2-dimensional models of thermal bridges into account.

Theodosiou and Papadopoulos (2008) presented a study on representative wall thermal insulation configurations in Greek buildings to investigate the impact of the thermal bridges on the energy consumption. All simulative calculations were carried out using the TRNSYS 16. The authors concluded that heating requirements are 30% higher when the thermal bridging effect is taken into account.

Evola et al. (2011) reported that correction of thermal bridges can achieve 21.5% of primary heating energy savings and 3.5% of cooling energy savings. The correction of thermal bridges measure reduces annual energy use approximately 8.5% in the mild Mediterranean climate.

Gomes et al. (2013) demonstrates that the peak thermal load can be increased by 10% due to thermal bridging through metal frame walls in commercial buildings located in Brazil. Thermal bridging resulted in 5% increase of annual energy use when the building is constructed with a conventional concrete structure.

Kammerud et al. (1984) accentuate that thermal mass with night ventilation is effective to reduce the maximum indoor air temperature in buildings in summer. Shaviv (1989) reported that comfort temperatures may be achieved by the proper application of passive cooling systems.

Braun (1990) developed optimization routines and applied to the computer simulations of cooling systems in a single thermal zone. The author concluded that both energy costs and peak electrical consumption can be significantly reduced when the building thermal storage is properly precooled by low ambient air at nighttime. Nighttime precooling reduces the cooling energy use by 10 to

50%. The proper management of the thermal storage in the building can achieve 10 to 35% of the peak electrical use.

Andresen and Brandemuehl (1992) modeled a single zone in an office building using TRNSYS to investigate the parameters that affect the interaction between the conditioned zone air and the building mass. The authors concluded that the nighttime mechanical precooling of the building thermal mass can reduce peak loads by 10 to 50% compared to a conventional strategy of turning off the HVAC system at night.

Florides et al. (2002) insist that night cooling with mechanical ventilation is much more reliable and controllable compared to natural nighttime cooling. The magnitude of heat gains and ventilation rates largely affect the natural nighttime cooling. Santamouris et al. emphasizes that the mechanical night precooling is effective when relatively high air flows can be used, maximizing the cooling effect.

Interaction between the structural thermal mass of building envelope and supply air allows significant use of building pre-treatment by overnight cooling or heating. The proper use of cool night air to pre-cool that slab in summer season provides the potential to significantly reduce the economic penalties associated with conventional cooling system.

Barnaby et al. (1980) simulated the thermal performance of a hollow core slab system in 100,000 ft^2 commercial building using NBSGLS energy analysis program developed by Berkeley Solar Group and concluded that the system could provide an energy reduction between 13% and 30% for the peak cooling load under dry climates of the United States: Sacramento, CA; Washington DC.

Givoni (1983) analyzed the behavior of a high thermal mass building ventilated during the night. The outdoor air temperature was varied from 19 to 34°C. Night ventilation during nighttime

reduced the maximum room air temperature during daytime by 2.5°C (28.5 to 26°C) compared to unventilated space case. Indeed, the nocturnal ventilation make the building thermal mass acted as a heat sink, and reduced the cooling load during the daytime.

Allen et al. (1984) simulated the effect of a hollow core slab in a passive solar house in Ottawa. The results indicated that the hollow core slab achieved approximately 13% energy savings.

Zmeureanu and Fazio (1988) developed a two-dimensional heat storing floor slab using a Crank-Nicolson's implicit finite difference model and presented a case study for a single zone office in Montreal, Canada. The model incorporates an implicit finite difference method with hourly time steps and includes predicted mean vote (PMV) estimation. Although it considered two-dimensional heat transfer in the hollow core slab, the slab cores were simplified as two parallel slab plates sharing the air passing cavity. The heat transfer coefficient along the air path was assumed to be a constant value. The authors concluded that the system both reduced by over 35% the daily total cooling load and also resulted in a PMV that was more acceptable under standard cooling conditions when compared to a conventional all air system in their particular study.

Willis and Wilkins (1993) examined the thermal performance of a ventilated slab system (TermoDeck system) in the part of BRE Air Conditioning Evaluation (ACE) Facility. The authors conclude that a ventilated slab system offers not only an enhanced alternative to mechanical ventilation systems but may also match the performance of comfort cooling or conventional air conditioning systems.

Shaw et al. (1994) concluded that ventilated slab systems can effectively control slab surface temperatures and maintain comfortable environment for the occupants within acceptable limits. The potential comfort can be achieved by the large proportion of radiative heat transfer associated with the operation of ventilated slab system. The author also reported 15-16°C of a total supply air temperature drop between the supply air temperature at 40°C and the air temperature entering the

room.

Monette (1994) utilized TRANSHEAT and HOTCAN programs to simulate the thermal effect of a composite concrete and steel floor system and obtained annual energy savings of 6 to 25%.

Winwood et al. (1994) gave the evaluation of the heat transfer behaviors of an active hollow core slab by using a computational fluid dynamic package (PHOENICS). The results of the simulations could successfully reproduce the pattern of the heat transfer in the hollow core slab measured in experiments. Subsequently Winwood et al. (1997) presented a multi-node model of the active hollow core slab in a real office building in UK. This multi-node heat transfer model was incorporated into an office model within the University of Strathclyde's building simulation program ESP-r, and was validated roughly based on experiment measurements.

Winwood et al. (1997) further presented the application of the active hollow core slab in a real office building and the thermal performance and the energy consumption of the building. A floor of approximately 1875 m^2 with active hollow core slabs is installed in the building. The authors reported that the building maintained a very steady internal temperature, and provided the opportunity to shift the heating demand at daytime to night-time cheat tariff. An active hollow core slab-based building could be able to attain an energy saving up to 70 kWh/m^2 per year.

Ren and Wright (1998) developed a simplified dynamic thermal network model of a hollow core concrete slab thermal storage system and associated room air. The model can address the heat exchange between the cores and the ventilation air, the thermal storage in the building fabric, and the effect of the heat disturbances on the room. The authors reported that the simulated mass and zone temperatures agreed well with RMSE no more than 0.5°C for the average slab mass temperature and 1.0°C for the zone air temperature. However, the heat flow from one surface to the other surface through the slab has not been included in the model.

Similarly, Russell and Surendran (2001) investigated the system performance through a two-

dimensional (2D) forward (explicit) finite difference model. In this study, 1.2 m long 0.4 m deep hollow core slab is considered and the internal-space temperature was considered fixed at 21ºC whereas during the unoccupied periods, a night set-back facility was modeled which suppressed the internal temperature to a value of 18ºC. When air at 16.9ºC was assumed to be continuously circulated through three cores in 1.2 m long 0.4 m deep slab for 14 h, the cooling potential of the system increased by 335% in comparison to a traditional slab configuration with night ventilation. The slab's cooling capacity was highest with the three active cores located near the room boundary. This configuration was 45% better than the alternative three-active core configuration.

Barton et al. (2002) developed a numerical model using a two-dimensional explicit finite difference model to investigate the thermal performance of the thermally activated building component system, a hollow core ventilated slab system. The authors assumed that the slab system is exposed to constant upper and lower room air temperatures, and only heat transfer through one half of the slab depth is modeled. The model considers air flows through a continuous straight core in x-direction. The heat transfer coefficient for a part of straight core representing the bend was increased by a multiplication factor where bend sections occurred in the system. The authors concluded that the impact of the bends of the core in the slab on overall heat transfer is negligible.

Agnieszka Isanska-Cwiek (2005) presented a CFD model of an air cooled slab system in multi-story steel framed buildings to understand the performance of the system under different operating conditions. The developed model was validated with experimental data. The author concluded that the efficiency of the system will have a strong dependence on convective heat transfer coefficient and the air flow rate.

Corgnati and Kindinis (2007) proposed a dynamic simulation of an active hollow core slab system using Simulink. The slab is considered as a heat exchanger with the explicit finite difference method. The authors implemented their model within a simulation tool to investigate the

performance of the free cooling potential and indoor thermal conditions in an office. The results show that the hollow core slab system with the night ventilation operation can drastically help on reducing cooling loads in Mediterranean climate compared to the traditional night ventilation system.

Sanjuan (2011) analyzed the thermal characteristic of a typical multi-opening laminated ventilated slab (open joint ventilated façade) in Madrid, Spain by using three-dimensional steady-state and quasi-steady-state CFD model. Air velocity profiles along with temperature and heat flux have been compared with those obtained from a conventional sealed cavity façade.

Chae and Strand (2013) developed a heat balance model suitable for EnergyPlus for the ventilated slab using a modification of the conduction transfer function (CTF) formulation with heat sources/sinks. The authors have found that daily total demand savings of 23% and peak demand savings of 28% can be achieved by the ventilated slab system if outdoor air is circulated through the hollow cores during unoccupied hours using the 4 ACH air flow rate.

The theoretical results for steady state and transient conditions showed that the corner sections of the cavity loop had little impact on the overall slab performance, while the bending or corner sections are regarded as important factor to the system performance by other studies.

Ma et al. (2013) built a simplified dynamic RC model in Matlab and Simulink to study the system requirement of a thermally activated building system (TABS) equipped room. The model aimed to explore the thermal characteristic of the room and evaluate the thermal performance of TABS. The authors concluded that the effectiveness of TABS radiant cooling requires the correct selection of TABS thermal mass at normal value and façade thermal resistance within minimum envelope resistance range.

1.3 Justification of the research

The most recently developed ventilated slab system module is integrated in the EnergyPlus. EnergyPlus uses the conduction transfer functions (CTF) for building heat balance calculations. The robustness of the CTF is that there is no need to calculated temperatures within the surface, because CTF relate the current surface heat flux and temperature to previous surface heat flux and temperature (ASHRAE, 2009). This feature of CTF significantly reduces the CPU time for heat balance calculation of building envelopes. The ventilated slab system module employs the conduction transfer function equation with source/sink of heat (QTF) as expressed as follow (Strand, 1995):

$$q''_{i,t} = \sum_{m=1}^{M} X_m T_{i,t-m+1} - \sum_{m=1}^{M} Y_m T_{o,t-m+1} + \sum_{m=1}^{k} F_m q''_{i,t-m} + \sum_{m=1}^{M} W_m q_{source,t-m+1}$$

where,

X_m = Inside CTF coefficient

Y_m = Cross CTF coefficient

T_i = Inside face temperature

T_o = Outside face temperature

F_m = Flux CTF coefficient

W_m = QTF inside term for the heat source/sink

q'' = surface heat balance including radiation from other surface, solar radiation, and convection heat flux on the inside surface

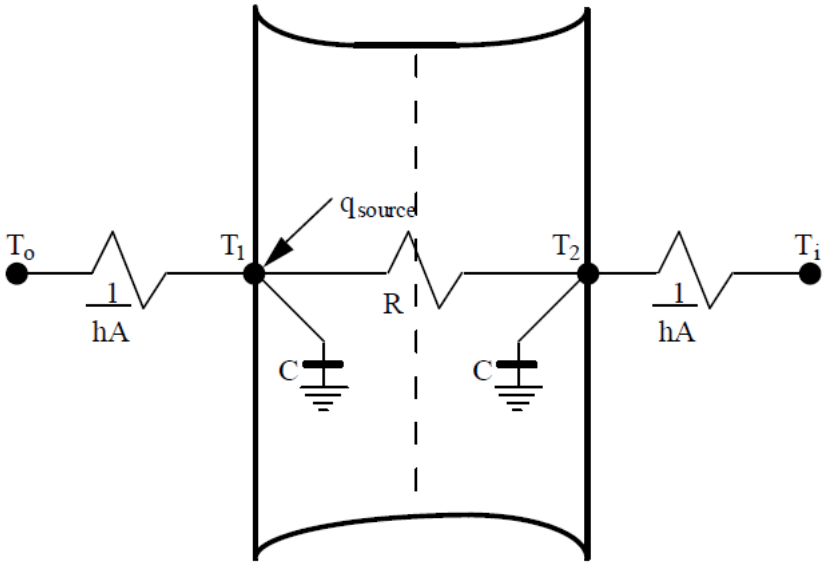

Figure 1.4: Two node state space example with a heat source at node 1 (EnergyPlus, 2013)

The two-node example introduced by Seem (1987) is utilized to examine the extension of the state space method to include heat sources or sinks. The nodal equations for the finite difference network are as follow:

$$C\frac{dT_1}{dt} = hA(T_o - T_1) + \frac{T_2 - T_1}{R} + q_{source}A$$

$$C\frac{dT_2}{dt} = hA(T_1 - T_2) + \frac{T_1 - T_2}{R}$$

$$q''_i = h(T_i - T_2)$$

$$q''_o = h(T_1 - T_o)$$

where,

$R = \frac{l}{kA}$

$C = \frac{\rho c_p V}{2}$

A = surface area

One of drawbacks of CTF calculation in EnergyPlus is that it is hard to monitor any internal processes inside building envelope. EnergyPlus thus provide an implicit conduction finite difference scheme, so called CondFD. The CondFD model in EnergyPlus above version 5 uses a Crank-Nicholson scheme, which is unconditionally stable (EnergyPlus, 2013). The CondFD involves a finite difference scheme in EnergyPlus, and now we can monitor the internal heat transfer processes inside building envelopes. But the CondFD in EnergyPlus is yet one-dimensional calculation as shown in Figure 1.5. CondFD is not able to accurately address the thermal bridge effect at floor-wall joint.

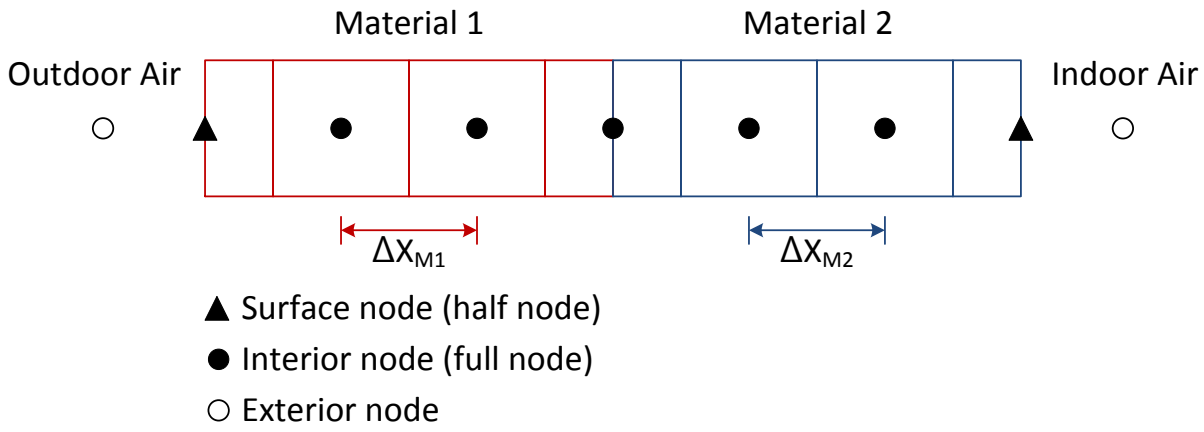

Figure 1.5: EnergyPlus finite difference node types (Tabares-Velasco, 2012)

For the building envelope and system design as well as the control strategy development, modeling the heat transfer processes associated with the hollow core slab simultaneously is important. Literature survey shows heat transfer models for the active slab can be categorized as two kinds as follows.

- The steady or the dynamic one-, two-, and three-dimensional heat transfer models. Numerical methods such as the finite difference and finite element method are used for two- or three-dimensional problem solving.

- The simplified steady-state or dynamic thermal network models which only consider the thermal resistance and heat capacity.

RC network models (i.e., simplified dynamic thermal network) are simple and easy to be developed, and can be integrated in existing whole building simulation packages for energy performance evaluation and project design. But simplified thermal network model may deteriorate accuracy of the model. Furthermore, most of the models developed for slab ventilated systems do not properly address thermal bridge effects which can be magnified due to the controlled slab temperatures. Indeed, higher slab surface temperature for hollow core ventilated slab system could possibly increase heat losses through slab-wall joints during the heating and cooling operation. There has been a lack of studies on how thermal bridges influence the performance of ventilated slab systems. Therefore, the dynamic numerical model of the hollow core ventilated slab system for practical applications with good accuracy needs to be investigated more.

Moreover, hollow core ventilated slab systems may be subject to condensation accumulation within the cores since air water vapor mixture is supplied and flows the hollow cores. If condensation occurs and condensate water remains inside hollow cores for a long time, mold can form and grow. Molds and fungi are most likely to affect and degrade the indoor air quality within buildings Thus, the potential risk of condensation for the hollow core ventilated slab systems should be carefully examined.

The literature survey indicates that significant energy savings can be achieved when the building thermal mass is actively used to cool the building in appropriate way. These active hollow core slabs are widely used in Europe, South Africa, and the Middle East countries. It is reported that the active hollow core slabs can achieve up to 50 W/m^2 cooling load reduction in Scandinavian countries and South Africa. The hollow core ventilated slab system can achieve up to 25% cooling energy use reduction. The peak cooling load or heat load can also be greatly reduced compared to

when conventional air-conditioning systems are used as supplements.

Although there are numerous researches on these active cooling/heating slabs, the works on the modeling of the hollow core ventilated slab system for practical applications with good accuracy is insufficient; the performance evaluations of actual building systems using active slabs for ventilation are still limited. The current available analysis level of water condensation that may occur inside hollow cores is also not complete and insufficient to assess potential indoor air quality issues within buildings served by ventilated slab systems. Potential and the duration of condensation problems inside hollow cores should be addressed in more details. More works on the thermally activated slabs are worthwhile for promoting these slabs to be used in energy efficient buildings for reduce energy expenses and improving occupant thermal comfort especially in Asia and the United States. These works may include development of dynamic simulation environment such as combination of RC network for exterior wall and FDM numerical solution for floor and ceiling where a hollow core ventilated slab system is installed, parameter identification of these models, performance evaluation of buildings with active slabs, development of enthalpy heat exchanger model to detect condensation issue and optimal control strategy to maximize the energy saving potentials while maintaining the indoor thermal comfort.

1.4 Research objectives

Numerous studies have shown that building components such as floors, ceilings, and walls can serve as passive thermal storage systems and effectively reduce thermal peak loads. The hollow core ventilated slab system actively utilizes building's mass by passing a hot/cold air within channels inside precast slab, enhancing the thermal-storage capabilities and the heat removal capabilities by actively using air channels as heat source/sinks. Various configurations of thermally activated slab systems have been employed in northern/western Europe, Australia and Middle East

region. Compared to conventional air systems, hollow core slab systems have the potential to greatly reduce energy use to heat and/or cool buildings. In particular, it is reported that ventilated slab systems can be effective to reduce the daytime cooling demand for various types of buildings. In addition, the benefits of ventilated slab systems include better thermal comfort, reduced heating and cooling energy consumption, and improved ventilation control compared to all air HVAC systems.

Most of the models developed for ventilated slab systems do not take account the multi-dimensional heat transfer associated with these systems. For instance, thermal bridge effects can be magnified for ventilated slab systems due to the controlled surface temperatures. Specifically, lower slab surface temperature for hollow core ventilated slab system could increase heat gains through slab edges during the cooling operation. This research focuses on the development of a comprehensive simulation environment to assess energy performance more accurately and explore optimal controls of the hollow core ventilated slab systems. The developed simulation environment combines a transient finite difference solution of a ventilated slab system with an RC network model for a multi-floor building. The developed simulation environment takes into account ventilated slab systems' thermal bridge effects on the energy performance of multi-floor buildings. The predictions of the developed simulation environment will be verified and validated. In addition, several parametric analyses will be performed to determine the performance of ventilated slab systems under various design and operating conditions.

Three-dimensional slab and wall joint coupled heat transfer model will be developed. A series of parametric studies for three-dimensional heat transfer will be carried out. The group of simulations will provide data for investigation of geometric effects including size and aspect ratio.

Models for enthalpy heat exchanger, condensate rate, and evaporate rate specific for hollow core ventilated slab systems will be first implemented in the simulation environment. Then, the

simulation environment will be applied to detect any potential water condensation inside the hollow cores or on the ceiling surfaces. Moreover, the developed simulation environment will be used to estimate the amount of condensate water, the water condensation hours, and the change in humidity ratio of the supply air used to condition indoor spaces.

Finally, the simulation environment will be utilized to develop optimal control strategies to operate ventilation slab systems effectively in order to enhance its energy performance compared to conventional control strategies and improve its thermal comfort for office buildings. A series of comparative analyses of the performance of the ventilated slab systems against all-air systems (i.e., variable air volume systems) will be utilized to develop some design and operation guidelines for the ventilated slab systems in order to foster their implementation in the US buildings.

1.5 Organization of the thesis

This thesis presents a detailed analysis of the performance of ventilated slab systems under various design and operating conditions using a proposed simulation environment for multi-floor buildings. A simulation environment is constituted by combining a two-dimensional transient FDM heat transfer model with RC thermal network model to assess the energy use and thermal comfort level within conditioned zones served by the hollow core ventilated slab system.

The thesis is organized into six chapters. The following sections describe briefly the scope of each chapter.

Chapter 1 presents an overview of some applications of the hollow core ventilated slab system and the current analysis methods and control strategies available to evaluate and operate the ventilated slab systems utilized within residential and commercial buildings.

In Chapter 2, a two-dimensional transient heat transfer model for a hollow core ventilated slab system is developed using the implicit finite difference method (FDM). The predictions from the

one-dimensional FDM numerical solution are validated with the experimental data. A series of parametric and sensitivity analysis is carried out to evaluate the performance of a hollow core ventilated slab systems. In particular, a series of the parametric analyses explores the effect of supply air inlet temperature, air mass flow rate, hollow core depth, and hollow core diameter on the performance of the hollow core ventilated slab system.

Chapter 3 presents relationship between three dimensional and two dimensional model. The average heat transfer along the floor as a function of perimeter as well as average heat transfer per unit area as a function of A/P is analyzed. Similarly, when the heat source exists inside the floor the heat flux on the floor surface is explored.

Chapter 4 outlines the basic features of the comprehensive simulation environment developed to assess the energy use and thermal comfort specific to a hollow core ventilated slab systems. The simulation environment includes the transient FDM two-dimensional model for ventilated slab system combined with an RC network model for exterior walls and windows in multi-story building. The predictions from the developed simulation environment are verified with results obtained from EnergyPlus, a detailed whole-building energy simulation tool. Furthermore, the impact of thermal bridging effects on energy consumption for ventilated slab systems is evaluated by using the developed simulation environment tool.

Chapter 5 describe enthalpy heat exchanger, condensate rate, and evaporate rate models for modeling the performance of hollow core ventilated slab systems. In particular, basic principles for the enthalpy heat exchanger model are derived and described in this chapter. In addition, the heat and mass air balance model is implemented in the simulation environment and verified with EnergyPlus results. Finally, specific design and operating conditions are investigated to assess when water condensation occurs either inside the hollow cores or along the ceiling surfaces. The annual water condensation hours are estimated and analyzed for office buildings located in three

different humid US climate zones.

Chapter 6 presents the evaluation of optimal control strategies specific for hollow core ventilated slab systems. In particular, optimum controls are developed not only to improve zone air set-point temperature regulation while maintaining the thermal comfort of occupants but also to minimize cooling energy costs for US office buildings. Some guidelines for optimal control of ventilated slab systems are developed for various design specifications, utility rates, and operation conditions. Chapter 7 is to summarize the main findings from the modeling, evaluation, and optimal control of ventilated slab systems to air conditioning commercial buildings. In addition, Chapter 7 provides general guidelines and suggest viable future work to enhance the design and operation of ventilated slab systems to improve the overall energy efficiency of buildings.

CHAPTER 2: DEVELOPMENT OF THE HOLLOW CORE VENTILATED SLAB SYSTEM MODEL

2.1 Introduction

Previous studies of the hollow core ventilated slab systems are based on simplified thermal analysis. Most of the numerical models developed for ventilated slab systems do not take account of the multi-dimensional heat transfer associated with the systems. For example, Energyplus, the most widely well-known whole building simulation program released by Department of Energy (DOE), uses state space method to establish the conduction transfer functions (CTFs) based on the solution of one-dimensional heat transfer function for building envelopes (Seem, 1987; Strand, 1995). One-dimensional heat transfer function neglects thermal bridging through the slab and wall joint as shown in Figure 2.1.

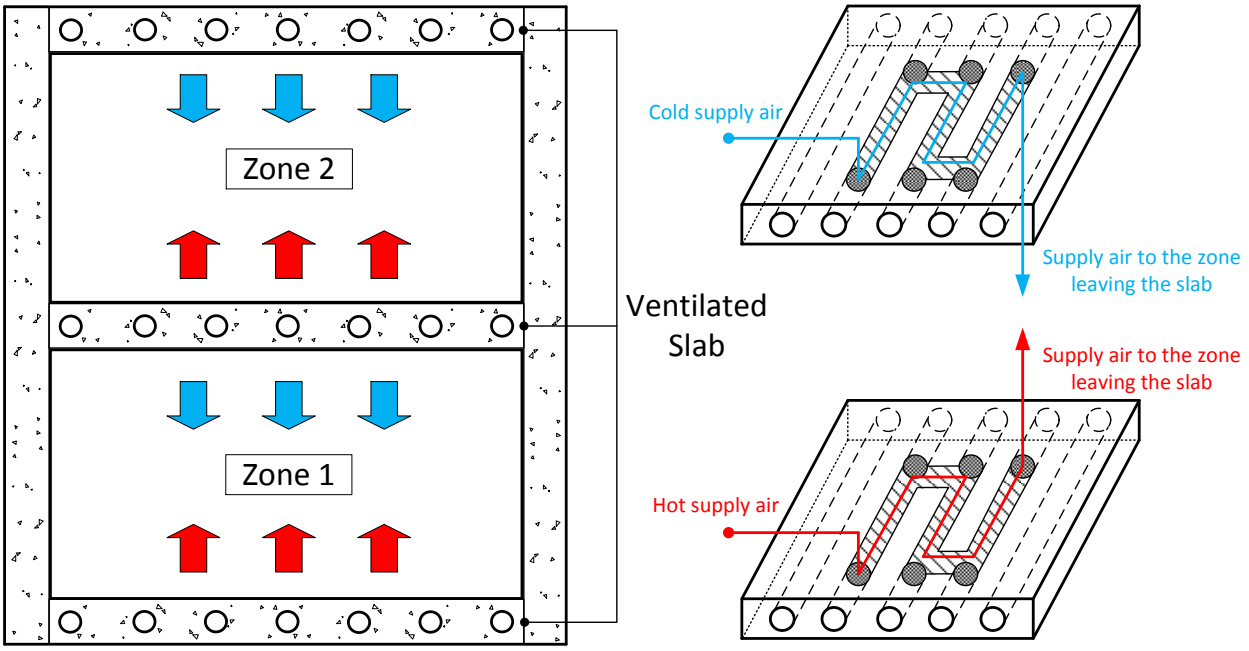

Figure 2.1: Schematic of the hollow core ventilated slab system

Thermal bridge effects can be magnified for ventilated slabs due to the controlled surface temperatures. Indeed, low slab surface temperature of the hollow core ventilated slab system could possibly increase heat gains through slab edges during the cooling operation. This research focuses on the development of a comprehensive simulation environment to assess energy performance more accurately and explore optimal controls of the hollow core ventilated slab systems. The first step is to develop a transient finite difference solution of a hollow core ventilated slab system. Slab-wall joint is a part of the numerical ventilated slabs model so impact of thermal bridging on the energy performance of ventilated slabs can be accurately evaluated. Besides, the numerical model of the ventilated slabs can be integrated with an RC network model of exterior walls to establish the simulation environment for a multi-floor building.

This chapter focuses on the development of a numerical model for a hollow core ventilated slab system using finite difference method (FDM). Finite difference equation formulation is briefly described. The prediction of FDM numerical model are validated with previously reported experimental results. A series of parametric analyses is carried out to determine the effect of a wide range of design and operating parameters for ventilated slabs.

2.2 Development of numerical solution for the ventilated slab systems

2.2.1 Differential equation formulation

Two dimensional numerical solutions for ventilated slab systems are developed by adding heat generation and extraction sources within the floor. By adding these sources, the heat conduction equation can be formulated as follows: (Pantankar, 1980)

$$\rho c_p \frac{\partial T}{\partial t} = k\frac{\partial^2 T}{\partial x^2} + k\frac{\partial^2 T}{\partial y^2} + q \qquad (2.1)$$

Where,

ρ = density [kg/m^3]

c_p = heat capacity [J/kg˚C]

k = thermal conductivity [kg/m^3]

t = time [sec]

q = generated heating or extracted cooling rate [W/m^3]

The heat conduction equation with heat sources represented by Eq. (2.1) can be solved, using a control volume approach and pure implicit finite difference method. The control volume and its associated nodal dimensions are shown in Figure 2.2 for a typical heat source node.

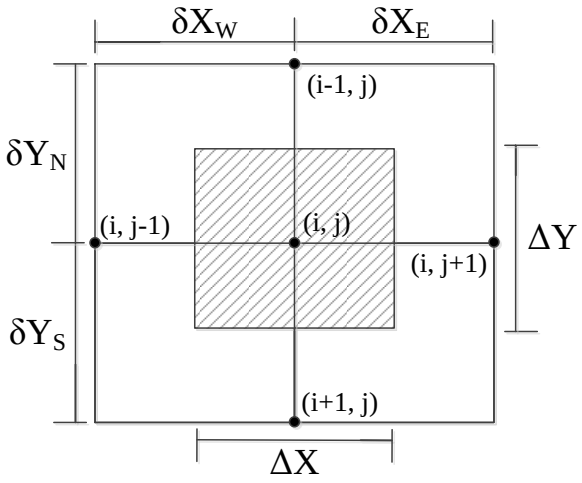

Figure 2.2: Control volume for the two-dimensional heat conduction problem with heat generation source

2.2.2 Finite difference formulation

The principle of conservation of energy for the control volume is defined as follows (Kreith and Bohn, 2001):

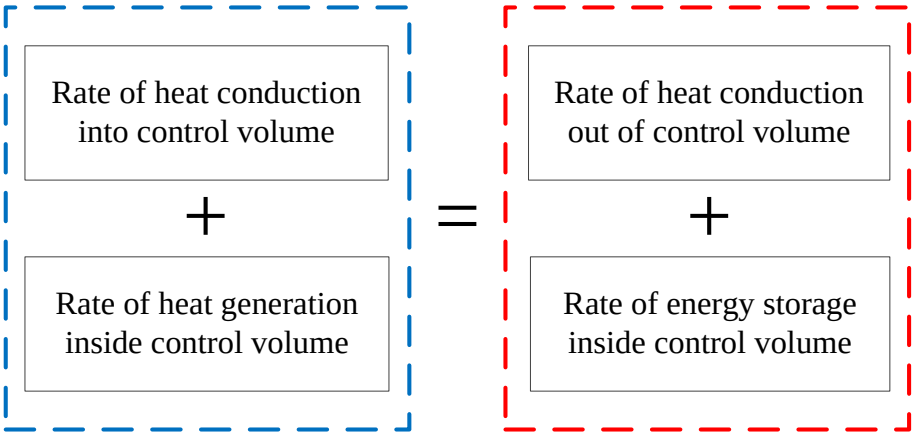

The energy conservation principle can be expressed using Eq. (2.2):

$$\begin{aligned} & -kA\frac{dT}{dx}\bigg|_{x} - kA\frac{dT}{dy}\bigg|_{y} + qA\Delta x \\ & = -kA\frac{dT}{dx}\bigg|_{x+\Delta x} - kA\frac{dT}{dy}\bigg|_{y+\Delta y} + \rho c_p A\Delta x \frac{dT(x+\frac{\Delta x}{2},t)}{dt} \end{aligned} \tag{2.2}$$

In this section, the solution of the implicit difference equation will be demonstrated. For two dimensional finite difference grid with non-uniform thermal conductivity, k, and different nodal distances, this form can be transformed to

$$\begin{aligned} & -k_W\Delta Y\frac{T_{i,j}^{p+1}-T_{i,j-1}^{p+1}}{\delta x_w} - k_S\Delta X\frac{T_{i,j}^{p+1}-T_{i+1,j}^{p+1}}{\delta y_S} \\ & = -k_E\Delta Y\frac{T_{i,j+1}^{p+1}-T_{i,j}^{p+1}}{\delta x_E} - k_N\Delta X\frac{T_{i-1,j}^{p+1}-T_{i,j}^{p+1}}{\delta y_N} + \rho c_p\Delta X\Delta Y\frac{T_{i,j}^{p+1}-T_{i,j}^{p}}{\Delta t} \end{aligned} \tag{2.3}$$

Where,

$T_{i,j}^{p}$ = temperature as i and j is noted spatial node and p is for the present time.

ΔX = distance between nodes in x-axis

ΔY = distance between nodes in y-axis

Δt = time step

Rearranging Eq. (2.3) to put terms with p+1 on the left-hand-side and terms with p on the right-hand-side gives

$$\left(\frac{\rho c_p \Delta X \Delta Y}{\Delta t} + \frac{k_E \Delta Y}{\delta x_E} + \frac{k_W \Delta Y}{\delta x_w} + \frac{k_N \Delta x}{\delta y_N} + \frac{k_S \Delta X}{\delta y_S}\right) T_{i,j}^{p+1} - \left(\frac{k_E \Delta Y}{\delta x_E}\right) T_{i,j+1}^{p+1} - \left(\frac{k_W \Delta Y}{\delta x_w}\right) T_{i,j-1}^{p+1} - \left(\frac{k_N \Delta X}{\delta y_N}\right) T_{i-1,j}^{p+1} - \left(\frac{k_S \Delta X}{\delta y_S}\right) T_{i+1,j}^{p+1} = \frac{\rho c_p \Delta X \Delta Y}{\Delta t} T_{i,j}^{p} \quad (2.4)$$

With some additional rearrangements, the differential equation Eq. (2.1) can be discretized as indicated as follows:

$$a_p T_p - a_E T_E - a_W T_W - a_N T_N - a_S T_S = a_p^0 T_p^0 + q \quad (2.5)$$

$$a_p = a_E + a_W + a_N + a_S + a_p^0$$

$$a_E = \frac{\Delta Y}{\frac{\delta x_E}{k_E}}$$

$$a_W = \frac{\Delta Y}{\frac{\delta x_W}{k_W}}$$

$$a_N = \frac{\Delta X}{\frac{\delta y_N}{k_N}}$$

$$a_S = \frac{\Delta X}{\frac{\delta y_S}{k_S}}$$

$$a_p^0 = \frac{\rho c_p \Delta x \Delta y}{\Delta t}$$

$$q = \varepsilon\left(\dot{m}c_p\right)_{air}(T_{air,in} - T_s)$$

The generated heat, q, is identical to the value calculated from Eq.(2.25). There could be numerous numbers of heat source/sink nodes where the core exists involves heat generation term, q. The rest of nodes where the core does not exist employ the 2-dimensional generic heat conduction equation without heat generation. To calculate q_{max}, the only unknown parameter is source location temperature, T_s. It is feasible to use the weighted average temperature of all nodes at core level as the source location temperature. Thus, using this source location temperature, the maximum heat transfer from the ventilated slab system can be calculated. The calculation of the effectiveness of the heat exchanger, ε, is straight forward. Eventually the actual heat generation can be obtained by Eq.(2.25). Note that it is empirically found that the source location temperature is very important parameter to determine generated heat by source term in heat conduction equation.

2.2.3 Boundary Conditions

Equations for the boundary conditions for a two-dimensional slab heat transfer problem are derived based on the principle of conservation of energy for the control volume. Basically the term in left-hand-side is the rate of heat conduction into a control volume and right-hand-side term presents the rate of heat conduction out of the control volume plus rate of energy storage inside the control volume. Note that long-wave radiation and short-wave radiation heat gains are not included in the equations. Equations for boundary conditions listed below are derived by solving conduction and convection heat transfer equations.

- Left Top Corner

$$-k_S\frac{\Delta X}{2}\frac{T_{i,j}^{p+1}-T_{i+1,j}^{p+1}}{\delta y_S} = -k_E\frac{\Delta Y}{2}\frac{T_{i,j+1}^{p+1}-T_{i,j}^{p+1}}{\delta x_E}+h\frac{\Delta X}{2}(T_{i,j}^{p+1}-T_\infty)+\rho c_p\frac{\Delta X}{2}\frac{\Delta Y}{2}\frac{T_{i,j}^{p+1}-T_{i,j}^{p}}{\Delta t} \quad (2.6)$$

- Top Edge

$$-k_W\frac{\Delta Y}{2}\frac{T_{i,j}^{p+1}-T_{i,j-1}^{p+1}}{\delta x_w}-k_S\Delta X\frac{T_{i,j}^{p+1}-T_{i+1,j}^{p+1}}{\delta y_S} = -k_E\frac{\Delta Y}{2}\frac{T_{i,j+1}^{p+1}-T_{i,j}^{p+1}}{\delta x_E}+h\Delta X(T_{i,j}^{p+1}-T_\infty)+\rho c_p\Delta X\frac{\Delta Y}{2}\frac{T_{i,j}^{p+1}-T_{i,j}^{p}}{\Delta t} \quad (2.7)$$

- Right Top Corner

$$-k_W\frac{\Delta Y}{2}\frac{T_{i,j}^{p+1}-T_{i,j-1}^{p+1}}{\delta x_w}-k_S\frac{\Delta X}{2}\frac{T_{i,j}^{p+1}-T_{i+1,j}^{p+1}}{\delta y_S} = h\frac{\Delta X}{2}(T_{i,j}^{p+1}-T_\infty)+\rho c_p\frac{\Delta X}{2}\frac{\Delta Y}{2}\frac{T_{i,j}^{p+1}-T_{i,j}^{p}}{\Delta t} \quad (2.8)$$

- Left Edge (Adiabatic)

$$-k_S\frac{\Delta X}{2}\frac{T_{i,j}^{p+1}-T_{i+1,j}^{p+1}}{\delta y_S} = -k_E\Delta y\frac{T_{i,j+1}^{p+1}-T_{i,j}^{p+1}}{\delta x_E}-k_N\frac{\Delta x}{2}\frac{T_{i-1,j}^{p+1}-T_{i,j}^{p+1}}{\delta y_N}+\rho c_p\frac{\Delta X}{2}\Delta Y\frac{T_{i,j}^{p+1}-T_{i,j}^{p}}{\Delta t} \quad (2.9)$$

- Right Edge (Adiabatic)

$$-k_W\Delta Y\frac{T_{i,j}^{p+1}-T_{i,j-1}^{p+1}}{\delta x_w}-k_S\frac{\Delta X}{2}\frac{T_{i,j}^{p+1}-T_{i+1,j}^{p+1}}{\delta y_S} = -k_N\frac{\Delta X}{2}\frac{T_{i-1,j}^{p+1}-T_{i,j}^{p+1}}{\delta y_N}+\rho c_p\frac{\Delta X}{2}\Delta Y\frac{T_{i,j}^{p+1}-T_{i,j}^{p}}{\Delta t} \quad (2.10)$$

- Left Bottom Corner

$$h\frac{\Delta X}{2}(T_\infty-T_{i,j}^{p+1}) = -k_E\frac{\Delta Y}{2}\frac{T_{i,j+1}^{p+1}-T_{i,j}^{p+1}}{\delta x_E}-k_N\frac{\Delta X}{2}\frac{T_{i-1,j}^{p+1}-T_{i,j}^{p+1}}{\delta y_N}+\rho c_p\frac{\Delta X}{2}\frac{\Delta Y}{2}\frac{T_{i,j}^{p+1}-T_{i,j}^{p}}{\Delta t} \quad (2.11)$$

- Bottom Edge

$$-k_W\frac{\Delta Y}{2}\frac{T_{i,j}^{p+1}-T_{i,j-1}^{p+1}}{\delta x_w}+h\Delta X(T_\infty-T_{i,j}^{p+1}) = -k_E\frac{\Delta Y}{2}\frac{T_{i,j+1}^{p+1}-T_{i,j}^{p+1}}{\delta x_E}-k_N\Delta X\frac{T_{i-1,j}^{p+1}-T_{i,j}^{p+1}}{\delta y_N}+\rho c_p\Delta X\frac{\Delta Y}{2}\frac{T_{i,j}^{p+1}-T_{i,j}^{p}}{\Delta t} \quad (2.12)$$

- Right Bottom Corner

$$-k_W\frac{\Delta Y}{2}\frac{T_{i,j}^{p+1}-T_{i,j-1}^{p+1}}{\delta x_w}+h\frac{\Delta X}{2}(T_\infty-T_{i,j}^{p+1}) = -k_N\frac{\Delta X}{2}\frac{T_{i-1,j}^{p+1}-T_{i,j}^{p+1}}{\delta y_N}+\rho c_p\frac{\Delta X}{2}\frac{\Delta Y}{2}\frac{T_{i,j}^{p+1}-T_{i,j}^{p}}{\Delta t} \quad (2.13)$$

- Between Layers (Say slab is constructed with 2 materials and they are horizontall y separated)

$$-k_{W_1}\frac{\Delta Y}{2}\frac{T_{i,j}^{p+1}-T_{i,j-1}^{p+1}}{\delta x_w}-k_{W_2}\frac{\Delta Y}{2}\frac{T_{i,j}^{p+1}-T_{i,j-1}^{p+1}}{\delta x_w}-k_S\Delta X\frac{T_{i,j}^{p+1}-T_{i+1,j}^{p+1}}{\delta y_S} = -k_{E_1}\frac{\Delta Y}{2}\frac{T_{i,j+1}^{p+1}-T_{i,j}^{p+1}}{\delta x_E}-k_{E_2}\frac{\Delta Y}{2}\frac{T_{i,j+1}^{p+1}-T_{i,j}^{p+1}}{\delta x_E}-k_N\Delta X\frac{T_{i-1,j}^{p+1}-T_{i,j}^{p+1}}{\delta y_N} + (\rho_1 c_{p_1}\Delta X\frac{\Delta Y}{2}+\rho_2 c_{p_2}\Delta X\frac{\Delta Y}{2})\frac{T_{i,j}^{p+1}-T_{i,j}^{p}}{\Delta t} \quad (2.14)$$

2.2.4 Effectiveness-NTU heat exchanger model

The actual heat transfer between the building element (i.e. slab) and the ventilated slab system is related to the temperature of the slab at the source location as well as the fluid inlet and outlet temperatures. To model the ventilated slab system, it is assumed that the air inlet temperature and the mass flow rate are known and the remaining parameters must be calculated (EnergyPlus, 2013). The air is a fluid that travels through a hollow core ventilated slab system. It is assumed that the thermal properties of the air do not vary significantly over the length of the core. The ventilated

slab system can be thought of as a heat exchanger. The effectiveness-NTU heat exchanger algorithm is used to define the heat flux to the slab from the heat sources. The effectiveness-NTU heat exchanger method is convenient to use when the air outlet temperature (at the end of path) is not known. Because the effectiveness-NTU heat exchanger algorithm does not involve any of the outlet temperatures. (Uiuc, 2005; Kreith and Bohn, 2001) The calculated heat flux can be thought of as a heat generation, and then employed to heat balance calculation using finite difference method.

Using these assumptions and the effectiveness-NTU heat exchanger algorithm, several equations can be defined which establish the relationship between the heat source (i.e. the ventilated slab system) and the air temperatures.

A heat balance on the hydronic loop result in Eq. (2.15)

$$\mathrm{q} = \left(\dot{m}c_p\right)_{air}(T_{air,in} - T_{air,out}) \tag{2.15}$$

where,

q = the heat transferred between the hydronic loop and the building element [W]

$\dot{m}$ = the mass flow rate of the air [kg/s]

c_p = the specific heat of the air [J/kg-K]

$T_{air,in}$ = the inlet temperature of the air [K]

$T_{air,out}$ = the outlet temperature of the air [K]

In accordance to the Second Law of Thermodynamics, the maximum heat transfer is:

$$\mathrm{q}_{\max} = \left(\dot{m}c_p\right)_{air}(T_{air,in} - T_s) \tag{2.16}$$

where,

$\mathrm{q}_{\max}$ = the maximum amount of heat transfer [W]

T_s = the source location temperature [K]

The effectiveness of the heat exchanger, ε, is defined as the ratio of the actual energy transfer to the maximum amount of energy transfer.

$$\varepsilon \equiv \frac{q}{q_{max}} \tag{2.17}$$

When one fluid is stationary for a heat exchanger, the effectiveness can be related to the number of transfer units (NTU). (Incorpera, 2006)

$$\varepsilon = 1 - e^{-NTU} \tag{2.18}$$

where NTU is defined by:

$$NTU \equiv \frac{UA}{(\dot{m}c_p)_{air}} \tag{2.19}$$

Since the effect of hollow cores are assumed to be neglected, the only term present in the heat transfer coefficient, UA, is a convection term as follow:

$$UA = h_{air}(\pi DL) \tag{2.20}$$

where,

h_{air} = the convective coefficient of the air [W/m^2-K]

D = the inside diameter of the core, [m]

L = the total length of the core. [m]

The convection coefficient, h, can be calculated from the internal flow correlations which are related to the Nusselt number, the Reynolds number, and the Prandtl number. The convective coefficient of air can be determined using the Dittus-Boelter correlation.

$$h_{air} = Nu \frac{k_{air}}{D} \tag{2.21}$$

where,

$$\text{Laminar internal flow (Re<2300): } Nu = \frac{hD}{k_{air}} = 3.66 \tag{2.22}$$

$$\text{Turbulent internal flow: } Nu = \frac{hD}{k_{air}} = 0.023 Re^{4/5} Pr^{n} \tag{2.23}$$

with n = 0.4 for heating of the fluid, and n=0.3 for cooling of the fluid,

and,

k_{air} = the thermal conductivity of the air, [W/m-K]

Pr = the Prandtl number of the air,

Re = the Reynolds number.

The Reynolds number determines the type of the flow. The Reynolds number is defined by:

$$Re = \frac{4\dot{m}}{\pi \mu D} \tag{2.24}$$

where,

μ = is the absolute viscosity of air. [N s/m^2]

Now q_{max} can be calculated using all equations indicated above. Rearranging Eq. (2.17) gives us the heat generation from the hydronic loop. To utilize the heat generation term in finite difference method, the unit has to be converted to W/m^3 as Eq. (2.25).

$$q \equiv \frac{\varepsilon q_{max}}{\frac{\pi D^2}{4} L} \tag{2.25}$$

2.2.5 Construction of linear system

With some additional rearrangements, for example, we can rewrite Eq. (2.6) and Eq. (2.7) as follows:

$$\left(\frac{\rho c_p}{\Delta t}\frac{\Delta X}{2}\frac{\Delta Y}{2}+\frac{k_S\Delta X}{2\delta y_S}+\frac{k_E\Delta Y}{2\delta x_E}+\frac{h\Delta X}{2}\right)T_{i,j}^{p+1}-\frac{k_E\Delta Y}{2\delta x_E}T_{i,j+1}^{p+1}-\frac{k_S\Delta X}{2\delta y_S}T_{i+1,j}^{p+1} = \frac{\rho c_p}{\Delta t}\frac{\Delta X}{2}\frac{\Delta Y}{2}T_{i,j}^{p}+\frac{h\Delta X}{2}T_\infty \tag{2.26}$$

$$\left(\frac{\rho c_p}{\Delta t}\Delta X\frac{\Delta Y}{2}+\frac{k_W\Delta Y}{2\delta x_W}+\frac{k_S\Delta X}{\delta y_S}+\frac{k_E\Delta Y}{2\delta x_E}+h\Delta X\right)T_{i,j}^{p+1}-\frac{k_W\Delta Y}{2\delta x_W}T_{i,j-1}^{p+1}-\frac{k_S\Delta X}{\delta y_S}T_{i+1,j}^{p+1} - \frac{k_E\Delta Y}{2\delta x_E}T_{i,j+1}^{p+1} = \frac{\rho c_p}{\Delta t}\Delta X\frac{\Delta Y}{2}T_{i,j}^{p}+h\Delta X T_\infty \tag{2.27}$$

This additional rearrangements can be applied to all equations for boundary conditions, Eq. (2.6) to Eq. (2.14). The entire set of difference equations with the additional rearrangement and simplification of coefficients for a floor can be expressed in matrix form as follows:

$$\begin{bmatrix} a_{P_1} & -a_{E_1} & \cdots & -a_{S_1} & & & & & & & \\ -a_{W_2} & a_{P_2} & -a_{E_2} & \cdots & -a_{S_2} & & & & & & \\ & -a_{W_3} & a_{P_3} & -a_{E_3} & \cdots & -a_{S_3} & & & & & \\ & & & & \ddots & & & & & & \\ & & & -a_{N_m} & \cdots & -a_{W_m} a_{P_m} & -a_{E_m} & \cdots & -a_{S_m} & & \\ & & & & & & \ddots & & & & \\ & & & & & & -a_{N_{n-2}} & \cdots & -a_{W_{n-2}} & a_{P_{n-2}} & -a_{E_{n-2}} \\ & & & & & & & -a_{N_{n-1}} & \cdots & -a_{W_{n-1}} & a_{P_{n-1}} & -a_{E_{n-1}} \\ & & & & & & & & -a_{N_n} & \cdots & -a_{W_n} & a_{P_n} \end{bmatrix} \begin{bmatrix} T_1^{p+1} \\ T_2^{p+1} \\ T_3^{p+1} \\ \vdots \\ T_m^{p+1} \\ \vdots \\ T_{n-2}^{p+1} \\ T_{n-1}^{p+1} \\ T_n^{p+1} \end{bmatrix}$$

$$= \begin{bmatrix} a_{P_1}^0 \mathrm{T}_{\mathrm{i,j}}^{\mathrm{p}} + a_{S_1} \mathrm{T}_\infty \\ a_{P_2}^0 \mathrm{T}_{\mathrm{i,j}}^{\mathrm{p}} + a_{S_2} \mathrm{T}_\infty \\ a_{P_3}^0 \mathrm{T}_{\mathrm{i,j}}^{\mathrm{p}} + a_{S_3} \mathrm{T}_\infty \\ \vdots \\ a_{P_m}^0 \mathrm{T}_{\mathrm{i,j}}^{\mathrm{p}} + q \\ \vdots \\ a_{P_{n-2}}^0 \mathrm{T}_{\mathrm{i,j}}^{\mathrm{p}} + a_{N_{n-2}} \mathrm{T}_\infty \\ a_{P_{n-1}}^0 \mathrm{T}_{\mathrm{i,j}}^{\mathrm{p}} + a_{N_{n-1}} \mathrm{T}_\infty \\ a_{P_n}^0 \mathrm{T}_{\mathrm{i,j}}^{\mathrm{p}} + a_{N_n} \mathrm{T}_\infty \end{bmatrix}$$

Blank placeholders in the matrix represent zeros. We can rewrite the matrix as

$$\mathrm{AT} = \mathrm{B}$$

and by inverting the matrix A, the solution for the temperature vector T is

$$\mathrm{T} = \mathrm{A}^{-1}\mathrm{B}$$

BiConjugate gradients squared method is employed to solve the linear system. Various alternative solution methods exist to solve the problem. We can use Gauss elimination method, iteration method (i.e. Jacobi iteration, Gauss-Seidel iteration or etc.) or LU decomposition method and so on.

2.2.6 Mesh generation

A non-uniform geometric discretization is applied to reduce computational CPU time as well as memory requirements. Generally, the discretization grid is very fine near the surface boundaries and/or interactions between two different materials as well as near boundaries of heat sources. The grid is then gradually expanded in the area where relatively smaller temperature changes are expected as illustrated in Figure 2.3 near a hollow core within a concrete slab.

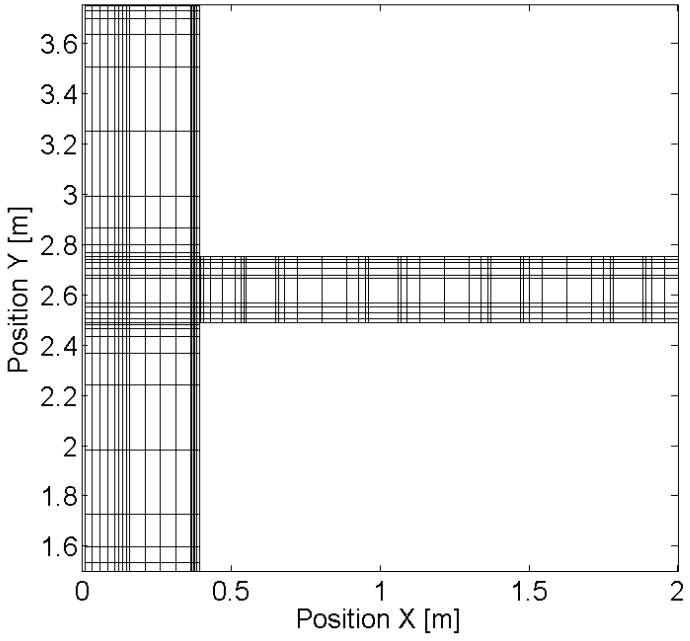

Figure 2.3: Selected mesh configuration used for the two-dimensional building model

2.3 Validation of a numerical model

The developed numerical model of a hollow core ventilated slab system is validated with experiment data reported by Steve Willis and John Wilkins in 1993. Willis and Wilkins (1993) evaluated the thermal performance of a hollow core ventilated slab system installed in British Research Establishment (BRE) Air Conditioning Evaluation (ACE) facility. An environmental room is 4.8 m by 4 m by 3.75 m, and it represents a small highly insulated office building in contact with office space above, below and on each internal side (Willis and Wilkins, 1993). The temperature of adjacent office space is assumed to be maintained at 20°C for 24 hours. A floor and a ceiling structure consists of four hollow core concrete floor modules. A thermal conductivity of the concrete floor modules is 1.2 W/m-K, its density is 1750 kg/m^3 and the specific heat is 800 J/kg-°C. Dimensions of each module is 4 m by 1.2 m by 0.27 m. Each module has five cylindrical bores of 0.18 m in diameter. A ceiling is covered with 35 mm screed. Only middle two of the four concrete slab modules are used as an air path to supply the room. Air supply rate of 40 litres/s is supplied to the room as CIBSE recommends. Typical operation during winter season in Sweden is to supply and circulate air at 40°C through the slabs prior to occupancy.

Figure 2.4 depicts the effect of supplying 40°C air through a cold hollow core ventilated slab. A temperature drop of 15 to 16°C at the air outlet diffuser was evident by the experiment. A prediction of the slab mass and the air outlet temperature obtained from the developed numerical model is also compared with the experimental data in Figure 2.4. The profiles of predictions are within ±0.5°C error range of the experimental data.

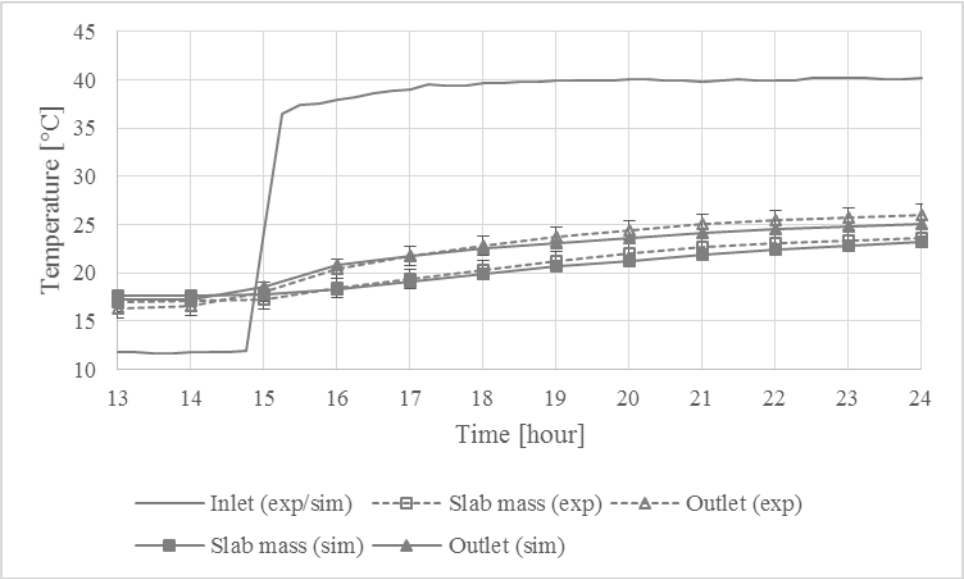

Figure 2.4: The effect of supplying 40°C air through a hollow core ventilated slab

2.4 Mesh grid sensitivity

To assess the impact of selecting the grid size used for the numerical slab model on the accuracy of the results from the simulation environment tool, a sensitivity analysis to assess the accuracy in predicting slab inside/outside surface temperatures, temperatures between slab layers, East/West wall inside/outside surface temperatures, zone mean air temperature and air outlet temperature is carried out using a detailed grid with 40,625 nodes as a reference. Figure 2.5 depicts the results of the assessment analysis to determine the impact of the grid size (expressed in terms of the number of nodes) on both the prediction accuracy (expressed in terms of RMSE between the predictions and the reference case results) as well as on the computational effort (expressed in terms of CPU of processing time). According to the Figure 2.5, when we consider RMSE as well as CPU time, 11165 of nodes is the best option by using a computer with Intel® Core ™ i7-2670 QM CPU @ 2.20 GHz.

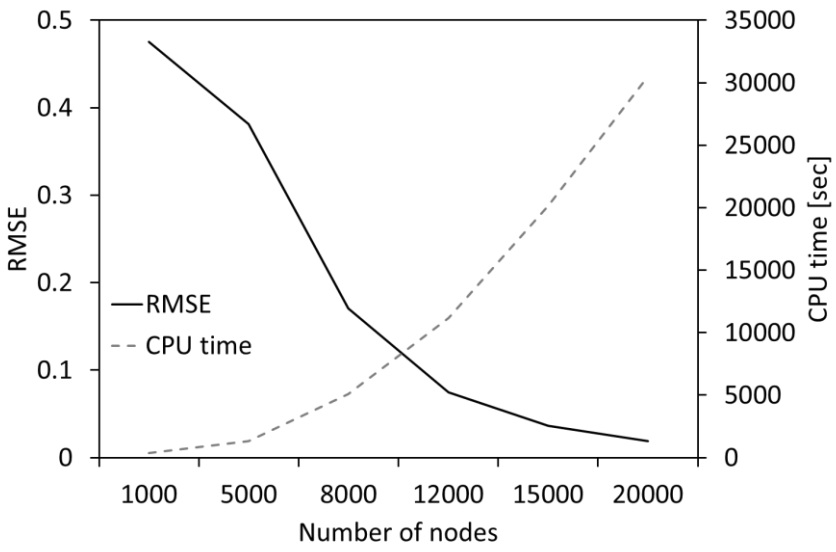

Figure 2.5: Impact of the number of nodes of the grid mesh on the prediction accuracy and computational effort

2.5 Timestep sensitivity

To determine the best time step to be used in the simulation environment, a sensitivity analysis is performed to determine the impact of the time step selection on the prediction accuracy of slab inside/outside surface temperatures, temperatures between slab layers, East and West wall inside/outside surface temperatures, zone mean air temperature and air outlet temperature. For the sensitivity analysis, the results obtained from of the numerical model with 1 minute time step is considered as a reference case. Various time step simulations are conducted with the selected grid size (refer to section 2.4). As shown in Figure 2.6, when we consider RMSE as well as CPU time, 15 minute timestep is the best option for a computer with Intel® Core ™ i7-2670 QM CPU @ 2.20 GHz.

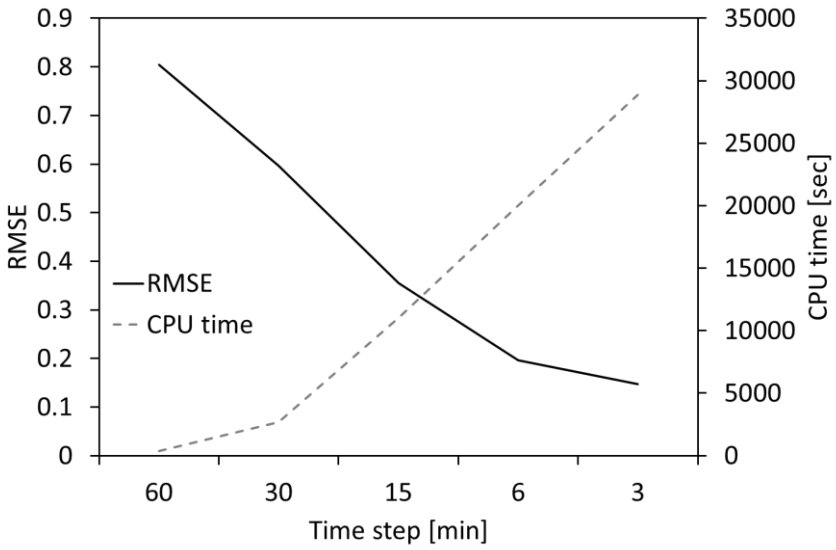

Figure 2.6: Impact of the time step on the prediction accuracy and CPU time

2.6 Parametric analysis

A series of parametric analyses is carried out to determine the effect of a wide range of design and operating parameters for ventilated slabs. Specifically, the impact of convective coefficient inside a hollow core, convective coefficient on a floor surface, inlet air temperature, air mass flow rate, depth of hollow core, and hollow core pitch is determined on the overall performance of ventilated slab system to maintain desired temperature for thermal zones. In order to account for the thermal bridging effects, the FDMRC-2D simulation environment is used for parametric analyses during heating season (January 15th to 18th) and summer season (August 17th to 20th) in Golden, CO. Figure 2.7 shows a cross-section view of the ventilated slab medium with the hollow cores. As defined in Figure 2.7, the average heat transfer rates along the top and bottom surfaces of the slab (Qup, Qdown) are obtained and compared for various parameters. For all parametric analyses, zone mean air temperature is assumed to be fixed at 20°C and 25°C as heating setpoint temperature

and cooling setpoint temperature, respectively.

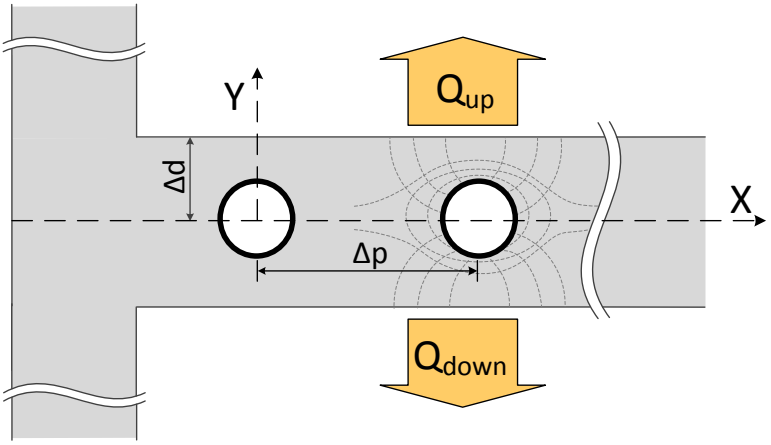

Figure 2.7: Cross-section view of ventilated slab and wall joint and variables used for parametric analyses

2.6.1 Effect of convective coefficient inside the hollow cores

The convective coefficient of the air that travels inside a hollow core is determined by Reynolds number. Reynolds number is varied from 1100 to 5300 to investigate the effect of convective coefficient of the air. Figure 2.9 depicts the average heat transfer rate along the slab surface as a function of Reynolds number. When Reynolds number is smaller than 2300, Nusselt number is assumed to be remain constant at 3.66. Therefore, no change on average heat transfer rate is observed for Reynolds number less than 2300. Significant increase of average heat transfer rate along the slab surface is evident as a transition from laminar flow (Re<2300) to turbulent flow (Re>2300). For turbulent flow region, the average heat transfer rate gradually increases with diminishing returns as Reynolds number gets larger.

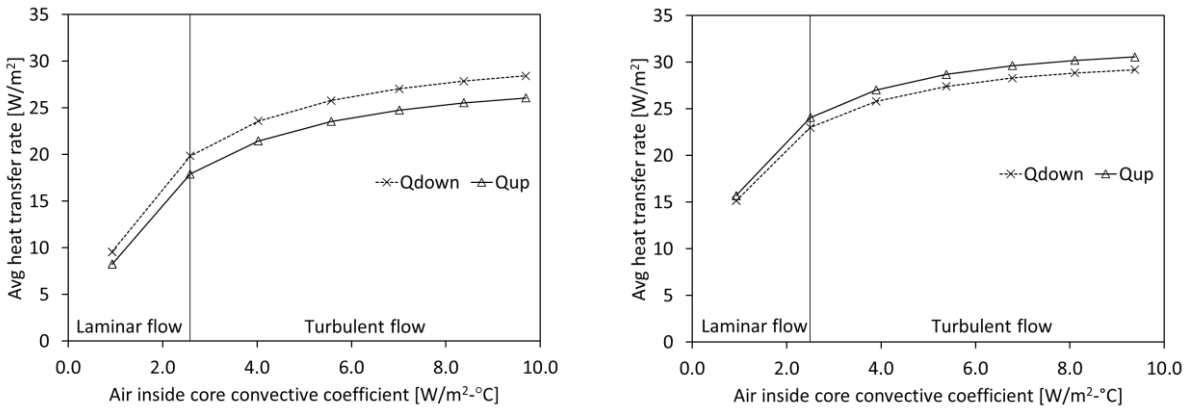

(a) Heating mode (b) Cooling mode

Figure 2.8: Average heat transfer rates along the slab surfaces with no insulation as functions of convective coefficient inside a hollow core

2.6.2 Effect of convective coefficient on the slab surface

Figure 2.9 shows the average heat transfer rate along the slab surfaces as a function of the convective heat transfer coefficient on the slab surface. The convective coefficient on the slab surface is varied from 1 to 11 W/m^2-°C with a constant mass flow rate of 0.6 kg/s, and a hollow core diameter of 0.1 m located in 0.25 m slab construction. The larger convective coefficient facilitates a heat transfer between a floor surface and zone air, but the effect gradually diminishes. It is observed that the average heat transfer rate along the slab surfaces more sensitively reacts to convective coefficient on the slab surface compared to convective coefficient inside the hollow cores.

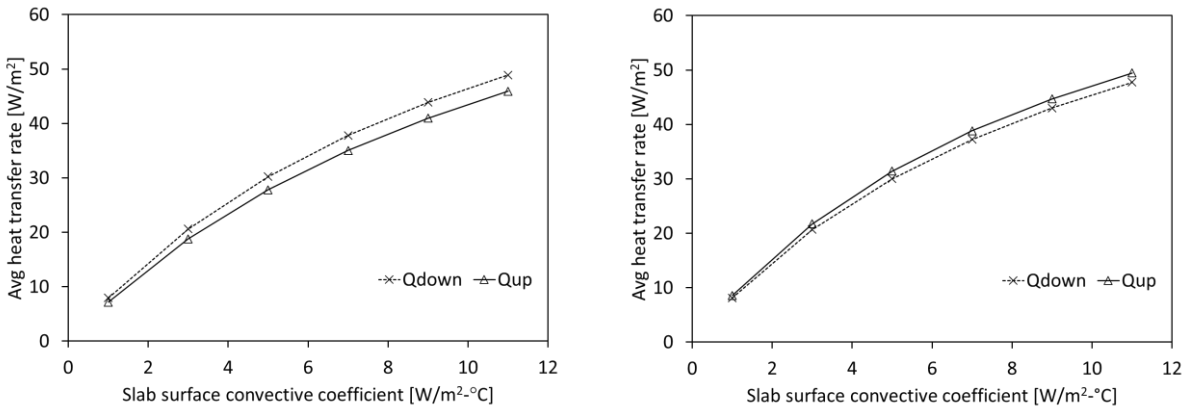

(a) Heating mode (b) Cooling mode

Figure 2.9: Average heat transfer rates along the slab surfaces with no insulation as functions of convective coefficient on a floor surface

2.6.3 Effect of inlet air temperature

The inlet air temperature is varied with a constant mass flow rate of 0.6 kg/s, and a hollow core diameter of 0.1 m located in 0.25 m slab construction. Figure 2.10 illustrates the average heat transfer rate through the slab surface as a function of inlet air temperature. It is observed that the change of supply air temperature dramatically influences the slab surface temperatures and average heat transfer rates along the slab surfaces. During heating mode, the increase in supply air temperature increases slab surface temperatures, and the larger temperature differences between zone air and slab surfaces result in an increase of the average heat transfer rates along the slab surfaces. Whereas, as the inlet air temperature increases, the average heat transfer rates on the slab surfaces rapidly decrease during cooling mode.

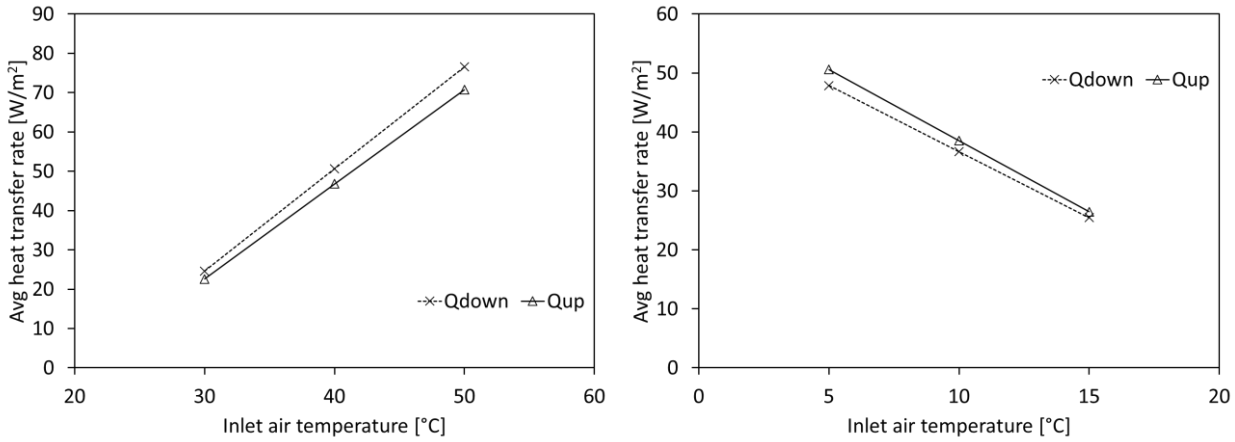

(a) Heating mode (b) Cooling mode

Figure 2.10: Average heat transfer rates along the slab surfaces with no insulation as functions of inlet supply air temperature

2.6.4 Effect of air mass flow rate

The mass flow rate of inlet hot air is varied from 0.1 kg/s to 2.0 kg/s with a constant supply air temperature of 27.5˚C and 12.5˚C for the heating mode and the cooling mode, respectively. Figure 2.11 shows the effect of air mass flow rate on average heat transfer rate along the slab surface. An increase of air mass flow rate increases the average slab surface heat transfer rate for both heating mode and cooling mode. It should be noted, however, that when the air mass flow rate is larger than 1.0 kg/s, but the impact gradually decreases.

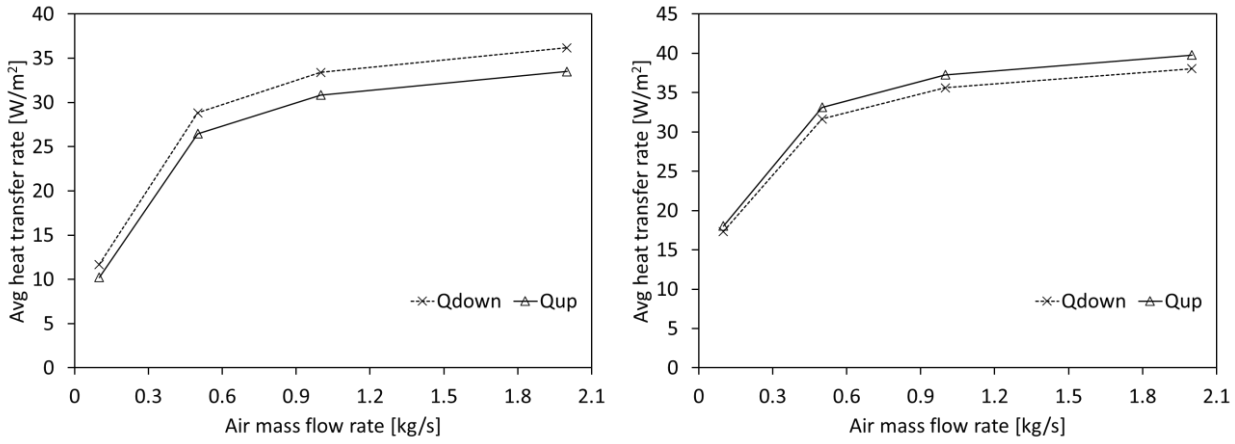

(a) Heating mode (b) Cooling mode

Figure 2.11: Average heat transfer rates along the slab surfaces with no insulation as functions of air mass flow rate

2.6.5 Effect of core depth

The depth of hollow core is varied by changing the slab thickness from 0.20 to 0.50 m. Thus, the depth of hollow cores, defined by the distance from center of heat source to slab surface, is varied from 0.1 to 0.25 m. The supply temperature is maintained at 27.5˚C and 12.5˚C, for heating season and cooling season, respectively. A diameter of hollow core is assumed to be 0.1m, and inlet air mass flow rate of 0.6 kg/s. As shown in Figure 2.12, an increase in core hollow depth proportionally reduces average heat transfer rates along the slab surfaces. As the core depth increases, lower increases of the slab surface temperatures in heating mode and decreases of the slab surface temperatures in cooling mode can be achieved due to the insulating effect of the concrete layer between the cores and the indoor space. As a result, the differences between zone air temperatures and slab surface temperatures are reduced, and the average heat transfer rates are

reduced.

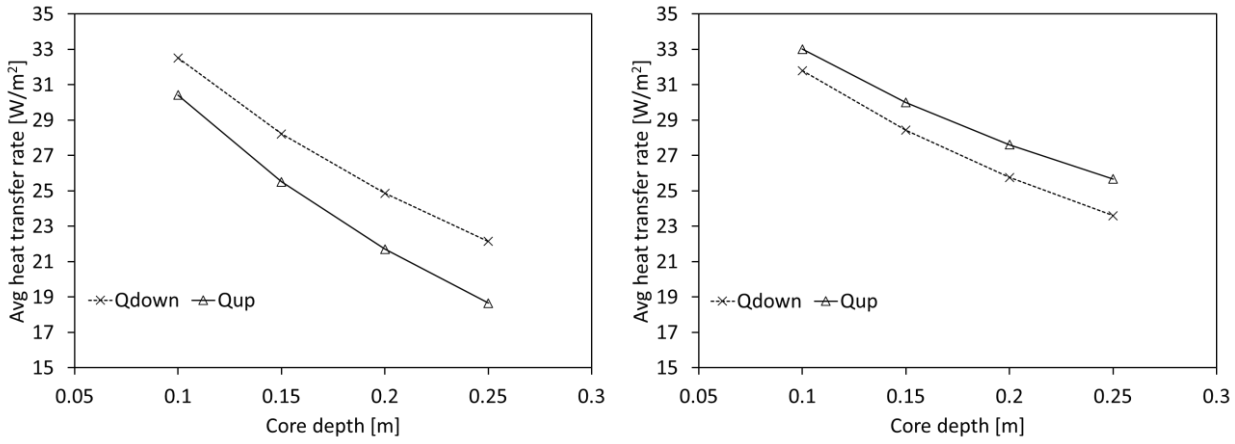

(a) Heating mode (b) Cooling mode

Figure 2.12: Average heat transfer rates along the slab surfaces with no insulation as functions of the depth of hollow cores

2.6.6 Effect of core pitch

In this analysis, the core pitch is varied by changing the number of hollow cores in the slab construction. The core pitch is large with the small number of cores in the slab. As the number of cores changes, the contact area, number of cores times circumference of cores, also varies. Diameter of 0.05 and 0.10 meter for a hollow core is considered. The heat generation rate of 1.8 kW and 1.2 kW for heating and cooling operation, respectively, is applied. Figure 2.13 combines all the results of the parametric analyses when both core diameters and pitches are varied and shows the average heat transfer rates along the top and bottom slab surface as functions of core contact area (number of core × circumference of core) for both heating and cooling modes. As shown in Figure 2.13, when the contact area of core increases, the average heat transfer rates along

the slab surfaces increases but with diminishing return until reaching asymptotic values. The smaller hollow cores need a larger number of cores to have the same contact area. When the contact area of cores is the same for all the diameters, the average heat transfer rates for the smaller cores are slightly greater than those for the larger cores as shown in Figure 2.13. Indeed, the higher density of small cores results in higher heat transfer along the surfaces even though they are located deeper in the concrete layer compared to the larger cores.

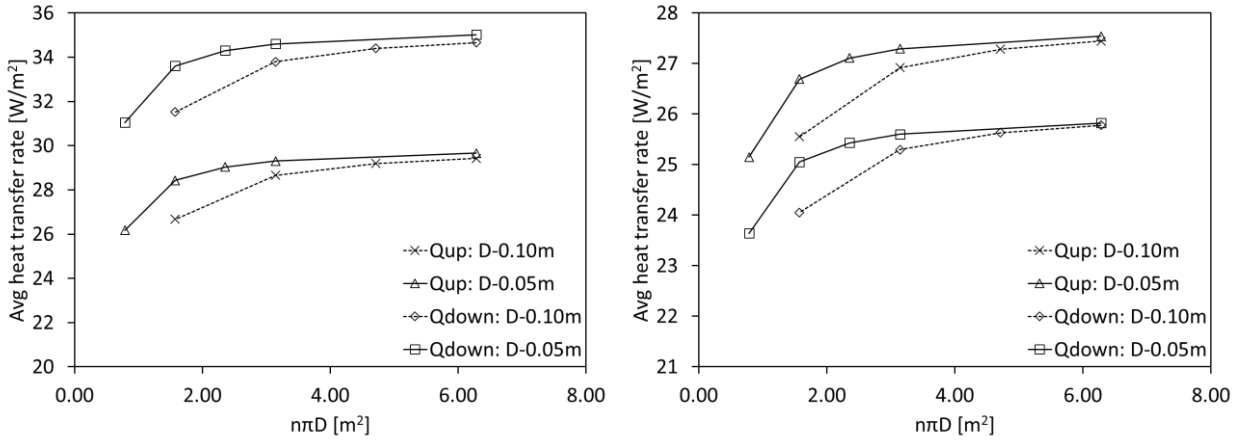

(a) Heating mode (b) Cooling mode

Figure 2.13: Average heat transfer rates along the slab surfaces with no insulation as functions of hollow cores contact area embedded in fixed concrete slab thickness for two core diameters

2.7 Summary and conclusions

In this chapter, a numerical solution for a two-dimensional slab heat transfer model is developed. The accuracy of the numerical solution is evaluated as a function of the mesh size using an analytical solution obtained for the case of one-dimensional slab heat transfer model.

The predictions of the numerical solution for both the temperature distribution and heat flux along

the slab surfaces are validated and analyzed. With the proper section of the mesh size, it is found that a good agreement between the numerical finite difference solution and the experimental data can be obtained with reasonable computational efforts to solve the transient heat conduction equation for the two-dimensional slab model.

Several parametric analyses are performed to determine the performance of ventilated slab systems under various design and operating conditions. In particular, the parametric analyses include the effect of convective coefficient inside the hollow cores, convective coefficient on the slab surface, supply air inlet temperature, air mass flow rate, depth of the hollow cores, and core pitch.

For convective coefficient of the air that travels inside the hollow cores, significant increase of average heat transfer rate along the slab surface is evident as a transition from laminar flow ($Re<2300$) to turbulent flow ($Re>2300$). For turbulent flow region, the average heat transfer rate slowly increases with diminishing returns as Reynolds number gets larger.

The larger convective coefficient on the slab surface facilitates a heat transfer between a floor surface and zone air, but the effect gradually diminishes. It is observed that the average heat transfer rate along the slab surfaces more sensitively reacts to convective coefficient on the slab surface compared to convective coefficient inside the hollow cores.

It is found that hollow core inlet air temperature greatly influences the performance of ventilated slab system. The average heat transfer rate on the upper surface of slab increases proportionally to the increase in supply air inlet temperature when heating is required. As the inlet air temperature increases, the average heat transfer rate on the slab surface rapidly decreases for cooling mode.

As the air mass flow rate increases, slab heat transfer rate is increased, but the impact gradually reduces. When the air mass flow rate is larger than 1.0 kg/s, the total slab heat transfer rate is found to be not significantly affected by the mass flow rate in the heating mode.

As the depth of embedded hollow core increases, the total slab heat transfer rate along the upper

slab surface proportionally decreases, but the total slab heat transfer rate on lower slab surface increases. The effect of the depth of hollow core follows a diminishing return pattern with a gradually reduced impact.

As the depth of embedded hollow core increases, the total slab heat transfer rates along the slab surfaces are found to be proportionally reduced. The effect of the depth of hollow core follows a diminishing return pattern with a gradually reduced impact.

The contact area of heat source/sink has less impact on the heat transfer rates along the slab surfaces. As the contact area of core increases, the average heat transfer rates along the slab surfaces increases gradually until reaching asymptotic values. When the contact area is the same, the average heat transfer rate for the smaller core is slightly greater than when the core is large.

CHAPTER 3: DEVELOPMENT OF THREE-DIMENSIONAL HEAT TRANSFER FLOOR MODEL

3.1 Introduction

Several attempts have been made to analyze the performance of the ventilated slab system with two-dimensional heat transfer model. No attempt has been reported to integrate three-dimensional slab and wall joint coupled heat transfer model with the ventilated slab system model. Moreover, most of researches neglect the impact of thermal bridging through slab and wall joint on the performance of the ventilated slab system. The accurate modeling technique is essential for adequate analysis of indoor thermal comfort and HVAC system performance since building envelope systems greatly affect not only thermal loads of building but also HVAC system operations.

The most recent whole building simulation tool, EnergyPlus, solves 1-dimensional conduction heat transfer formulation for building envelopes by using state space method to generate conduction transfer functions (CTFs) (Seem, 1987; Strand, 1995). The conduction heat transfer in reality is not as simple as 1-dimensional heat conduction solution. When building is equipped with the passive thermal storage system such as a hydronic radiant slab system or a hollow core ventilated slab system, it can be much more complex since it controls the slab mass surface temperature. Therefore, 2-D numerical floor model is developed to address this complex heat transfer more accurately that is presented in the previous chapter.

This chapter presents the development of a 3-D floor heat transfer model for the ventilated slab system. The correlation of heat flux along a floor surface obtained from 2-D and 3-D hollow core ventilated slab model is explored so that 2-D floor model can effectively reflect a thermal behavior of 3-D floor model. A slab and wall joint is included in the multi-dimensional ventilated slab

model. The results from the parametric studies for three-dimensional floor heat transfer model is presented. The series of simulation provide data for investigation of geometric effects including floor size and aspect ratio.

3.2 Three-dimensional numerical solution

This section describes the three-dimensional numerical method and its implementation in the Matlab. The numerical model employed in this chapter simulates a floor, exterior walls, and a heat source within the floor. Three dimensional numerical solutions in a Cartesian coordinate system for the hollow core ventilated slab are developed by adding heat generation and extraction sources within the floor. A three-dimensional heat conduction equation with heat source term under transient conditions can be formulated as follows: (Pantankar, 1980)

$$\rho c_p \frac{\partial T}{\partial t} = k\frac{\partial^2 T}{\partial x^2} + k\frac{\partial^2 T}{\partial y^2} + k\frac{\partial^2 T}{\partial z^2} + q \qquad (3.1)$$

Where,

ρ = density [kg/m^3]

c_p = heat capacity [J/kg˚C]

k = thermal conductivity [kg/m^3]

t = time [sec]

q = generated heating or extracted cooling rate [W/m^3]

Three types of boundary conditions are considered for the multi-dimensional floor model: (a) exposed to outdoor air, (b) exposed to indoor air and (c) adiabatic. The outside surfaces of walls are exposed to outdoor air and the inside surfaces of walls and floor are exposed to indoor air. The

boundary condition of top and bottom edge of wall is adiabatic. The calculation method of longwave radiation exchange between interior surfaces used in EnergyPlus is employed in the numerical models.

Using a control volume approach and pure implicit finite difference method, the heat conduction equation with heat sources represented by Eq. (3.1) with associated boundary conditions can be solved. The control volume in Cartesian coordinate and its associated nodal dimensions are shown in Figure 3.4. The small cube with dimensions of ΔX, ΔY and ΔZ is the control volume of node located in (i, j, k) position.

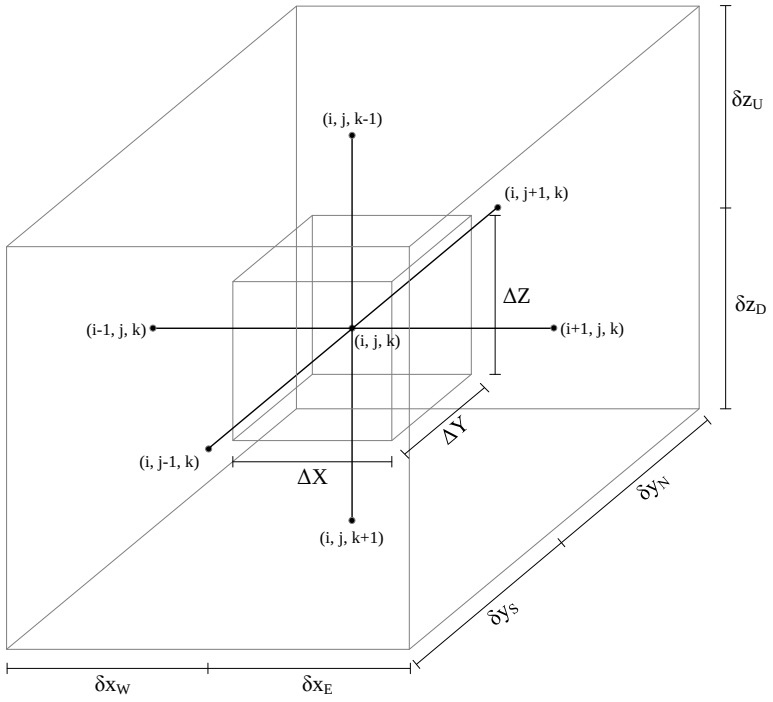

Figure 3.1: Three-dimensional control volume

The difference equation of three-dimensional heat conduction can be formulated from Eq. (3.1). For three dimensional finite difference grid with non-uniform thermal conductivity values and different nodal distances, Eq. (3.1) can be transformed to

$$k_E \Delta Y \Delta Z \frac{T_{i+1,j,k}^{p+1} - T_{i,j,k}^{p+1}}{\delta x_E} - k_W \Delta Y \Delta Z \frac{T_{i,j,k}^{p+1} - T_{i-1,j,k}^{p+1}}{\delta x_w}$$
$$+ k_N \Delta X \Delta Z \frac{T_{i,j+1,k}^{p+1} - T_{i,j,k}^{p+1}}{\delta y_N} - k_S \Delta X \Delta Z \frac{T_{i,j,k}^{p+1} - T_{i,j-1,k}^{p+1}}{\delta y_S} + k_U \Delta X \Delta Y \frac{T_{i,j,k-1}^{p+1} - T_{i,j,k}^{p+1}}{\delta z_U} \quad (3.2)$$
$$- k_D \Delta X \Delta Y \frac{T_{i,j,k}^{p+1} - T_{i,j,k+1}^{p+1}}{\delta z_D} = \rho c_p \Delta X \Delta Y \Delta Z \frac{T_{i,j,k}^{p+1} - T_{i,j,k}^{p}}{\Delta t}$$

Where,

$T_{i,j,k}^{p}$ = temperature as i, j and k are noted spatial node and p is for the present time.

ΔX = distance between nodes in x-axis

ΔY = distance between nodes in y-axis

ΔZ = distance between nodes in z-axis

Δt = time step

Rearranging Eq. (3.2) to put terms with p+1 on the left-hand-side and terms with p on the right-hand-side gives

$$\left(\frac{\rho c_p \Delta X \Delta Y \Delta Z}{\Delta t} + \frac{k_E \Delta Y \Delta Z}{\delta x_E} + \frac{k_W \Delta Y \Delta Z}{\delta x_w} + \frac{k_N \Delta X \Delta Z}{\delta y_N} + \frac{k_S \Delta X \Delta Z}{\delta y_S} + \frac{k_U \Delta X \Delta Y}{\delta z_U} + \frac{k_D \Delta X \Delta Y}{\delta z_D}\right) T_{i,j,k}^{p+1} - \left(\frac{k_E \Delta Y \Delta Z}{\delta x_E}\right) T_{i+1,j,k}^{p+1} - \left(\frac{k_W \Delta Y \Delta Z}{\delta x_w}\right) T_{i-1,j,k}^{p+1}$$
$$- \left(\frac{k_N \Delta X \Delta Z}{\delta y_N}\right) T_{i,j+1,k}^{p+1} - \left(\frac{k_S \Delta X \Delta Z}{\delta y_S}\right) T_{i,j-1,k}^{p+1} - \left(\frac{k_U \Delta X \Delta Y}{\delta z_U}\right) T_{i,j,k-1}^{p+1} \quad (3.3)$$
$$- \left(\frac{k_D \Delta X \Delta Y}{\delta z_D}\right) T_{i,j,k+1}^{p+1} = \frac{\rho c_p \Delta X \Delta Y \Delta Z}{\Delta t} T_{i,j,k}^{p}$$

With some additional rearrangements, the differential equation Eq. (2.4) can be discretized as indicated as follows:

$$a_p T_p - a_E T_E - a_W T_W - a_N T_N - a_S T_S - a_U T_U - a_D T_D = a_p^0 T_p^0 + q \quad (3.4)$$

$$a_p = a_E + a_W + a_N + a_S + a_U + a_D + a_p^0$$

$$a_E = \frac{k_E \Delta Y \Delta Z}{\delta x_E}$$

$$a_W = \frac{k_W \Delta Y \Delta Z}{\delta x_w}$$

$$a_N = \frac{k_N \Delta X \Delta Z}{\delta y_N}$$

$$a_S = \frac{k_S \Delta X \Delta Z}{\delta y_S}$$

$$a_U = \frac{k_U \Delta X \Delta Y}{\delta z_U}$$

$$a_D = \frac{k_D \Delta X \Delta Y}{\delta z_D}$$

$$a_p^0 = \frac{\rho c_p \Delta X \Delta Y \Delta Z}{\Delta t}$$

$$q = \varepsilon \left(\dot{m} c_p\right)_{air} (T_{air,in} - T_s)$$

As described in Chapter 2, the entire set of equations can be expressed in matrix form (i.e. linear algebraic equation). The temperature distribution can be calculated by solving the linear algebraic equation for all 3-dimensional nodal network. BiConjugate gradients stabilized (BiCGSTAB) method is used to solve the system of linear algebraic equations in this research. BiCGSTAB is an iterative matrix solver developed by Van Der Vorst (1992). Incomplete LU factorization technique is applied as a preconditioner to accelerate convergence of BiCGSTAB.

3.3 Effect of the exterior wall height

The impact of a height of exterior walls in multi-dimensional slab and wall joint model on the heat flux along floor inside surface and edge surface is explored in this section. The exterior wall height is varied from 0.1 to 3 meter. The wall height of 3 meter, typical wall height of buildings, is considered as a reference. Figure 3.2 depicts the comparison result of the floor inside surface heat

flux and the floor edge heat flux obtained from 2-dimensional and 3-dimensional FDM model with various exterior wall heights.

When 0.1 meter height exterior wall is modeled in 2-D or 3-D floor model, the heat flux along the floor inside and edge surface can be inaccurate by approximately 15% and 6%, respectively, compared to the case when 3 meter exterior wall is modeled. The difference of the floor inside surface heat flux and floor edge heat flux between 3m wall and various wall heights diminishes as the greater wall height is defined. However, larger number of nodes are required for multi-dimensional FDM model when the taller wall height is considered. The numerical model then requires much more computational effort due to an increase of number of nodes. The wall height greater than 0.5 meter is acceptable with percent difference of heat flux along floor surfaces less than 5% as shown in Figure 3.2.

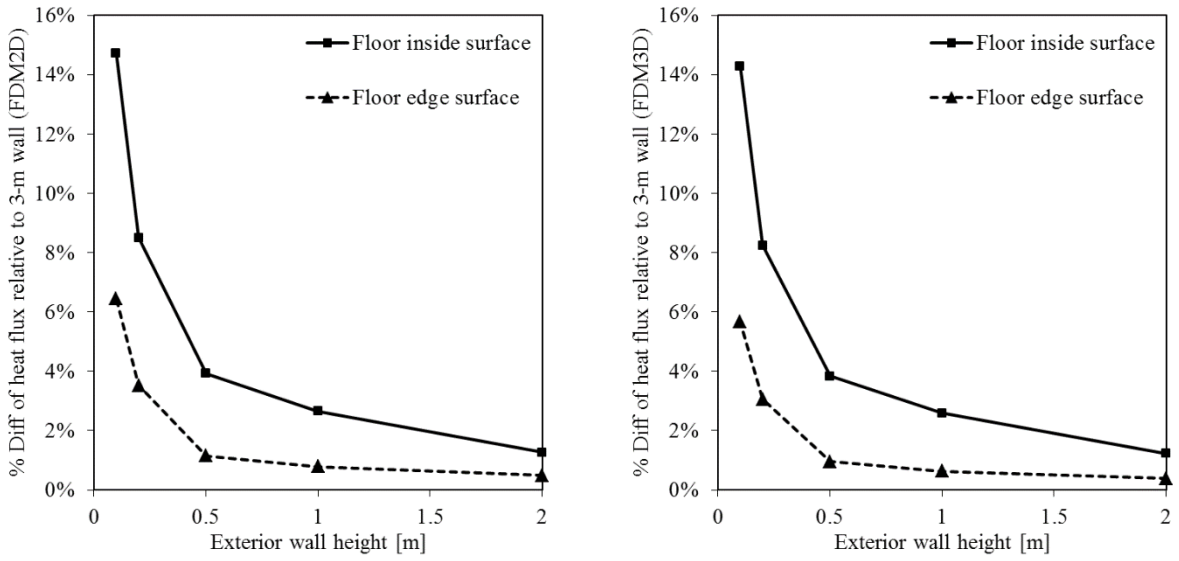

Figure 3.2: Variation of heat flux along the floor inside surface and heat flux at floor edge for (a) 2D and (b) 3D FDM floor model with various exterior wall heights in Golden, CO

3.4 Effect of floor shape and size

Figure 3.3 shows the annual average heat loss as a function of perimeter for twenty simulation runs. It is observed that the total heat transfer could be fitted to the power curve with R^2=0.99. Replot of Figure 3.3 (a) as average heat flux at floor inside surface vs. A/P becomes Figure 3.3 (b). The data in Figure 3.3 (b) lie on a single curve approximated by the exponential function:

By using this logarithmic function, the average heat flux can be estimated. For example, even though the only given information about the floor is dimensions, the average heat flux along with the floor surface can be estimated.

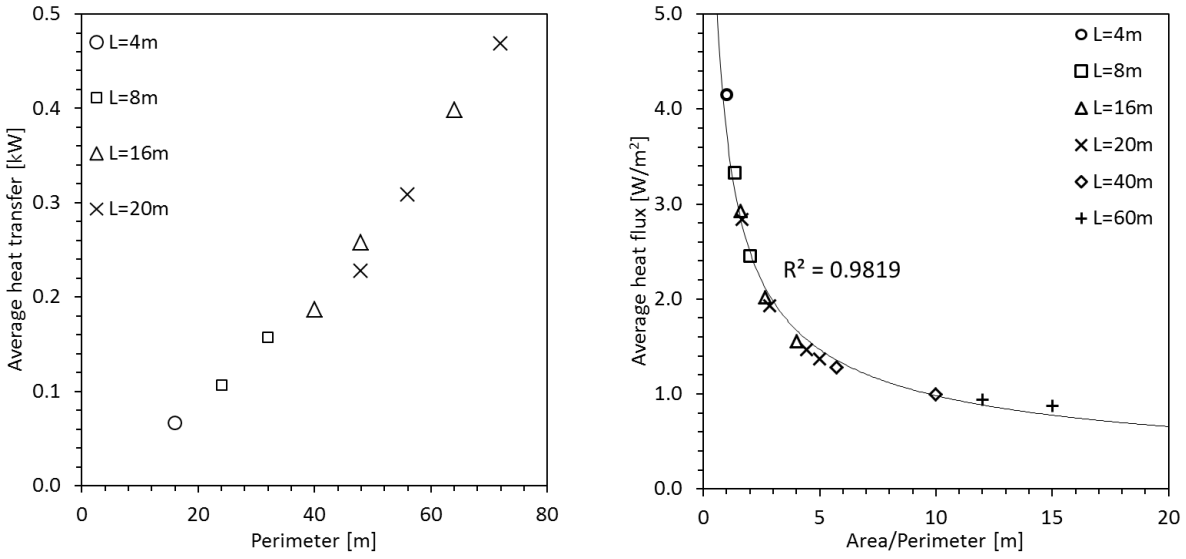

(a) (b)

Figure 3.3: (a) Heat loss vs. perimeter length for uninsulated floors (b) Heat loss per unit area vs. A/P for uninsulated slabs in Golden, CO.

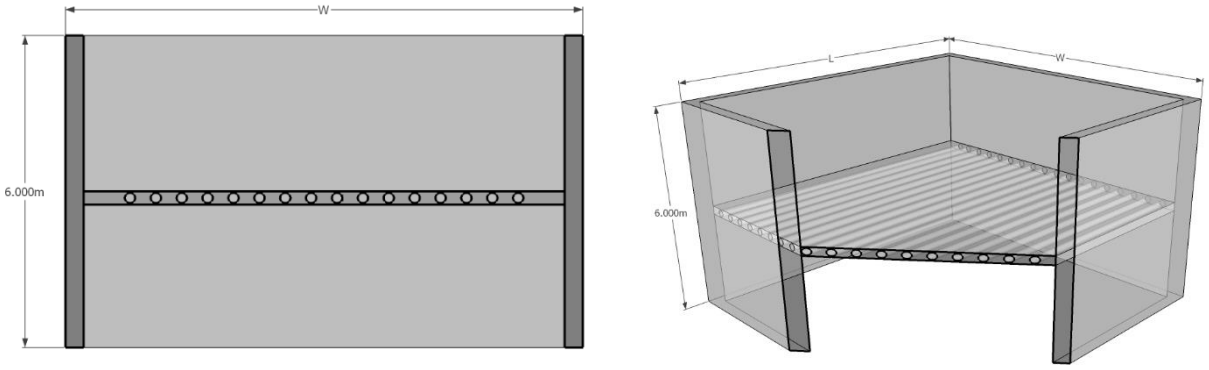

Figure 3.4: Section view of multi-dimensional slab and wall joint model: (a) 2-D and (b) 3-D model

In this section, the effect of the floor size for the floor with the exterior wall as shown in Figure 3.4 is analyzed. Figure 3.4 illustrates the schematic of building models that includes 2 vertically adjacent zones used for the analysis.

Table 3.1 summarizes input parameters used for all simulation analysis. A slab area is ranged from 16 to 6400 m^2 and an aspect ratio, area/perimeter, is varied from 1 to 20 m. Bahnfleth (1989) concluded that the shape of floor is not a significant influence on heat transfer. Thus, only square shaped floor is taken into account.

Table 3.1: Input parameters used for the analysis

Parameter	Value
Site location	Golden, CO
Floor U-value	5.94 W/m^2-K
Ext. Wall U-value	3.33 W/m^2-K
Mean air temperature	18°C (remains constant for 1^{st} floor and 2^{nd} floor)

3.4.1 Steady state

Two methods of dealing with the area dependence are considered in this analysis; (a) Heat loss as a function of perimeter length for the floor, and (b) area-perimeter scaling relationship. The annual average outdoor air temperature of Golden, CO (9.69°C) is considered. The mean air temperatures of two zones are assumed to be maintained at 18°C. Figure 3.5 (a) shows the total heat transfer as a function of perimeter for sets of simulations of the developed 1-D, 2-D, and 3-D FDM floor model. The heat transfer along the floor inside surface is calculated by the function as follow:

$$\mathrm{q} = \mathrm{h_{floor}A(T_{zone} - }T_{floor,in})$$

It is observed that the average heat transfer obtained from 2-D and 3-D FDM floor model can be fitted to the power curve with R^2 value greater than 0.9. As the area/perimeter increases, the average heat flux for 2-D and 3-D FDM floor model converges to the average heat flux for 1-D FDM floor model. It is also observed that the data in Figure 3.5 (b) lie on a single curve approximated by the exponential function:

$$\mathrm{q} = a\left(1 - \mathrm{e}^{-\mathrm{bx}}\right)^{-1}$$

Note that the average heat flux along the floor surface for the 1D model is 0 because the upper surface and the lower surface of the 1D floor is exposed to the same zone air temperature, 18°C. Therefore, when aspect ratio (A/P) comes to infinity, the average heat flux converges to 0 for 2-D and 3-D model.

Since 2-D heat transfer from a floor corresponds to the 3-D, infinite aspect ratio case (for which A/P=L/2), there is an equivalent two-dimensional case for any three-dimensional floor. To verify this, the exponential curve fit for 2D floor model is corrected to have the same coefficient a with 3D floor model. Table 3.2 verifies that the coefficient b for corrected exponential curve fit of 2-D floor model is two times greater than that of 3-D floor model.

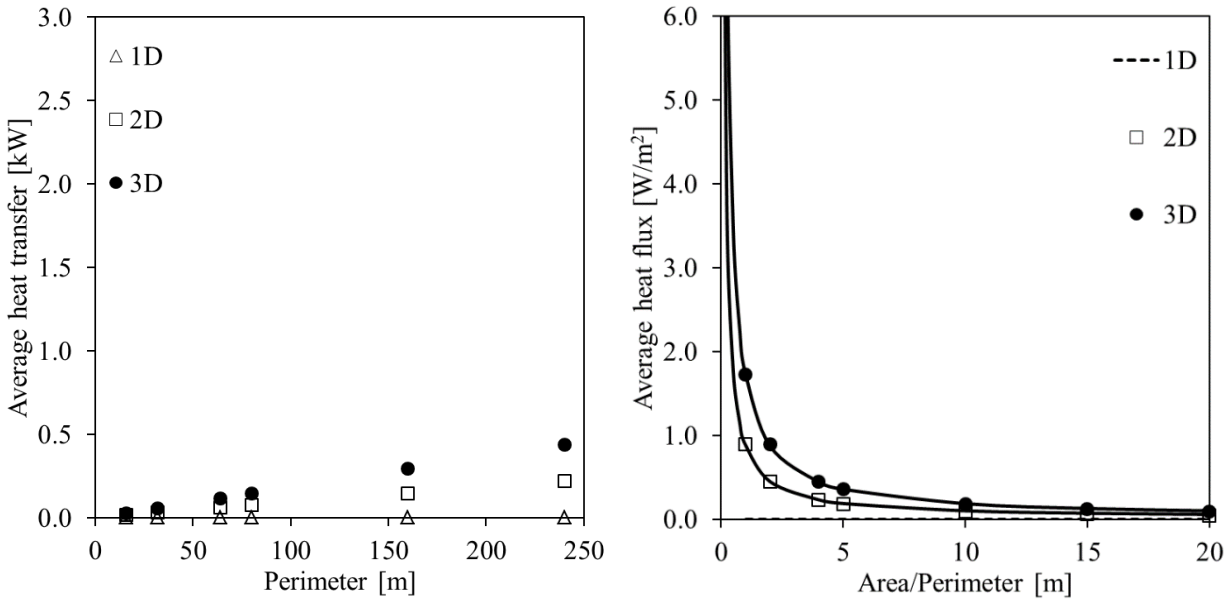

Figure 3.5: (a) Heat loss vs. perimeter length and (b) Heat loss per unit area vs. A/P for 1-D, 2-D, and 3-D floor model with no heat source in Golden, CO.

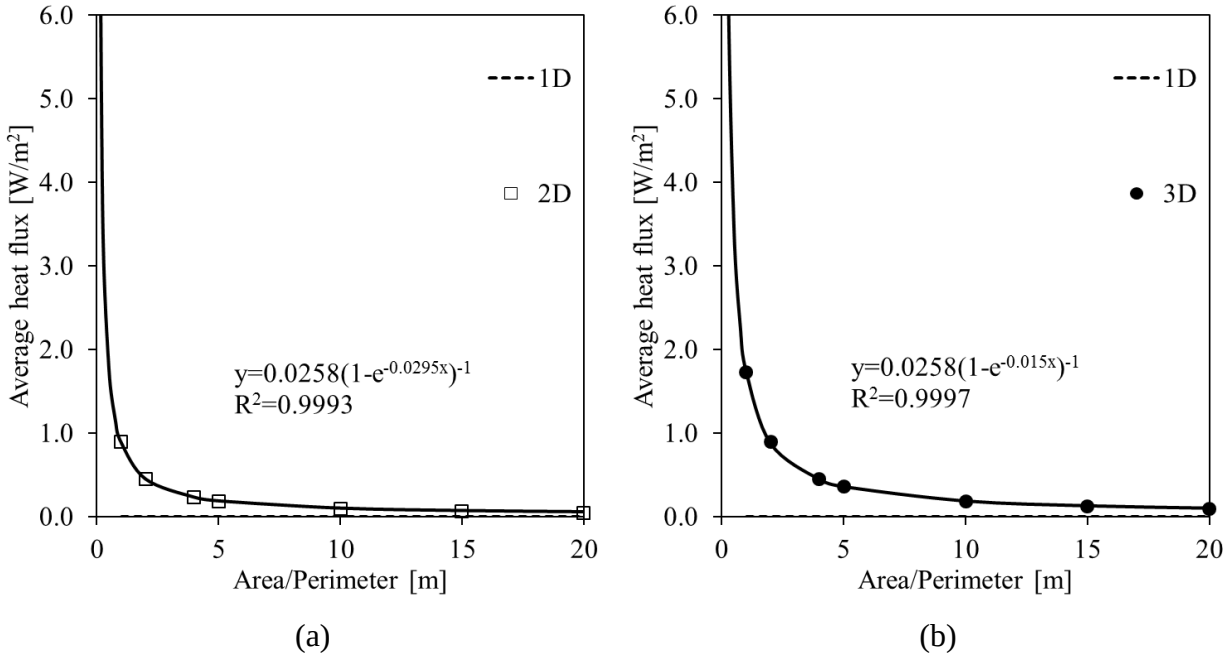

Figure 3.6: (a) 2-D floor model exponential curve fit and (b) 3-D floor model exponential curve fit with no heat source in Golden, CO.

Table 3.2: Comparison of exponential curve fit coefficients for 2-D and 3-D floor model with no heat source in Golden, CO

Curve fit coefficients	2-D	3-D
a	0.0258	0.0258
b	0.0295	0.0150
R^2	0.9993	0.9997

Table 3.3: Heat transfer and heat flux for steady-state 1-D, 2-D, and 3-D floor model with no heat source in Golden, CO

Perimeter	Area	A/P	Heat Transfer [W]			Heat Flux [W/m^2]		
			1-D	2-D	3-D	1-D	2-D	3-D
16	16	1	0.00	14.24	27.60	0.00	0.89	1.72
32	64	2	0.01	28.88	56.94	0.00	0.45	0.89
64	256	4	0.06	58.21	115.52	0.00	0.23	0.45
80	400	5	0.09	72.89	144.84	0.00	0.18	0.36
160	1600	10	0.35	146.39	291.56	0.00	0.09	0.18
240	3600	15	0.80	220.08	438.47	0.00	0.06	0.12
320	6400	20	1.42	293.95	585.58	0.00	0.05	0.09

1000 Watt per cubic meter of heat generation rate is added to the floor to investigate the impact of

heat sources on the correlation between multi-dimensional FDM floor models. Figure 3.7 (a) shows the average heat transfer as a function of perimeter for sets of simulations of the developed 1-D, 2-D, and 3-D FDM floor model. Figure 3.7 (a) shows that the average heat transfer increases as the size of the floor increases. Heat transfers have the negative sign because the surface temperature of floor is larger than the mean air temperature (18°C). Figure 3.8 depicts that the average heat flux obtained from 2-D and 3-D FDM floor model can be also fitted to the power curve with R^2 value greater than 0.9. As the area/perimeter increases, the average heat flux for 2-D and 3-D FDM floor model converges to the average heat flux for 1-D FDM floor model. Because the heat losses through the floor and wall joint have less impact on average floor surface temperature with the increase of aspect ratio (A/P) on the floor. Thus the average temperature of 2-D and 3-D floor model gets close to 1-D floor model, and the average heat flux on the floor surface for 2-D and 3-D model approaches that of 1-D model. The data in Figure 9 (b) lie on a single curve approximated by the exponential function:

$$\mathrm{q} = a\left(1 - \mathrm{e}^{-\mathrm{bx}}\right)^{-1} + c$$

Note that the coefficient c is added to the exponential function forms for the floor model with no heat source. The coefficient c represents the reference average heat flux amount obtained from 1-D floor model.

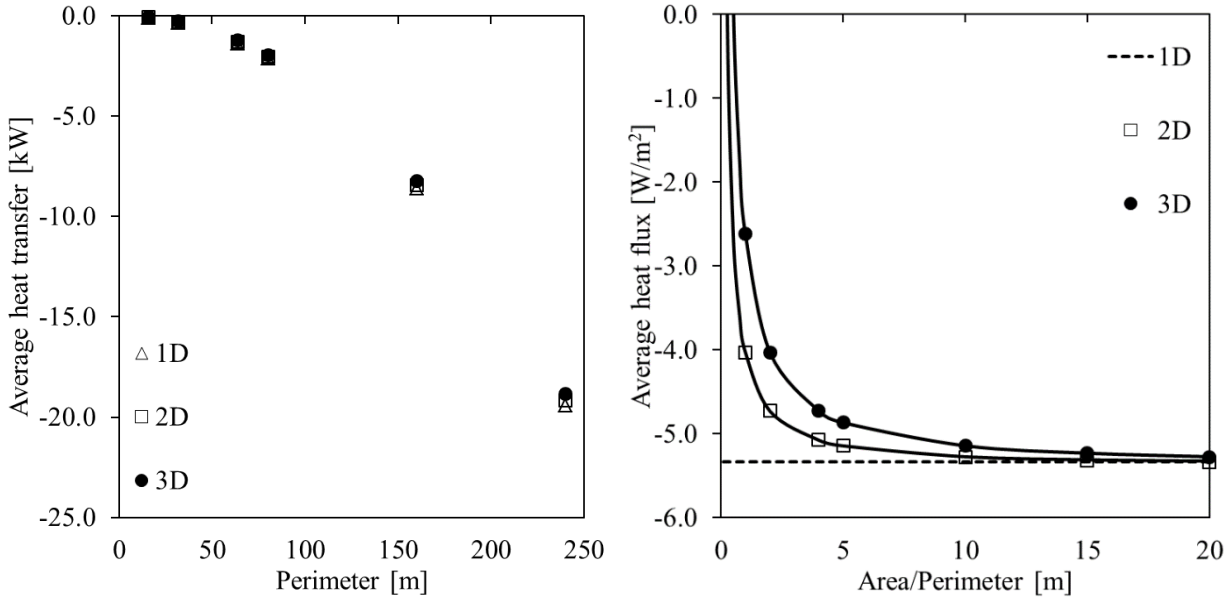

Figure 3.7: (a) Heat loss vs. perimeter length and (b) Heat loss per unit area vs. A/P for 1D, 2D, and 3D floor model with 1000 W/m^3 heat source in Golden, CO.

An average heat flux calculated from 2-D floor model corresponds to that of 3-D floor model, infinite aspect ratio case (for which A/P=L/2), there is an equivalent two-dimensional case for any three-dimensional floor. To verify this, the coefficient b in exponential curve fit equation for 2-D floor model should be two times greater than the coefficient b for 3-D floor model curve fitting. Table 3.4 verifies that the coefficient b in the adjusted exponential curve fit for 2-D floor model is two times greater than that of 3-D floor model regardless of a presence of heat source.

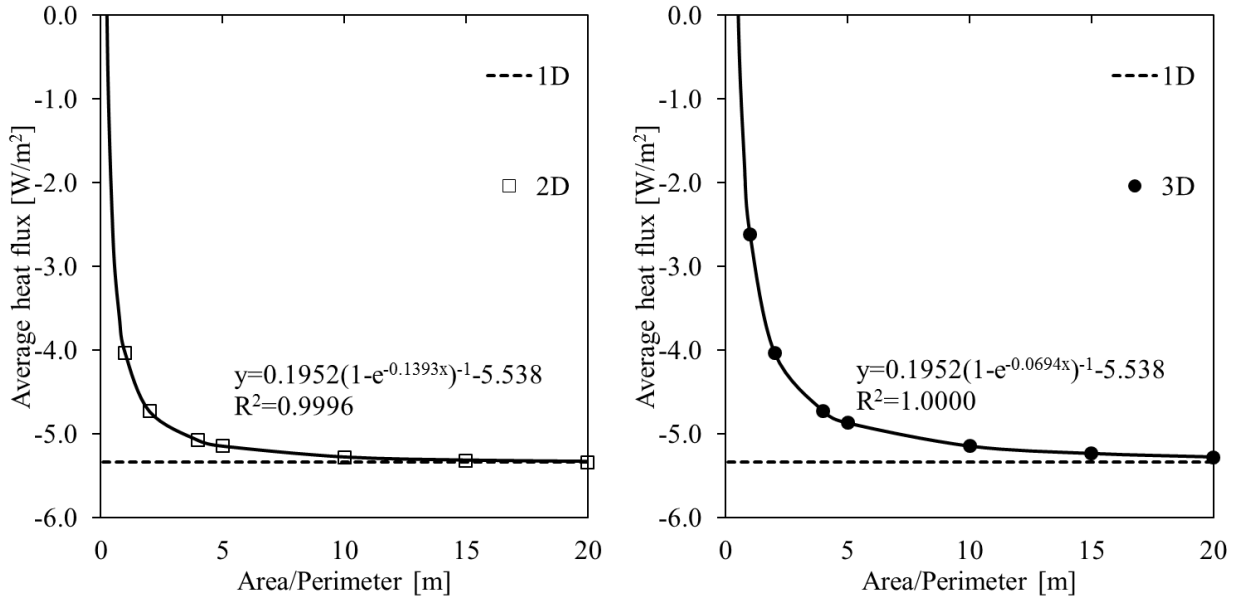

Figure 3.8: (a) 2-D floor model exponential curve fit and (b) 3-D floor model exponential curve fit with 1000 W/m^3 heat source in Golden, CO.

Table 3.4: Comparison of exponential curve fit coefficients for 2-D and 3-D floor model with 1000 W/m^3 heat source in Golden, CO

Curve fit coefficients	2D	3D
a	0.1952	0.1952
b	0.1393	0.0694
c	-5.538	-5.538
R^2	0.9996	1

Table 3.5: Heat transfer and heat flux for steady-state 1-D, 2-D, and 3-D floor model with 1000 W/m^3 heat source in Golden, CO

Perimeter	Area	A/P	Heat Transfer [W]			Heat Flux [W/m^2]		
			1D	2D	3D	1D	2D	3D
16	16	1	-83.02	-64.62	-41.99	-5.34	-4.04	-2.62
32	64	2	-338.57	-302.91	-258.49	-5.34	-4.73	-4.04
64	256	4	-1369.66	-1299.43	-1211.64	-5.34	-5.08	-4.73
80	400	5	-2145.21	-2057.69	-1948.16	-5.34	-5.14	-4.87
160	1600	10	-8623.21	-8449.24	-8230.78	-5.34	-5.28	-5.14
240	3600	15	-19434.93	-19174.49	-18847.01	-5.34	-5.33	-5.24
320	6400	20	-34580.38	-34233.46	-33796.94	-5.34	-5.35	-5.28

3.4.2 Dynamic outdoor condition

The correlation of the average heat flux along the floor surface among 1-D, 2-D and 3-D FDM floor model is evaluated under dynamic outdoor condition in this section. Figure 3.9 shows the outdoor air temperature profile and mean air temperatures used for the analysis. The outdoor temperature represents a typical daily temperature profile during winter season in Golden, CO. The mean air temperatures of upper zone and lower zone consistently maintain 18°C for a day.

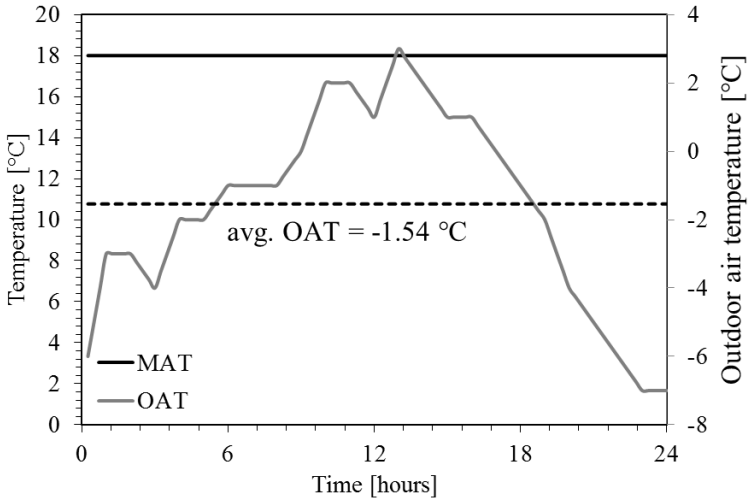

Figure 3.9: Daily outdoor air temperature profile used for dynamic boundary condition

It is also observed that the heat flux along the floor with no heat source corresponds to the aspect ratio of the floor obtained from 2-D and 3-D floor model lie on the exponential curve:

$$q = a\left(1 - e^{-bx}\right)^{-1}$$

There is an equivalent two-dimensional case for any three-dimensional floor since two-dimensional heat transfer from a floor corresponds to the three-dimensional, infinite aspect ratio case (for which A/P=L/2). The coefficient b in the exponential curve fit for 2-D floor model is compared to that for 3-D floor model. Table 3.6 verifies that the coefficient b for 2-D floor model is twice that for 3-D floor model.

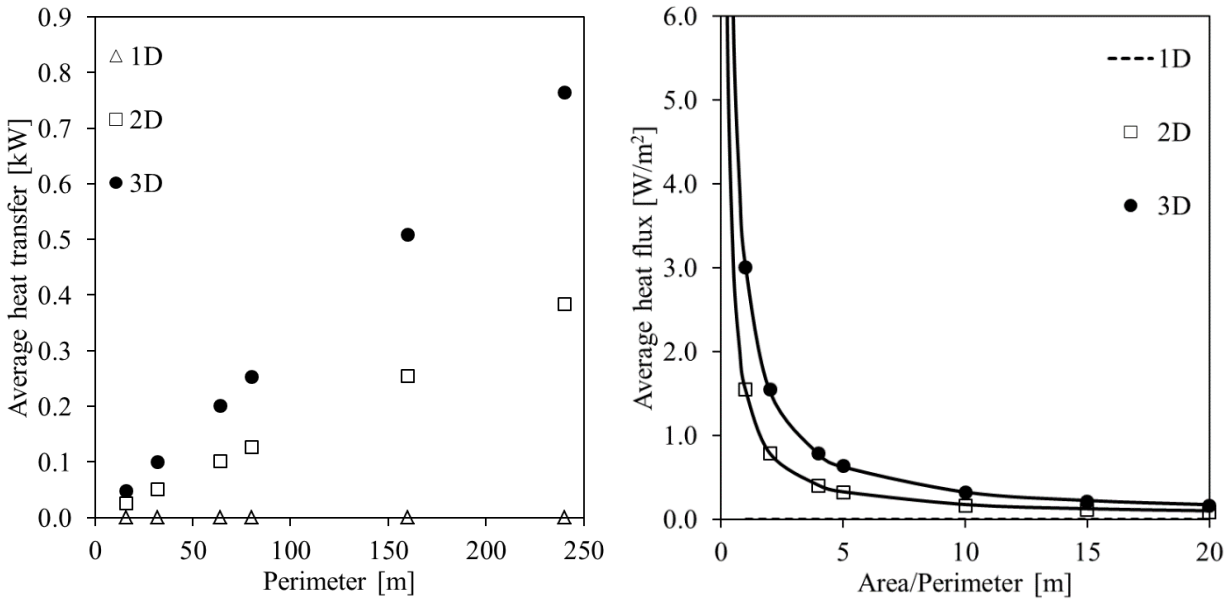

Figure 3.10: (a) Heat loss vs. perimeter length and (b) Heat loss per unit area vs. A/P for 1-D, 2-D, and 3-D floor model with no heat source in Golden, CO.

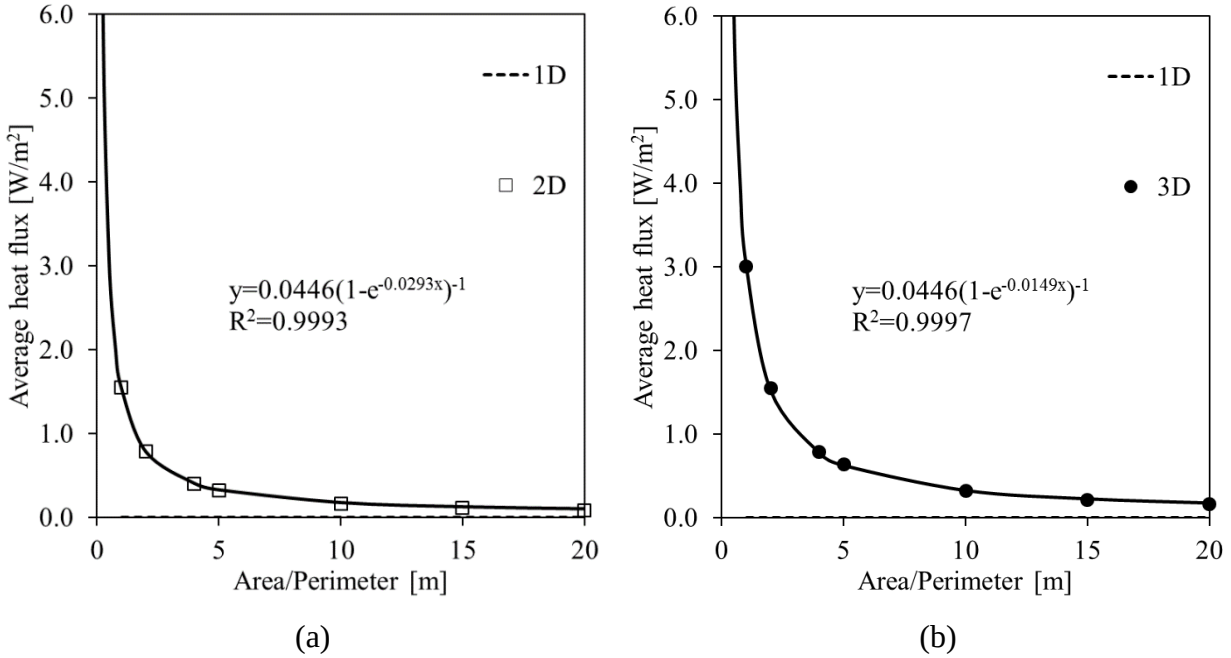

Figure 3.11: (a) 2-D floor model exponential curve fit and (b) 3-D floor model exponential curve fit with no heat source in Golden, CO.

Table 3.6: Comparison of exponential curve fit coefficients for 2-D and 3-D floor model with no heat source in Golden, CO

Curve fit coefficients	2D	3D
a	0.0446	0.0446
b	0.0293	0.0149
R^2	0.9993	0.9997

Table 3.7: Heat transfer and heat flux for transient 1-D, 2-D, and 3-D floor model with no heat source in Golden, CO

Perimeter	Area	A/P	Heat Transfer [W]			Heat Flux [W/m^2]		
			1D	2D	3D	1D	2D	3D
16	16	1	0.00	24.81	48.10	0.00	1.55	3.01
32	64	2	0.01	50.33	99.26	0.00	0.79	1.55
64	256	4	0.06	101.41	201.32	0.00	0.40	0.79
80	400	5	0.09	126.97	252.38	0.00	0.32	0.63
160	1600	10	0.35	254.87	507.88	0.00	0.16	0.32
240	3600	15	0.80	382.96	763.59	0.00	0.11	0.21
320	6400	20	1.42	511.22	1019.48	0.00	0.08	0.16

If the heat source present in the floor model, the heat flux data lie on the following exponential curve:

$$q = a\left(1 - e^{-bx}\right)^{-1} + c$$

There is an equivalent two-dimensional case for any three-dimensional floor since two-dimensional heat transfer from a floor corresponds to the three-dimensional, infinite aspect ratio case (for which A/P=L/2). Table 3.8 verifies that the coefficient b for 2-D floor model is twice that for 3-D floor model.

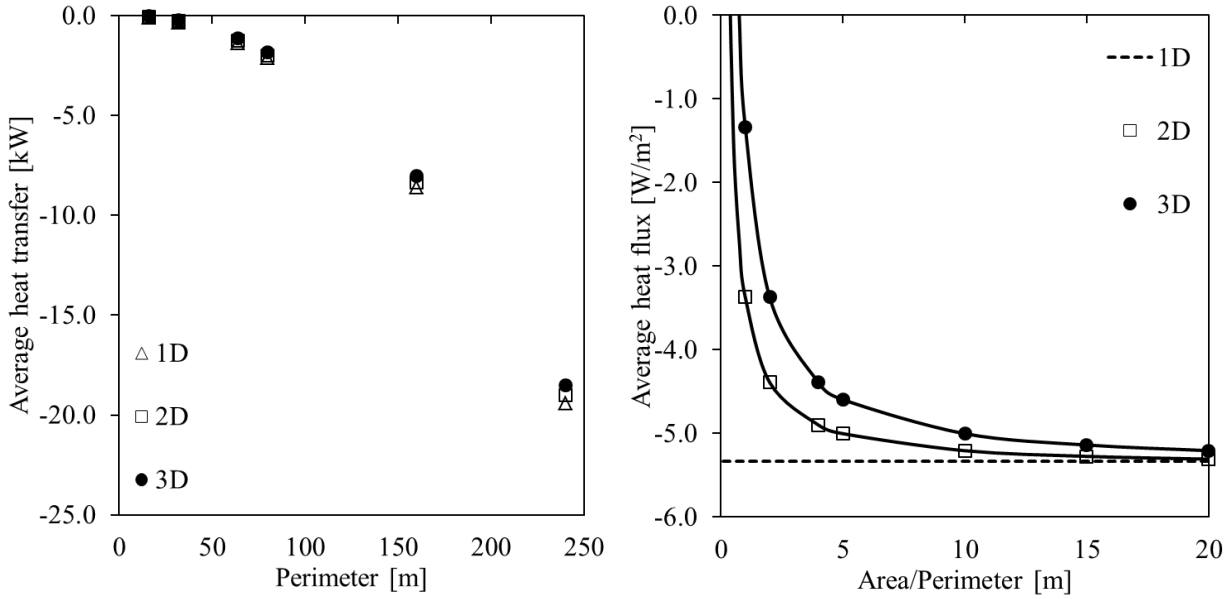

(a) (b)

Figure 3.12: (a) Heat loss vs. perimeter length and (b) Heat loss per unit area vs. A/P for 1D, 2D, and 3D floor model with 1000W/m^3 heat source in Golden, CO.

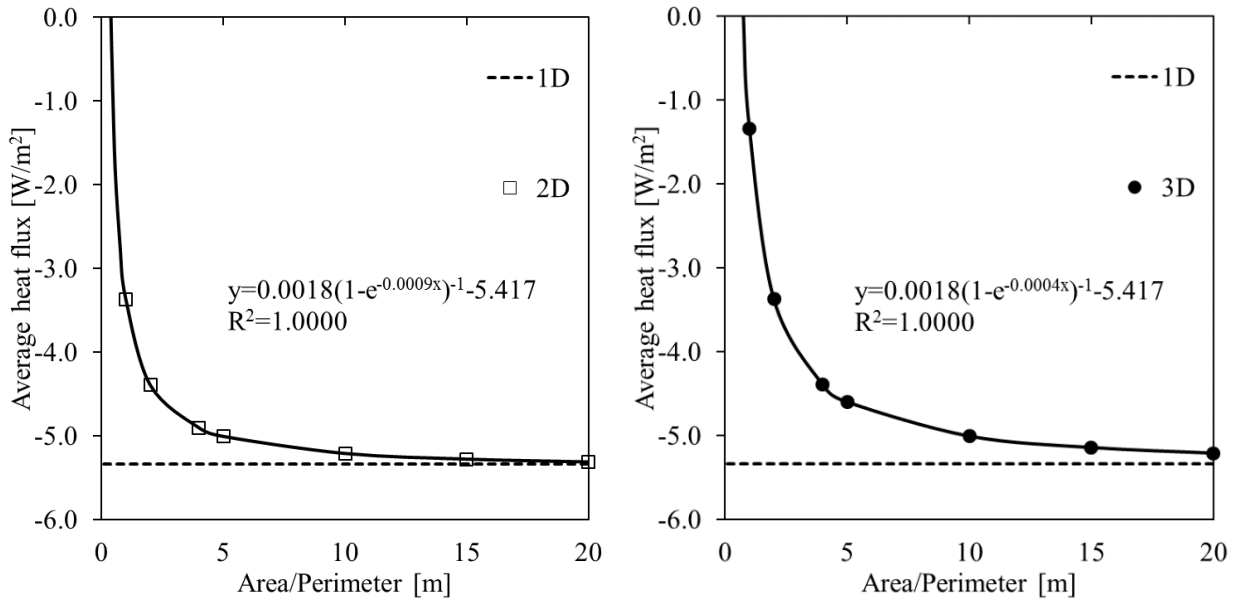

Figure 3.13: (a) 2D floor model exponential curve fit and (b) 3D floor model exponential curve fit with 1000 W/m^3 heat source in Golden, CO.

Table 3.8: Comparison of exponential curve fit coefficients for 2D and 3D floor model with 1000 W/m^3 heat source in Golden, CO

Curve fit coefficients	2D	3D
a	0.0018	0.0018
b	0.0009	0.0004
c	-5.417	-5.417
R^2	1	1

Table 3.9: Heat transfer and heat flux for transient 1D, 2D, and 3D floor model with 1000 W/m^3 heat source in Golden, CO

Perimeter	Area	A/P	Heat Transfer [W]			Heat Flux [W/m^2]		
			1D	2D	3D	1D	2D	3D
16	16	1	-83.0	-54.0	-21.5	-5.34	-3.38	-1.34
32	64	2	-338.6	-281.5	-216.2	-5.34	-4.40	-3.38
64	256	4	-1369.7	-1256.2	-1125.8	-5.34	-4.91	-4.40
80	400	5	-2145.2	-2003.6	-1840.6	-5.34	-5.01	-4.60
160	1600	10	-8623.2	-8340.8	-8014.5	-5.34	-5.21	-5.01
240	3600	15	-19434.9	-19011.6	-18521.9	-5.34	-5.28	-5.14
320	6400	20	-34580.4	-34016.2	-33363.0	-5.34	-5.32	-5.21

3.5 Summary and conclusions

It is possible to obtain results valid in three dimensions directly from two-dimensional models with the aspect ratio (A/P) scaling relationship. For example, a 20-by-20 meter three-dimensional square floor (A/P=400m^2/80m=5m) should have the same heat loss per unit area as that of a 10 meter wide two-dimensional floor. It is well known that the characteristic lengths for a large plane wall of thickness 2L, a long cylinder of radius R, and a sphere of radius R are L (half of thickness of plane wall), R/2, and R/3, respectively. An average heat transfer from a two-dimensional floor corresponds to the three-dimensional floor model, infinite aspect ratio case (for which A/P=L/2),

thus there is an equivalent case of two-dimensional floor for any three-dimensional floor.

In this chapter, an average heat transfer along the floor surface as a function of perimeter as well as average heat transfer per unit area as a function of A/P is analyzed. It is observed that the heat flux could be fitted to the exponential curve with R^2 value greater than 0.99.

$$q = a\left(1 - e^{-bx}\right)^{-1}$$

Similarly, when the heat source exist inside the floor, the heat flux on the floor surface lies on the following exponential curve with R^2 greater than 0.99.

$$q = a\left(1 - e^{-bx}\right)^{-1} + c$$

The equivalent two-dimensional case for any three-dimensional floor is verified by comparison of the curve fit coefficient. The coefficient "b" for two-dimensional floor and three-dimensional floor is compared. The coefficient "b" for two-dimensional floor model is always two times greater than three-dimensional floor model. This verifies that the A/P scaling correlation for two-dimensional model is effective to reflect the thermal behavior of the floor in three-dimensional model.

CHAPTER 4: DEVELOPMENT OF SIMULATION ENVIRONMENT FOR HOLLOW CORE VENTILATED SLAB SYSTEM

4.1 Development of a simulation environment

Figure 4.1 illustrates the schematic of the simulation analysis environment that combines the RC thermal network model for the exterior walls and windows, and the FDM model for the hollow core ventilated slab. The floor and ceiling surface temperatures are obtained from the FDM solution while the radiative and convective heat transfer exchanges between other surfaces are accounted for the RC network model combined with indoor air heat balance.

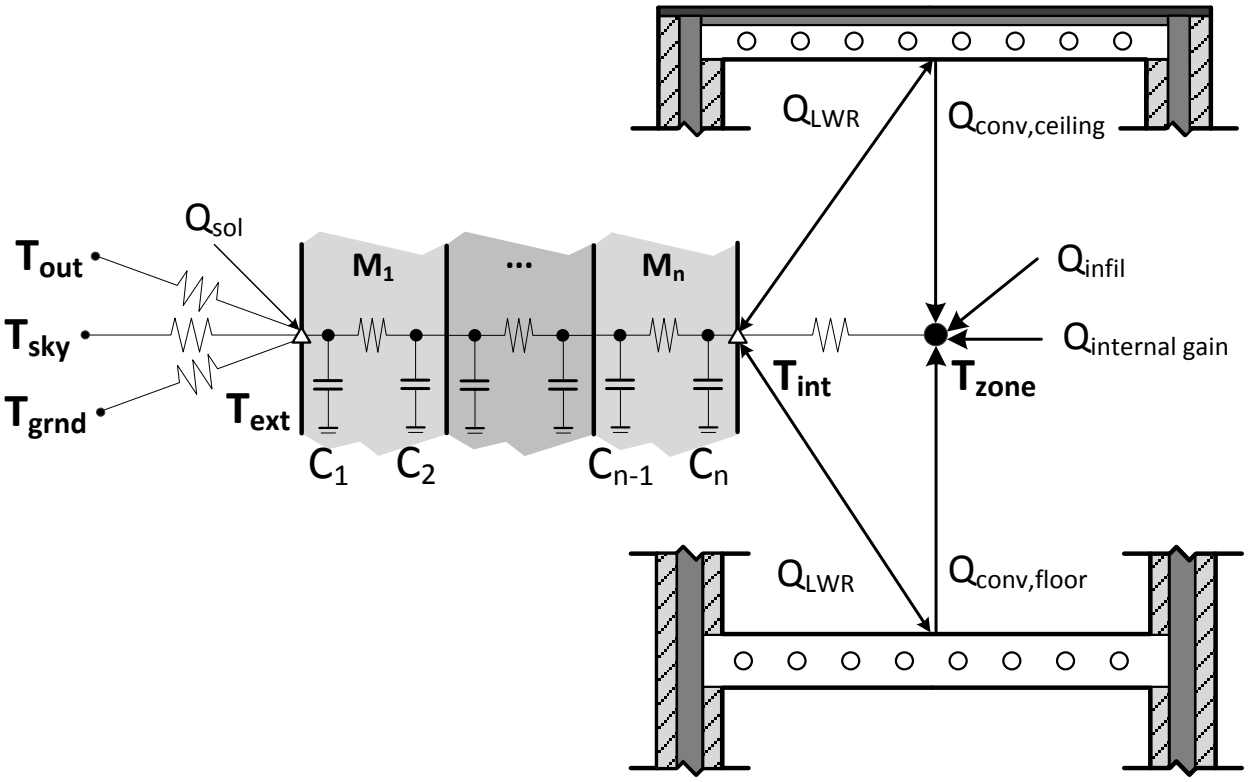

Figure 4.1: Schematic of the FDMRC simulation environment tool

The flow chart of the integrated simulation environment is shown in Figure 4.2.

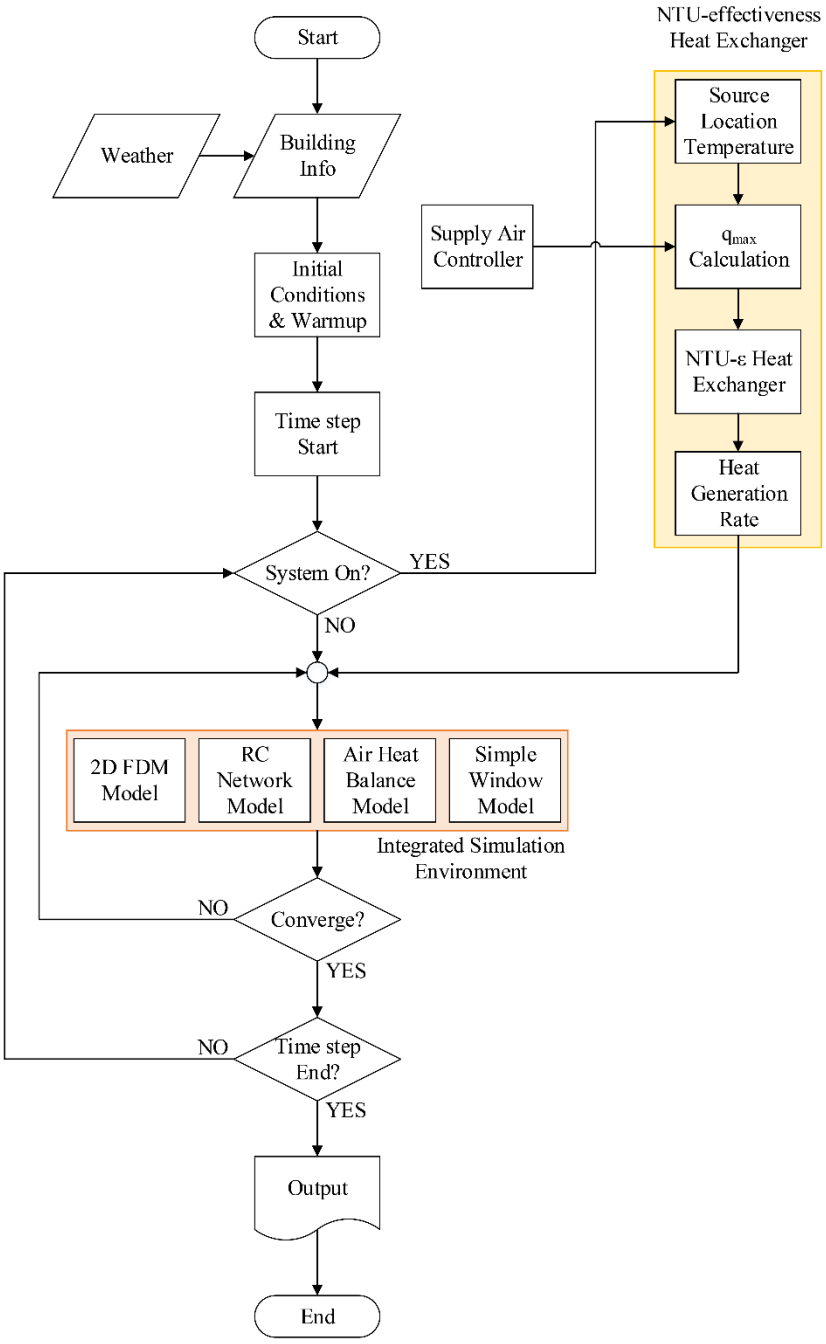

Figure 4.2: Flow chart of the integrated simulation environment

Figure 4.3 shows the relationship between the heat balance processes of the developed FDMRC simulation environment for the thermal zones equipped with the hollow core ventilated slab systems. The calculation procedure denoted in the top part of Figure 4.2, inside the blue dashed box, is applied to all exterior walls and windows. The heat balance calculation process inside the red dashed box is to calculate heat transfer from surfaces where the hollow core ventilated slab system is installed by using FDM technique. Finally, indoor air heat balance module collects convective heat transfer from all interior surfaces, and compute indoor air temperature.

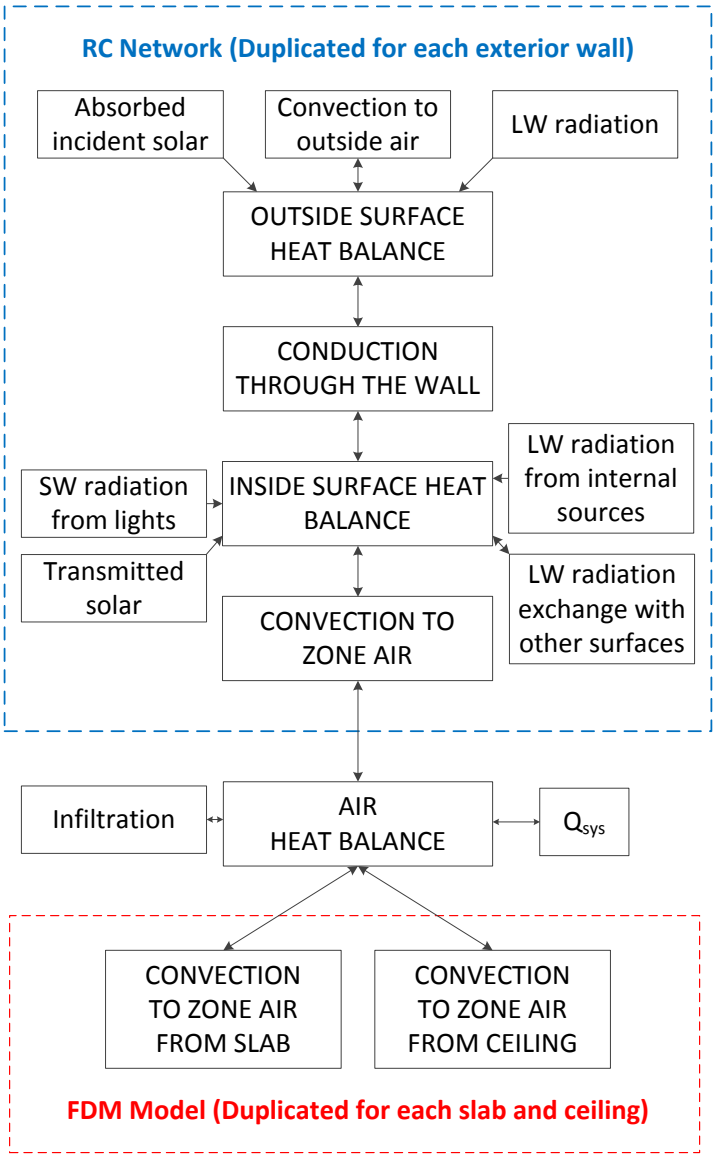

Figure 4.3: Schematic of heat balance calculation procedure

4.2 Outside-face heat balance

The heat balance on the outside surfaces can be expressed using Eq. (4.1). The net heat flux from outside to inside of the wall is taken to be positive in the direction. The first three terms (solar radiation heat flux, convective exchange flux, and long-wave radiation flux exchange) can be combined together by using the concept of a sol-air temperature. Instead of a sol-air temperature, EnergyPlus considers each of these heat balance components separately. The same concept with EnergyPlus is applied to the developed FDMRC model. The direct and diffuse solar radiation is influenced by location, surface azimuth and tilt angle, and material properties. The long-wave radiation flux exchange term calculates radiation exchange between the surface, the sky, and the ground.

$$q''_{sol} + q''_{conv} + q''_{LWR} - q''_{ko} = 0 \qquad (4.1)$$

Where,

q''_{sol} = absorbed direct and diffuse solar radiation heat flux,

q''_{conv} = convective exchange flux with outside air,

q''_{LWR} = long-wave radiation flux exchange with outdoor air and surroundings,

q''_{ko} = conductive flux (q/A) into wall.

4.3 Conduction through the wall

Heat conduction through the opaque wall can be solved by various methods. For instance, Energyplus uses Conduction Transfer Function (CTF) and eQUEST uses z-transformation of response factor to solve transient heat transfer through the building envelopes. We will derive the conduction equation for a one-dimensional, rectangular coordinate system in this section. The temperature in the material is a function of the x coordinate and time ($T = T(x, t)$). According to

the principle of conservation of energy for the control volume, the conduction equation can be expressed as follows:

$$\rho c_p \frac{\partial T}{\partial t} = \mathrm{k} \frac{\partial^2 T}{\partial x^2} \tag{4.2}$$

where,

ρ = density (kg/m^3),

c_p = specific heat (J/kg-°C)

t = time (sec)

T = temperature (°C),

k = thermal conductivity (W/m-°C),

x = distance in x direction (m).

4.4 Inside-face heat balance

The heart of the heat balance method is the internal heat balance. The internal heat balance involving the inside facades of the surfaces can be written as Eq. (4.3) involving several heat transfer components (ASHRAE, 2013):

$$q"_{LWX} + q"_{SW} + q"_{LWS} + q"_{ki} + q"_{conv} = 0 \tag{4.3}$$

Where,

$q"_{LWX}$ = net long-wave radiant flux exchange between zone surfaces

$q"_{SW}$ = net short-wave radiation flux to surface from lights

$q"_{LWS}$ = long-wave radiation flux from equipment in zone

$q"_{ki}$ = conductive flux through the interior surface

$q"_{conv}$ = convective heat flux to zone air

4.5 Indoor air heat balance

The air heat balance technique is applied to determine the heating and cooling thermal load for each thermal zone. The indoor air heat balance combines convective heat transfer from building envelope surfaces, air infiltration, and internal loads. The air heat balance can be written as indicated by Eq. (4.4) with relevant heat transfer components (ASHRAE, 2013).

$$\rho c_p \frac{(T_{air}^{n+1} - T_{air}^{n})}{\Delta t} = \sum Q_{conv} + Q_{internal} + Q_{vent} + Q_{inf} + Q_{sys} \quad (4.4)$$

where,

ρ = density of air (kg/m^3)

c_p = specific heat (J/kg-°C)

Δt = timestep (sec)

T_{air} = zone air temperature (°C)

Q_{conv} = convective heat transfer rate (W)

$Q_{internal}$ = convective parts of internal loads (W)

Q_{vent} = sensible load caused by ventilation (W)

Q_{inf} = sensible load caused by infiltration (W)

Q_{sys} = heat transfer to/from HVAC system (W)

4.6 RC network formulation

Outside surface heat balance, conduction through the wall, and inside surface heat balance can be calculated by the RC thermal network. Also, the building thermal loads and energy use can be evaluated by using the RC thermal network model and the heat balance technique (Hagentoft, 2001; ASHRAE 2005). The RC thermal networks have been widely used to simulate the thermal performance of the building envelope. In particular, 3R2C models have been successfully applied

to simulate the building envelopes for transient building load predictions (Braun, 2002; Seem, 1987; Dewson, 1993; Wang, 2006; Fux, 2011). For instance, Dewson et al. have demonstrated that a 3R2C model is capable of capturing accurately thermal behavior of a test solar cell (Seem, 1987). Moreover, Fux et al. have shown that a 3R2C thermal network model can accurately predict the room air temperature compared to the measured average room air temperature for a lodging building in the Swiss Alps (Fux, 2011). A generic 3R2C thermal network model is modified to have a virtual node at wall surface exposed to surroundings. A virtual node, a wall surface node, has no thermal capacitance so that the surface temperature can react quickly to the environment conditions. If a generic 3R2C thermal network model is used, Sol-air temperature must be employed instead T_o and Q_{solar}. Figure 4.4 depicts a thermal network of exterior wall connecting the indoor space to the outdoor environment. All resistances and capacitances are assumed to be time invariant.

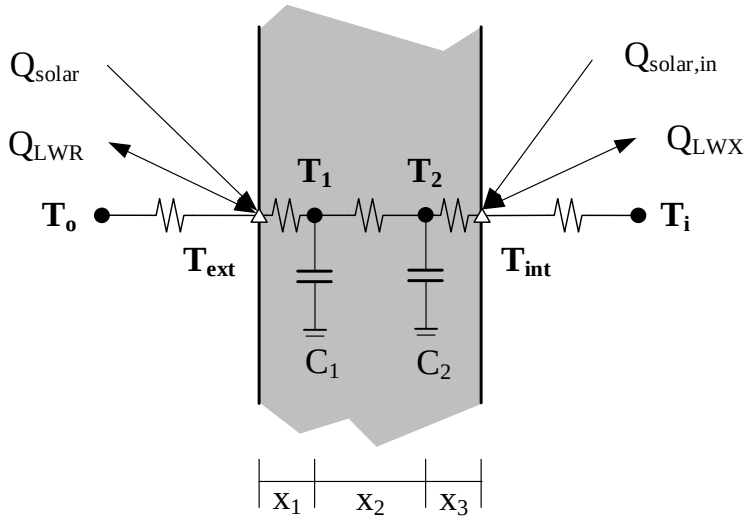

Figure 4.4: Description of RC thermal network for a single layer exterior wall

Convection and long-wave radiation exchanges occur at both sides while short-wave solar radiation is considered only at the outer surface of an exterior wall. Note that the thermal capacity at surface nodes (virtual air film nodes) is neglected so that it can rapidly reacts to the surroundings. The transient heat balance analysis for both nodes yields the following difference equations:

$$k\frac{T_1 - T_{ext}}{x_1}A + h_o A(T_o - T_{ext}) + Q_{LWR} + Q_{solar} = 0 \quad (4.5)$$

$$k\frac{T_{ext} - T_1}{x_1}A + k\frac{T_2 - T_1}{x_2}A = C_1\frac{dT_1}{dt} \quad (4.6)$$

$$k\frac{T_1 - T_2}{x_2}A + k\frac{T_{int} - T_2}{x_3}A = C_2\frac{dT_2}{dt} \quad (4.7)$$

$$k\frac{T_2 - T_{int}}{x_3}A + h_i A(T_i - T_{int}) + Q_{LWX} + Q_{solar,in} = 0 \quad (4.8)$$

where,

k = thermal conductivity of materials (W/m-^{o}C),

x = distance between nodes (m),

C = thermal capacitance of materials (J/^{o}C),

A = area of surfaces (m^2),

T_o = the outdoor air temperature (°C),

T_i = the zone air temperature (°C),

T = the surface temperature of exterior walls (°C),

h_o = the convective coefficient at outer surface of exterior walls (W/m^2-^{o}C),

h_i = the convective coefficient at inner surface of exterior walls (W/m^2-^{o}C),

Q_{LWR} = net longwave radiation (W),

Q_{solar} = exterior solar radiation incident (W),

$Q_{solar,in}$ = transmitted solar radiation incident (W),

Q_{LWX} = longwave radiant heat exchange between surfaces (W).

Note that the thermal capacity at surface node is neglected so that it can rapidly reacts to the surroundings. Figure 4.5 illustrates the RC thermal network for multi-layer exterior wall separating outdoor ambient air and a thermal zone characterized by its indoor temperature, T_i.

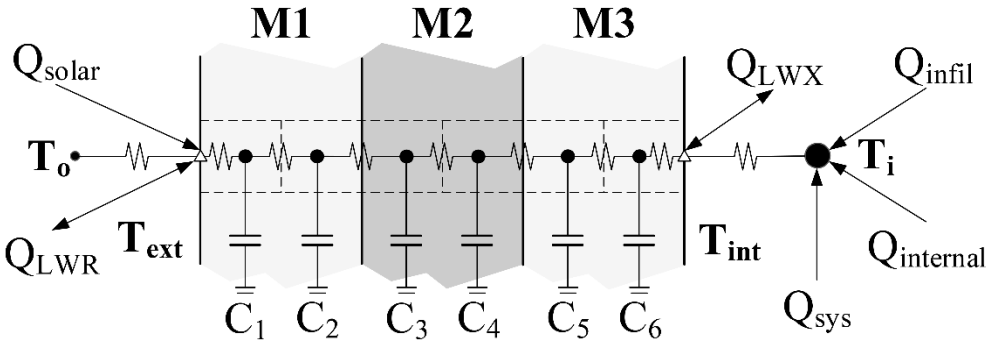

Figure 4.5: Thermal network for the multi-layer exterior walls and a thermal zone

4.7 Window heat balance model

The developed simulation environment utilizes the simplified window model based U-factor and SHGC values to determine the properties of the window glazing. Arasteh et al. (2009) outlined a procedure to determine window properties such as glass-to-glass resistance, thickness, thermal conductivity, transmittance, and glazing reflectance by using only U-value and SHGC values (Arasteh, 2009). Eq. (4.9) expresses the heat balance for single-glazing window. Few assumptions are made in deriving the window heat balance equations. It is assumed that the glass is thin enough so that heat storage within the glazing is neglected and that the short wave radiation absorbed is equally distributed to the two faces of the window glazing.

$$\begin{aligned} E_o\varepsilon_{win} - \varepsilon_{win}\sigma A_{win}\left(T_{win,ext} + 273.15\right)^4 + U_{win}A_{win}\left(T_{win,int} - T_{win,ext}\right) \\ + h_o A_{win}\left(T_o - T_{win,ext}\right) + S_{win,ext} = 0 \end{aligned} \tag{4.9}$$

$$\mathrm{E_i}\varepsilon_{win} - \varepsilon_{win}\sigma A_{win}\left(T_{win,int} + 273.15\right)^4 + U_{win}A_{win}\left(T_{win,int} - T_{win,ext}\right) + h_i A_{win}\left(T_i - T_{win,int}\right) + S_{win,int} = 0 \quad (4.10)$$

where,

$\mathrm{E_o}$ = net long wave radiation on outside face (W),

$\mathrm{E_i}$ = net long wave radiation on inside face (W),

ε_{win} = emittance of glazing (=0.84),

σ = Stefan-Boltzmann constant,

A_{win} = area of glazing (m^2),

U_{win} = U-factor of glazing (W/m^2-^oC),

h_o = the convective coefficient at outer surface of windows (W/m^2-^oC),

h_i = the convective coefficient at inner surface of windows (W/m^2-^oC),

$\mathrm{T_o}$ = the outdoor air temperature (°C),

$\mathrm{T_i}$ = the zone air temperature (°C),

$T_{win,ext}$ = the outside surface temperature of windows (°C),

$T_{win,int}$ = the inside surface temperature of windows (°C),

$S_{win,ext}$ = absorbed solar radiation at outer surface of windows (W),

$S_{win,int}$ = absorbed solar radiation at inner surface of windows (W).

Apart from window heat balance, it is also necessary to consider the interior surfaces that absorb solar radiation that has been transmitted through the fenestration. The developed simulation environment uses a simplified interior solar distribution model that assumes that all transmitted direct radiation is incident on the floor and absorbed as a function of the floor solar absorptance. The reflected portion is assumed to be diffuse and is uniformly absorbed by all surfaces. All

transmitted diffuse radiation is uniformly absorbed by all of the zone surfaces including floor surface. If the total transmitted diffuse radiation and the reflected direct radiation (from the floor) are divided by the total interior surface area of the zone and distributed uniformly, then for all surfaces except for the floor. Eq. (4.11) and Eq. (4.12) provide expressions for the absorbed solar radiation for interior surfaces and floor, respectively.

$$q_{solar,in,j,\theta} = \frac{\sum \dot{q}_{TSHG,diffuse} + (1-\alpha_{floor})\sum \dot{q}_{TSHG,direct}}{\sum_{j=1}^{N} A_j} \tag{4.11}$$

$$q_{solar,in,floor,\theta} = \frac{\sum \dot{q}_{TSHG,diffuse} + (1-\alpha_{floor})\sum \dot{q}_{TSHG,direct}}{\sum_{j=1}^{N} A_j} + \frac{\alpha_{floor}\sum \dot{q}_{TSHG,direct}}{A_{floor}} \tag{4.12}$$

where,

$\dot{q}_{TSHG,diffuse}$ = transmitted diffuse solar radiation through the glazing (W),

$\dot{q}_{TSHG,direct}$ = transmitted direct solar radiation through the glazing (W),

α_{floor} = short wave radiation absorptance of floor surface,

A_j = area of j surface (m^2).

The entire set of difference equations for a single layer opaque wall can be expressed in matrix form as follows:

$$\begin{bmatrix} \left(h_o A + k\frac{A}{x_1}\right) & -k\frac{A}{x_1} & & \\ -k\frac{A}{x_1} & \left(k\frac{A}{x_1} + k\frac{A}{x_2} + \frac{C_1}{\Delta t}\right) & -k\frac{A}{x_2} & \\ & -k\frac{A}{x_2} & \left(k\frac{A}{x_2} + k\frac{A}{x_3} + \frac{C_2}{\Delta t}\right) & -k\frac{A}{x_3} \\ & & -k\frac{A}{x_3} & \left(h_i A + k\frac{A}{x_3}\right) \end{bmatrix} \begin{bmatrix} T_{ext}^{n+1} \\ T_1^{n+1} \\ T_2^{n+1} \\ T_{int}^{n+1} \end{bmatrix}$$

$$= \begin{bmatrix} h_o A T_o + Q_{LWR} + Q_{solar} \\ \frac{C_1}{\Delta t} T_1^n \\ \frac{C_2}{\Delta t} T_2^n \\ h_i A T_i^n + Q_{LWX} + Q_{solar,in} \end{bmatrix}$$

The set of difference equations for a window can be expressed in matrix form as follows:

$$\begin{bmatrix} (Hr_{ext}A_{win} + U_{win}A_{win} + h_o A_{win}) & -U_{win}A_{win} \\ -U_{win}A_{win} & (Hr_{int}A_{win} + U_{win}A_{win} + h_i A_{win}) \end{bmatrix} \begin{bmatrix} T_{win,ext}^{n+1} \\ T_{win,int}^{n+1} \end{bmatrix}$$

$$= \begin{bmatrix} h_o A_{win} T_o + \mathrm{E_o}\varepsilon_{win} + S_{win,ext} - Hr_{ext}A_{win}(273.15) \\ h_i A_{win} T_i^n + \mathrm{E}_i\varepsilon_{win} + S_{win,int} - Hr_{int}A_{win}(273.15) \end{bmatrix}$$

We can express building model in matrix form by combine all sets of difference equations for building surfaces and windows, and indoor air heat balance model as follows:

$$\begin{bmatrix} [n \times n\ A_{roof}] & & & & \\ & [n \times n\ A_{floor}] & & & \\ & & [n \times n\ A_{walls}] & & \\ & & & [n \times n\ A_{wins}] & \\ & & & & [indoor\ air\ ] \end{bmatrix} \begin{bmatrix} [n \times 1\ T_{roof}^{p+1}] \\ [n \times 1\ T_{floor}^{p+1}] \\ [n \times 1\ T_{walls}^{p+1}] \\ [n \times 1\ T_{wins}^{p+1}] \\ T_i^{p+1} \end{bmatrix}$$

$$= \begin{bmatrix} [n \times 1\ B_{roof}] \\ [n \times 1\ B_{floor}] \\ [n \times 1\ B_{walls}] \\ [n \times 1\ B_{wins}] \\ T_i^p + \sum Q_{conv} + Q_{internal} + Q_{vent} + Q_{inf} + Q_{sys} \end{bmatrix}$$

Blank placeholders in the matrix represent zeros. We can rewrite the matrix as

$$\mathrm{AT} = \mathrm{B}$$

and by inverting the matrix A, the solution for the temperature vector T is

$$\mathrm{T} = \mathrm{A}^{-1}\mathrm{B}$$

BiConjugate gradients squared method is employed to solve the linear system. Various alternative solution methods exist to solve the problem. We can use Gauss elimination method, iteration method (i.e. Jacobi iteration, Gauss-Seidel iteration or etc.) or LU decomposition method and so on.

4.8 Convective coefficient calculation

A comprehensive convective algorithm developed by Walton (1983) is adopted in the RC network model for interior convective coefficient for floor and surfaces where the hollow core ventilated slab system exist. The convective coefficients along the surfaces depend on the direction of heat flow and the buoyancy as shown by Eq. (4.13) and Eq. (4.14), respectively. Difference between the surface temperature of ceiling/floor and zone air temperature determines the direction of heat flow ($\Delta T = T_{surf} - T_a$).

If ($\Delta T < 0$ and $\cos(tilt\ angle) > 0$) or ($\Delta T > 0$ and $\cos(tilt\ angle) < 0$)

$$\mathrm{h} = \frac{9.482|\Delta T|^{\frac{1}{3}}}{7.283 - |\cos(tilt\ angle)|} \tag{4.13}$$

elseif ($\Delta T < 0$ and $\cos(tilt\ angle) < 0$) or ($\Delta T > 0$ and $\cos(tilt\ angle) > 0$)

$$\mathrm{h} = \frac{1.810|\Delta T|^{\frac{1}{3}}}{1.382 - |\cos(tilt\ angle)|} \tag{4.14}$$

A correlation to estimate heat transfer coefficient for natural convection along vertical walls can be found in ASHRAE (2005).

$$\mathrm{h} = 1.31|\Delta T|^{0.33} \tag{4.15}$$

The DOE-2 convection model is adopted to calculate convective coefficient of exterior surfaces. The DOE-2 convection model combines the MoWiTT and BLAST detailed convection algorithms [10]. The convection coefficient for very smooth surfaces is calculated by Eq. (4.16):

$$\mathrm{h_{c,glass}} = \sqrt{h_n^2 + [aV^b]^2} \tag{4.16}$$

Where, V is a local wind speed, $\mathrm{h_n}$ is calculated using either Eq. (4.13) or Eq. (4.14), and the

constants *a* and *b* are given in Table 4.1 [11]. For rough surfaces, the convection coefficient is modified according to the Eq. (4.17).

$$h_o = h_n + R_f(h_{c,glass} - h_n) \tag{4.17}$$

Where, R_f is the roughness of surfaces, and it is given in Table 4.2.

Table 4.1: MoWiTT coefficients

Wind Direction	Ct ($W/m^2K^{4/3}$)	a ($W/m^2K(m/s)^b$)	b (-)
Windward	0.84	3.26	0.89
Leeward	0.84	3.55	0.617

Table 4.2: Roughness multiplier

	very smooth	smooth	medium smooth	medium rough	rough	very rough
R_f	2.17	1.67	1.52	1.13	1.11	1.00

4.9 Outside surface longwave radiation heat exchange

Surface tilt angle of roof is 0°, floor is 180°, and wall is 90°. View factors to sky, air and ground can be calculated as follows:

$$\begin{aligned} \beta &= \sqrt{0.5(1 + \cos(surf\ tilt\ angle)} \\ F_{sky} &= 0.5(1 + \cos(surf\ tilt\ angle)\,\beta \\ F_{air} &= F_{sky}(1 - \beta) \\ F_{grd} &= 0.5(1 - \cos(surf\ tilt\ angle)) \end{aligned} \tag{4.18}$$

Thus, the longwave radiation at the outside surface of the building envelopes can be expressed as:

$$
\begin{aligned}
Q_{rad,sky} &= \sigma\varepsilon F_{sky}\left(\left(T_{sky}+273.15\right)^4-\left(T_{s,o}+273.15\right)^4\right)\\
Q_{rad,OA} &= \sigma\varepsilon F_{air}\left((T_o+273.15)^4-\left(T_{s,o}+273.15\right)^4\right)\\
Q_{rad,grd} &= \sigma\varepsilon F_{grd}\left((T_o+273.15)^4-\left(T_{s,o}+273.15\right)^4\right)\\
Q_{LWR} &= Q_{rad,sky}+Q_{rad,OA}+Q_{rad,grd}
\end{aligned}
\tag{4.19}
$$

Note that ground temperature is assumed to be the same as outdoor air temperature.

4.10 Internal longwave radiation heat exchange

Two surfaces at different temperatures exchange heat energy by thermal radiation. The FDMRC network simulation environment uses a grey interchange model to account for thermal radiation heat exchange between interior surfaces. In particular, the radiosity concept developed by Hottel and Sarofim (1967) is used by the simulation environment. The net radiative heat exchange at a surface can be determined by Eq.(4.20).

$$
\mathrm{Q_{LWX}} = \sum \sigma ScriptF_{ij}\left[(T_{si}+273.15)^4-\left(T_{sj,send}+273.15\right)^4\right] \tag{4.20}
$$

Where $ScriptF_{ij}$ is the exchange coefficient that includes all reflections, absorptions and re-emissions from other surface in the enclosure (EnergyPlus, 2010), and expressed as follows:

$$
\begin{aligned}
if\ i=j, \mathrm{ScriptF_{ij}} &= \frac{\varepsilon_i}{1-\varepsilon_i}\left(J_{ij}-\varepsilon_i\right)\\
\mathrm{else, ScriptF_{ij}} &= \frac{\varepsilon_i}{1-\varepsilon_i}J_{ij}
\end{aligned}
\tag{4.21}
$$

Where *J*, is the matrix of partial radiosity, can be expressed as follows:

$$
\mathrm{J_{ij}} = \frac{C_{ij}}{-\dfrac{A_i\varepsilon_i}{1-\varepsilon_i}} \tag{4.22}
$$

$$\text{if i} = \text{j}, \text{C}_{\text{ij}} = \text{F}_{\text{ij}} A_i - \frac{\text{A}_\text{i}}{1 - \varepsilon_i}$$

$$\text{else}, \text{C}_{\text{ij}} = \text{F}_{\text{ij}} A_i$$

Where F_{ij} is the traditional view factor from surface i to j (Yunus, 2001).

4.11 Model verification

Figure 4.6 shows the FDMRC environment that is used for the verification analysis. The boundary at floor edge is set as adiabatic so that the floor has a 1-dimensional thermal behavior. The predictions of mean air temperature and energy consumptions for representative heating and cooling seasons are compared to EnergyPlus simulation results.

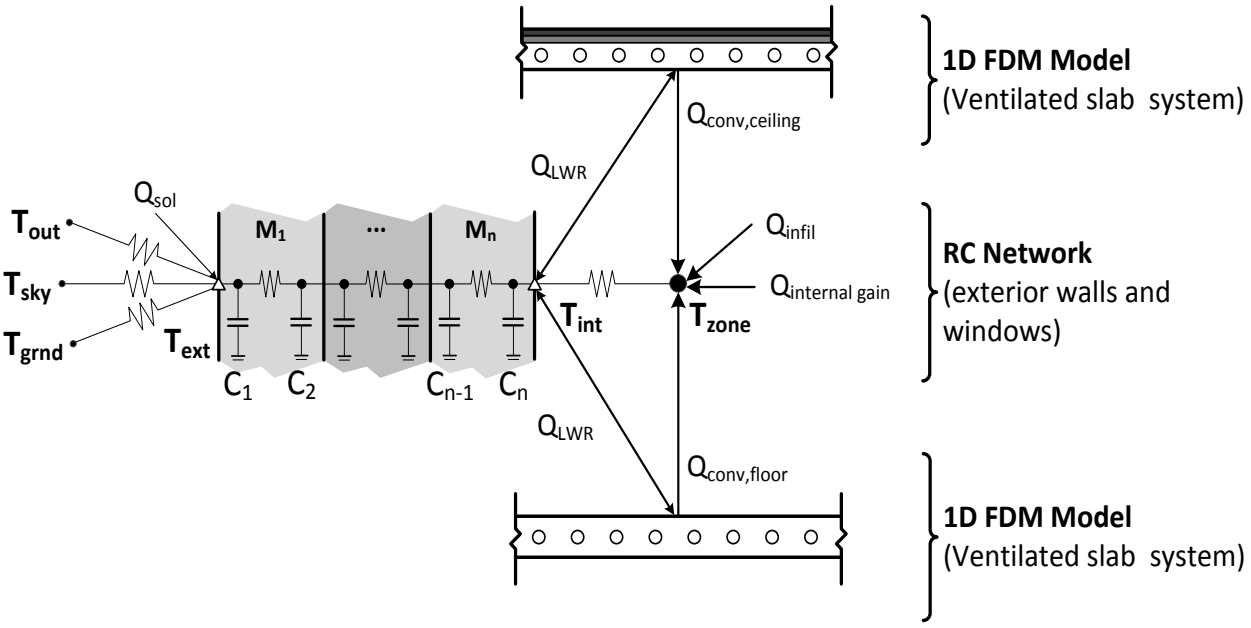

Figure 4.6: FDMRC environment validated with EnergyPlus

Predictions from EnergyPlus are considered as reference results, and used to validate the predictions from the simulation environment that combines RC thermal network model and one-dimensional FDM model for floor heat transfer (FDMRC). To do so, exactly the same thermal

zones with the same HVAC system are modeled in EnergyPlus and FDMRC. Figure 4.7 presents a section view of two thermal zones modeled used for both the developed FDMRC simulation environment and EnergyPlus. The zone model includes a hollow core ventilated slab system with uniform horizontal insulation underneath. The length of the floor is 4.3m. The thickness of the exterior walls is 0.15m. The pitch size of a hollow core is 0.3m. The total area of a hollow core precast concrete floor is 18.49m^2. Heating and cooling set point temperature is assumed to be 19ºC and 26ºC, respectively, during 24 hours. The exterior walls and roofs are exposed to outdoor air. The slab in the lower zone is assumed to contact a ground. As the ground has enormous thermal mass, it maintains a constant temperature at 18°C throughout a year.

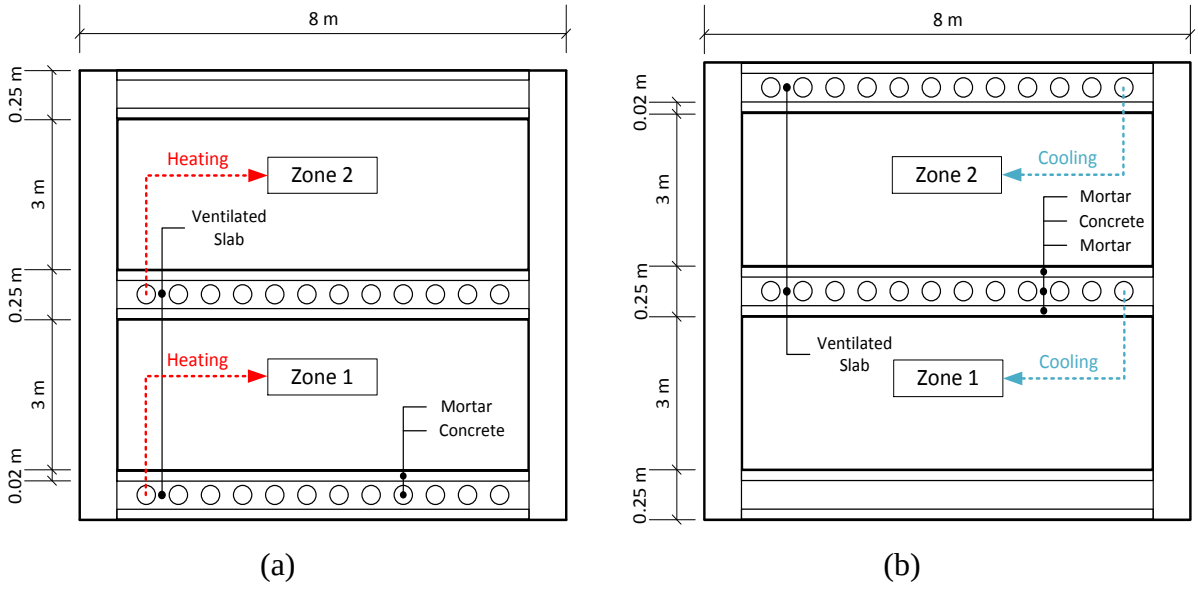

Figure 4.7: A section view of the building slab and exterior walls for two thermal zones used for the verification analysis: (a) ventilated heating slab and (b) ventilated cooling slab

The variable temperature control algorithm is modulated to control the zone air temperature within selected set point temperature and throttling ranges. Specifically, the ventilated slab systems can vary the inlet air temperature from a designed low temperature up to a specified high temperature

limit. The inlet air temperature is varied linearly on an hourly basis (or any selected time step). In the analysis presented in this study, the mean indoor air temperature is used as a thermal comfort indicator to control the inlet air temperature. However, other thermal comfort indicators (such as mean radiant temperature or operative temperature) can be used to control the air inlet temperature. While the inlet air temperature is controlled, the mass flow rate of the inlet air remains constant. Graphical descriptions of the implemented variable temperature control strategies utilized for the ventilated slab systems are presented in Figure 4.8.

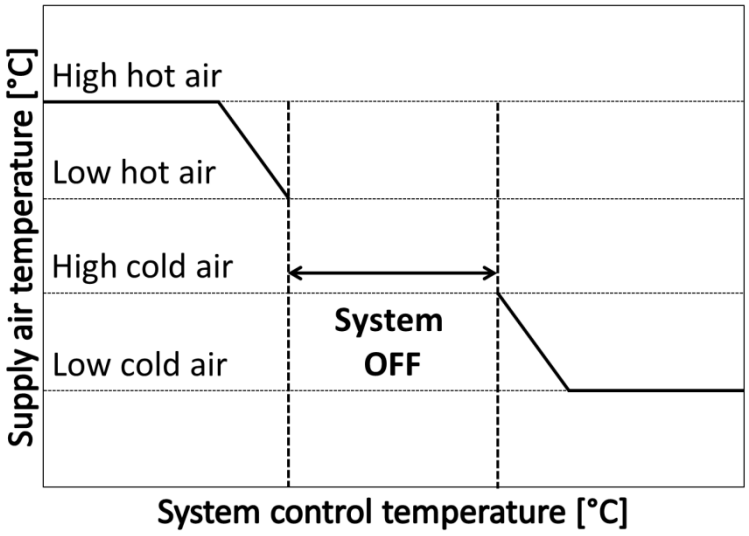

Figure 4.8: Variable temperature control strategy for the hollow core ventilated slab system

The predictions obtained for the two-zone model from the developed simulation environment (that combines an RC thermal network and a numerical solution of the ventilated slab system) are compared against the results obtained from EnergyPlus simulation tool. In particular, the mean air temperatures and heating and cooling energy consumptions are compared.

The results for the hourly heating and cooling energy consumption of EnergyPlus are simply obtained from its output report. For the developed simulation environment (FDMRC), the heating

and cooling energy consumption is calculated for each time step using following equation:

$$E_{heating} = \dot{m}_h c_{p,h}(T_{hot\ air,in} - T_{hot\ air,out}) \quad (4.23)$$

$$E_{cooling} = \dot{m}_c C_{p,c}(T_{chilled\ air,out} - T_{chilled\ air,in}) \quad (4.24)$$

Where,

$E_{heating}$ = Heating energy consumption [J]

$\dot{m}_h$ = Hot air mass flow rate [kg/s]

$c_{p,h}$ = specific heat of hot air [J/kg-ºC]

$E_{cooling}$ = Cooling energy consumption [J]

$\dot{m}_c$ = cold air mass flow rate [kg/s]

$c_{p,c}$ = specific heat of cold air [J/kg-ºC]

Non-dimensional forms of the RMSE are useful because often one wants to compare RMSE with different units. There are two approaches: normalize the RMSE to the range of the observed data, or normalize to the mean of the observed data.

$$NRMSE = \frac{RMSE}{x_{obs,max} - x_{obs,min}} \quad (4.25)$$

The validation analysis is conducted using weather data for Golden, CO obtained from TMY3 weather file (Wilcox and Marion, 2008). The total solar radiation incident on the outside of the exterior wall surfaces are calculated and include several components solar beam, solar sky diffuse, solar ground diffuse, and reflected solar radiations. Figure 4.9 and Figure 4.10 depict outdoor dry bulb temperature and exterior surface incident solar radiation on the exterior walls during representative winter season (January 15th to 18th) and summer season (August 17th to 20th) in

Golden, CO, respectively.

Table 4.3: Description of the building model used for validation

Slab (Floor)	U-value	0.219 W/m^2-K	
Exterior wall	U-value	0.493 W/m^2-K	
Roof (ceiling)	U-value	0.221 W/m^2-K	
Fenestration	U-value	1.98 W/m^2-K	
	SHGC	0.39	
	Window-to-wall ratio	34.6% (East and West)	
Internal load	Infiltration	0.015 m^3/s	
Ventilated slab system	Core diameter		0.10 m
	Throttling range		±1℃
	Setpoint	Heating	19˚C
		Cooling	26˚C
	Air inlet temperature	Min. heating	25˚C
		Max. heating	30˚C
		Min. cooling	15˚C
		Max. cooling	20˚C
	Air mass flow rate	Heating	0.3 kg/s
		Cooling	0.3 kg/s

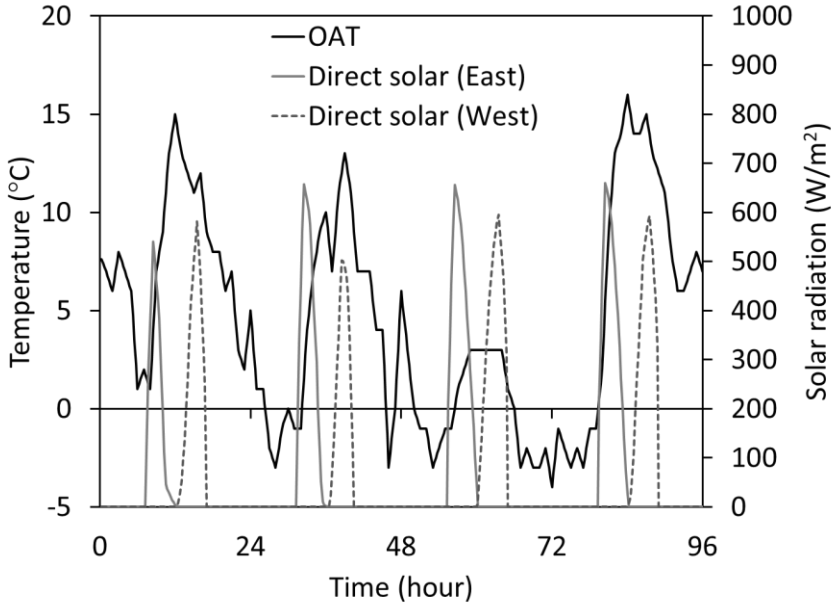

Figure 4.9: Outdoor air temperature and exterior incident solar radiation from January 15th to 18th in Golden, CO.

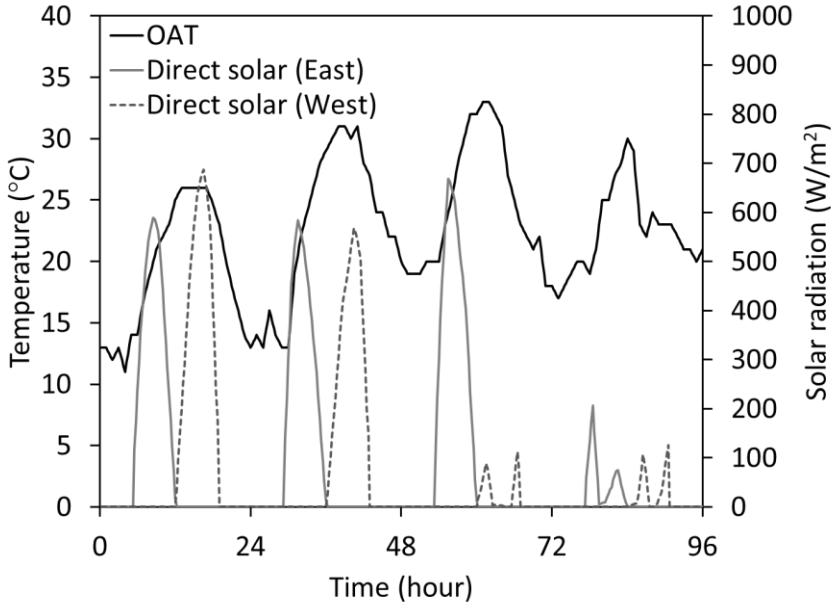

Figure 4.10: Outdoor air temperature and exterior incident solar radiation from August 17th to 20th in Golden, CO.

As part of the verification analysis, the predictions of mean air temperature and ventilated slab system energy consumption for the lower zone (zone 1) and the upper zone (zone 2) obtained from the one-dimensional FDMRC model during heating season (January 15th to 18th) and summer season (August 17th to 20th) are verified against results obtained from EnergyPlus. It should be noted that the one-dimensional FDM solution is obtained by setting adiabatic boundary conditions at the slab and wall joint in the model of Figure 4.6.

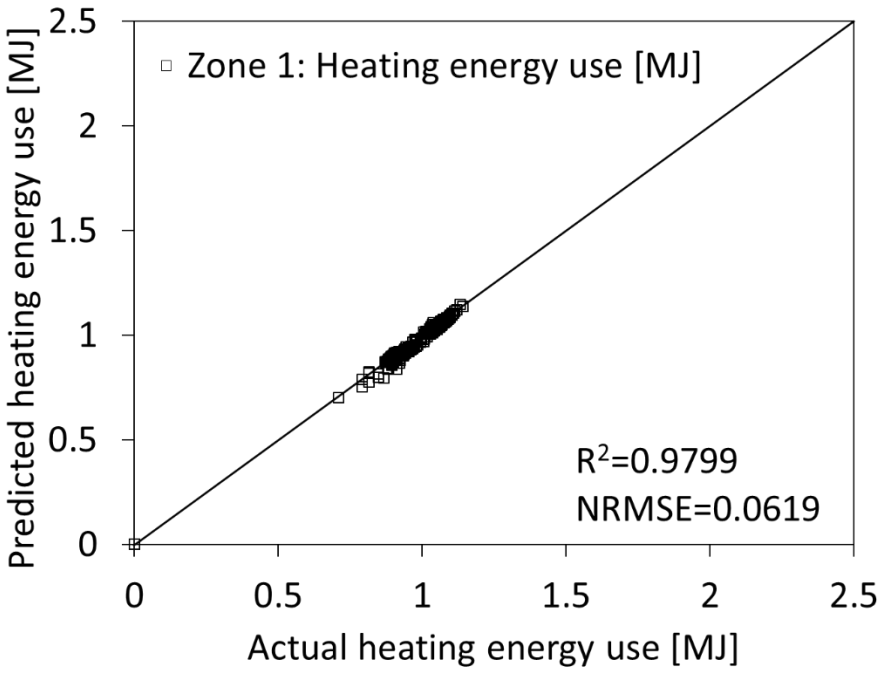

(a)

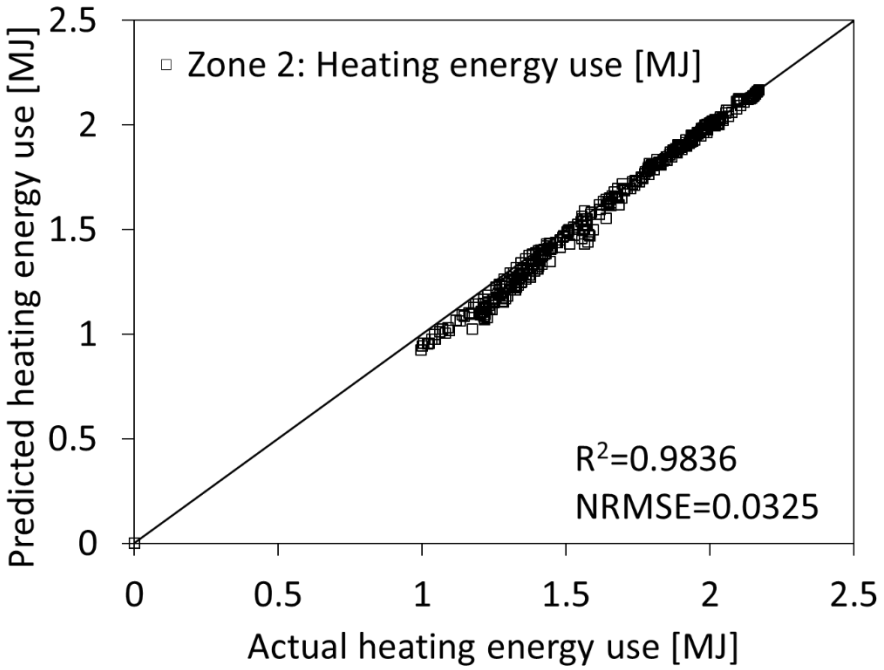

(b)

Figure 4.11: Histogram of heating energy use for (a) Zone 1 and (b) Zone 2 obtained from EnergyPlus and FDMRC during representative heating season

Figure 4.12 shows a comparative analysis of mean air temperature and heating energy consumption of ventilated slab system for each zone obtained from one-dimensional FDMRC and EnergyPlus. The mean air temperature of the upper zone is lower than that of the lower zone because the roof in the upper zone is exposed to outdoor conditions, whereas the lower zone is in contact with the ground medium set at a constant temperature. Moreover, the heating thermal load of the upper zone is greater than that of the lower zone. By comparing the mean air temperatures and ventilated heating energy consumption during the heating season, the results of both simulation tools showed good agreement with similar patterns under the same operation and environment conditions.

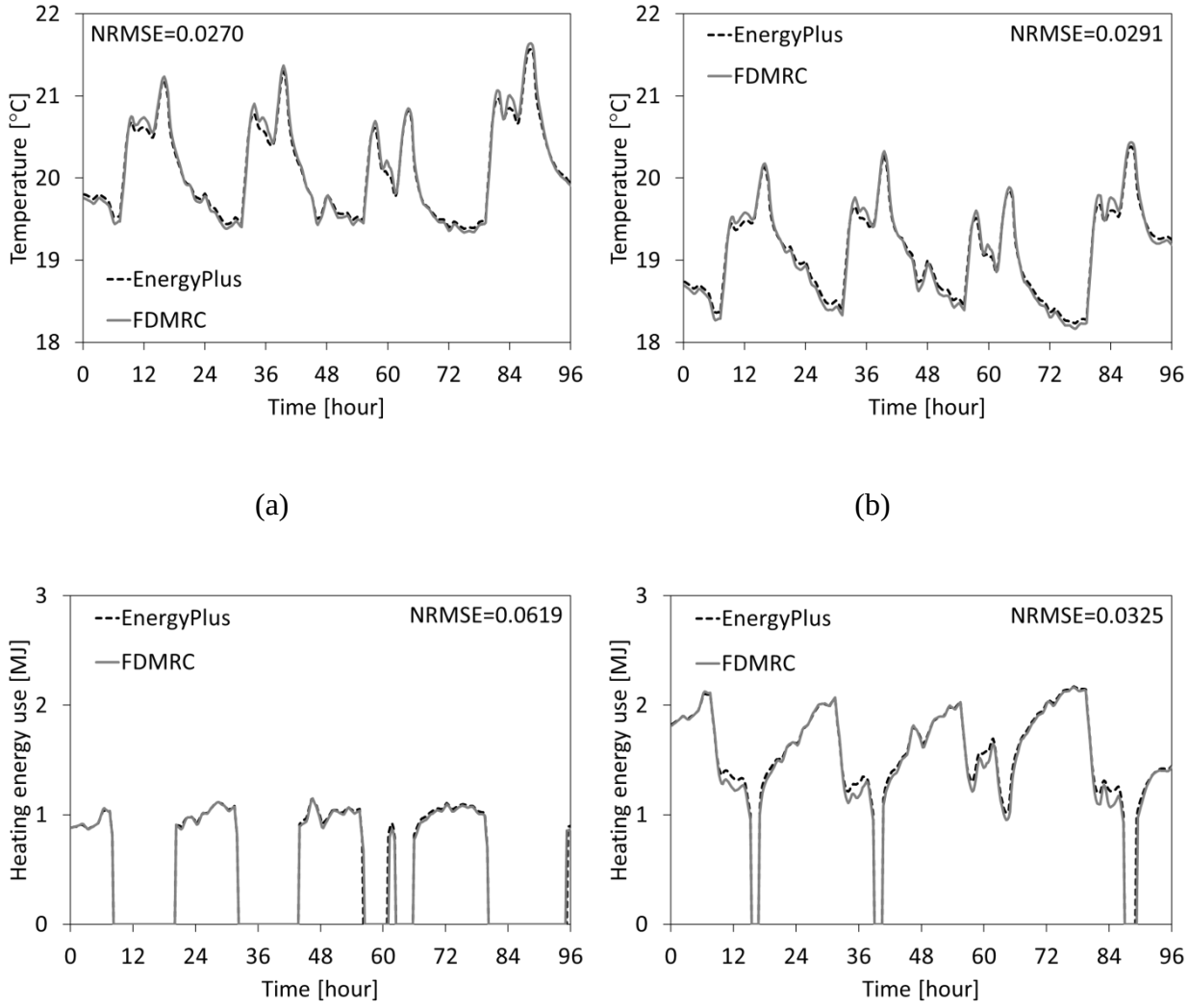

Figure 4.12: Time series mean air temperature and heating energy use comparison between EnergyPlus and FDMRC: (a) Mean air temperature in Zone 1, (b) Mean air temperature in Zone 2, (c) Heating energy use in Zone 1, and (d) Heating energy use in Zone 2

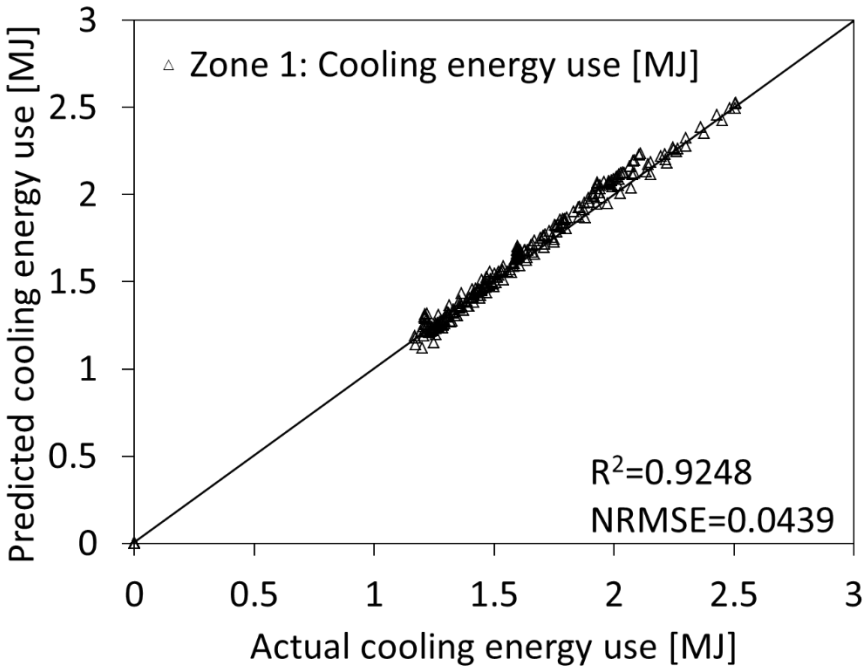

(a)

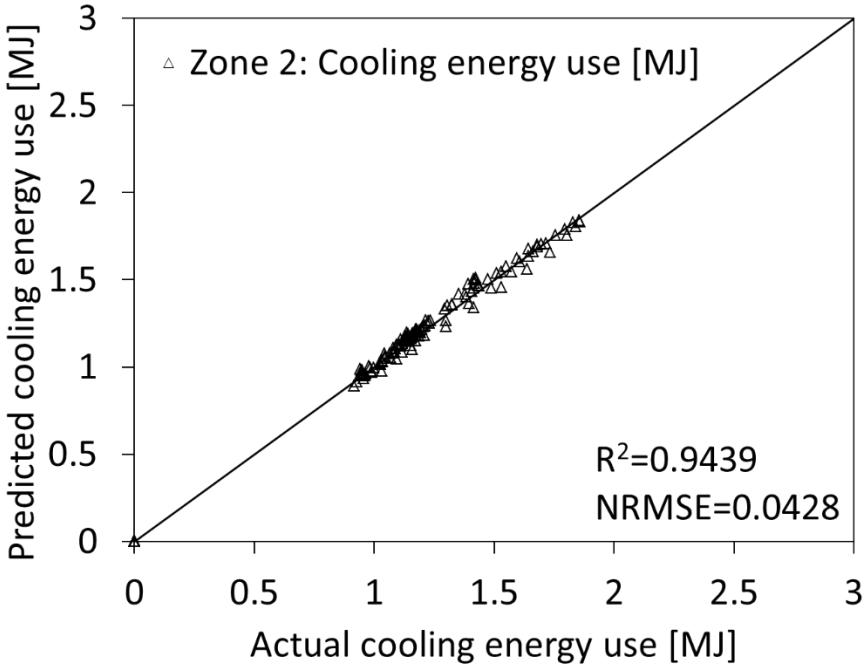

(b)

Figure 4.13: Histogram of cooling energy use for (a) Zone 1 and (b) Zone 2 obtained from EnergyPlus and FDMRC during representative cooling season

Time variations of outdoor temperature, zone mean air temperatures, and ventilated slab cooling energy usage for each zone predicted by the two simulation tools during four summer days are depicted in Figure 4.14. The predictions of mean air temperature and radiant cooling energy consumption obtained from the one-dimensional FDMRC agreed well with the results of EnergyPlus.

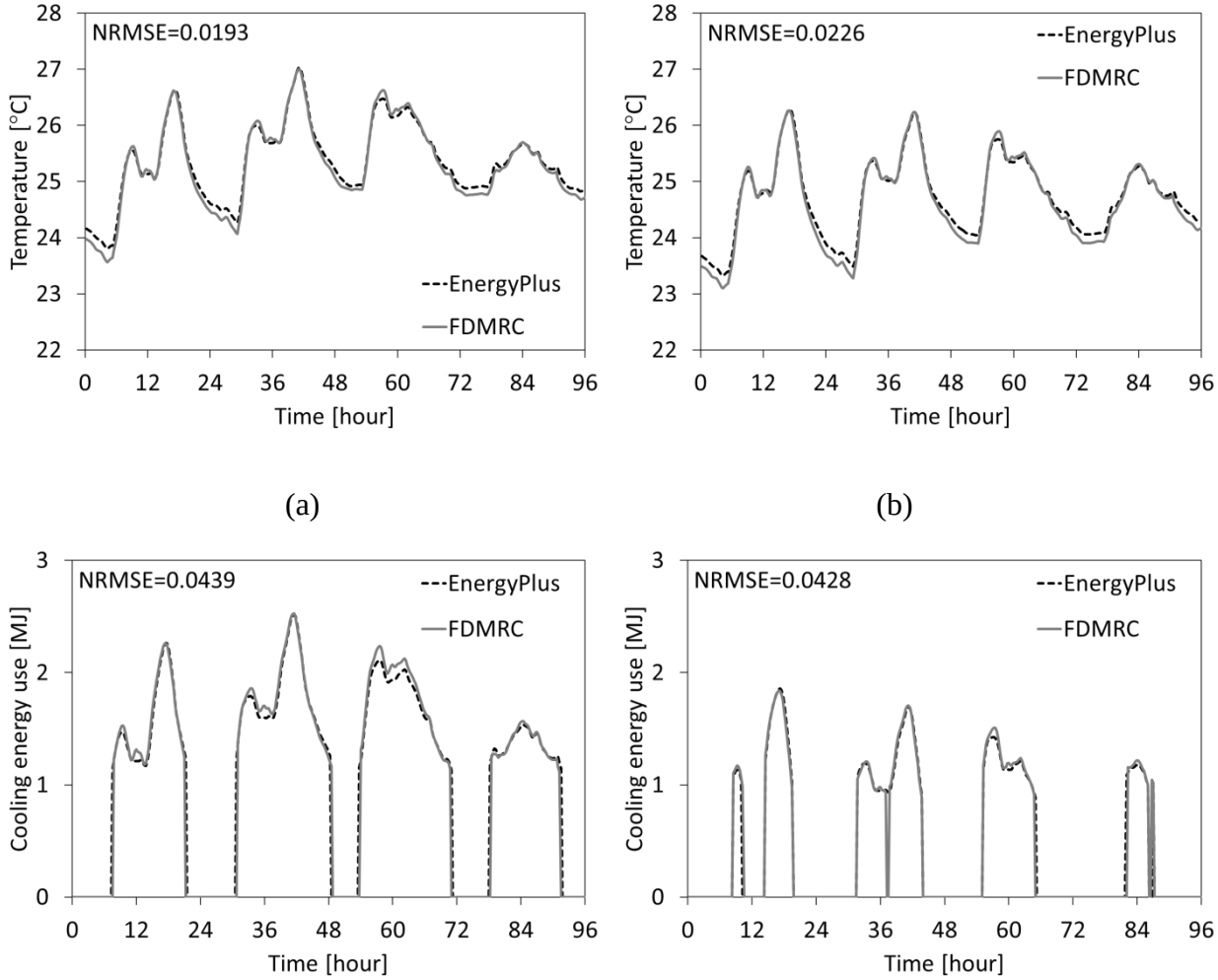

Figure 4.14: Time series mean air temperature and cooling energy use comparison between EnergyPlus and FDMRC: (a) Mean air temperature in Zone 1, (b) Mean air temperature in Zone 2, (c) Cooling energy use in Zone 1, and (d) Cooling energy use in Zone 2

4.12 Impact of thermal bridge on performance of a hollow core ventilated slab

In this section, the effect of thermal bridging caused by the floor slab-wall joint is investigated by estimating the total heating and cooling energy consumption of the ventilated slab system operated with variable temperature control strategy. To estimate the impact of thermal bridging effects, predictions of the developed simulation environment, combining the RC network model with the 2-dimensional FDM numerical solution (FDMRC-2D), are compared to those obtained from FDMRC-1D simulation model. Specifically, the FDMRC-1D simulation model, which agrees well with EnergyPlus, does not account for thermal bridging and has no heat losses through the slab and wall joint. In the other hand, the 2-dimensional FDMRC simulation model accounts for the thermal bridging between the floor slab-wall joint and has heat transfer through the slab and wall joint. As shown in Figure 4.15, two typical insulation placements are considered for the analysis: (a) Internal insulation and (b) Middle insulation.

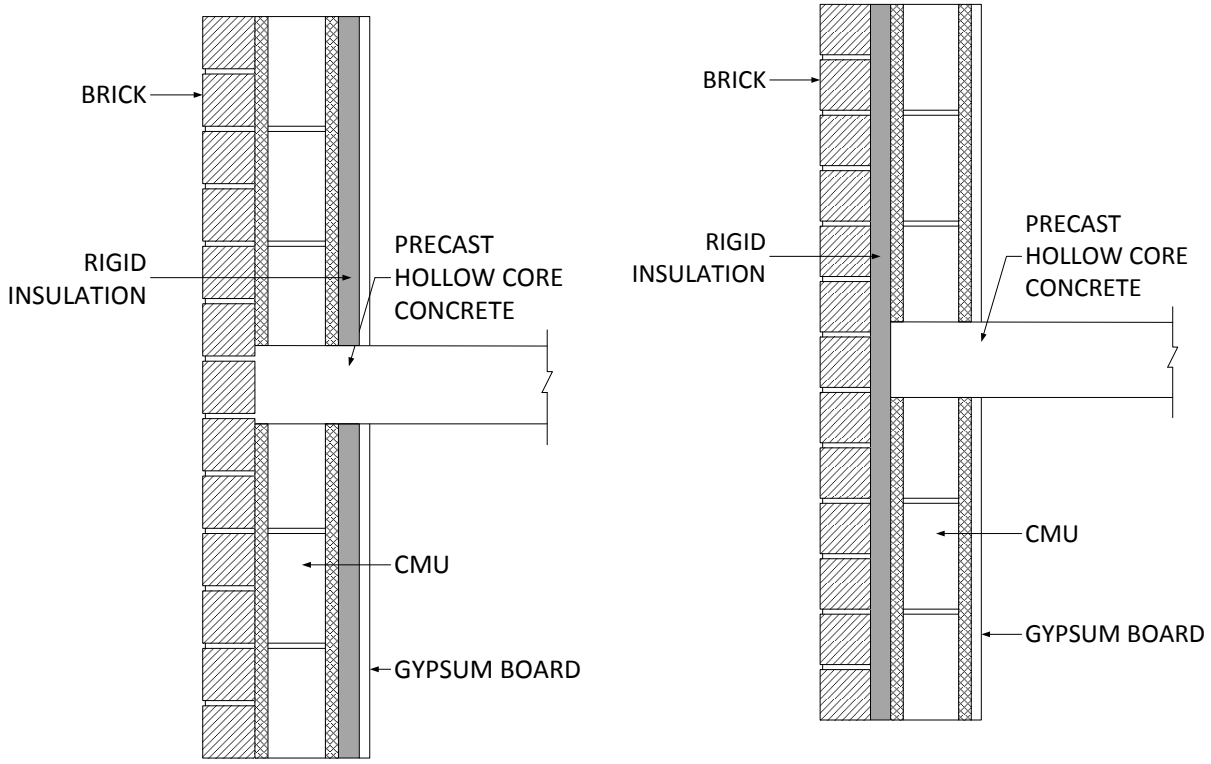

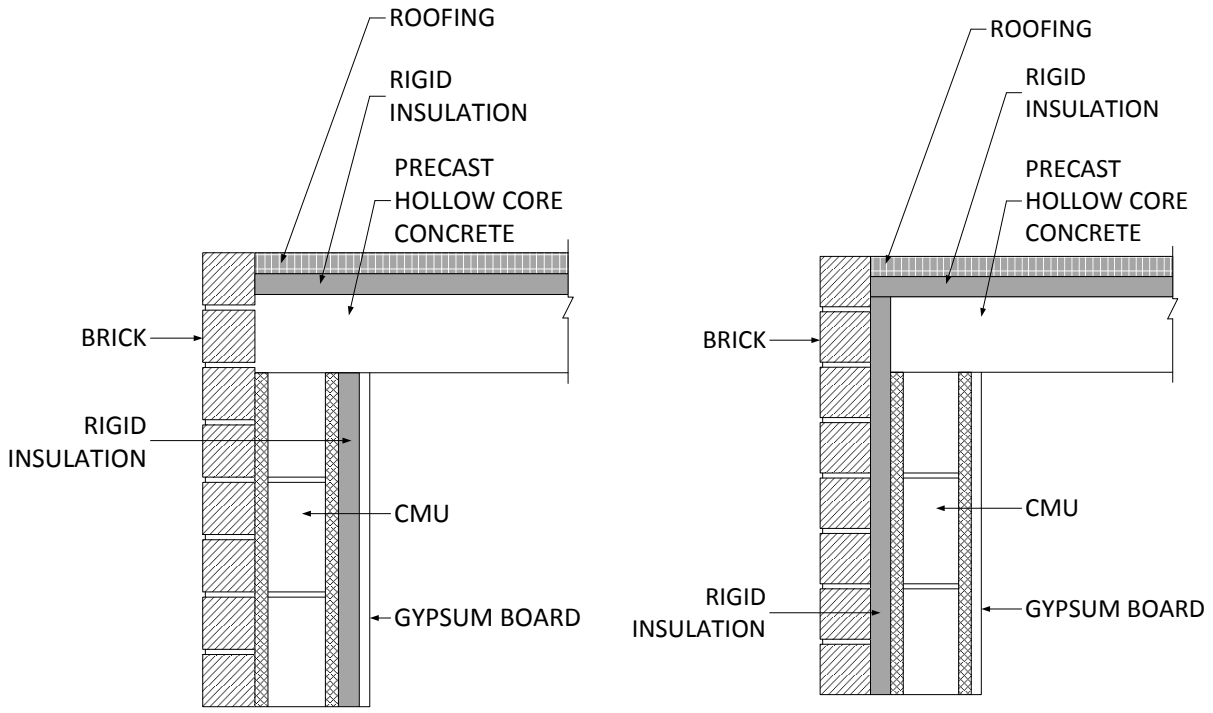

Figure 4.15: (a) Insulation in the inner surface of the wall and (b) Insulation in the center plane of the wall

Table 4.4 summarizes the characteristics of the building envelope, the internal loads, and the ventilated slab system considered in the simulation analysis.

Table 4.4: Characteristics of building envelope, internal loads, and the ventilated slab system

Slab (Floor)	U-value	0.219 W/m^2-K
Exterior wall	U-value	0.493 W/m^2-K
Roof (ceiling)	U-value	0.221 W/m^2-K
Fenestration	U-value	1.98 W/m^2-K
	SHGC	0.39

	Window-to-wall ratio	34.6% (East and West)	
Internal load	Infiltration	0.015 m^3/s	
Ventilated slab system	Core diameter		0.10 m
	Throttling range		±1℃
	Setpoint	Heating	20˚C
		Cooling	25˚C
	Air inlet temperature	Min. heating	25˚C
		Max. heating	30˚C
		Min. cooling	10˚C
		Max. cooling	15˚C
	Air mass flow rate	Heating	0.0031 $kg/s/m^2$
		Cooling	0.0023 $kg/s/m^2$

Figure 4.16 to Figure 4.19 show the time variations of zone mean air temperature and energy consumption predicted by the developed simulation environment using both the 1-dimensional numerical solution and 2-dimensional numerical solution during heating and cooling season. The internal insulation placement is considered as shown in Figure 4.15 (a).

Substantial difference is observed in heating and cooling energy use predicted by the 1-dimensional and 2-dimensional numerical solutions. The un-insulated ventilated slab system without accounting for the thermal bridging effects (i.e., estimated with FDMRC-1D) consumes 657 MJ of heating source energy, meanwhile the same ventilated slab system but with consideration of the thermal bridging effects (i.e., estimated with FDMRC-2D) consumes 770 MJ of heating energy in the heating season, that is, a 14% difference. Moreover, the uninsulated ventilated slab system without accounting for the thermal bridging effects (i.e., computed using

FDMRC-1D) consumes 360 MJ of cooling source energy, meanwhile the same ventilated slab system but with consideration of the thermal bridging effects (i.e., computed using FDMRC-2D) consumes 392 MJ of cooling energy in the cooling season, that is a 10% difference. Thus, the FDMRC-1D neglects the additional heating and cooling thermal loads caused by thermal bridging at the slab-wall joint.

Figure 4.20 through Figure 4.23 show the time variations of zone mean air temperature and heating energy consumption predicted by the 1-dimensional and 2-dimensional numerical solution during heating season. The insulation in the middle of the exterior wall is considered. The detailed slab and wall joint is depicted in Figure 4.15 (b). The assembly R-value of the exterior wall is 0.493 in accordance with ASHRAE 90.1-2007 requirement.

Based on the results, the time-variations of mean air temperatures computed by FDMRC-1D and FDMRC-2D are almost identical because the variable temperature control strategy is maintaining the same desired indoor temperature for each thermal zone. However, there is a substantial difference in heating energy use as well as cooling energy use predicted using the two numerical solutions.

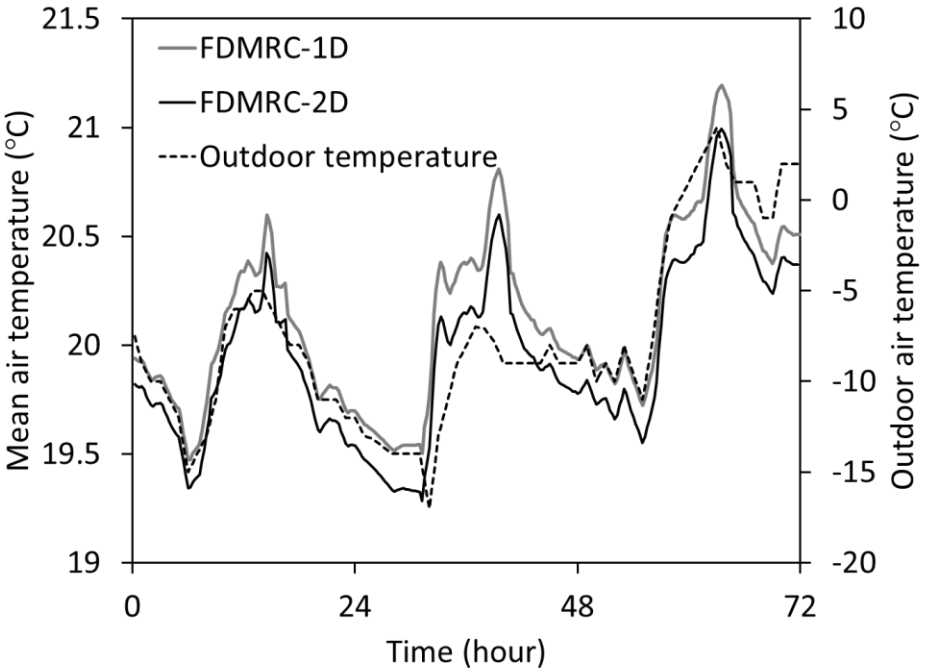

(a)

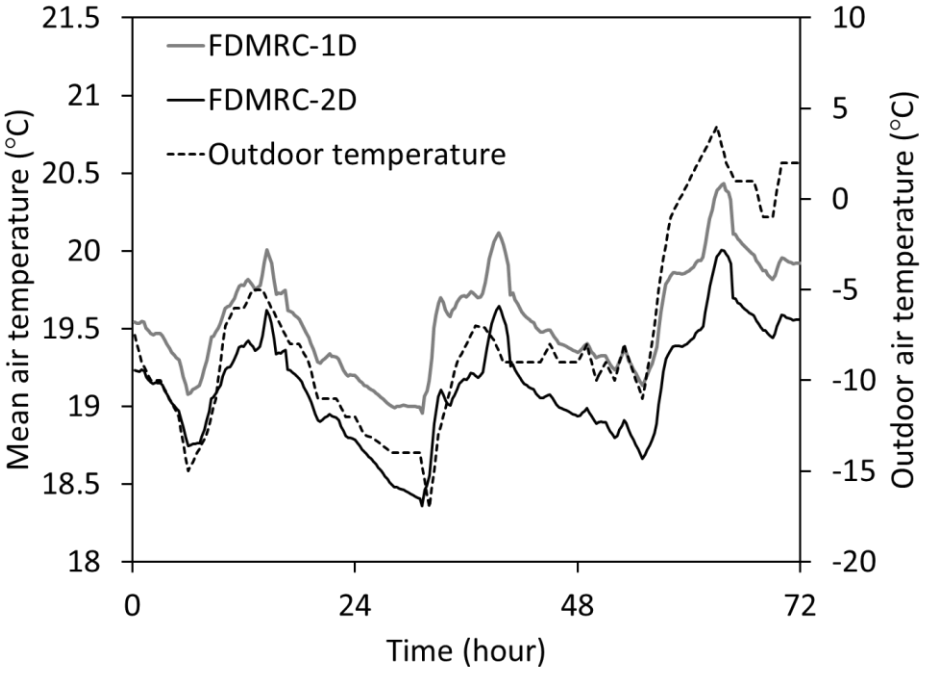

(b)

Figure 4.16: (a) Zone 1 mean air temperature and (b) Zone 2 mean air temperature obtained from FDMRC-1D and FDMRC-2D during heating season (January 15th to 18th)

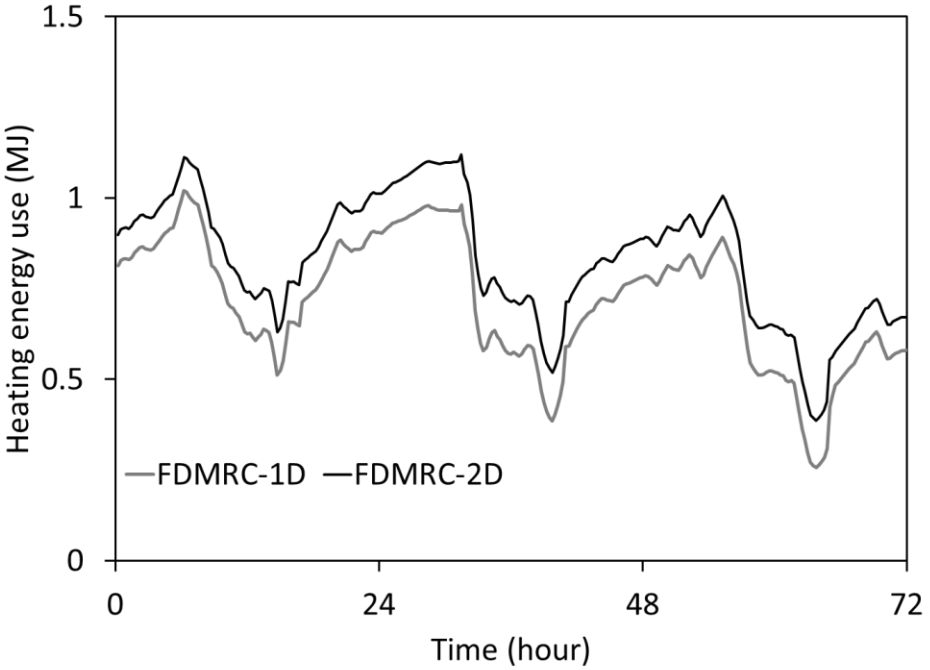

(a)

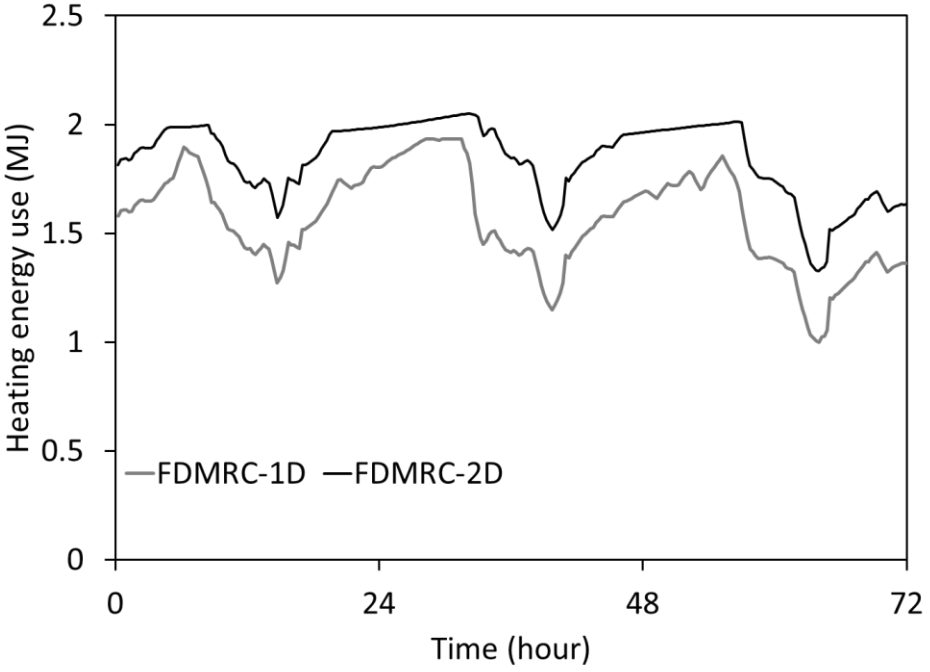

(b)

Figure 4.17: (a) Zone 1 heating energy use and (b) Zone 2 heating energy use obtained from FDMRC-1D and FDMRC-2D during heating season (January 15th to 18th)

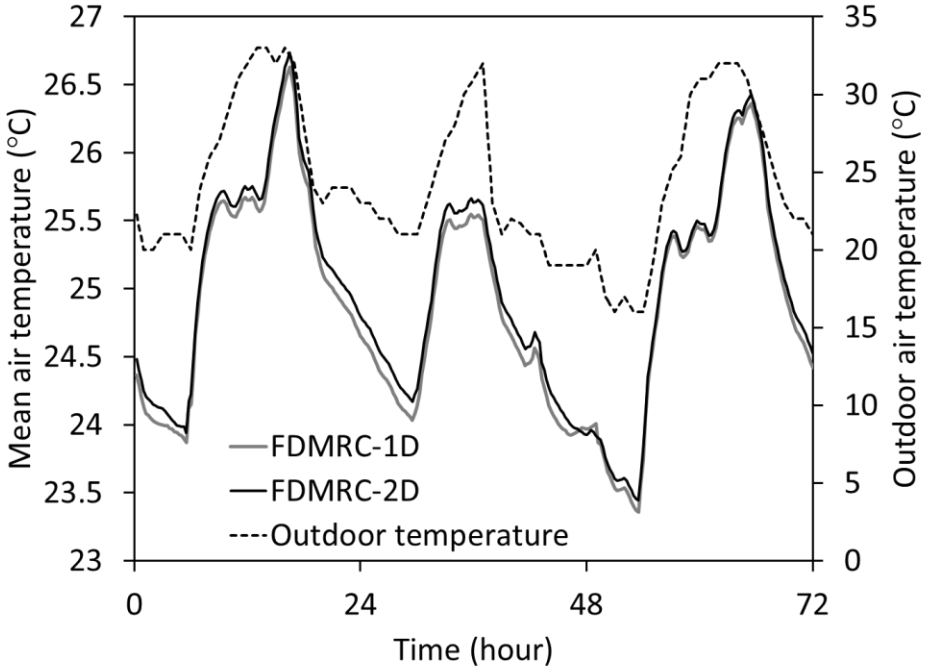

(a)

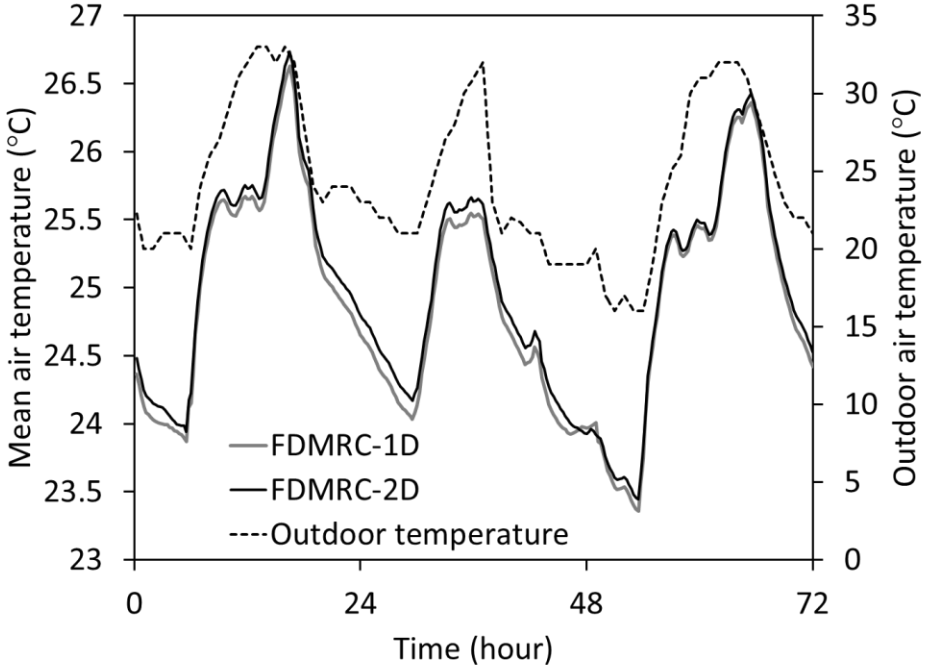

(b)

Figure 4.18: (a) Zone 1 mean air temperature and (b) Zone 2 mean air temperature obtained from FDMRC-1D and FDMRC-2D during cooling season (August 17th to 19th)

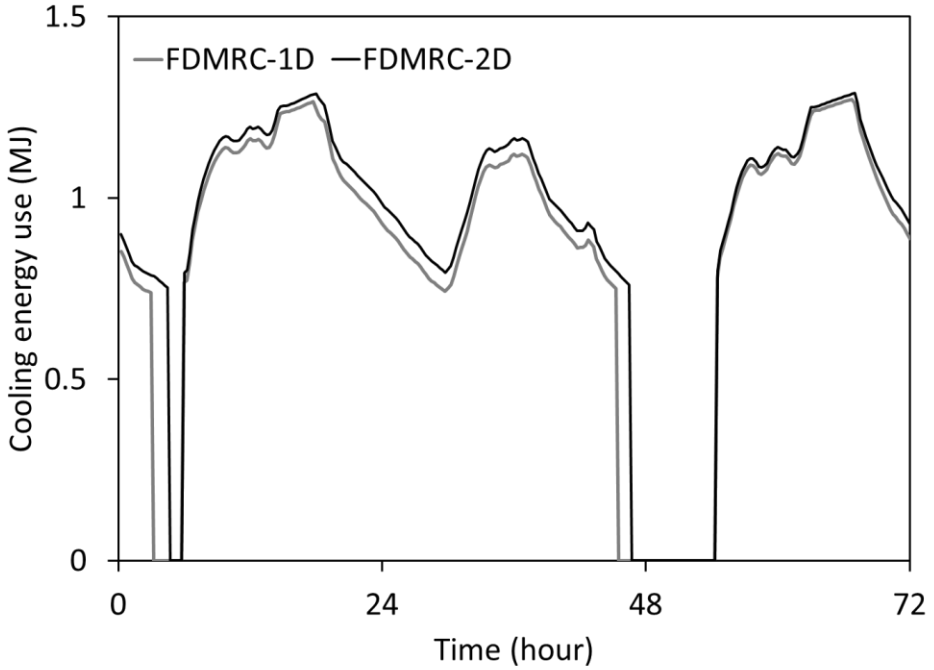

(a)

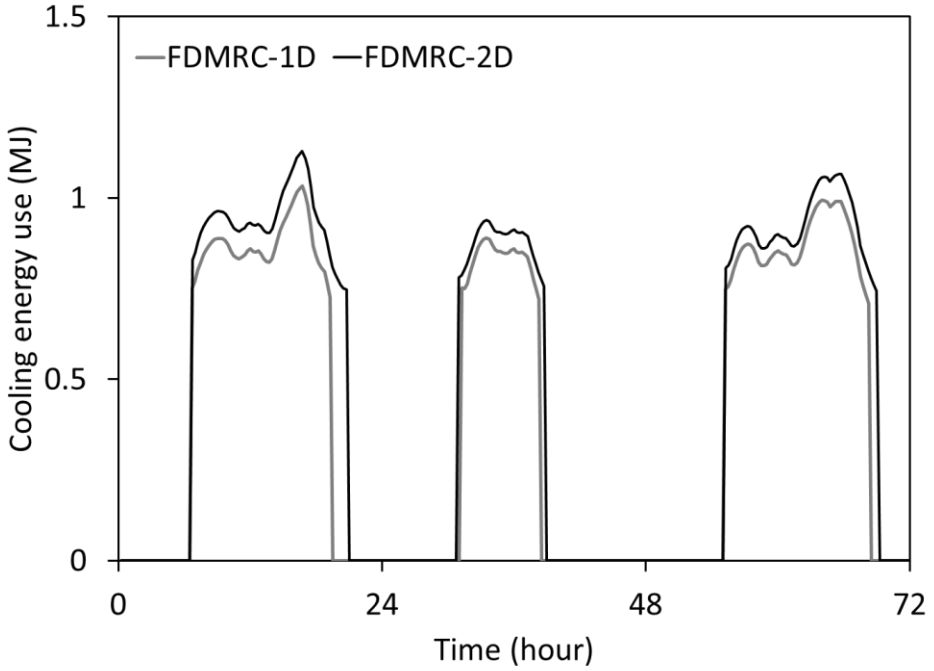

(b)

Figure 4.19: (a) Zone 1 cooling energy use and (b) Zone 2 cooling energy use obtained from FDMRC-1D and FDMRC-2D during cooling season (August 17th to 19th)

Table 4.5: Comparison of energy consumption by the ventilated slab system and estimation of thermal bridging effects during heating season (January 15th to 17th) and cooling season (August 17th to 19th) for 8 meter wide slab in Golden, CO

	Heating energy use [MJ]			Cooling energy use [MJ]		
	Zone 1	Zone 2	Total	Zone 1	Zone 2	Total
FDMRC-1D	450	889	1339	567	311	878
FDMRC-2D	540	991	1531	605	361	966
Absolute Diff.	90	101	191	38	50	89
% Diff.	20%	11%	14%	7%	16%	10%

As summarized in Table 4.6, the ventilated slab system without accounting for the thermal bridging effects (i.e., estimated with FDMRC-1D) consumes 692 MJ of heating source energy, meanwhile the same ventilated slab system but with consideration of the thermal bridging effects (i.e., estimated with FDMRC-2D) consumes 721 MJ of heating energy in the heating season, that is, a 4% difference. Moreover, the ventilated slab system without accounting for the thermal bridging effects (i.e., computed using FDMRC-1D) consumes 358 MJ of cooling source energy, meanwhile the same ventilated slab system but with consideration of the thermal bridging effects (i.e., computed using FDMRC-2D) consumes 369 MJ of cooling energy in the cooling season, that is a 3% difference. Even though the difference of source energy usage between FDMRC-1D and FDMRC-2D is smaller than the slab and wall joint as Figure 4.15 (a), the ventilated slab system with consideration of the thermal bridge still consumes certain amount of more source energy compared to 1-dimensional model.

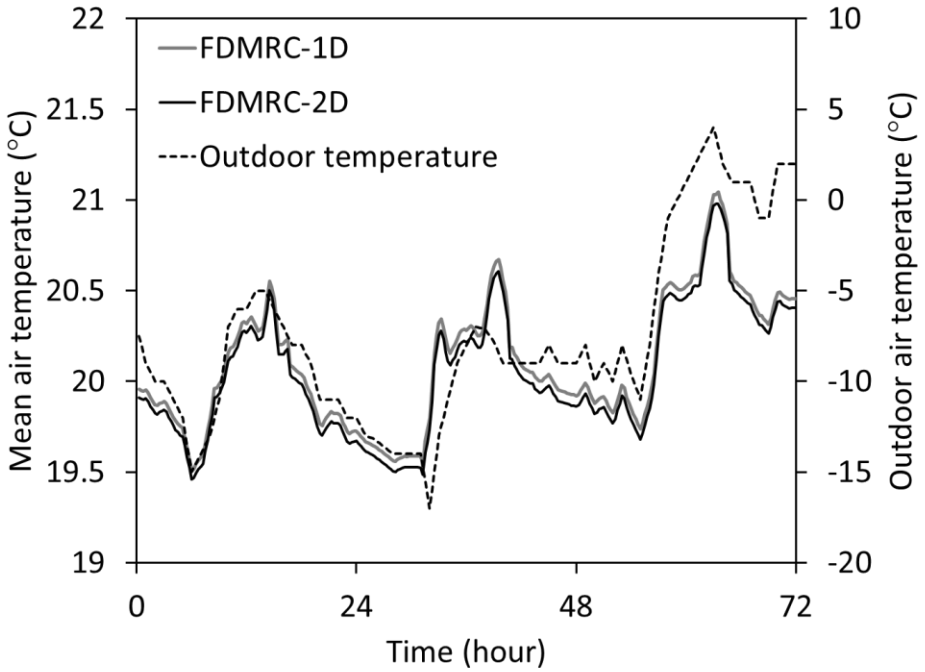

(a)

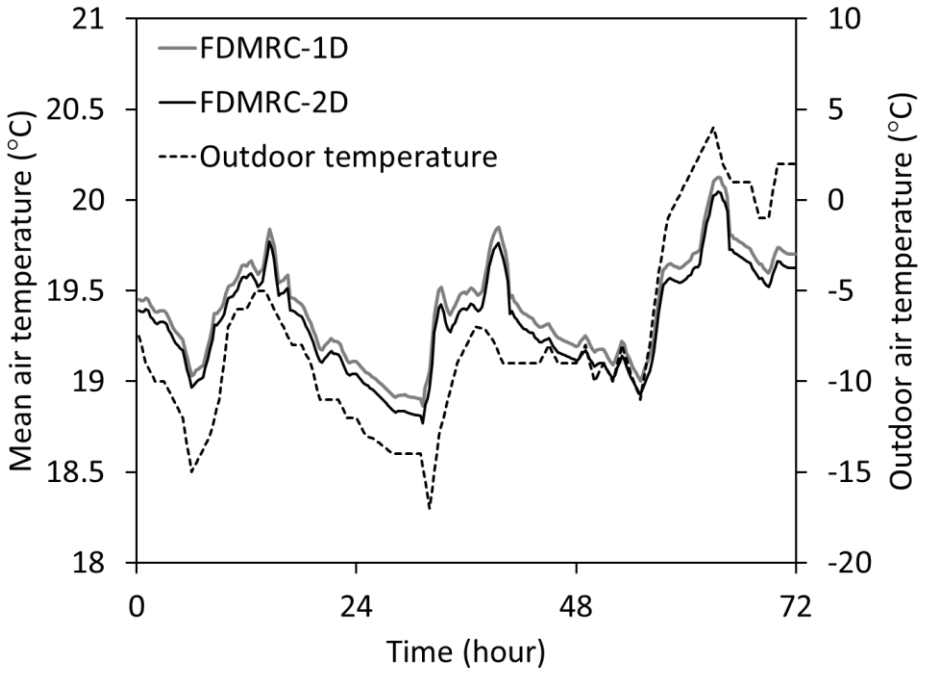

(b)

Figure 4.20: (a) Zone 1 mean air temperature and (b) Zone 2 mean air temperature obtained from FDMRC-1D and FDMRC-2D during heating season (January 15th to 17th)

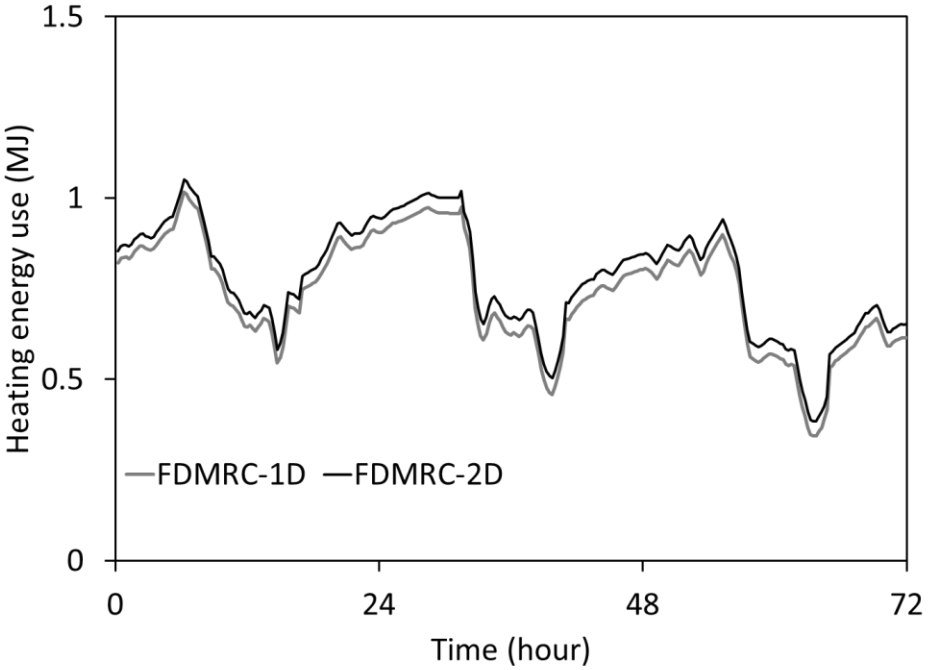

(a)

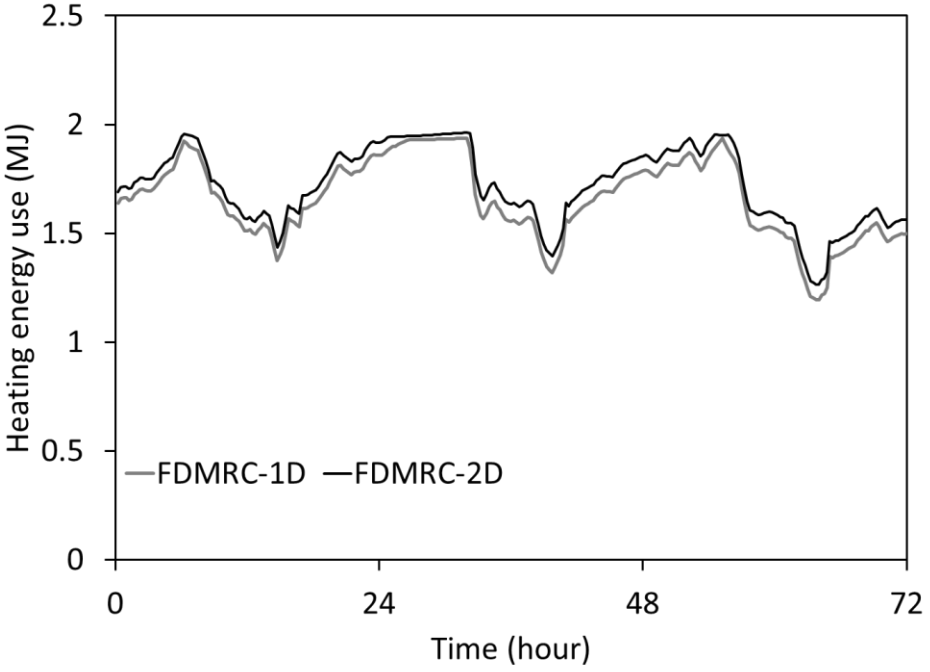

(b)

Figure 4.21: (a) Zone 1 heating energy use and (b) Zone 2 heating energy use obtained from FDMRC-1D and FDMRC-2D during heating season (January 15th to 17th)

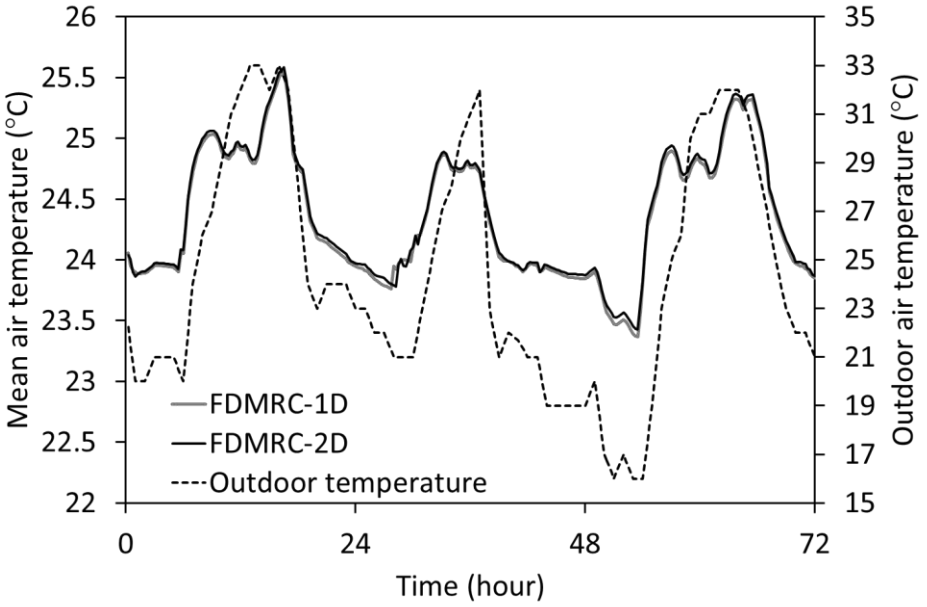

(a)

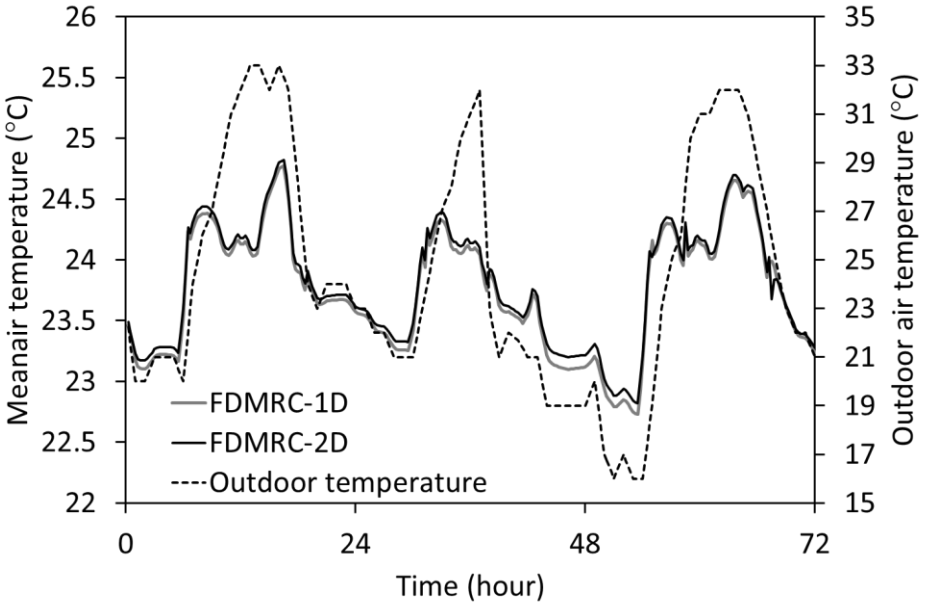

(b)

Figure 4.22: (a) Zone 1 mean air temperature and (b) Zone 2 mean air temperature obtained from FDMRC-1D and FDMRC-2D during cooling season (August 17th to 19th)

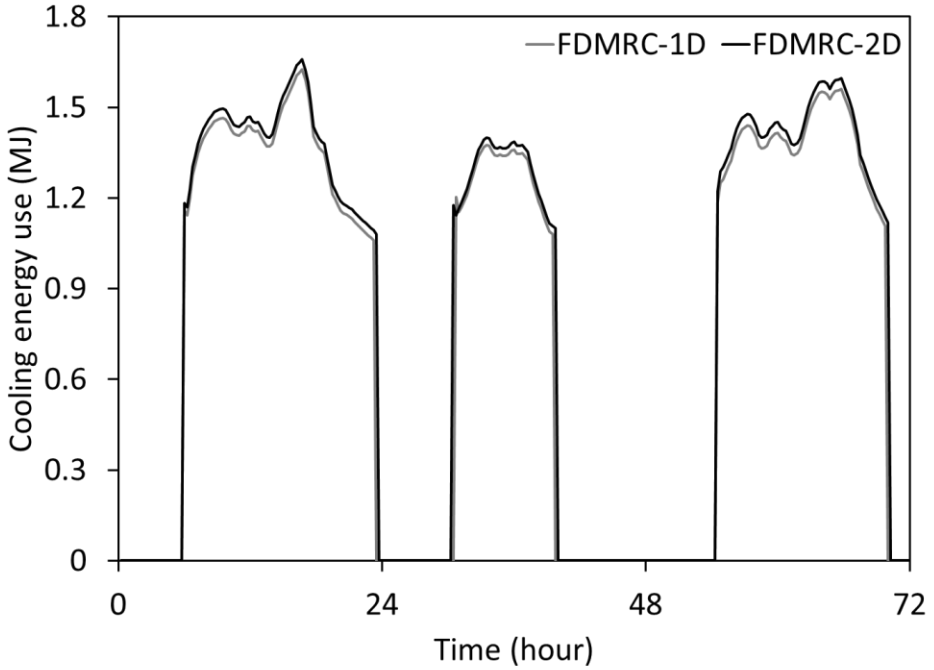

(a)

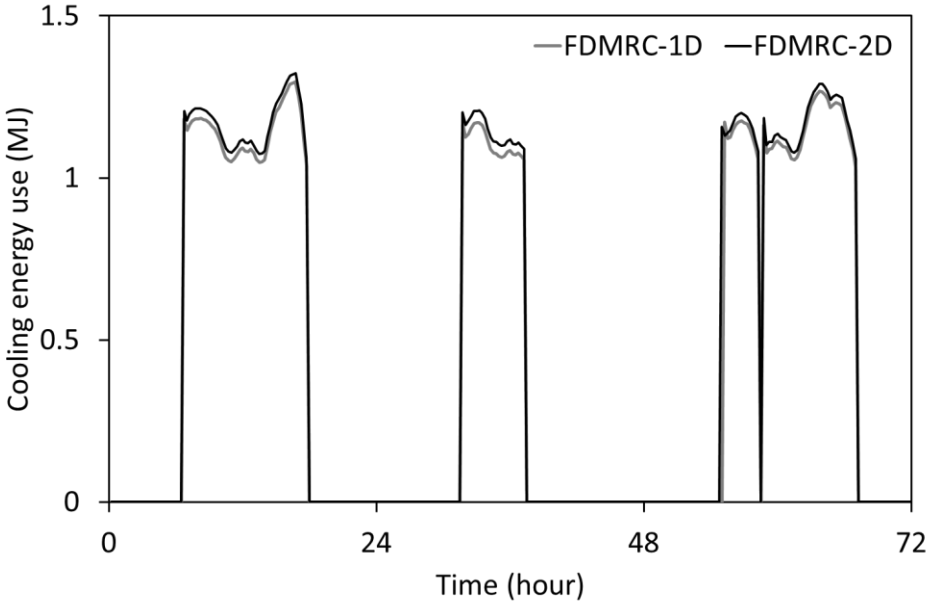

(b)

Figure 4.23: (a) Zone 1 cooling energy use and (b) Zone 2 cooling energy use obtained from FDMRC-1D and FDMRC-2D during cooling season (August 17th to 19th)

Table 4.6: Comparison of energy consumption by the ventilated slab system and estimation of thermal bridging effects during heating season (January 15th to January 17th) and cooling

season (August 18th to August 19th) for 8 meter wide slab in Golden, CO

	Heating energy use [MJ]			Cooling energy use [MJ]		
	Zone 1	Zone 2	Total	Zone 1	Zone 2	Total
FDMRC-1D	389	858	1247	599	278	877
FDMRC-2D	409	898	1307	616	291	907
Absolute Diff.	20	40	60	18	13	31
% Diff.	5%	5%	5%	3%	5%	4%

To assess the impact of thermal bridging effects on energy performance of the ventilated slab system, energy consumption obtained from the 2-dimensional solution (FDMRC-2D) with slab edge insulation placement with various R-values are compared to energy consumption of the radiant system predicted by the 1-dimensional numerical solution (FDMRC-1D) . Two types of insulation placement as depicted in Figure 4.15 are considered.

Figure 4.24 to Figure 4.27 illustrates the energy performance of the ventilated slab system as a function of R-value of insulation placed in two different locations of the walls during winter and summer seasons with various slab widths. Figure 4.24 and Figure 4.25 are the results with the insulation at the inner surface of the wall. As the R-value of the slab edge insulation increases, energy consumption obtained from FDMRC-2D becomes closer to that predicted by FDMRC-1D. Without any insulation, the FDMRC-2D model predicts that the ventilated slab system consumes up to 14% more heating energy and 10% more cooling energy than those predicted by the FDMRC-1D model for a 16-m wide slab due to thermal bridge effects. As the insulation is added, the thermal bridging effects are significantly reduced especially for smaller slabs. In particular, the energy impact associated with thermal bridging can be approximately halved during winter and summer

seasons with the addition of R-5 (hr-ft2-ºF/Btu) thermal insulation at the wall-slab joint. Furthermore, Figure 4.25 shows that the relative percentage of energy losses due to thermal bridges is greatly increased as the width of the slab is decreased.

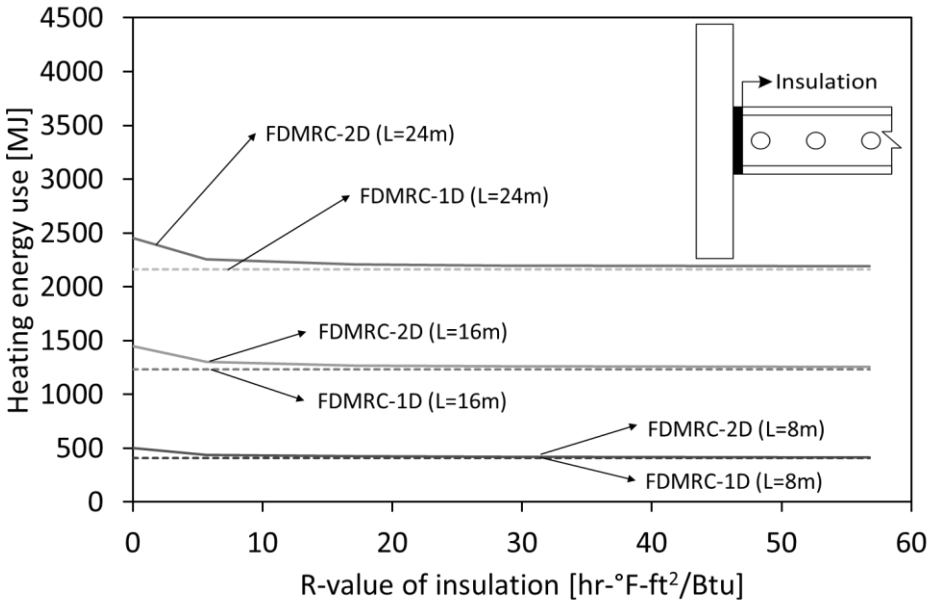

(a)

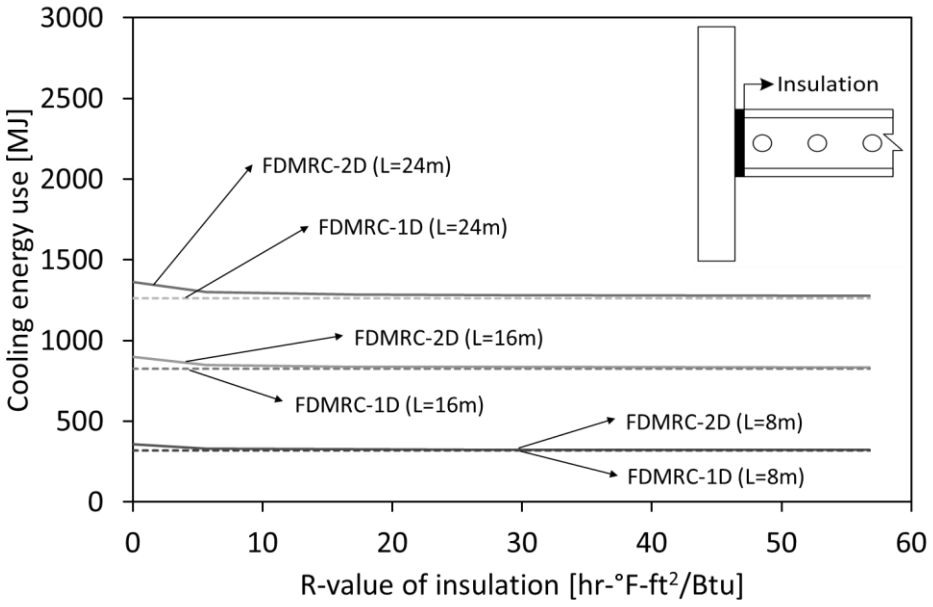

(b)

Figure 4.24: Impact of R-value of insulation at slab/wall joint on ventilated slab system energy consumption with various slab width in Golden, CO during (a) Heating and (b) Cooling season

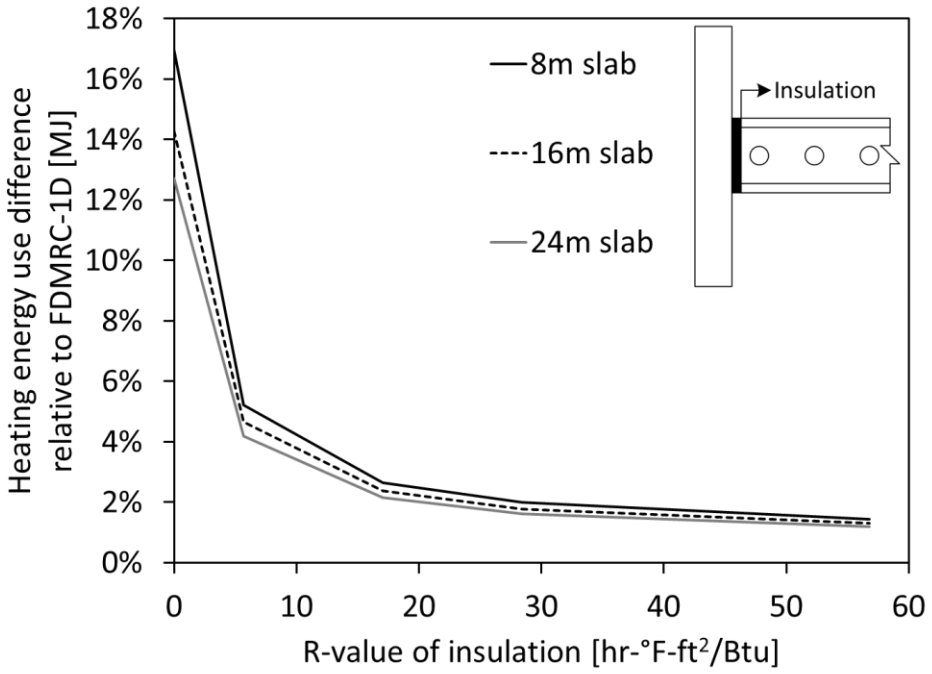

(a)

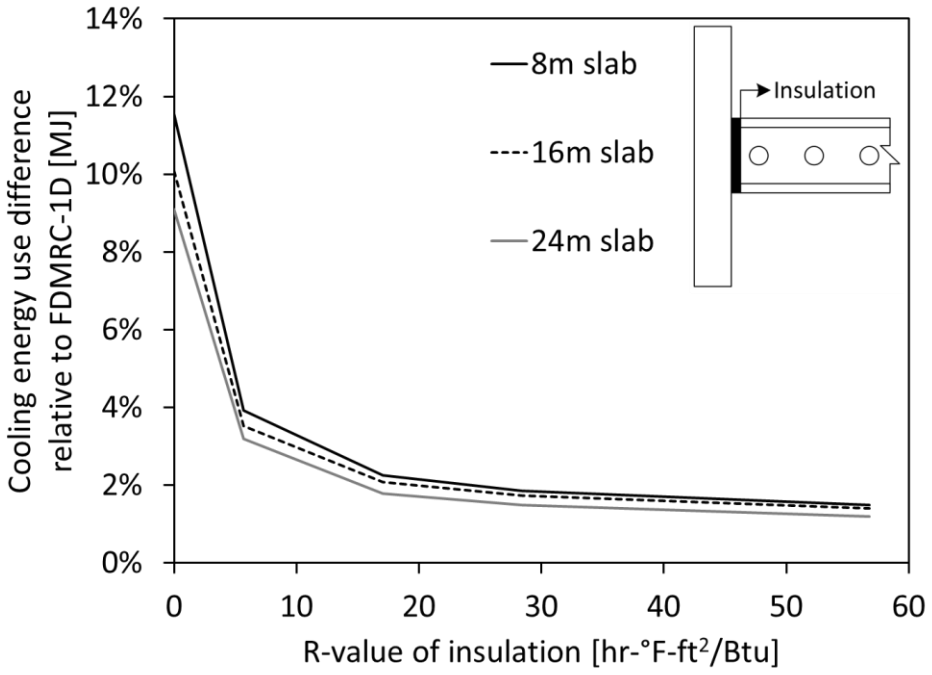

(b)

Figure 4.25: Impact of R-value of insulation at slab/wall joint on ventilated slab system energy consumption with various slab width in Golden, CO during (a) Heating and (b) Cooling season

Figure 4.26 and Figure 4.27 show the results with the insulation placed in the center plane of the wall. Similar to previous analysis, without any insulation, the FDMRC-2D model predicts that the ventilated slab system consumes up to 10% more heating energy and 8% more cooling energy than those predicted by the FDMRC-1D model for an 8-m wide slab due to thermal bridge effects. As the R-value of insulation in the center plane of the wall increases, energy consumption obtained from FDMRC-2D becomes closer to that predicted by FDMRC-1D. However, the energy use obtained from FDMRC-2D converges to those of FDMRC-1D very slower compared to the insulation placed at inner surface of the wall case because the heat losses still exist at the slab-wall joint.

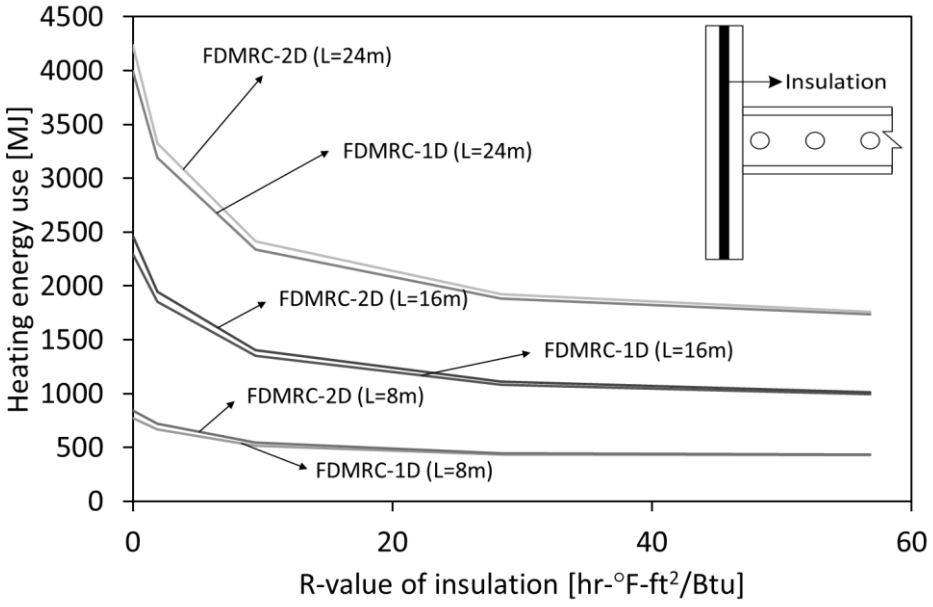

(a)

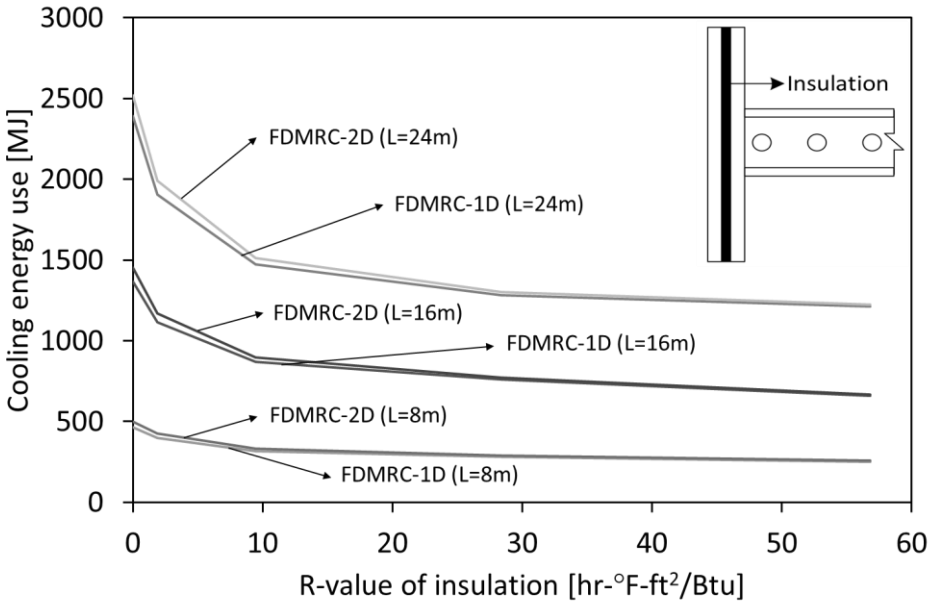

(b)

Figure 4.26: Impact of R-value of insulation inside exterior wall on ventilated slab system energy consumption with various slab width in Golden, CO during (a) Heating and (b) Cooling season

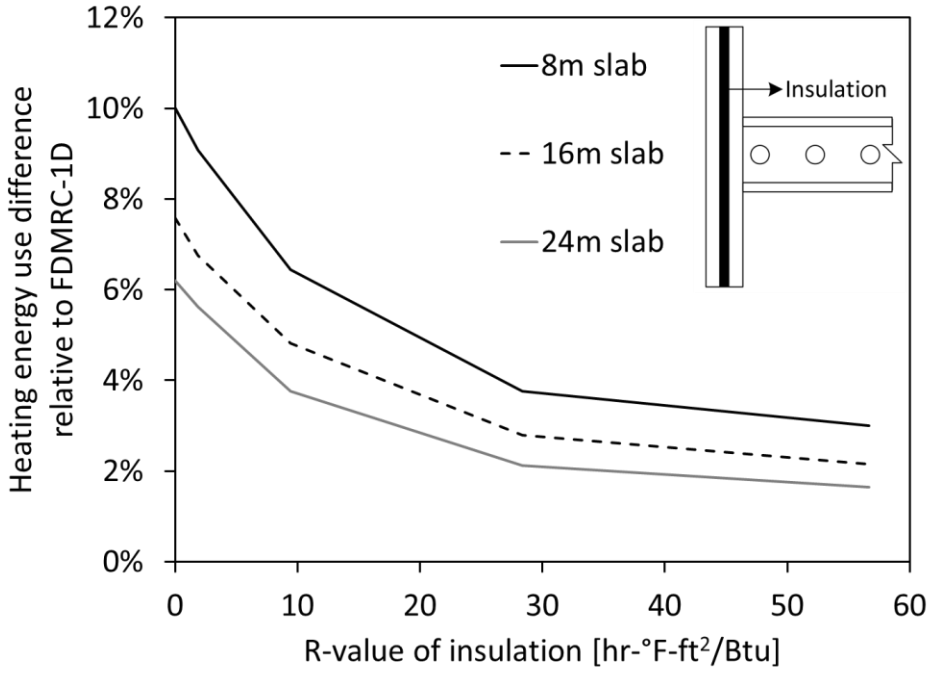

(a)

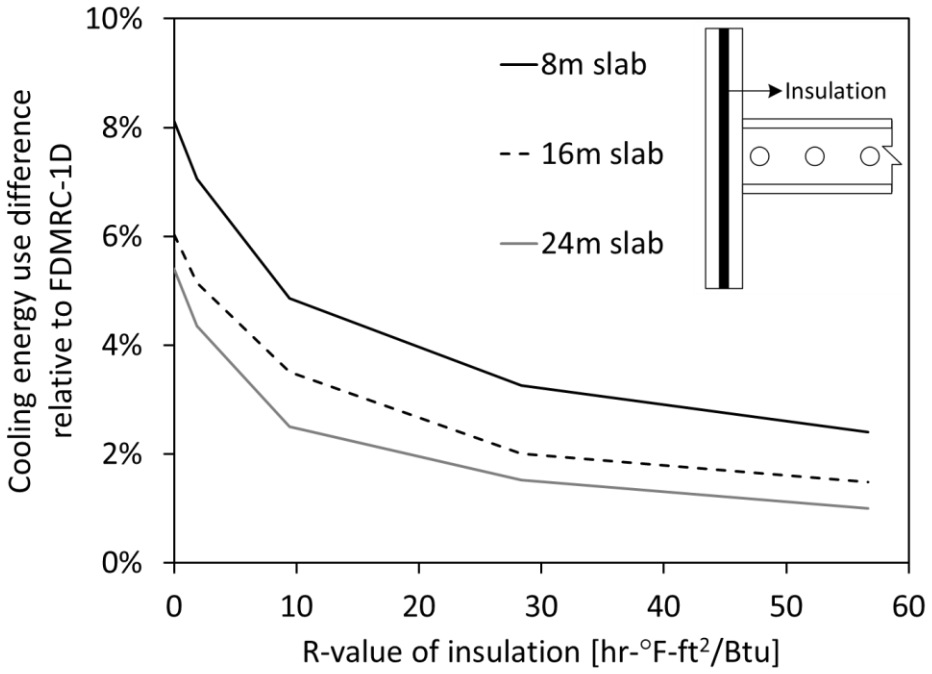

(b)

Figure 4.27: Impact of R-value of insulation inside exterior wall on ventilated slab system energy consumption with various slab width in Golden, CO during (a) Heating and (b) Cooling season

4.13 Summary and conclusions

In this chapter, a simulation environment that combines a two-dimensional numerical solution for slab and roof with an RC network model for the exterior walls is developed for the ventilated slab systems in 2-story buildings. The predictions from the simulation environment are verified against results obtained from EnergyPlus simulation for two-zone building located in Golden, CO and air-conditioned with a ventilated slab system. Then, the impact of thermal bridging effects on energy performance of a ventilated slab system is explored using the developed simulation environment tool. The impact of thermal bridge effects on the performance of ventilated slab system is explored by comparing the thermal and energy performance of ventilated slab systems obtained from FDMRC-1D to FDMRC-2D. Two insulation placements are considered to

evaluate the energy performance of a ventilated slab system: (a) insulation at inner surface and (b) insulation placed in the center of the wall.

It is found that 14% of heating energy consumption can be attributed to thermal bridging effects for the 16 meter wide uninsulated ventilated slabs in Golden, CO. Moreover, a ventilated slab system consumes 10% more cooling energy due to thermal bridging when no insulation is placed for the 16 meter wide slabs in Golden, CO. It is observed that the relative percentage of energy losses due to thermal bridges is significantly increases as the width of the slab is reduced. Based on the verification results, it is found that detailed whole-building simulation tools such as EnergyPlus ignore the impact of thermal bridges associated with slab-wall joints. In addition, it is found that the heat losses through slab-wall joints due to thermal bridge effect can be significantly reduced by adding insulation at the edges of the slab.

When the insulation is placed in the center plane of the exterior wall, thermal bridging effect increases heating and cooling energy consumption of a 16 meter ventilated slab system by 9% and 8%, respectively. The relative percentage of energy losses due to thermal bridges is greatly increases as the width of the slab is reduced. However, the magnitude of the energy loss is smaller in comparison with the insulation placed at inner surface of the wall case. Moreover, the energy use obtained from FDMRC-2D converges to energy use prediction of FDMRC-1D much slower compared to the insulation placed at inner surface of the wall case because the heat losses still exist at the slab-wall joint.

For a representative winter period (Jan 15th to Jan 18th) and summer season (Aug 17th to 20th), adding a slab edge insulation can significantly improve the energy efficiency of the ventilated slab system. Indeed, additional energy use caused by heat losses through wall-slab joint can be halved with R-5 vertical insulation relative to the case where the ventilated slab has no insulation. Based on the results of the simulation analysis, it found that thermal bridging effects on the

performance of the ventilated slab systems can be significant especially for small and un-insulated slabs, and should be considered in whole-building simulation analysis to assess the benefits of the ventilated systems compared to other more conventional air conditioning systems.

CHAPTER 5: DEVELOPMENT OF ENTHALPY HEAT EXCHANGER MODEL

5.1 Introduction

Water condensation can occur when utilizing passive cooling systems coupled with building thermal storage such as radiant slabs and ventilated slabs in specific operating conditions. Indeed and because these passive thermal storage systems may have to be operated at low temperatures to control during cooling mode, slab surface temperatures can cool down below the dew-point temperature of indoor air resulting in water condensation to occur. Depending on the degree of water condensation, it may cause mold problems along surfaces, inside cavities and hollow cores, and eventually may influence indoor air quality. Therefore, water condensation needs to be monitored and controlled when passive cooling systems are considered. In particular, it is important to detect the potential risk and duration of water condensation when operating ventilated slab systems. The water condensation can be predicted by employing enthalpy heat exchanger model. This chapter describes the development of the heat and mass zone balance model as well as enthalpy heat exchanger model that account for both water condensation and evaporation suitable for the evaluation of the performance of ventilated slab systems.

5.2 Heat and mass balance model

In addition to zone air heat balance model, the transient mass balance model for the zone air is implemented in the FDMRC simulation environment so that water condensation can be predicted along the ceiling surface. Eq. (5.1) describes the transient air mass balance equation to estimate zone humidity ratio accounting for internal latent loads, mass transfers by convection at the zone surfaces, and latent loads associated with infiltration and HVAC system:

$$\rho_{\text{air}} V_z \frac{dW_z}{dt} = \sum kg_{mass,load} + \sum A_i h_{mi} \rho_{air} (W_{surf,i} - W_z) + \dot{m}_{inf}(W_\infty - W_z) + \dot{m}_{sys}(W_{sup} - W_z) \quad (5.1)$$

Note that since the mass transfer through the building envelope was neglected in the development of the FDMRC simulation environment, the latent loads associated with convection at the zone surfaces are neglected in Eq. (5.2). The mass transfer through the building envelope can be solved by Effective Moisture Penetration Depth (EMPD) or Combined Heat and Moisture Transfer (HAMT) algorithm.

$$\rho_{\text{air}} V_z \frac{dW_z}{dt} = \sum kg_{mass,load} + \dot{m}_{inf}(W_\infty - W_z) + \dot{m}_{sys}(W_{sup} - W_z) \quad (5.2)$$

5.3 Enthalpy heat exchanger model

To model the ventilated slab systems, it is assumed that the air inlet temperature and the mass flow rate are known. That is, air flow flowing through hollow cores of the ventilated slab system is defined based on thermal loads required to heat and cool the indoor space. A ventilated slab system can be thought of as a heat exchanger between air flowing through the hollow cores and the slab floor. Two approaches have been widely used to size, analyze, or design heat exchangers: Log mean temperature difference (LMTD) and the effectiveness-number of transfer unit (effectiveness-NTU) method. In several cases, air leaving temperatures from a heat exchanger (i.e. ventilated slab) are unknown. The effectiveness-NTU heat exchanger method has been shown to be convenient to utilize when air outlet temperature is not known (McQuiston, 1982; Kreith, 1997). In this Chapter, we apply the effectiveness-NTU method to develop the enthalpy heat exchanger model. Air flowing in the hollow cores is assumed to lose or gain moisture when it is heated or cooled. In addition, air humidity ratio changes due to water condensation or evaporation. Similar processes can occur when moist air flows through a heat exchanger. Combined heat and mass

released or absorbed from the air flowing in the hollow cores can be estimated using Eq. (5.3).

$$\mathrm{Q} = \dot{m}_a(i_{a,in} - i_{a,out}) \tag{5.3}$$

The enthalpy of the moist air per unit mass of dry air is given by:

$$i_a = i_{da} + i_v W \tag{5.4}$$

Each term in Eq. (5.3) has the units of energy per unit mass of dry air. With the assumption that air follows a perfect gas behavior, its enthalpy depends only on temperature. If 0°C is selected as the reference state where the enthalpy of dry air is 0, and if the specific heat coefficients c_{pa} and c_{pv} are assumed to be constant, the enthalpies for dry and moist air can be determined:

$$\begin{aligned} i_{da} &= c_{pa}T \\ i_v &= i_g + c_{pv}T \end{aligned} \tag{5.5}$$

Where, the enthalpy of saturated water vapor i_g at 0°C is 2501.3 kJ/kg.

Based on these expressions, Eq. (5.3) can be rearranged and written as

$$\mathrm{Q} = \dot{m}_a\left[(c_{pa}T_{a,in} + \left(i_g + c_{pv}T_{a,in}\right)W_{a,in}) - (c_{pa}T_{a,out} + \left(i_g + c_{pv}T_{a,out}\right)W_{a,out})\right] \tag{5.6}$$

The maximum heat transfer potential between the air and the slab is then estimated based on the heat source or sink temperature, T_{src}:

$$\mathrm{Q_{max}} = \dot{m}_a\left[(c_{pa}T_{a,in} + \left(i_g + c_{pv}T_{a,in}\right)W_{a,in}) - (c_{pa}T_{src} + \left(i_g + c_{pv}T_{src}\right)W_{a,src})\right] \tag{5.7}$$

The effectiveness of the heat exchanger, ε, is defined as the ratio of the actual energy transfer to the maximum amount of energy transfer.

An energy balance on fluid in a differential section of the heat exchanger can be expressed as:

$$\delta Q = -\dot{m}_a di_a \tag{5.8}$$

$$\delta Q = Q_{sen} + Q_{lat} = h_a dA_s(T_a - T_s) + h_m dA_s(W_a - W_s)i_g \tag{5.9}$$

Where,

$\dot{m}_a$ = mass flow rate of air [kg/s]

i_a = enthalpy of air [J/kg]

h_a = convective heat transfer coefficient of air [W/m^2-°C]

h_m = convective mass transfer coefficient of air [kg/m^2-sec]

A_s = surface area [m^2]

T_a = dry-bulb temperature of air [°C]

T_s = temperature of water/wetted surface [°C]

W_a = humidity ratio of air [kg/kg]

W_s = humidity ratio of saturated air at T_s [kg/kg]

i_g = latent heat of vaporization [J/kg]

Since the transport mechanism that controls the convective heat transfer between air and water also determines the moisture transfer between air and water, a relation between heat and mass transfer coefficients exits (Mansour et al., 2012; ASHRAE, 2013):

$$\mathrm{Nu} = \frac{\mathrm{h_a L}}{\mathrm{k}} = \mathrm{C Re^m Pr^n} \tag{5.10}$$

$$\mathrm{Sh} = \frac{\mathrm{h_m L}}{\rho \mathrm{D}} = \mathrm{C Re^m Sc^n} \tag{5.11}$$

Since the same conservation principle applies to both mass and heat, the constant C and the exponent m and n of the above relationships must be equal. Lewis number that represents the relative magnitude of heat and mass diffusion is defined as:

$$\mathrm{Le} = \frac{\mathrm{Sc}}{\mathrm{Pr}} = \frac{\alpha}{D} = \frac{Thermal\ diffusivity}{Mass\ diffusivity} \tag{5.12}$$

Comparing the correlation for the heat and mass transfer, we can find the ratio:

$$\frac{\mathrm{Sh}}{\mathrm{Nu}} = \left(\frac{\mathrm{Sc}}{\mathrm{Pr}}\right)^{\mathrm{n}} \tag{5.13}$$

By replacing Nu and Sh, we can obtain

$$\frac{\mathrm{h_m k}}{\mathrm{h_a} \rho \mathrm{D}} = \frac{h_m c_{pa}}{h_a} \frac{\alpha}{D} = \left(\frac{\mathrm{Sc}}{\mathrm{Pr}}\right)^{\mathrm{n}} \tag{5.14}$$

ASHRAE (2013) reports that heat and mass transfer coefficients are highly related at the same Reynolds number. At low diffusion rates, where the heat and mass transfer analogy is valid for air-water vapor mixtures:

$$\frac{h_m c_{pa}}{h_a} = \left(\frac{\mathrm{Sc}}{\mathrm{Pr}}\right)^{\mathrm{n}-1} \; and \; \frac{\mathrm{Sc}}{\mathrm{Pr}} = Le \approx 1.0 \tag{5.15}$$

and hence

$$h_m = \frac{h_a}{c_{pa}} \tag{5.16}$$

The value of unity for the Lewis relation is used extensively in the calculations for air-humidification and dehumidification equipment. It is also a good approximation for simultaneous heat and water vapor transfer in air (Simonson, 1998; Stoecker, 1968). Hence the total heat transfer can be expressed as:

$$\begin{aligned} \delta Q = Q_{sen} + Q_{lat} &= h_a dA_s (T_a - T_s) + h_m dA_s (W_a - W_s) i_g \\ &= \frac{h_a dA_s}{c_{pa}} [\mathrm{c_{pa}}(T_a - T_s) + (W_a - W_s) i_g] \end{aligned} \tag{5.17}$$

Note that the term $c_{pv} T_{src} W$ in the enthalpy calculation has a minimal impact of less than 3% on the total enthalpy value and thus can be neglected (Zhang, 2002). By manipulating the term in Eq. (5.17), we obtain:

$$\delta Q = Q_{sen} + Q_{lat} = \frac{h_a dA_s}{c_{pa}} (i_a - i_s) \tag{5.18}$$

The governing equations for energy conservation are thus Eq. (5.8) and (5.18). Solving the energy balance equations for di_a gives:

$$di_a = -\frac{\delta Q}{\dot{m}_a} \tag{5.19}$$

Substituting Eq. (5.18) into Eq. (5.19) and rearranging give:

$$di_a = -\frac{h_a dA_s}{\dot{m}_a c_{pa}} (i_a - i_s) \tag{5.20}$$

Transposition the term, $(\mathrm{i_a} - i_s)$, from the right-hand side to the left-hand side of Eq. (5.19). Then,

integrating from the inlet of the heat exchanger to its outlet, we obtain:

$$\ln\left(\frac{\mathrm{i_{a,o}} - i_s}{i_{a,i} - i_s}\right) = -\frac{h_a A_s}{\dot{m}_a c_{pa}} \tag{5.21}$$

Rewriting the logarithmic form of Eq. (5.21) into the exponential form, then adding and subtracting $i_{a,i}$ gives:

$$\frac{\mathrm{i_{a,o}} - i_s + i_{a,i} - i_{a,i}}{i_{a,i} - i_s} = e^{-\frac{h_a A_s}{\dot{m}_a c_{pa}}} \tag{5.22}$$

Rearranging Eq. (5.22) provides:

$$\frac{i_{a,i} - i_s - (i_{a,i} - \mathrm{i_{a,o}})}{i_{a,i} - i_s} = e^{-\frac{h_a A_s}{\dot{m}_a c_{pa}}} \tag{5.23}$$

Manipulating the definition of effectiveness leads to:

$$\varepsilon = \frac{\mathrm{Q}}{\mathrm{Q_{max}}} = \frac{\dot{m}(i_{a,i} - \mathrm{i_{a,o}})}{\dot{m}(i_{a,i} - i_s)} = \frac{i_{a,i} - \mathrm{i_{a,o}}}{i_{a,i} - i_s} \tag{5.24}$$

Substituting this definition into Eq. (5.23) and solving for ε gives the following expression for the effectiveness of all heat exchanger types:

$$\varepsilon = 1 - e^{-\frac{h_a A_s}{\dot{m}_a c_{pa}}} \tag{5.25}$$

It is expressed in terms of ε-NTU relationship with C=0. When one fluid is stationary for a heat exchanger, the effectiveness can be related to the number of transfer units (NTU) (Incropera, 2007):

$$\varepsilon \equiv \frac{\mathrm{Q}}{\mathrm{Q_{max}}} = 1 - e^{-NTU} \tag{5.26}$$

where NTU is defined by (Simonson,1998):

$$\mathrm{NTU} \equiv \frac{\mathrm{UA}}{\dot{m}_a c_{pa}} \tag{5.27}$$

The heat transfer coefficient, UA, can be estimated using the convection heat transfer along the contact surface area of the cores:

$$\mathrm{UA_s} = \mathrm{h_a A_s} = \mathrm{h_a}(\pi \mathrm{DL}) \tag{5.28}$$

The air convection heat transfer coefficient, h_a, can be determined using the Dittus-Boelter correlation:

$$Nu = \frac{h_a D}{k} = 0.023 Re^{0.8} Pr^n \tag{5.29}$$

The total heat transfer from the heat source/sink can then be defined as:

$$Q_{total} = \varepsilon \mathrm{Q}_{\max} \tag{5.30}$$

Using Eq. (5.26), the heat generation per volume of air flowing in the hollow cores can be expressed in W/m^3 as shown by Eq. (5.31):

$$\mathrm{Q}_{\mathrm{gen}} \equiv \frac{\varepsilon \mathrm{Q}_{\max}}{\frac{\pi D^2}{4} L} \tag{5.31}$$

Once $\mathrm{Q}_{\mathrm{total}}$ is found, air outlet temperature can be determined by Eq. (5.32):

$$\mathrm{i}_{a,out} = \mathrm{i}_{\mathrm{a,in}} - \frac{Q_{total}}{\dot{m}_a} \tag{5.32}$$

The outlet air temperature can be expressed by using Eq. (5.33):

$$\mathrm{T}_{a,out} = \frac{\mathrm{i}_{\mathrm{a,out}} - i_g W_{a,out}}{c_{pa} + c_{pv} W_{a,out}} \tag{5.33}$$

5.4 Condensate rate model

In the cooling mode, if part of the heat exchanger surface (i.e. core surface in the ventilated slab) or a ceiling surface in the room is below the dew point temperature of the air, water condensation occurs. Although water condensation occurs practically before it reaches the saturation line in psychrometric chart, we will assume that water condenses only when the air is cooled below its saturation level to simplify the calculations. To estimate the time duration of water condensation, it is assumed that the airflow in the ventilated slab system is not turn off even when a potential of water condensation is detected. Two condensate rate calculation methods are described in this

section: a simplified calculation method and a detailed calculation method.

5.4.1 Simplified calculation method

The process of water condensation is shown in Psychrometric chart as noted in Figure 5.1. The mixture is cooled until it reaches the saturation curve without any loss of water vapor (i.e., humidity ratio remains constant). As it is cooled further, it moves down the saturation curve to T_{surf} which has a lower dry bulb temperature and humidity ratio.

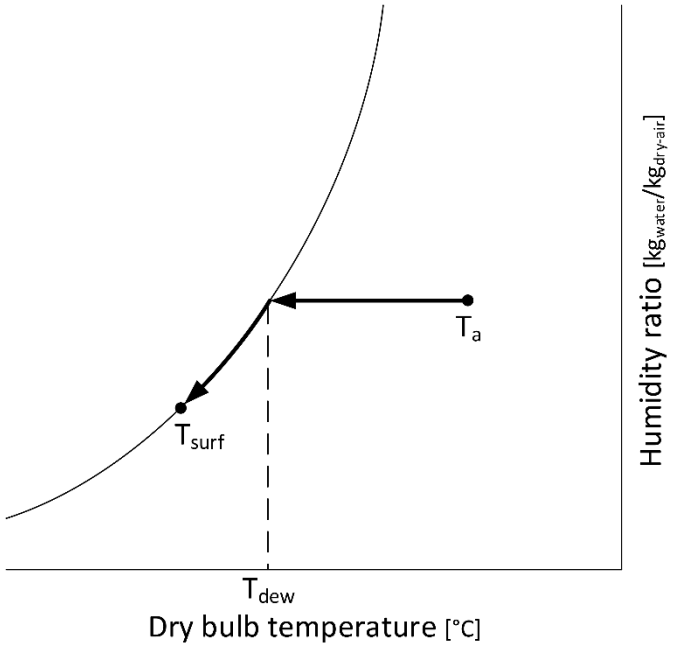

Figure 5.1: The process of water condensation (dehumidification) in the idealized case

Using a mass balance, the water condensation is proportional to the humidity ratio difference between the ambient air temperature and the saturated air at the surface temperature (i.e., the ceiling inner surface or the hollow core surface):

$$CR = \dot{m}_w = \dot{m}_a(W_a - W_{sat,surf}) \quad (5.34)$$

Where,

CR = water condensate rate [kg_{water}/s]

$\dot{m}_w$ = water mass flowrate [kg_{water}/s]

$\dot{m}_a$ = air mass flowrate [kg_{air}/s]

W_a = humidity ratio of air [$kg_{water}/kg_{dry\text{-}air}$]

$W_{sat,surf}$ = humidity ratio of saturated air at the surface temperature [$kg_{water}/kg_{dry\text{-}air}$]

5.4.2 Detailed calculation method

If moist air flows over a surface with a given water vapor density, transfer of water vapor by convection can occur. The convective mass transfer for the entire surface may be expressed as:

$$q_{cond} = \dot{m}_w i_g A = h_m \left(\rho_{v_{air}} - \rho_{v_{sat,surf}}\right) i_g A \tag{5.35}$$

where,

$\dot{m}_w$ = water mass flowrate [$kg_{water}/s\text{-}m^2$]

i_g = the enthalpy of vaporization [J/kg]

h_m = mass transfer coefficient [m/s]

ρ_v = water vapor density [kg_{water}/m^3]

A = area where condensation/evaporation occurs [m^2]

From Eq. (5.35), the water condensate rate can be determined as follows:

$$CR = \dot{m}_w A = h_m \left(\rho_{v_{air}} - \rho_{v_{sat,surf}}\right) A \tag{5.36}$$

where,

CR = water condensate rate [kg_{water}/s]

The convection heat transfer coefficient is normalized using the Nusselt and is expressed using the

Nusselt number as a function of the Reynolds and Prandtl number. Similarly, the mass transfer coefficient is normalized using the Sherwood number defined as a function of Reynolds and Schmidt numbers:

$$\begin{aligned} \mathrm{Nu} &= \mathrm{f}(\mathrm{Re}, \mathrm{Pr}) \\ \mathrm{Sh} &= \mathrm{f}(\mathrm{Re}, \mathrm{Sc}) \end{aligned} \tag{5.37}$$

The natural convection, the flow is driven by buoyancy as a result of density difference in the air volume. The dimensionless number characterizing the natural convection flow is the Grashof number given by:

$$\mathrm{Gr} \equiv \frac{g\beta(T_s - T_\infty)L_c^3}{v^2} \tag{5.38}$$

where,

g = gravity acceleration [m/s^2] ($g = 9.81$ m/s^2)

β = coefficient of volume expansion [1/K] ($\beta = \frac{1}{T_f} \equiv \frac{1}{\frac{T_s+T_\infty}{2}}$ for ideal gas)

L_c = characteristic length [m]

v = kinematic viscosity [m^2/s]

For natural convection, the Grashof number replaces the Reynolds number used in forced convection to determine the convection coefficients. The Rayleigh number is defined as simply the product of the Grashof and Prandtl numbers for heat transfer and the Grashof and Schmidt numbers for mass transfer:

$$\begin{aligned} \mathrm{Ra} &= \mathrm{f}(\mathrm{Gr}, \mathrm{Pr}) = \mathrm{Gr} \cdot \mathrm{Pr} \\ \mathrm{Ra} &= \mathrm{f}(\mathrm{Gr}, \mathrm{Sc}) = \mathrm{Gr} \cdot \mathrm{Sc} \end{aligned} \tag{5.39}$$

The Schmidt number can be calculated by:

$$\mathrm{Sc} = \frac{\mu}{\rho \mathrm{D_{AB}}} \tag{5.40}$$

where,

μ = dynamic viscosity of the fluid [kg/m-s]

ρ = density of the fluid [kg/m^3]

Mass diffusivity, D_{AB}, at certain Kelvin temperature, T, can be calculated by

$$D_{AB}(T) = D_{AB}(298\ K)\left(\frac{T}{298}\right)^{\frac{3}{2}} \tag{5.41}$$

where, $D_{AB}(298\ K) = 0.026 \times 10^4$ (Incropera, 2007).

For the hollow cores, the mass transfer coefficient, h_m, can be calculated using the Sherwood correlation:

$$\begin{aligned} Sh &= \frac{h_m D}{D_{AB}} = 0.023 Re^{0.8} Sc^{\frac{1}{3}};\ \text{forced convection when system is on.} \\ Sh &= \frac{h_m D}{D_{AB}} = 0.52 Ra^{\frac{1}{5}};\ \text{natural convection when system is off.} \end{aligned} \tag{5.42}$$

Where,

D = diameter of the hollow core [m]

D_{AB} = mass diffusivity [m^2/s]

Re = Reynolds number

Sc = Schmidt number

Ra = Rayleigh number

It should be noted that the Reynolds number is defined as:

$$Re = \frac{\rho V D_H}{\mu A} \tag{5.43}$$

ρ = density of the fluid [kg/m3]

V = volume flow rate [m3/s]

D_H = hydraulic diameter [m]

μ = dynamic viscosity of the fluid [kg/m-s]

For the ceiling surface, the mass transfer coefficient, h_m, can be calculated the appropriate Sherwood correlation:

$$\text{Sh} = \frac{h_m L_c}{D_{AB}} = 0.54 Ra^{\frac{1}{4}}; 10^4 \leq Ra \leq 10^7$$
$$\text{Sh} = \frac{h_m L_c}{D_{AB}} = 0.15 Ra^{\frac{1}{3}}; 10^7 \leq Ra \leq 10^{11} \quad (5.44)$$

Where,

L_c = characteristic length of the ceiling surface [m]

D_{AB} = mass diffusivity [m^2/s]

Ra = Rayleigh number

5.5 Evaporate rate model

The calculation of water evaporation is essential to accurately assess the existence of condensate water inside a hollow core or on slab ceiling surfaces. Several researchers reported methods and expressions for the calculation of water evaporation from indoor swimming pools, vessels/tanks with low water levels, and water spills. Some of the calculation methods were validated with measured data (Shah, 1992; Shah, 2008; Shah, 2012a; Shah, 2013). In this research, the water condensate is assumed to be of the water spills type because no large amounts of condensation are expected due to the boundary conditions.

The temperature of spilled water on the surface will be cooled down quickly, approaching the wet-bulb temperature of air. If the web bulb temperature becomes the same, density of room air and air at water surface will be the same. Therefore, there will be no natural convection, and evaporation

will occur by forced convection.

Shah (2014) suggests to use Eq. (5.45) to calculate water evaporation for spills inside buildings. It was derived using the analogy between heat and mass transfer (Shah, 2014).

$$\mathrm{ER} = \mathrm{b}(\mathrm{p_w} - \mathrm{p_r})/3600 \tag{5.45}$$

Where,

ER = Evaporation rate [$kg_{water}/m^2/s$]

b = 0.00005

p_w = water-vapor pressure in air, air saturated at water temperature [Pa]

p_r = water-vapor pressure in air, air at room/core condition [Pa]

5.6 Update humidity ratio of air

The water condensate and evaporate rate can change the humidity ratio of air which is in contact with the surface. The major assumption used in this analysis is that water condensation and evaporation would not happen at the same time. Because when condensation occurs, the relative humidity ratio of the air layer would be very close to 100%. It would be difficult to observe evaporation of condensate water while condensation is in effect. Thus, the humidity ratio of the air in contact with the ceiling or core surface will be updated based on the condensate rate and evaporate rate as:

If condensation is observed:

$$\begin{aligned} \frac{\rho_a V_{zone}}{\Delta t_{cond}} \left({W_{zone}}^{n+1} - {W_{zone}}^{n} \right) &= -CR_{\mathrm{zone}} \\ \frac{\rho_a V_{core}}{\Delta t_{cond}} \left({W_{core}}^{n+1} - {W_{core}}^{n} \right) &= -CR_{core} \end{aligned} \tag{5.46}$$

If evaporation is observed and condensate water exists:

$$\frac{\rho_a V_{zone}}{\Delta t_{evap}}\left({W_{zone}}^{n+1} - {W_{zone}}^{n}\right) = +ER_{zone}$$

$$\frac{\rho_a V_{core}}{\Delta t_{evap}}\left({W_{core}}^{n+1} - {W_{core}}^{n}\right) = +ER_{core}$$

Where,

W_{zone} = humidity ratio of zone air [$kg_{water}/kg_{dry\text{-}air}$]

W_{core} = humidity ratio of air in hollow cores [$kg_{water}/kg_{dry\text{-}air}$]

ρ_a = density of air [$kg_{dry\text{-}air}/m^3$]

V_{zone} = volume of air in zone [m^3]

V_{core} = volume of air in hollow cores [m^3]

Δt_{cond} = condensation duration time [sec]

Δt_{evap} = evaporation duration time [sec]

CR = condensate rate [kg_{water}/s]

ER = evaporate rate [kg_{water}/s]

It should be noted that water condensation and evaporation will not take place during the entire zone timestep (15 minutes of timestep is considered in the simulation environment). The duration time of the water condensation and evaporation is calculated by an iterative approach until the vapor density of air reaches its limit. For example, the minimum humidity ratio of air that can be lowered by condensation is the humidity ratio of saturated air at surface temperature. If the air vapor density reaches the vapor density of saturated air at surface temperature, $\rho_{v_{sat,surf}}$, water condensation will stop occurring. Similarly, evaporation will take place until the humidity ratio of the air reaches its saturation level. Then, the accumulation of condensation water can be calculated by:

$$\text{CondenseWater} = \text{CR}\Delta t_{cond} - \text{ER}\Delta t_{evap} \qquad (5.47)$$

5.7 Description of the simulation environment

Refer to Chapter 4 for a detailed description of the simulation environment. It should be noted that air heat balance model is replaced by the air heat and mass balance model as outlined in this Chapter. Specifically, the water condensate/evaporate calculation algorithms with the enthalpy heat exchanger model are included in the air heat and mass balance model. The flow chart of the new integrated simulation environment is shown in Figure 5.2.

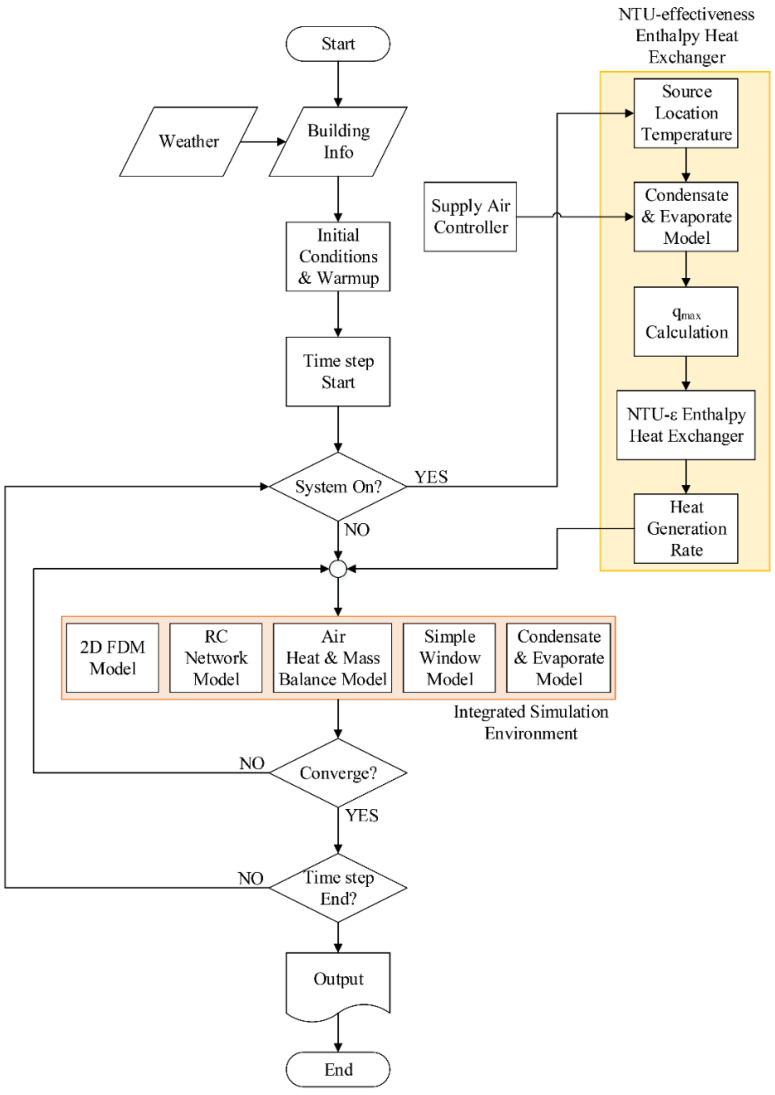

Figure 5.2: Flow chart of the integrated simulation environment including heat and mass air heat balance model and water condensate/evaporate models

5.8 Model verification

The predictions obtained from the implemented heat and mass balance model as well as the enthalpy heat exchanger model are verified using the calculations of zone air temperatures and energy end-uses obtained from the EnergyPlus for a 2-story office building model. Specifically, the office building model consists of two 8 by 8 m floors with each floor having 3 m height exterior walls. A 15% window-to-wall ratio is considered for all orientations. The ground floor is in contact with the ground that remains at a constant temperature, and it has an R-value of 4.56 K-m^2/W. The exterior walls and roof are exposed to the outdoor ambient air and have R-values of 2.50 and 4.56 K-m^2/W, respectively. The building occupancy density is set to be 6.4 m^2/person. Each occupant contributes 120 W in total internal heat gains with 70% are assumed to be sensible and 30% are latent. Peak lighting power density is set to be 10.38 W/m^2.

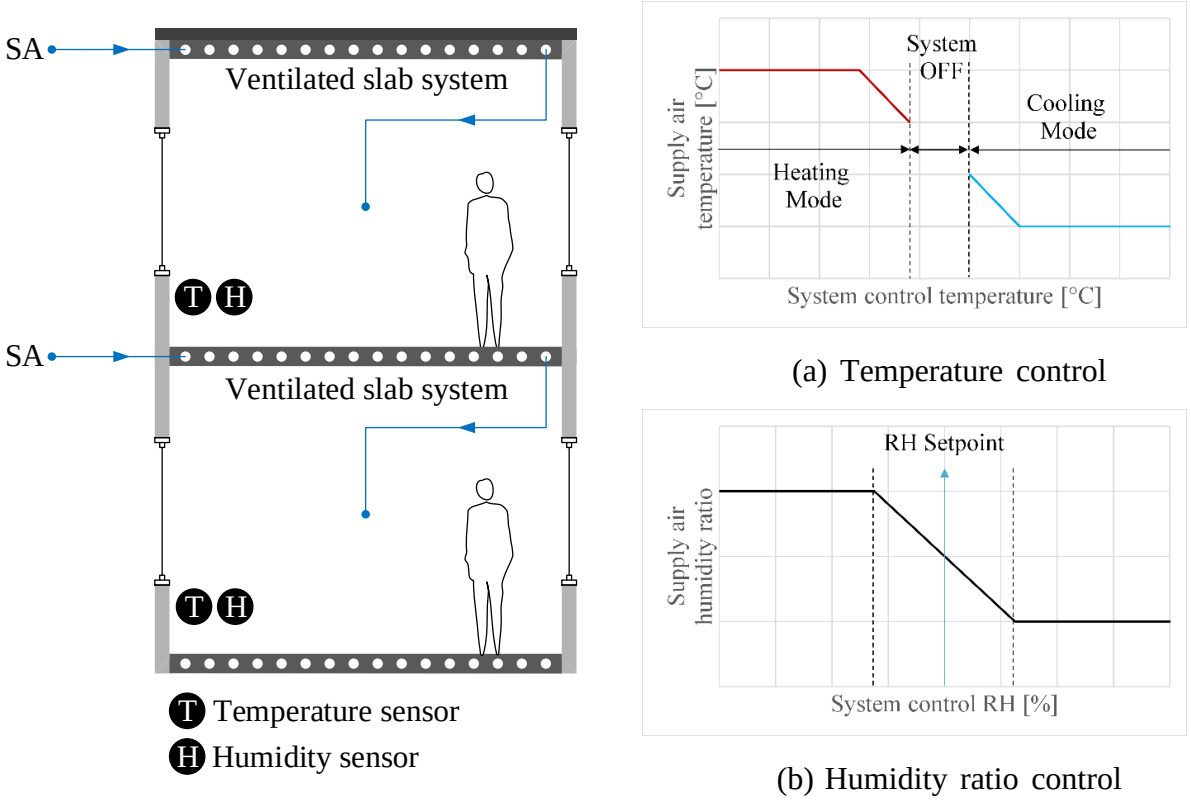

Figure 5.3: Description of room model and temperature and humidity ratio control scheme

The performance of two control strategies is examined in this section: 25°C for 24 hours and a nighttime precooling strategy. Figure 5.4 shows the two control strategies considered in the analysis presented in this section. For precooling strategy, the building is operated at a constant set-point of 25°C with throttling range of 1°C from 7 a.m. to 8 p.m. The set-point temperature is lowered to 18°C during the unoccupied period.

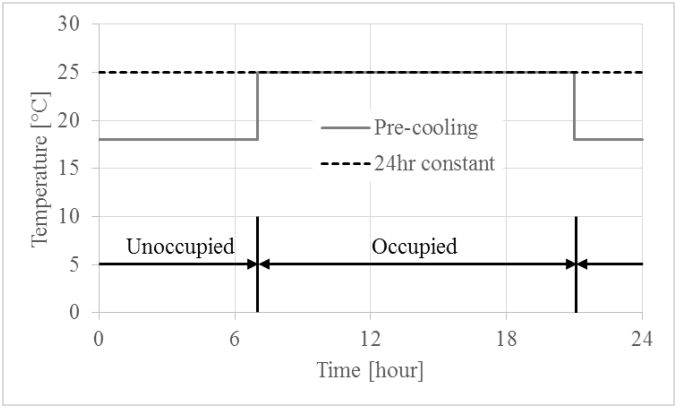

Figure 5.4: Zone air set-point temperature control strategy

Predictions of mean air temperature, humidity ratio, and relative humidity obtained from the FDMRC simulation environment are compared with results obtained from EnergyPlus as outlined in Figure 5.5. For all the parameters, the predictions from the FDMRC model and EnergyPlus agree generally well with small normalized root mean square error (NRMSE) values.

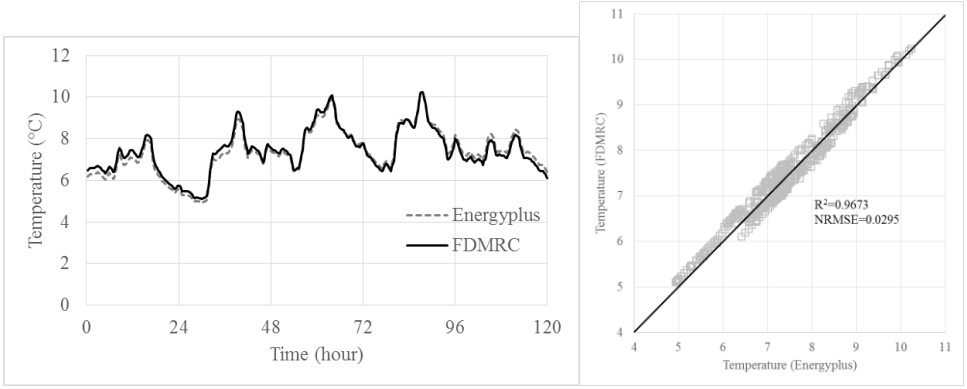

(a) Mean air temperature

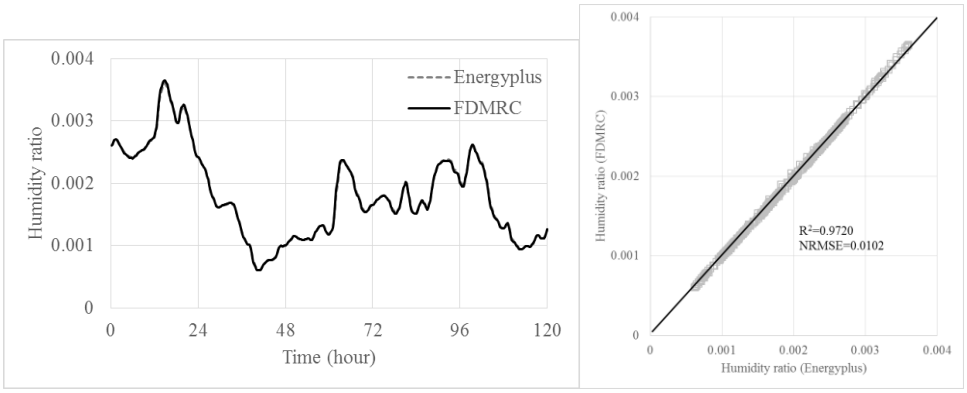

(b) Humidity ratio

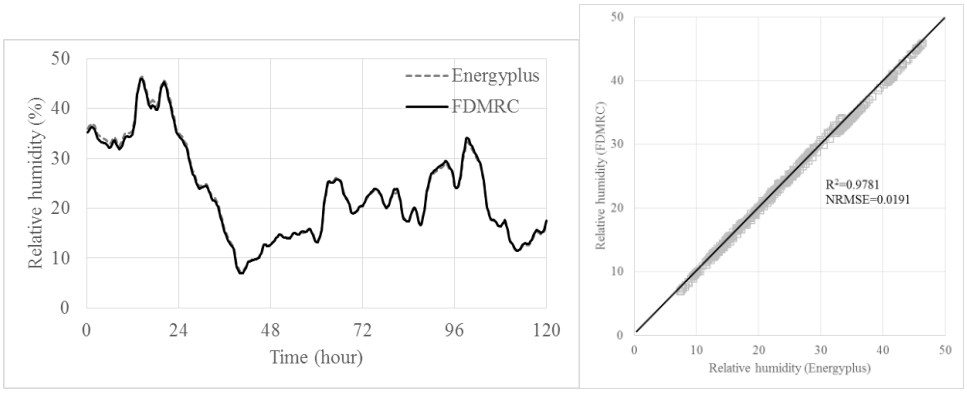

(c) Relative humidity

Figure 5.5: Comparison of results from FDMRC and EnergyPlus for (a) mean air temperature, (b) humidity ratio, and (c) relative humidity ratio obtained during representative days for the cooling season (Aug 16th to 20th) in Golden, CO

Comparisons of results for mean air temperature and energy consumption obtained from three simulation environments (i.e. EnergyPlus, FDMRC with sensible heat exchanger, and FDMRC with enthalpy heat exchanger) during both representative days of heating and cooling seasons are shown in Figure 5.6 and Figure 5.7, respectively. Humidity ratio of supply air is assumed to be 0.010 for the FDMRC model with enthalpy heat exchanger. The results obtained from EnergyPlus are considered as references, to assess predictions for the temperatures and energy uses obtained from FDMRC models. For zone mean air temperatures, the NRMSE values are lower than 0.04

indicating acceptable prediction accuracy. For energy uses, the NRMSE values are slightly higher but not exceeding 0.066 which still shows an acceptable accuracy level. The energy use difference obtained between sensible heat exchanger and enthalpy exchanger models is rather small with a NRMSE value of less than 0.01.

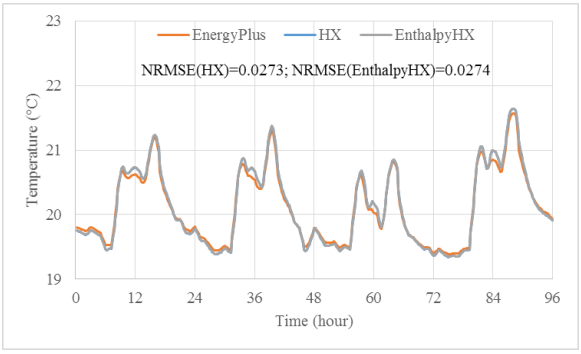

(a) Zone 1 mean air temperature

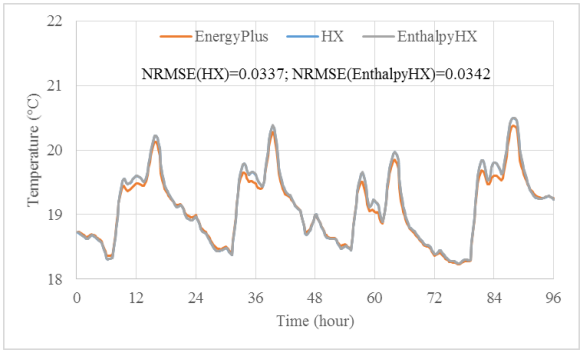

(b) Zone 2 mean air temperature

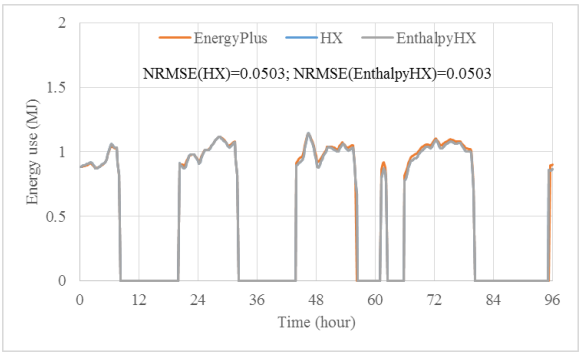

(c) Zone 1 heating energy use

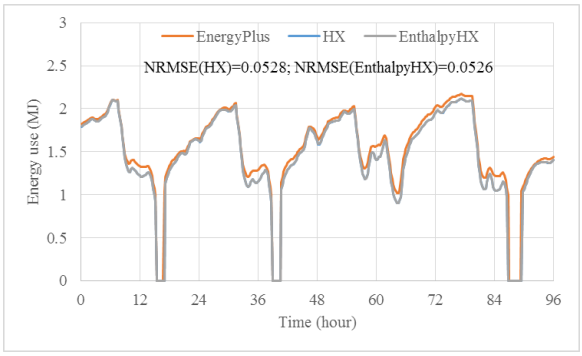

(d) Zone 2 heating energy use

Figure 5.6: Comparison of results from EnergyPlus, FDMRC with sensible heat exchanger model, and FDMRC with enthalpy heat exchanger model obtained during representative days of the heating season

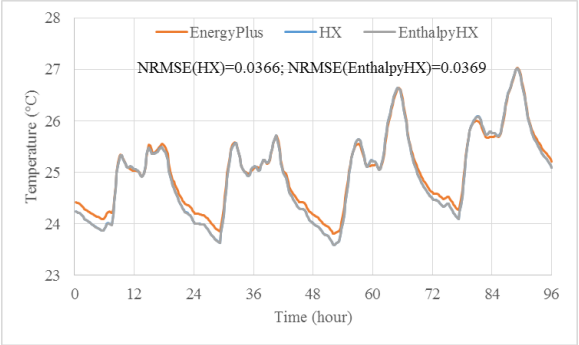

(a) Zone 1 mean air temperature

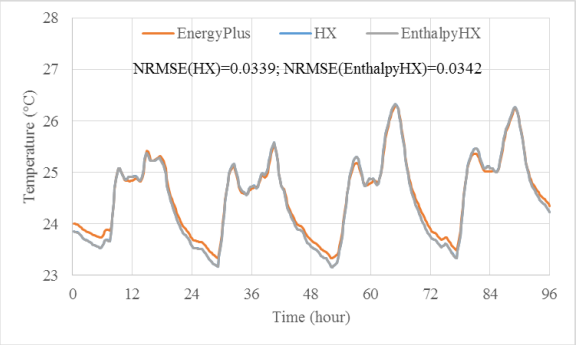

(b) Zone 2 mean air temperature

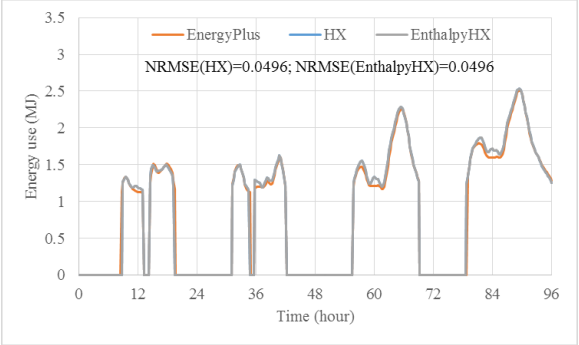

(c) Zone 1 cooling energy use

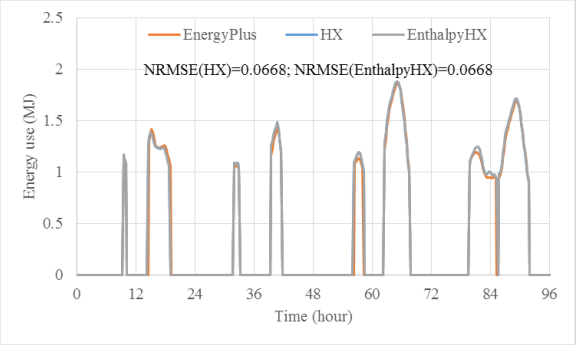

(d) Zone 2 cooling energy use

Figure 5.7: Comparison of results from EnergyPlus, FDMRC with sensible heat exchanger model, and FDMRC with enthalpy heat exchanger model obtained during representative days of the cooling season

5.9 Simulation results

The selective results obtained from the water condensate/evaporate rate models are described in this section. The simulation analysis sets are divided into two main categories based on the control strategy: 25°C for 24 hours and 25°C during occupied period with a precooling strategy. The set-point temperature for precooling is set to 18°C. The supply air temperature is assumed to be fixed at 18°C during occupied period. For nighttime precooling, the supply air temperature is varied

from 12 to 15°C. The relative humidity of the supply air is varied from 80 to 95%. Two slab materials are considered for the analysis: lightweight concrete and heavyweight concrete. Material properties for the slab are summarized in Table 5.1.

Table 5.1: Material properties for a hollow core slab: Lightweight concrete and heavyweight concrete

Material	Conductivity [W/m-K]	Density [kg/m^3]	Specific heat [J/kg-K]
LW concrete	0.49	512	880
HW concrete	1.73	2300	653

Table 5.2 outlines the values of the supply air temperature, relative humidity and hollow core slab construction considered for various cases in the simulation analysis. Figure 5.8 depicts the conditions associated with the supply air on the psychrometric chart. It should be noted that supply air with high relative humidity values is chosen mainly to investigate the potential condensation risk inside the hollow cores.

Table 5.2: Description of simulation cases

Case	SA Temp. [°C] (Occupied)	SA Temp. [°C] (Unoccupied)	SA RH [%]	Hollow core slab construction
1	18	18	80, 90, 95	HW conc.
2	18	12	80, 90, 95	HW conc.
3	18	15	80, 90, 95	HW conc.
4	18	12	80, 90, 95	LW conc.
5	18	15	80, 90, 95	LW conc.

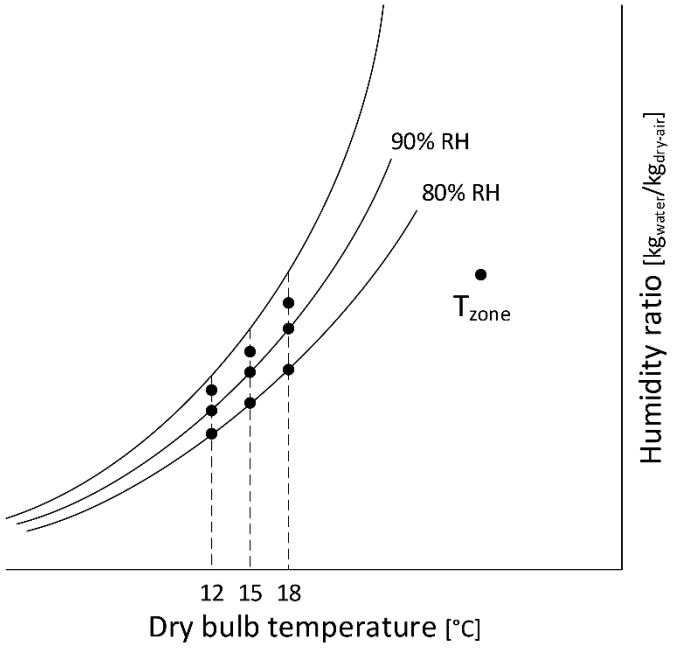

Figure 5.8: Supply air conditions for various analysis cases

Figure 5.9 illustrates the time variations of the ceiling surface temperature, the inside core surface temperature, the dew-point temperature at ceiling surface, and the dew-point temperature inside core surface for two supply air conditions during one day. The supply air temperature is assumed to be either (a) 18°C with 80% RH or (b) 18°C with 95% RH while the room air temperature is maintained at 25°C for 24 hours. As shown in Figure 5.9, both surface temperatures (i.e. ceiling surface and core surface temperature) are higher than the air dew-point temperature even with 95% RH supply air. During cooling operation, the ventilated slab system perform as a heat sink since cold air flows through the cores. The ventilated slab is exposed to relatively hot indoor environment. The core surface temperature is between the hollow cores and zone air temperature. Thus, the core surface temperature is inevitably greater than the supply air that flows through the cores. It is difficult to have water condensation along the core surfaces when the system operates for 24 hours.

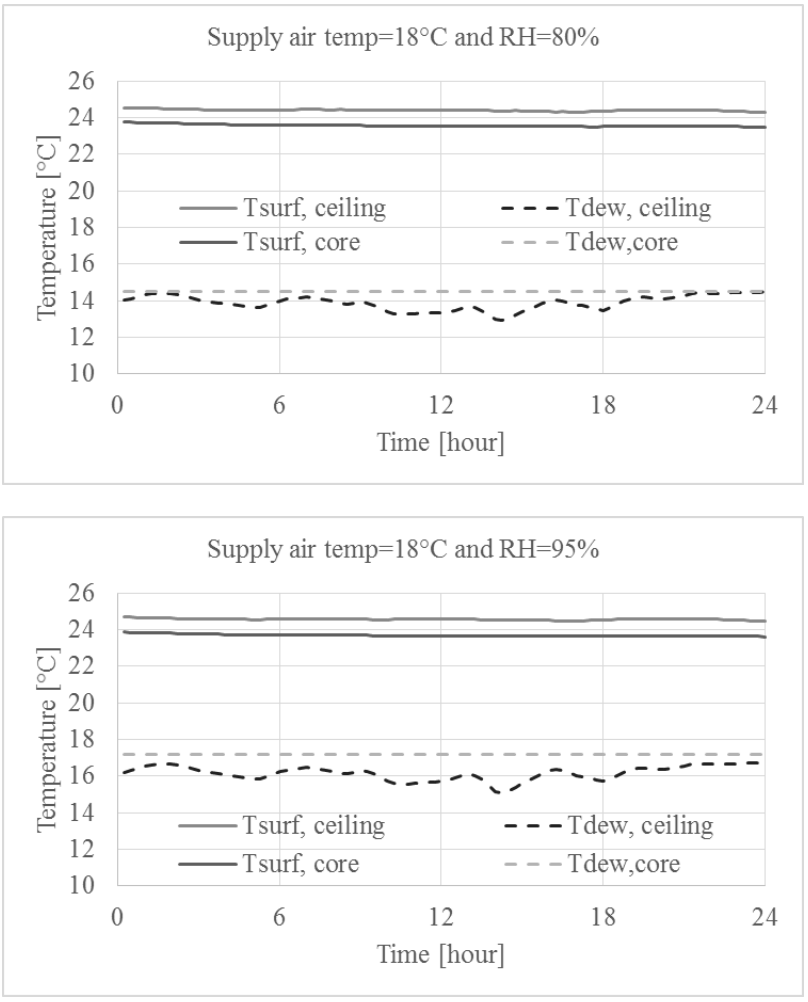

Figure 5.9: Time variations of ceiling and core surfaces and dew-point temperatures when the room air temperature is maintained at 25°C for 24 hours with: (a) supply air temperature=18°C and RH = 80% and (b) supply air temperature=18°C and RH=95%

When slab mass is dramatically cooled down using pre-cooling strategy and relatively air high temperature is introduced to the hollow cores, water condensation can occur inside the hollow cores. Figure 5.10 and Figure 5.11 show time variations of the ceiling surface temperature, the inside core surface temperature, dew-point temperature at the ceiling surface, and the dew-point temperature at the inside core surface for two supply air conditions using detailed and simple

methods, respectively. The slab mass is precooled by supplying 15°C of air before the building is occupied. When the building is occupied, the temperature of supply air is increased to 18°C. No water condensation is observed along the surfaces when RH of the supply air is 80%. When 95% RH air is supplied to the ventilated slab system, the risk of condensation on each surface (i.e. ceiling surface and core surface) increases as the dew-point temperature increases. Again, no water condensation has observed even when the building is precooled with 15°C supply air.

(a)

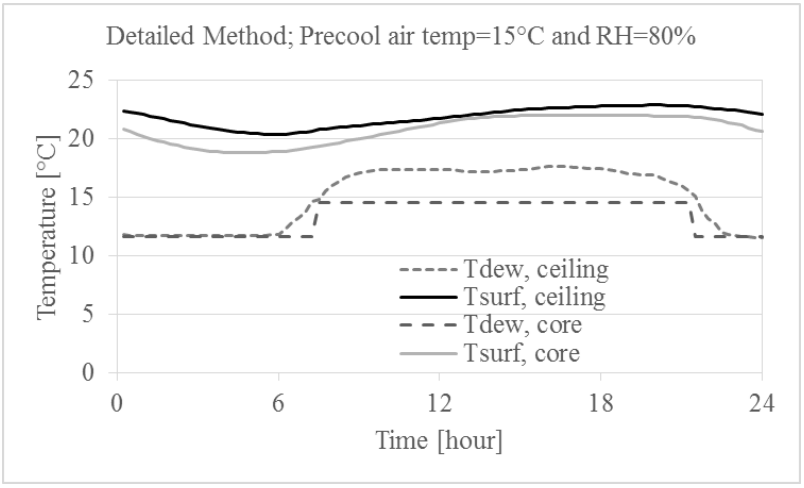

(b)

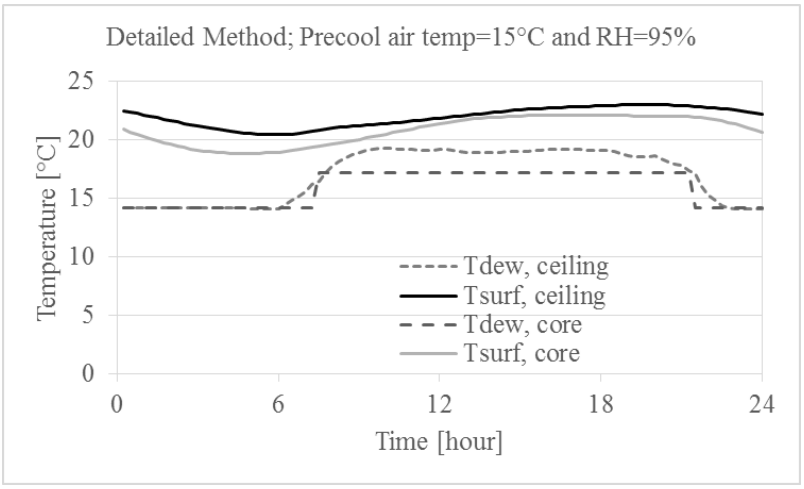

Figure 5.10: Time variations of the ceiling and core surfaces and dew-point temperatures when the heavyweight slab is precooled during unoccupied period with: (a) supply air temperature=15°C and RH = 80% and (b) supply air temperature=15°C and RH=95%

(a)

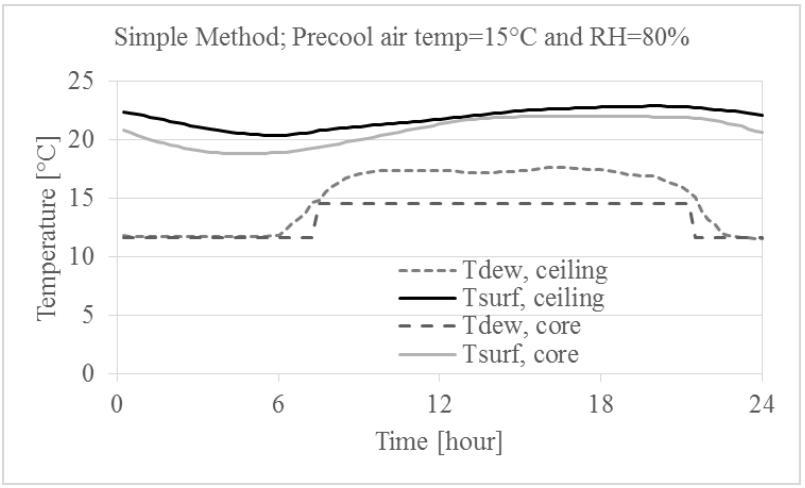

(b)

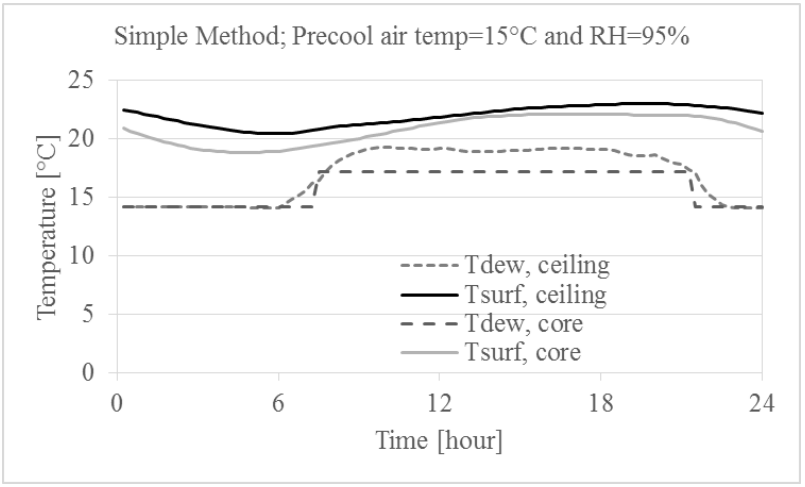

Figure 5.11: Time variations of the ceiling and core surfaces and dew-point temperature when the heavyweight slab is precooled during unoccupied period: (a) supply air temperature=15°C and RH = 80% and (b) supply air temperature=15°C and RH=95%

Figure 5.12 and Figure 5.13 illustrate the time variations of the ceiling surface temperature, the inside core surface temperature, the dew-point temperature at ceiling surface, the dew-point temperature at the inside core surface for two supply air conditions using detailed and simple methods, respectively. The slab mass is precooled by supplying 12°C of air before the building is occupied. As the building is occupied, the temperature of supply air is increased to 18°C. No condensation issues have been noted during the occupied period. Especially when 95% of RH air is supplied through the hollow cores, the temperature difference between slab mass temperature and the dew-point temperature becomes smaller as shown in Figure 5.12 and Figure 5.13. In other words, the risk of condensation significantly increases as the temperature of the air used for precooling decreases and RH of supply air increases. However, ceiling surface temperature and core surface temperatures are still higher than the dew-point temperatures so no condensation has observed.

(a)

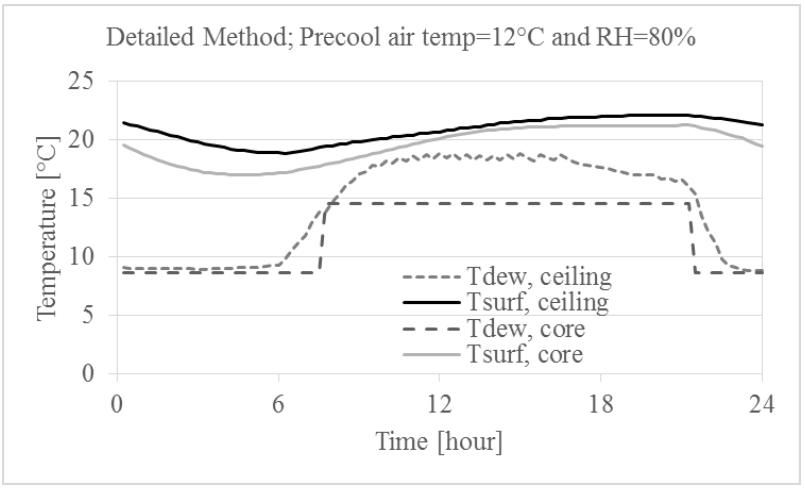

(b)

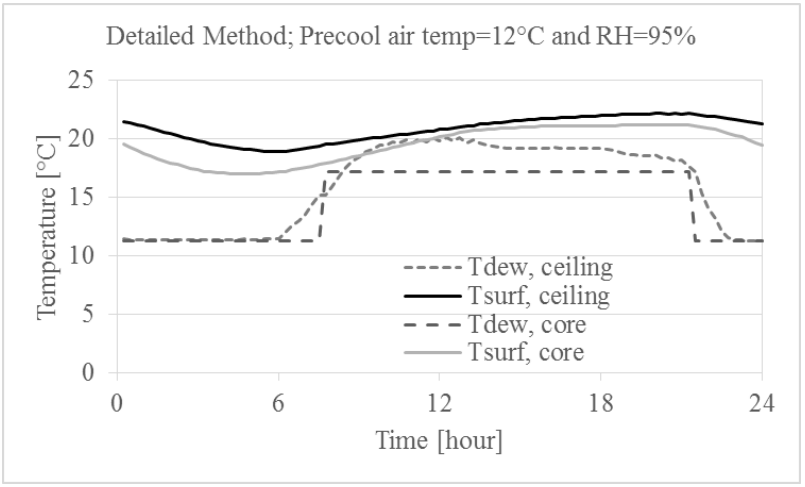

Figure 5.12: Time variations of the ceiling and core surfaces and dew-point temperature when the heavyweight slab is precooled during unoccupied period with: (a) supply air temperature=12°C and RH = 80% and (b) supply air temperature=12°C and RH=95%

(a)

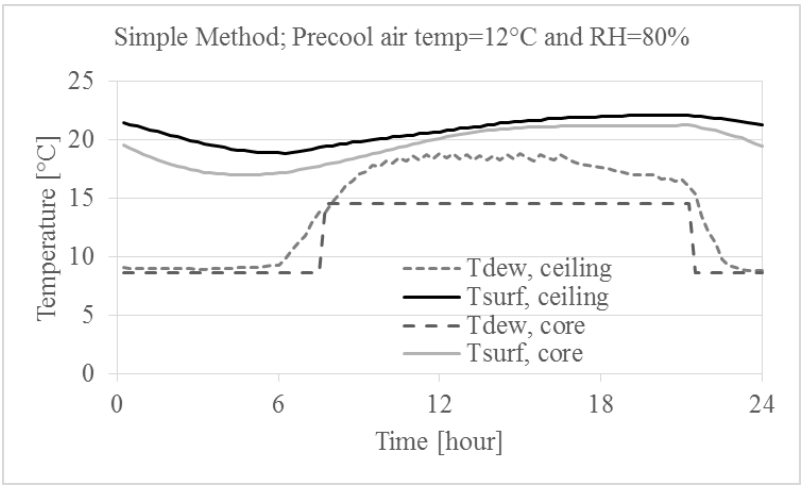

(b)

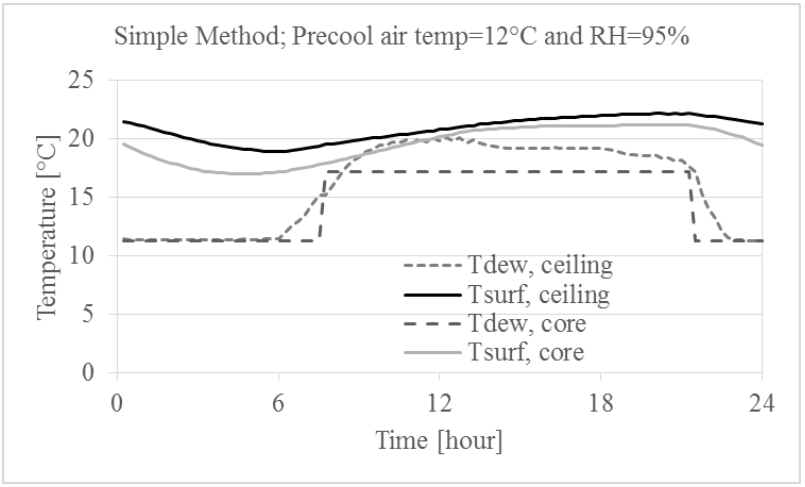

Figure 5.13: Time variations of the ceiling and core surfaces and dew-point temperature when the heavyweight slab is precooled during unoccupied period with: (a) supply air temperature=12°C and RH = 80% and (b) supply air temperature=12°C and RH=95%

So far, the potential impact of the pre-cooling strategy on water condensation is evaluated when the heavyweight precast concrete slab has been used. Now, the same analysis is carried out when lightweight concrete slab is utilized. The lightweight slab mass is expected to be cooled rapidly by supplying cold air during nighttime. Figure 5.14 and Figure 5.15 show that high risk of water condensation on core surface is indeed observed when 95% RH air is supplied to the ventilated slab system. However, the risk of condensation on each surface (i.e. ceiling surface and core surface) remarkably decreases as the dew-point temperature of each surface is decreased.

(a)

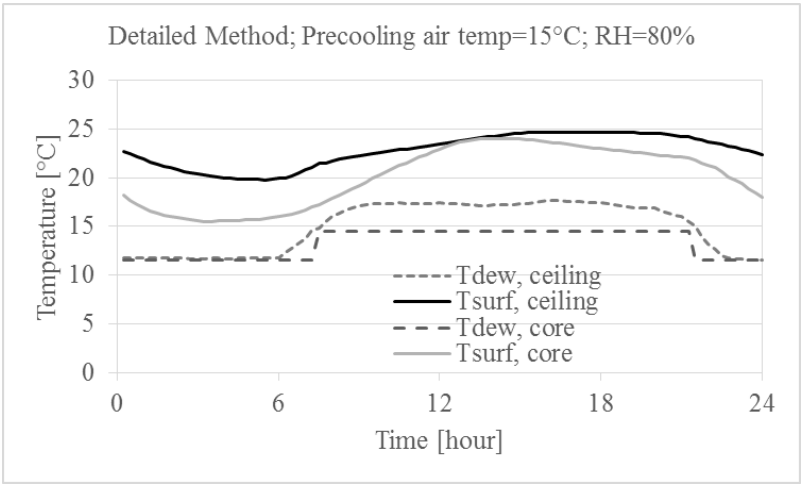

(b)

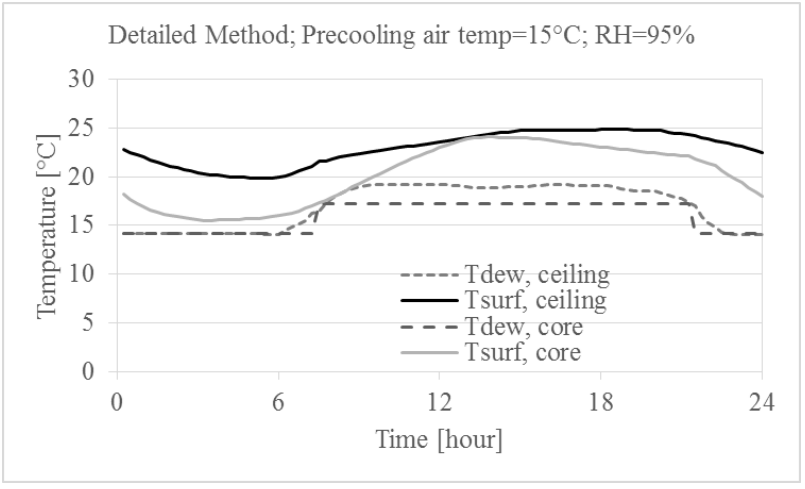

Figure 5.14: Time variations of the ceiling and core surfaces and dew-point temperature when the lightweight slab is precooled during unoccupied period with: (a) supply air temperature=15°C and RH = 80% and (b) supply air temperature=15°C and RH=95%

(a)

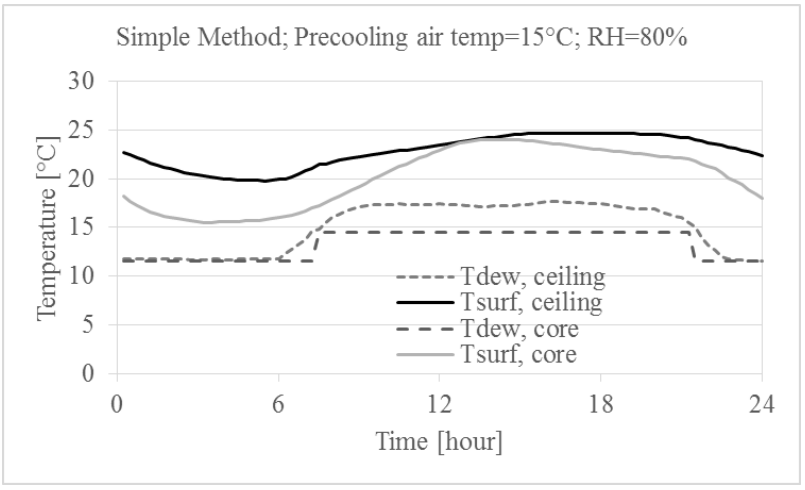

(b)

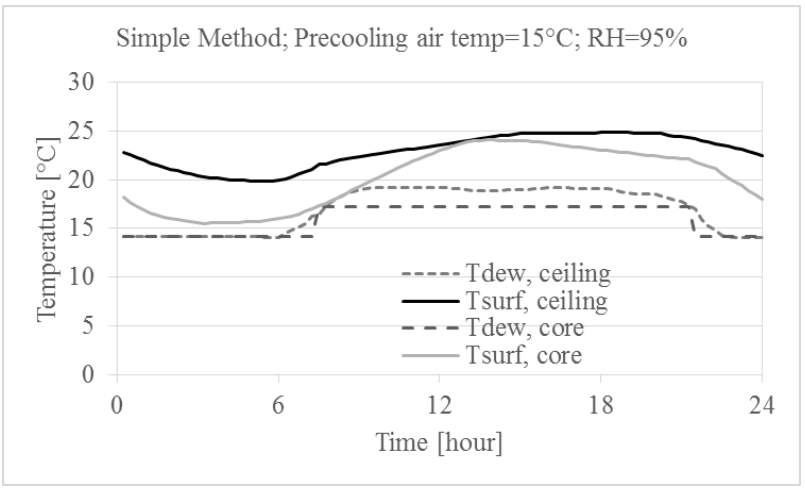

Figure 5.15: : Time variations of the ceiling and core surfaces and dew-point temperature when the lightweight slab is precooled during unoccupied period with: (a) supply air temperature=15°C and RH = 80% and (b) supply air temperature=15°C and RH=95%

A potential risk of water condensation dramatically increases when a hollow core ventilated slab system is constructed with lightweight concrete. In this case, the slab mass temperature reacts quickly to any supply air temperature change. During the night-time pre-cooling period, the slab mass temperature can be lowered to below 15°C by introducing 12°C of supply air as shown in Figure 5.16 and Figure 5.17. Note that the dew point temperature inside hollow cores remains constant because it is assumed that the temperature and the humidity ratio of the supply air is constant. However, the dew point temperature in the zone changes because it is calculated based on the mass balance of the zone air; the changes are more obvious during the daytime due to the moisture generated from occupants. When the building is occupied (i.e. 7 a.m. to 5 p.m.) after a pre-cooling period, the cooling set-point temperature and supply air temperature is reset to 25°C and 18°C, respectively. As the building indoor condition changes with relatively higher zone set-point temperature and supply air temperature for the daytime cooling period, the dew point temperature of supply air inside hollow cores rapidly increases. Although the hollow core surface temperature also gradually increases as the building operation schedule changes, the hollow core surface temperature remains lower than the dew point temperature from 7 a.m. to 9 a.m. as shown in Figure 5.16 and Figure 5.17. The water condensation occurs during the transition period of building operation from pre-cooling to daytime occupied cooling when 95% RH supply air is introduced in cores for lightweight ventilated slab system. High risk of water condensation along the core surfaces is observed even when 12°C and 80% RH supply air is used to pre-cool the ventilated slab system.

(a)

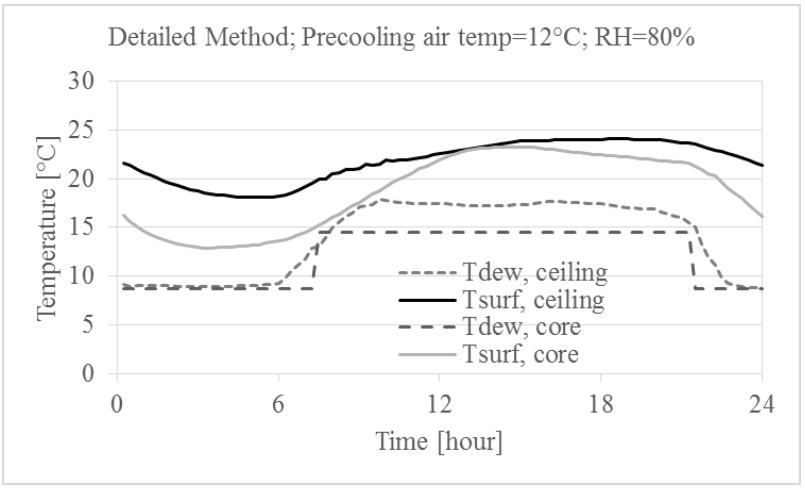

(b)

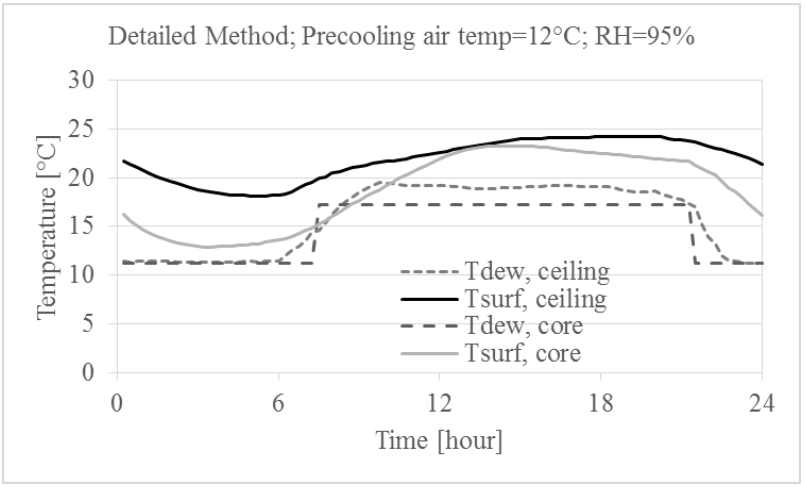

Figure 5.16: : Time variations of the ceiling and core surfaces and dew-point temperature when the lightweight slab is precooled during unoccupied period with: (a) supply air temperature=12°C and RH = 80% and (b) supply air temperature=12°C and RH=95%

(a)

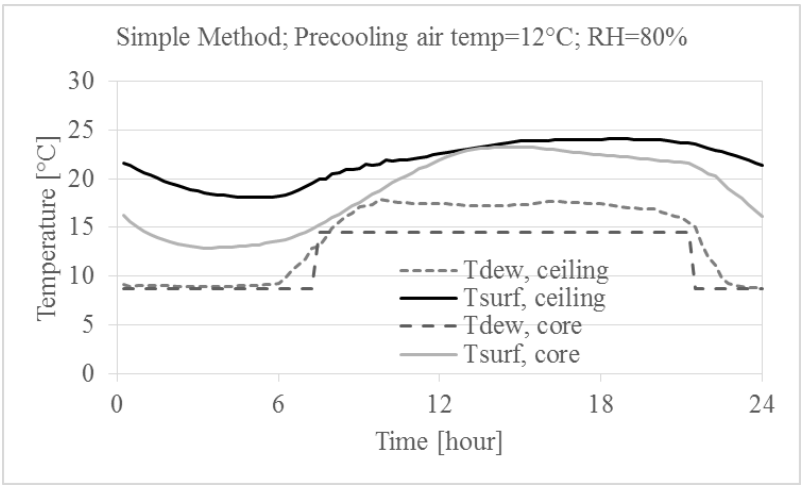

(b)

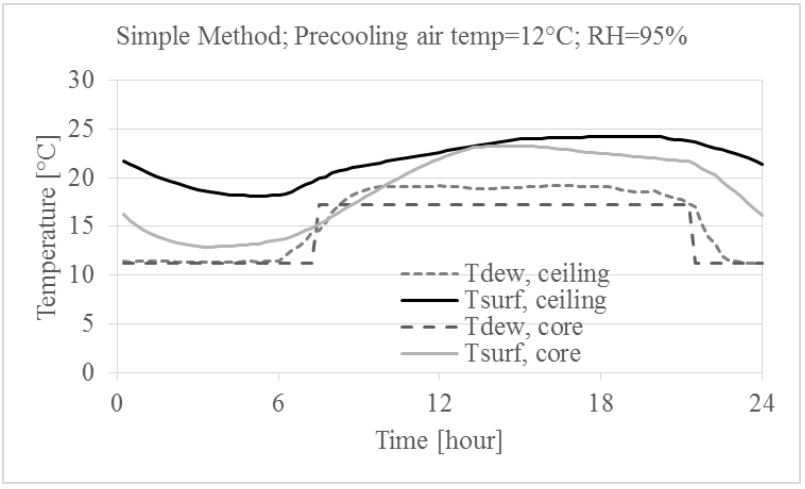

Figure 5.17: : Time variations of the ceiling and core surfaces and dew-point temperature when the lightweight slab is precooled during unoccupied period with: (a) supply air temperature=12°C and RH = 80% and (b) supply air temperature=12°C and RH=95%

The condensation rate, evaporation rate and the amount of condense water obtained from the detailed calculation method is compared to those calculated by the simple calculation method in Figure 5.18. The two different methods provide the same results for both the condensation and evaporation rates since only forced convection occurs inside the hollow cores. Unlike the simple condensation calculation method, the detailed condensation calculation method can calculate the condensation caused by a natural convection. It should be noted that the ventilated slab system

continuously operates regardless of any water condensation occurrence. Based on Figure 5.18 (c), condensate water exists in hollow cores for less than 1.5 hours. Therefore, a very low probability of mold growth risk exists inside hollow cores.

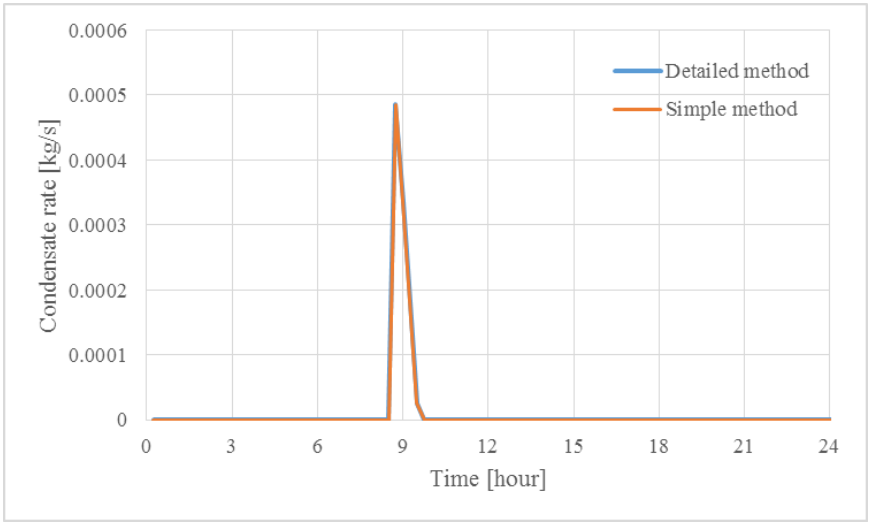

(a)

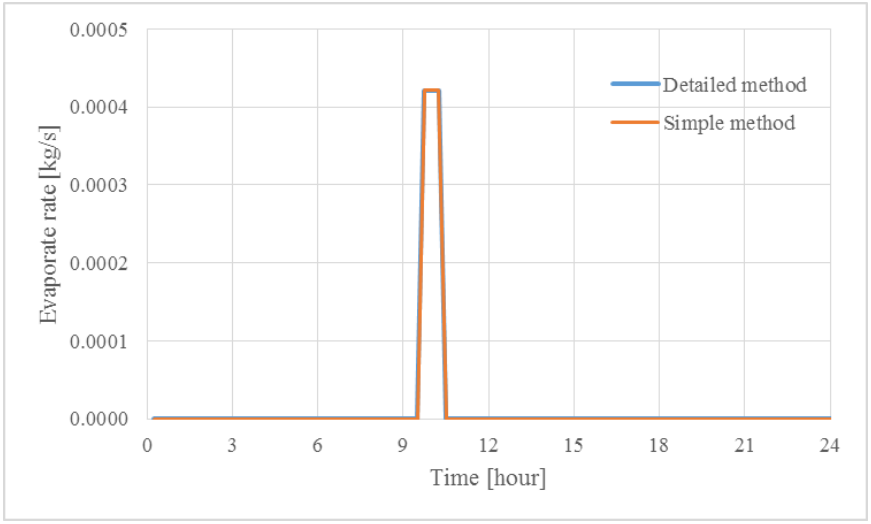

(b)

(c)

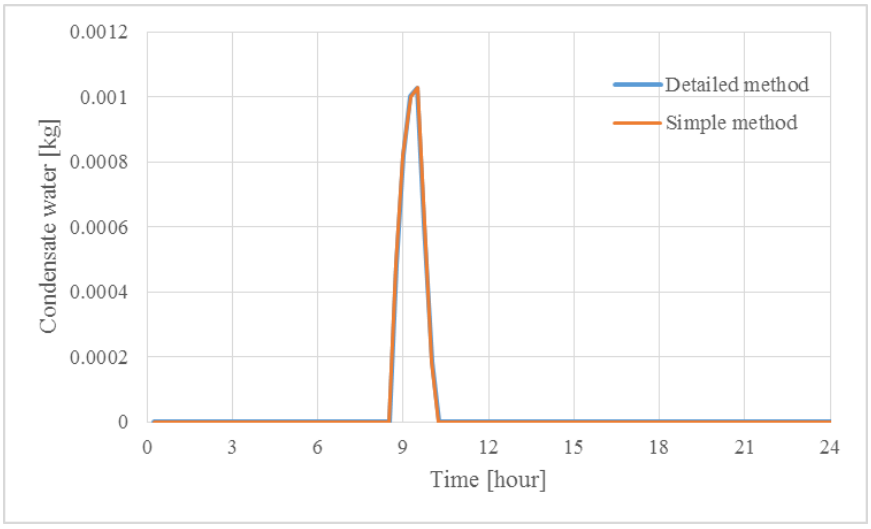

Figure 5.18: Comparison of condensate and evaporate rates as well as the amount of condense water obtained from detailed and simple calculation methods

Table 5.3: Condense water calculated by detailed and simple methods

Parameter	Detailed Method	Simple Method	Difference
Condense water [kg]	0.00412814	0.00412814	0%

5.10 Annual simulation results

This section investigates the annual performance of the enthalpy heat exchanger model implemented to better predict the performance of hollow core ventilated slab systems especially for humid climates. Specifically, the number of hours when water condensation occurs is estimated for various design, operating, and climate conditions during one year. Specifically, two thermal mass levels are considered for the analysis conducted for this section as listed in Table 5.1. Moreover, typical nighttime precooling strategy for an office building located in three US sites is considered in the analysis. The set-point temperature for precooling is set to 18°C, and the set-point temperature during occupied period is 25°C. Relative humidity ratio of the zone is

maintained in the range of 60 – 65% on average throughout the year. Three humid climates in the US are considered in the analysis: San Francisco, CA, Port Arthur, TX, and Miami, FL. According to the definition of climate zones by ASHRAE Standard 90.1-2007, these locations are considered to be part of the hot and humid climate zone in the United States. The slab core supply air temperature is controlled based on the thermal load of the zone rather than set at 18°C during occupied period. The supply air temperature is allowed to vary from 12°C to 17°C depending on the cooling thermal load.

Based on the results obtained from the enhanced simulation environment, no water condensation is observed for the three US locations when the building is constructed with heavyweight precast concrete slabs. However and when the building is made up of lightweight ventilated slabs, water condensation occurred inside the hollow cores for 2 hours during the entire year if the building is located in Miami, FL as shown in Figure 5.19. Water condensation inside the hollow cores is not seen in other locations (i.e. San Francisco, CA and Port Arthur, TX). Moreover, no water condensation on the ceiling surface is noted for all three locations.

The U.S. Environmental Protection Agency (2008) indicates that a period of 24 to 48 hours is needed for mold to grow and states that "even if materials are dried within 48 hours, mold growth may have occurred." This is the generally accepted time frame used by water damage responders to determine when mold begins to grow. Krause et al. (2006) reported that it took at least a week to confirm that invisible microscopic growth structures (hyphae) had formed on wet untreated wallboard in a closed office based on the experiment. Mold growth was not visible on untreated drywall until three weeks (21 days).

Based on the observations from the annual simulation, water condensation does not last more than 30 minutes and condensed water inside the hollow cores fully evaporates within 30 minutes. Thus, there is a very low risk of mold growth inside hollow cores even for the humid climate of Miami.

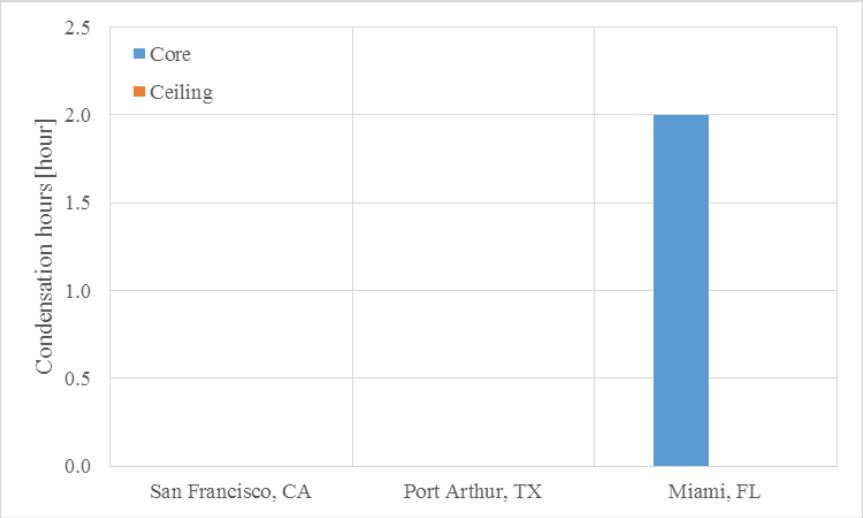

Figure 5.19: Number of hours per year of water condensation occurring inside hollow cores or on ceiling surfaces in three US locations: San Francisco, CA, Port Arthur, TX, and Miami, FL

Based on the previous annual analysis, it was found that water condensations rarely occurs inside the hollow cores or on the ceiling surfaces even if the building is located in humid climates. To consider the worst case scenarios, the water condensation hours are determined when the ventilated slabs operate with the conditions described in Section 5.9. The set-point temperature is set to 12°C for nighttime precooling, and supply air temperature is set to be fixed at 18°C during the occupied period. The relative humidity of the supply air is assumed to be 95% for the worst case scenario. Water condensations inside the hollow cores are estimated for three US locations as shown in Figure 5.20. The total annual hours of water condensation is found to be the largest in Miami, FL with 33.5 hours with condensations occurring inside the hollow cores. For Port Arthur, TX and San Francisco, CA, the number of hours when water condensation occurs is less than 12 hours throughout one year. It should be noted that water condensation does not occur on ceiling surfaces for the three US climates.

Based on the observations from the annual simulation, it is found that water condensation does not

last more than 1 hour and that the condensed water inside the hollow cores evaporates within 45 minutes. Thus, there is a very low probability of mold growth inside hollow cores.

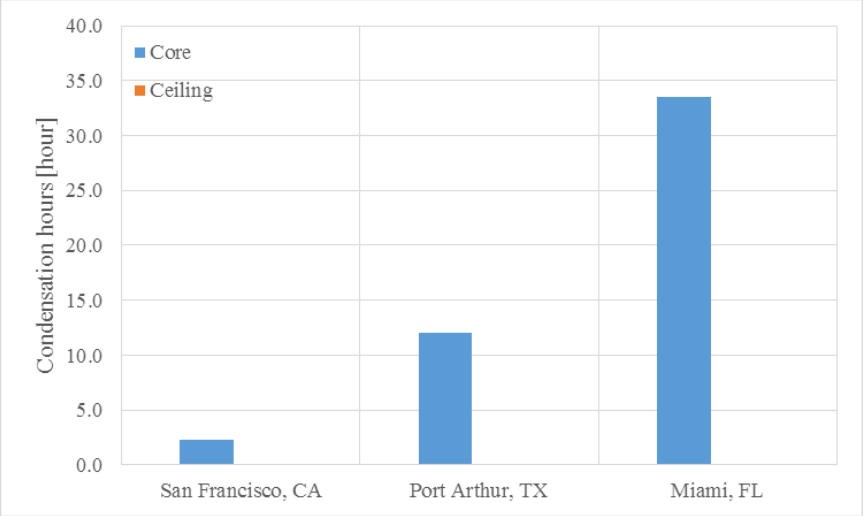

Figure 5.20: Number of hours per year of water condensation occurring inside hollow cores or on ceiling surface in three US locations: San Francisco, CA, Port Arthur, TX, and Miami, FL

5.11 Summary and conclusions

In this chapter, an effectiveness-NTU based method for the enthalpy heat exchanger model is derived. Air in the hollow cores can be heated or cooled with potential loss or gain of moisture that may results in changes of air humidity ratio due to water condensation or evaporation. Such processes can occur when moist air flows through a heat exchanger. The developed enthalpy heat exchanger model is capable to compute the combined heat and mass released or absorbed from the air flowing inside the hollow cores.

Two water condensation models are considered in this Chapter: simple and detailed calculation methods. The analysis results shows that the two methods provide the same results for water condensation and evaporation rates when forced convection is prevalent inside the hollow cores.

The simple calculation method is based on water vapor mass balance. The water mass flow rate, $\dot{m}_w$, can simply be calculated by the product of the air mass flow rate of the difference in humidity ratios. The simple method neglects any condensation when no air flows inside the hollow cores. Also, natural convective mass transfer is not considered to calculate the condensation rate on the ceiling surface. The detailed condensation calculation method overcomes these weakness of the simple method. In particular, the detailed condensation calculation method can estimate the condensation caused by a natural convection. Therefore, the detailed model is expected to more accurately estimate the water condensation rate inside the hollow cores when the ventilated slab system is turned off (i.e. no forced air flow inside the hollow cores) as well as along the ceiling surface when compared to the simple calculation method.

The calculation of water evaporation is essential to accurately assess the existence of condensate water inside a hollow core or along the ceiling surface. Using calculation method based on water spills is implemented in the simulation environment. The evaporation calculation method was validated with available measured data (Shah, 1992; Shah, 2008; Shah, 2012a; Shah, 2013).

During cooling operation, the ventilated slab system perform as a heat sink by introducing a cold air through the hollow cores. The core surface temperature is always between the hollow cores and zone air temperatures. Thus, the core surface temperature is inevitably greater than the supply air that flows through the cores.

When slab mass is dramatically cooled and relatively high temperature air is introduced to the hollow cores, water condensation is likely to occur inside the hollow cores. The slab mass is precooled by supplying cold air before the building is occupied. As the building is occupied, the temperature of supply air is increased to 18°C. Water condensation is observed when 12°C of the supply air with 95% of relative humidity is introduced to a lightweight ventilated slab system during nighttime (before occupied period). Specifically, condensation occurred from 7 a.m. to 9

a.m. inside hollow cores. The hollow core surface temperature is lower than the dew point temperature of supply air during the transition period of building operation from pre-cooling to daytime cooling.

The simple and detailed calculation methods gave the same results for water condensation and evaporation rates since condensation is caused mainly by forced convection inside the hollow cores. It should be noted that the ventilated slab system continuously operates regardless of water condensation occurrence. For the conditions used in the analysis performed in this Chapter, it was found that condensate water exists in hollow cores during less than 1.5 hour with very low probability of mold growth risk to occur inside hollow cores.

The annual performance of the enthalpy heat exchanger model of the hollow core ventilated slab systems is investigated. Specifically, the annual number of hours when water condensation occurs inside the hollow cores or on the ceiling surfaces is estimated for three US humid sites: San Francisco, CA, Port Arthur, TX, and Miami, FL. No water condensation is observed for the three US locations when the building is constructed with heavyweight precast concrete slabs. When the building is made up of lightweight ventilated slabs, water condensation occurred inside the hollow cores only for 2 hours throughout a year when the building is located in Miami, FL. Water condensation is not seen when the building is located in the other two locations (i.e. San Francisco, CA and Port Arthur, TX). Moreover, it is found that water is not condensed on the ceiling surfaces for all three locations. Based on the results obtained from the annual simulation analysis, it is noted that water condensation does not last more than 30 minutes and that the condensed water inside the hollow cores fully evaporates within 30 minutes. Thus, it can be concluded that there is a very low probability of mold growth inside hollow cores.

CHAPTER 6: DEVELOPMENT OF OPTIMAL CONTROL STRATEGY FOR HOLLOW CORE VENTILATED SLAB SYSTEM

6.1 Introduction

While reducing energy consumption should be considered when designing and operating buildings, maintaining acceptable thermal comfort for the occupants should always be a priority. The utilization of thermal storage systems such as hydronic/electric radiant ceiling/floor systems and hollow core ventilated slab systems provide effective alternative to conventional air conditioning systems to achieve indoor thermal comfort and energy efficiency. Indeed, several reported studies have indicated that thermal storage systems can effectively reduce energy consumption and provide more thermal comfort compared to conventional air-based HVAC systems. Hollow core ventilated slab systems can actively use the thermal mass of the slab floor to effectively keep thermal comfort by controlling mean radiant temperature through adjustment of air supply temperature and slab surface temperature.

However, control strategies for ventilated slab systems are more challenging than those utilized to operate conventional air-based HVAC systems. The ventilated slab systems slowly response to the thermal needs of space (Shaw, 1994). Indeed and due to the inherent heat transfer time lag associated to the slab thermal mass, controlling the operation of ventilated slab systems can be rather complex to maintain indoor space air temperature or other thermal comfort indicators within acceptable range. Previous reported investigations have evaluated control strategies for ventilated slab to maintain space temperature using temperature or heat flux modulation techniques. Therefore, there is a need to explore and possibly develop new control strategies to both improve temperature regulation and reduce energy use when using ventilated slab systems. Specific guidelines have to be developed to be considered to effectively operate ventilated slab systems.

6.2 Mean radiant temperature calculation

Mean Radiant Temperature (MRT) plays an important role to calculate indoor thermal comfort. ASHRAE standard 55 defines thermal comfort zone as a function of operative temperature using the psychrometric chart as shown in Figure 6.1. Thus, operative temperature coupled with MRT can affect significantly thermal comfort.

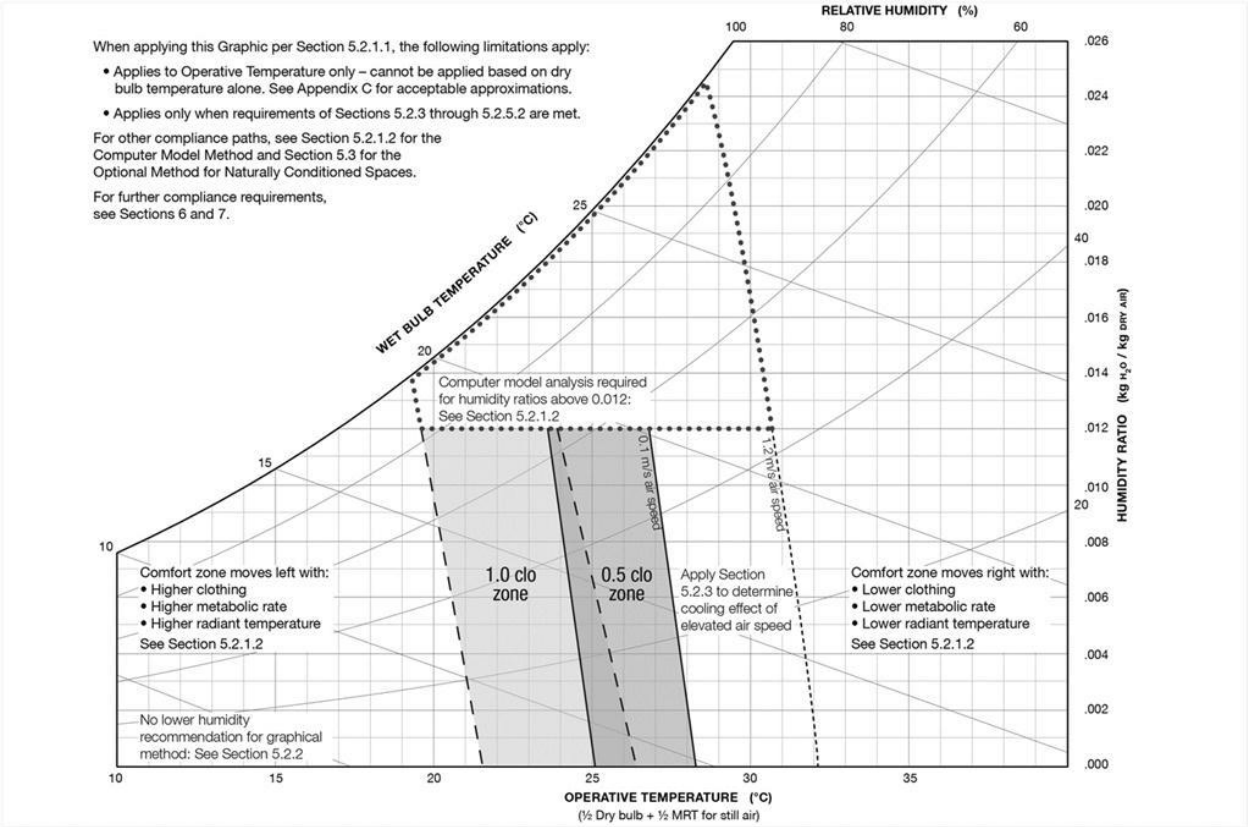

Figure 6.1: The psychrometric thermal comfort chart from the ANSI/ASHRAE Standard 55

ANSI/ASHRAE Standard 55 suggests that spaces where the occupants are engaged in near sedentary physical activity with metabolic rates between 1.0 and 1.3; not in direct exposure to sunlight and to air velocities greater than 0.20 m/s; and where the difference between MRT and dry-bulb is less than 4°C (7°F), the operative temperature (t_o) can be approximated with sufficient accuracy using Eq. (6.1).

$$t_o = \frac{t_{mr} + t_{db}}{2} \quad (6.1)$$

where,

t_o = operative temperature [K]

t_{mr} = mean radiant temperature [K]

t_{db} = drybulb temperature [K]

This simplified operative temperature calculation indicates that for a given operative temperature, the mean radiant temperature within a space needs to be increased if the air temperature is decreased. Likewise the mean radiant temperature needs to be decreased if the dry bulb temperature is increased. It is the basic principle to maintain thermal comfort within spaces conditioned with thermal storage systems such as radiant floor systems and hollow core ventilated slab systems using lower dry bulb temperatures during the heating operation mode and higher dry bulb temperatures during the cooling operation mode.

6.2.1 AUST method

The easiest but least representative method to assess indoor thermal comfort is to use the weighted average of all the surface temperatures in the space (AUST). This simplified MRT calculation method is implemented into EnergyPlus. The simplified MRT is the theoretical uniform surface temperature of an enclosure in which an occupant would exchange the same amount of radiant heat. This simplification is an acceptable solution to assess thermal comfort level for occupants even though the method is not able to address actual ambiguous or non-uniform conditions affecting localized discomfort. When relatively small temperature differences exist between all surfaces of the enclosure, the mean radiant temperature can be simplified to:

$$t_{mr} = (t_1 A_1 + t_2 A_2 + \cdots + t_N A_N)/(A_1 + A_2 + \cdots + A_N) \quad (6.2)$$

where,

t_{mr} = mean radiant temperature [K] (MRT≈ AUST)

t_N = temperature of the inside surface N [K]

A_N = Area of surface N [m^2]

6.2.2 Plane radiant method

Mean radiant temperature may also be calculated from the plane radiant temperature in six directions (up, down, right, left, front, back) and for the projected area factors of a person in the same six directions (ASHRAE, 2009). Plane radiant method recognizes the position of the occupant within the space and considers two options standing or seated. The plane radiant temperature can be calculated using Eq. (6.3) and (6.4).

$$t_{mr(standing)} = \frac{\{0.08[t_{pr(up)} + t_{pr(down)}] + 0.23[t_{pr(right)} + t_{pr(left)}] + 0.35[t_{pr(front)} + t_{pr(back)}]\}}{[2(0.08 + 0.23 + 0.35)]} \quad (6.3)$$

and,

$$t_{mr(seated)} = \frac{\{0.18[t_{pr(up)} + t_{pr(down)}] + 0.22[t_{pr(right)} + t_{pr(left)}] + 0.30[t_{pr(front)} + t_{pr(back)}]\}}{[2(0.18 + 0.22 + 0.30)]} \quad (6.4)$$

where,

t_{pr} = plane radiant temperature, [K]

pr(up) = ceiling temperature above the occupant

pr(down) = floor temperature below occupant

pr(right) = wall temperature to the right of the occupant

pr(left) = wall temperature to the left of the occupant

pr(front) = wall temperature in front of the occupant

pr(back) = wall temperature behind the occupant

The following equation can be used to calculate the plane radiant temperature:

$$t_{pr} = \sqrt[4]{\sum F_{p-i}(t_i + 273)^4} - 273 \quad (6.5)$$

Where,

t_i = surface temperature of surface i [°C]

F_{p-i} = angle factor between a small plane (person) and surface i $\left(\sum F_{p-i} = 1\right)$

The angle factor (F_{p-i}) describes the geometric relationship or view angle of an occupant to each surface. The larger and closer the surface is to a person the more potential it has to thermally influence the occupant. We intuitively know that as we get closer to cold windows we can sense some discomfort. Likewise radiant floors for a seated person in a tall space would have more influence on the occupant than radiant ceilings at the same temperature simply because of the comparative distance from the occupant to those surfaces.

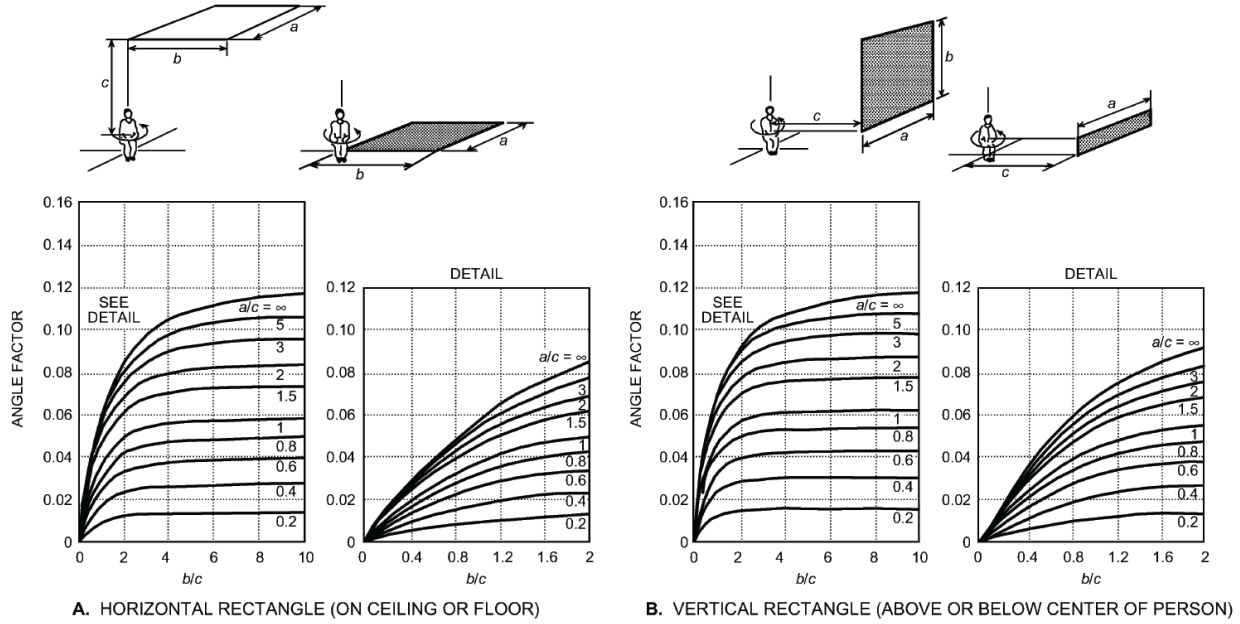

Figure 6.2: Average values of the angle factor between a siting person and horizontal or vertical rectangle surfaces when the person rotates around a vertical axis (Fanger, 1982)

Fanger (1970) analyzed the influence of surface temperatures on occupants based on the person's geometric coordinates within a space. Along with the angle factors and surface temperatures, one can define the MRT for an individual within any space. Together with the indoor air temperature, one can then also define the operative temperature and thus be able to provide at least one key ingredient for the thermal comfort analysis. Although not entirely practical for very simple uniform spaces with low loads where MRT and dry bulb temperature are essentially equal, it is extremely useful for non-uniform environments with complex geometries. The challenge with using graphs such as those shown in Figure 6.2 in general is the error in interpreting intersection points. For simplification and improvement in accuracy, the Federation of European Heating, Ventilation and Air Conditioning Associations (REHVA) published the following formulas:

$$F_{p-i} = F_{MAX}(1 - e^{-\frac{a/c}{\tau}})(1 - e^{-\frac{b/c}{\gamma}}) \quad (6.6)$$

Where,

F_{p-i} = angle factor between a person and surface i

$\tau = A+B\ (a/c)$

$\gamma = C+D\ (b/c) + E(a/c)$

Values for A through E can be found in Table 6.1:

Table 6.1: Coefficients A-E for calculating angle factors for a seated person

Occupant position	F_{max}	A	B	C	D	E
Seated person, Figure B Vertical surfaces: wall, window	0.118	1.216	0.169	0.717	0.087	0.052
Seated person, Figure A Horizontal surfaces: floor, ceiling	0.116	1.396	0.130	0.951	0.080	0.055

(Source: Table 2.1 REHVA Guidebook No.7, Low Temperature Heating, High Temperature Cooling, pg.11, 2007)

6.2.3 Angle factor method

For greater accuracy for more complex spaces, the MRT should be calculated from surfaces above and below the center of gravity of the occupant and from all six sides.

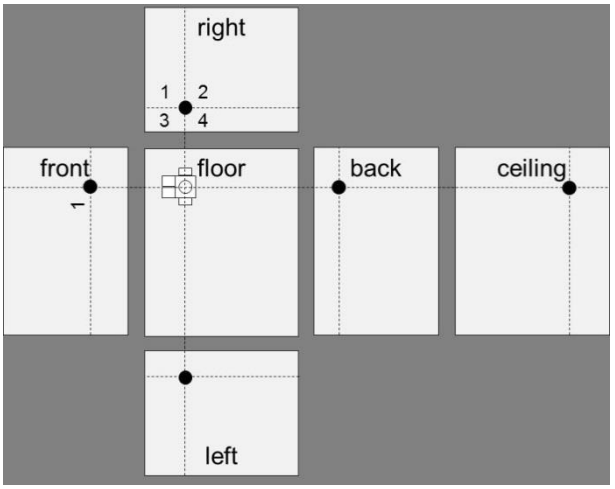

Figure 6.3: Six sides of an enclosure with occupant positioned off-centered.

And the calculation considers the coordinates of the occupant in relation to each enclosing surface. Mathematically it is shown as MRT can be estimated as follows:

$$T_{mrt}^4 = T_1^4 F_{p-1} + T_2^4 F_{p-2} + \cdots + T_N^4 F_{p-N} \quad (6.7)$$

This equation requires that surface temperatures and the angle factors between the occupant and all indoor space surfaces be known. Because the sum of the angle factors is unity, the fourth power of mean radiant temperature equals the mean value of the surrounding surface temperatures to the fourth power, weighted by the respective angle factors. In general, angle factors are difficult to determine, although Figure 6.2 (a) and (b) may be used to estimate them for rectangular surfaces. The angle factors depend also on the position and orientation of the person (Fanger, 1982). Further simplification of the above equation to the linear form yields:

$$T_{mrt} = T_1 F_{p-1} + T_2 F_{p-2} + \cdots + T_N F_{p-N} \quad (6.8)$$

where,

T_{mrt} = mean radiant temperature [K]

T_i = surface temperature of surface i [K]

F_{p-i} = angle factor between a person and surface i (Refer to Section 6.2.2 to see the angle factor calculation)

6.3 Thermal comfort model

The predicted mean vote (PMV) is often used an indicator for indoor thermal comfort using the Fanger's model. Fanger developed the thermal comfort model based on experimental research performed at Kansas State University and Technical University of Denmark. In particular, Fanger's model takes into account various heat losses (L) from the human body to its surroundings including losses by convection and radiation from the outer surface of the clothing, by water vapor diffusion through the skin, by evaporation of sweat from the skin surface, by respiration, and by heat transfer from the skin to the outer surface of the clothing. Note that some of the Fanger model's equations are adjusted based on the ASHRAE standard 55-2004 Appendix D.

$$L = Q_{res} + Q_{dry} + E_{sk} + W \tag{6.9}$$

Where,

L = energy loss from body [W/m^2]

Q_{res} = respiratory heat loss [W/m^2]

Q_{dry} = sensible heat flow from skin [W/m^2]

E_{sk} = the total evaporative heat loss from skin [W/m^2]

W = heat loss due to the performance of work [W/m^2]

The respiratory heat loss can be divided into two components: the latent and dry respiration heat loss. Based on ASHRAE standard 55-2004, the respiratory heat loss can be expressed as follow:

$$Q_{res} = E_{res} + C_{res} = 1.7 \times 0.00001M(5733 - P_a) + 0.0014M(34 - T_a) \tag{6.10}$$

Where,

E_{res} = latent respiratory heat loss [W/m^2]

C_{res} = dry respiratory heat loss [W/m^2]

M = metabolic rate per unit area [W/m^2]

P_a = water vapor pressure in ambient air [Torr]

T_a = air temperature [°C]

The convection and radiant heat losses from the outer surface of the clothing can be expressed as follow:

$$\mathrm{Q_{dry}} = Q_c + Q_r \tag{6.11}$$

Where,

Q_c = convective heat loss [W/m^2]

Q_r = radiative heat loss [W/m^2]

The convective heat losses from the outer surface of the clothing can be estimated as:

$$\mathrm{Q_c} = h_c f_{cl}(T_{cl} - T_a) \tag{6.12}$$

Where,

h_c = convective heat transfer coefficient [W/m^2-°C]

f_{cl} = the ratio of clothed body

T_{cl} = clothing surface temperature [°C]

T_a = air temperature [°C]

According to ASHRAE standard 55-2004, the radiative heat losses from the outer surface of the clothing can be estimated as:

$$Q_r = 3.96 f_{cl}\left(\left(\frac{T_{cl}+273.15}{100}\right)^4 - \left(\frac{T_{ra}+273.15}{100}\right)^4\right) \tag{6.13}$$

Where,

f_{eff} = the fraction of surface effective for radiation (=0.72)

ε = the emissivity of clothing-skin surface

σ = the Stefan-Boltzman constant (=5.67e-8)

T_{cl} = clothing surface temperature [°C]

T_{ra} = the mean radiant temperature [°C]

$$f_{cl} = 1.05 + 0.1clo \tag{6.14}$$

Where,

clo = clothing unit

The clothed surface temperature can be computed using iteration calculation procedure:

While $\left|X_n - X_f\right| > 0.00015$

$$X_f = \frac{X_f + X_n}{2}$$

$$H_{c,for} = 12.1\sqrt{V_a}$$

$$H_{c,nat} = 2.38 \cdot \left|100 \cdot X_f - (T_a + 273.15)\right|^{0.25}$$

$$H_c = \max(H_{c,for}, H_{c,nat}) \tag{6.15}$$

$$X_n = \frac{P_4 + P_1 H_c - P_2 X_f^4}{100 + P_3 H_c}$$

end

$$AbsCloSurfTemp = 100X_n$$

$$T_{cl} = AbsCloSurfTemp - 273.15$$

Where,

$P_1 = (T_a + 273.15)clo$

$P_2 = 3.96clo$

$P_3 = 100clo$

$P_4 = 308.7 - 0.028(ActLevel - WorkEff) + P_2 \left(\frac{(T_{mrt}+273.15)}{100}\right)^4$

The heat losses by evaporation of sweat from the skin surface and the heat losses by water vapor diffusion through the skin are determined as shown below:

$$E_{sk} = E_{rsw} + E_{diff} \tag{6.16}$$

Where,

E_{rsw} = heat loss from the evaporation of regulatory seating at the state of comfort [W/m^2]

E_{diff} = heat loss from the diffusion of water vapor through the skin [W/m^2]

$$E_{rsw} = 0.42(H - 58.2), if\ H > 58.2$$

$$E_{rsw} = 0, else \tag{6.17}$$

$$E_{diff} = 3.05 \times 0.001(5733 - 6.99H - P_a)$$

Where,

H = internal heat production rate of an occupant per unit area (M-W) [W/m^2]

P_{sk} = saturated water vapor pressure at required skin temperature [Torr]

P_a = water vapor pressure in ambient air [Torr]

The Predicted Mean Vote (PMV) scale is based on the difference between the metabolic rate and the heat energy loss as indicated in the following expression:

$$\mathrm{PMV} = (0.303\mathrm{e}^{-0.036\mathrm{M}} + 0.028)(M - W - Q_{res} - Q_{dry} - E_{sk}) \quad (6.18)$$

Where,

M = metabolic rate per unit area [W/m^2]

The Predicted Percentage Dissatisfied (PPD) is calculated by using following equation:

$$\mathrm{PPD} = 100 - 95\mathrm{e}^{-0.03353\mathrm{PMV}^4 - 0.2179PMV^2} \quad (6.19)$$

6.4 Optimal control strategy

Optimization methods could be divided into derivative and non-derivative methods. Derivative methods requires that the objective function be smooth and differentiable. Derivative methods might have difficulties to find the optimal solution when the objective function is non-convex.

Non-derivative methods are much more robust in locating the global optimal solution, and are better suited for general optimization problems (Goldberg, 1988). Non-derivative methods do not require derivatives or gradients of the objective function in order to find the optimal solution. Indeed, non-derivative methods only require values of the objective function.

When the objective function is computed based on the results obtained from complex computer simulations, the derivatives of the objective function are not explicitly known. Thus, the study presented in this thesis focuses on non-derivative methods. There are numerous studies discussing the basic principles and applications of non-derivative methods (Andersson, 2001). The Complex method developed by Box in the 60's (Box, 1965). Genetic algorithms and the similar evolutionary algorithms developed by Holland and Rechenberg, respectively, in the 70's (Holland, 1975; Rechenberg, 1973). Simulated annealing was developed by Kirkpatrick in the early 80's (Kirkpatrick et al., 1983). Besides these methods, there are also other promising optimization

techniques developed more recently such as Tabu search, response surface approximations, and Taguchi methods (Glover, 1989; Connor, 1999). Several comparative studies of different non-derivative methods are reported (Borup, 1992; Jansson, 1994; Hajela, 1999; Mongeau, 2000). Selection of suitable optimization algorithm depends generally on the nature of the problem and how well the different methods were tuned to fit the particular problem.

In the study performed in this thesis, Complex method, genetic algorithm and particle swarm algorithm are considered. The Complex method is not only fast, but also easy to implement and parameterize (Borup, 1992; Jansson, 1994). Genetic algorithm is known to be the most robust and thorough method in finding the global optimum and they have been widely employed in various field of applications. Particle swarm algorithm is similar to Genetic algorithm because the technique utilizes stochastic and population-based selection approach. Particle swarm algorithm possibly arrive at optimum solution faster than Genetic algorithm (Matlab, 2015).

6.4.1 Complex method

The Complex method was first developed by Box (1965) from the Simplex method by Spendley (1962), and later improved by Guin (1968). The term "Complex" is a contraction of the words "Constrained and Simplex". A complex consists of several potential solutions (sets of parameters) that can be manipulated in the Complex Method. Each set of parameters represents a point in the solution space. The main idea of the Complex Method is to replace the worst point by a new and better point. Figure 6.4 shows an example the iterative search process of the complex method. The circles in the graph indicate the values of solution for the objective function. The optimal solution is placed in the middle.

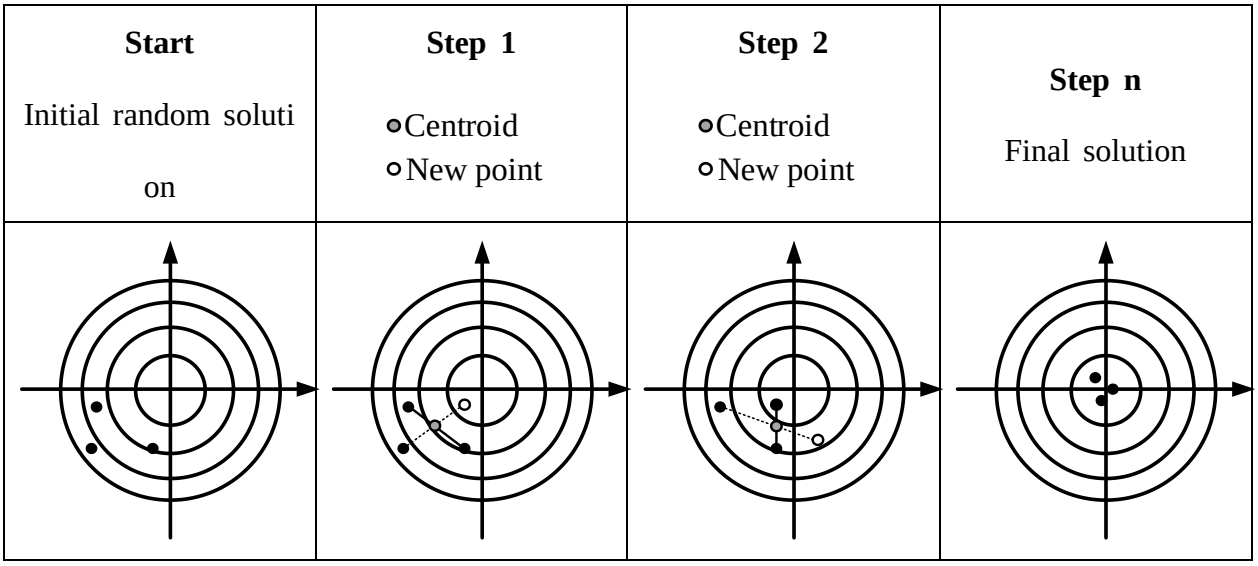

Figure 6.4: An example of Complex method procedure

The new point is calculated as the reflection of the worst point through the centroid of the remaining points in the complex.

$$x^r = \bar{x} + \alpha(\bar{x} - x^l)$$

Where,

α = the reflection coefficient (=1.3 according to Box, 1965)

The point x^r is examined with constraints, and if it is feasible, it replaces x^l unless it repeats by being the worst. In that case, it is moved halfway towards the centroid of the reaming points. This process is repeated until it stops repeating the worst point. However, this procedure cannot handle the situation where there is a local minimum at the centroid. Krus et al. (2003) modified the method so that the point is gradually moved towards the maximum value if it continues to be the worst. The modified algorithm is based on the following adjustment for x^r:

$$x^{r(new)} = \frac{\left[x^{r(old)} + \varepsilon\bar{x} + (1-\varepsilon)x^h\right]}{2} + (\bar{x} - x^h)(1-\varepsilon)(2R-1)$$

Where,

$$\varepsilon = \left(\frac{n_{\mathrm{r}}}{n_r + k_r - 1}\right)^{\frac{n_r + k_r - 1}{n_r}}$$

k_r is the number of times the point has repeated itself as worst value, and $n_r = 4$ is a constant. R is a random number in the interval [0,1].

6.4.2 Genetic Algorithms

Genetic algorithms are one of the non-gradient optimization methods and is very popular in various research topics. Genetic algorithms mimic the mechanisms of natural selection. Each parameter ($\mathrm{x_n}$) is encoded by a gene using a real number or a string of bits. The combination of all parameters ($\mathrm{x_1}, \dots, \mathrm{x_n}$) form a chromosome which is capable in describing an individual solution. A set of chromosomes comprises a population. Among the various individuals in a population, the fittest are selected to reproduce. While the offspring is produced by mating technique, the crossover and mutation take place to combine genes from parents. The children are inserted into the population and the procedure repeats. The description of the genetic algorithms presented in this section is based on 'Simple Genetic Algorithm' (Goldberg, 1989). Each of parameter variables is represented by a binary number of N bits in Goldberg's Simple Genetic Algorithm. A set of binary string represents individual solutions in the population. To evaluate the fitness of an individual, each bit in an individual is decoded to a real value for each variable. The steps of the genetic algorithm optimization technique are described as follows:

1. For the first generation, a population of individuals is randomly generated. A set of binary number of N bits represents each individual.

   $$pop_{gen} = \{B_{1,gen}, B_{2,gen}, \dots, B_{maxpop,gen}\}$$

   Where,

B = an individual (N bits binary number) in the population,

maxpop = population size,

gen = the number of generation.

2. Decode $B_{i,gen} \in pop_{gen}, i = 1, 2, \dots, maxpop$ to $R_{i,gen} \in pop_{gen},\ i = 1, 2, \dots, maxpop$. Where R is the real value of B, binary number of N bits.
3. Evaluate the objective function for each decoded individual, $R_{i,gen}$, among the population. Then, the fitness of each individual, $R_{i,gen}$, is computed to evaluate the objective function value and feasibility. If a solution violates the feasibility criteria, the solution will be penalized by means of a penalty function.
4. Generate a new population by the following techniques:
    a. Reproduction: Select individuals in the old population based on the fitness value of each individual. The weight of each individual determines the probability of being selected. The weight (i.e., the probability of being selected) of an individual is defined by:

$$\mathrm{p}(\mathrm{B_{i,gen}}) = \frac{\mathrm{fitness}(\mathrm{B_{i,gen}})}{\sum_{j=1}^{maxpop} \mathrm{fitness}(B_{j,gen})}, i = 1, 2, \dots, maxpop$$

    b. Mutation: If a randomly generated probability is lower than the mutation probability, $\mathrm{p_m}$, the mutation operator flips the value of the $\mathrm{j^{th}}$ bit of the $\mathrm{i^{th}}$ individual, $\mathrm{X_{j,i,gen}}$, in the old population by the following algorithm.

$$\mathrm{X_{j,i,gen}} = \mathrm{X_{j,i,gen}}, in\ probalility\ of\ (1 - P_m)$$

$$\mathrm{X_{j,i,gen}} = \overline{\mathrm{X}}_{\mathrm{j,i,gen}}, in\ probalility\ of\ (P_m)$$

where,

$$\overline{\mathrm{X}}_{\mathrm{j,i,gen}} = 0, if\ \mathrm{X_{j,i,gen}} = 1;$$

$$\overline{\mathrm{X}}_{\mathrm{j,i,gen}} = 1, if\ \mathrm{X_{j,i,gen}} = 0;$$

c. Crossover: If a randomly generated probability is lower than the crossover probability, p_c, the crossover operator randomly selects a crossover position at which it swaps the two parent strings of bits.

$$B_{i,gen+1} = B_{i,gen}, in\ probalility\ of\ (1 - P_c)$$

$$B_{i,gen+1} = B'_{i,gen}, in\ probalility\ of\ (P_c)$$

where, $Y'_{i,gen}$ is one of the new child individual after crossover.

d. Add new individuals to the new population set.

5. Repeat the procedure from step 2 to 4 in order to obtain the next generation.

6.4.3 Particle Swarm Optimization

Particle swarm optimization (PSO) technique is a population based stochastic optimization technique developed by Eberhart and Kennedy in 1995. PSO mimics the social behavior of bird flocking or fish schooling. PSO is similar to any evolutionary computation techniques such as Genetic Algorithms (GA), but PSO has no evolutionary operators such as crossover and mutation utilized in GA.

Population size significantly affects the robustness and computational cost of evolutionary optimization algorithm. Although the best swarm size highly depends on the nature of the problem such as dimensions and constraints of the objective function. Bratton and Kennedy (2007) reported that "no swarm size between 20 – 100 particles produced results that were clearly superior or inferior to any other value for a majority of the tested problems". Moreover, Shi and Eberhart (1999) reported that the performance of PSO is not sensitive to the population size.

PSO generates a random initial populations and searches for optimum solution by updating generations. The potential solutions in PSO, called particles, travels the problem space by

following the current optimal particles. In every generation, each particle is updated by two best solutions. The first is the best fitness value of each particle achieved so far, called as pbest. The second is the best fitness value of all the particles in the population, called as lbest. When a particle takes all the population as its topological neighbors, the best solution is a global optima value, called as gbest.

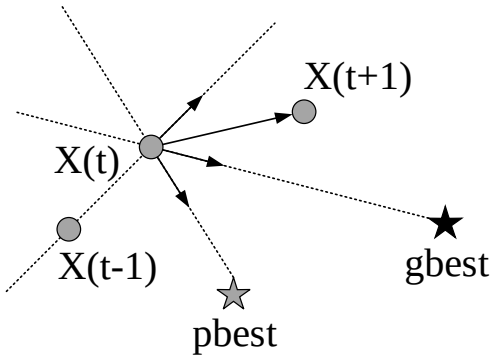

Figure 6.5: An example of particle swarm procedure

Each particle keeps track of its coordinates in the problem space associated with the best solution at current step. Each particle moves toward the current best solution with a random acceleration rate:

$$v_{i,j}(t+1) = wv_{i,j}(t) + c_1 r_{2,j}(t)\left(y_{i,j}(t) - x_{i,j}(t)\right) + c_2 r_{2,j}(t)\left(\hat{y}_i(t) - x_{i,j}(t)\right)$$

Where,

w = inertia weight

c = acceleration constants

Larger *w* has greater global search ability, and smaller *w* has greater local search ability. Second term in right hand side of equation is the cognitive component, which represents the particle's own experience as to where the best solution is. Third term is the social component, which represents the belief of the entire swarm as to where the best solution is located.

Position update in PSO:

$$x_{i,j}(t+1) = x_{i,j}(t) + v_{i,j}(t+1)$$

PSO technique has been successfully applied to various research applications. In particular, it is demonstrated that PSO gets feasible solutions with less computational effort compared to other optimization methods.

6.4.4 Hybrid function

We can employ an additional optimization function in the Matlab Global Optimization Toolbox to ensure that the obtained solution is actually the global minima. It is called a hybrid function in the Matlab. A hybrid function is an optimization function that runs after one of the available optimization algorithms, e.g., genetic algorithm or particle swarm, terminates in order to improve the fitness value of the objective function. The final variables from the optimization algorithm is handed over to the hybrid function, and they are used as an initial variables for the hybrid function. Constrained nonlinear optimization (CNO) technique is specifically used as the hybrid function in this study. CNO attempts to find a constrained minimum of a scalar function of several variables starting at an initial estimate.

6.5 Description of the analysis

6.5.1 Commercial building

A two-story building with one thermal zone per floor is considered for the study. The building has a floor area of 3200 m^2 and a ceiling height of 3 m. The total area per floor is thus 1600 m^2. The U-value of the building envelope is determined based on ASHRAE 90.1 2004. The U-value of the

exterior walls are 0.088 $W \cdot K^{-1} \cdot m^{-2}$. The U-value of the exterior roof and floor is assumed to be 0.033 $W \cdot K^{-1} \cdot m^{-2}$. Peak occupancy is set to be 32 m^2 per person. Each person contributes 120 W of internal gain where 70% is assumed to be sensible and 30% latent. Peak lighting power density is defined as 10.38 W/m^2. Figure 6.6 shows the occupancy and lighting schedules considered for a weekday. The length of peak period is 14 hours (from 8 a.m. to 10 p.m.). The building is occupied from 6 a.m. to 6 p.m. Unlike residential buildings, a ventilated system is available to operate even though the building is unoccupied to actively utilize building thermal mass. The graphs in this section are created on the basis of simulation results using weather data on August 11th in Golden, CO. 10 days of simulation period is utilized as a warm-up to attain steady-state conditions before actual optimization simulation.

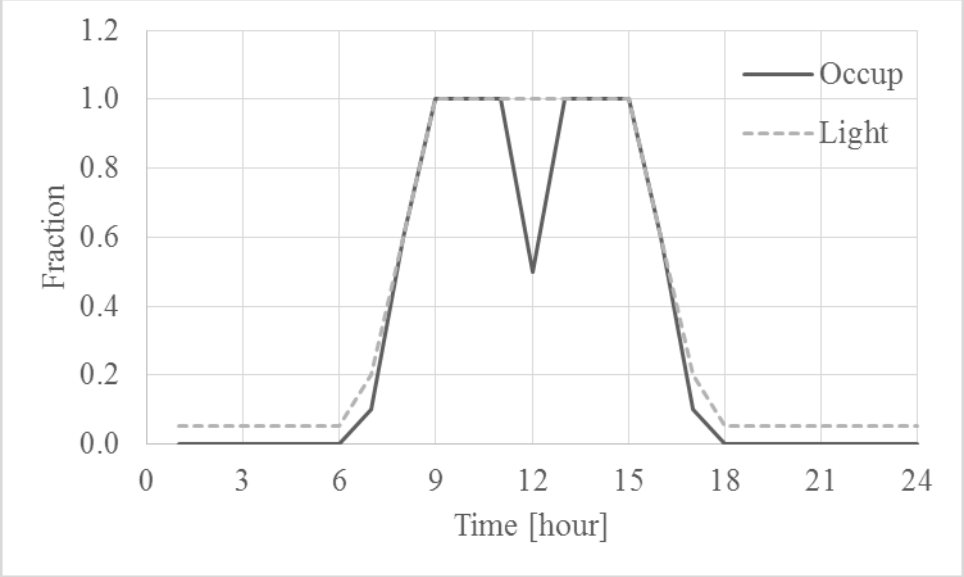

Figure 6.6: Occupancy and lighting schedule for the commercial building

6.5.2 Optimal controller structure

Figure 6.7 depicts the structure of the optimal schedule controller for the developed building

energy model. The controller is to search for the optimal zone air set-point temperature schedules. There are two optimization techniques that can be employed: consecutive time block optimization (CTBO) and the alternative is closed-loop optimization (CLO). CTBO searches for an optimal solution over a predefined horizon L (e.g., a horizon of 24 hours). CTBO executes the complete optimal strategy over the entire predefined horizon L and the optimal strategy minimizes the objective function value. CLO controller also carries out an optimal solution over a horizon L. Unlike CTBO, only the first of the optimization solution is executed for the first time step within a horizon L. This process repeats at the next time step while the time window of L time steps moves forward. The final optimal control strategy over the entire horizon of K steps (i.e. K steps in the predefined horizon L) is composed of the first control strategy variables of K optimal strategies of the horizon L. CLO can reflect a new forecast at each time step and the control strategy can also be updated based on a new forecast at each time step (Henze, 2004).

The essential assumption in this study is that weather, occupancy, lighting loads are perfectly known and predicted. In the case of perfect prediction scenario, the controller is expected to produce identical solution regardless of optimization techniques. When the future is subject to uncertainty, CLO technique is expected to have superior performance compared to CTBO technique (Henze, 2004). In this study, CTBO technique is employed to investigate the effectiveness of the optimal controller for a hollow core ventilated slab system over a 24-hour deterministic simulation analysis.

The optimal controller carries out the optimal set-point temperature schedule based on the energy cost and thermal comfort constraints predicted by the developed building model. The Genetic algorithm and Particle swarm techniques are selected among the various optimization algorithms.

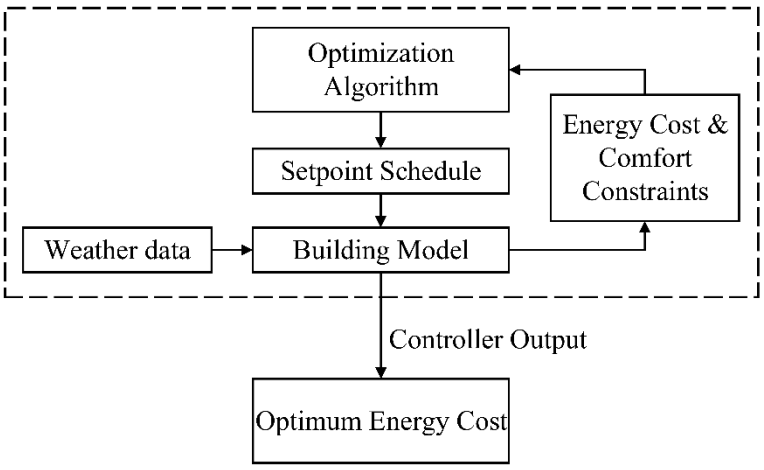

Figure 6.7: The structure of the optimal controller for deterministic simulation

6.5.3 Objective function

An optimization process is to find the set of variables that minimize the objective function value (fitness value), the total operation cost of the ventilated slab system, with certain constraints. In this study, the optimization algorithm searches for an optimal set of zone set-point temperature schedules that minimize the total daily operating cost while thermal comfort is maintained within acceptable level during occupied period. The energy costs are penalized to ensure that the best optimum solution are feasible and are not violating the constraints. The first term in the right-hand side of the objective function expresses the penalized electricity charge for any 24 hour period. Rates of electricity charge and demand charge are assumed to be $0.10 per kWh and $10 per kW, respectively. Utility structure of a commercial building is usually more subdivided compared to that of a residential building. Utility rate structure of a commercial building consists of time of use charge and demand charge. Time of use charge rate varies depending on periods: on-peak or off-peak period. Demand charge is the highest average demand during the month. The demand kW is billed each month. To assess the impact of optimal control strategy of ventilated slab system on

electrical energy cost, the monthly demand charge is extrapolated to daily utility cost by assuming that all days in the month are identical. In particular, sum of the estimated peak demand charge is divided by 30 (number of days in a month), and added to the daily time of use electrical charge. The objective function for office buildings can be expressed as follows:

$$E = \sum_{k=1}^{24} \left\{ r_{e,onpeak,k} EC_{onpeak,k} + r_{e,offpeak,k} EC_{offpeak,k} + f(PMV_k) \right\} + \frac{r_{d,onpeak} D_{onpeak} + r_{d,offpeak} D_{offpeak}}{30}$$

Where,

E = the total cost

$r_{e,onpeak}$ = on-peak electricity rate

$r_{e,offpeak}$ = off-peak electricity rate

k = hour

$r_{d,onpeak}$ = on-peak demand charge

$r_{d,offpeak}$ = off-peak demand charge

EC_{onpeak} = on-peak energy consumption at hour k [kWh]

$EC_{offpeak}$ = off-peak energy consumption at hour k [kWh]

D_{onpeak} = on-peak demand [kW]

$D_{offpeak}$ = off-peak demand [kW]

$f(PMV)$ = penalty cost

The objective function is constrained by the thermal comfort of occupants. The predicted mean vote (PMV) is chosen as the index for assessing thermal comfort of occupants. PMV value ranging between -0.5 and +0.5 is generally acceptable (ASHRAE, 2005). To maintain the thermal comfort

within the acceptable range during the occupied hours, the zone set-point temperature of the considered commercial building is limited as follows:

$$20°C \leq T_{set} \leq 24°\text{C} \text{ (Occupied period)}$$

$$15°C \leq T_{set} \leq 30°\text{C} \text{ (Unoccupied period)}$$

Two techniques are generally used to penalize the fitness value of infeasible solutions. One is the simple rejection of infeasible solutions, and the other is to penalize the fitness value based on the degree of infeasibility. The latter technique is selected since it is able to search for the better optimal solution compared to the former even though it slightly violates the PMV constraints.

$$f(PMV) = w(e^{PMV^2} - 1) \tag{6.20}$$

Or

$$f(PMV) = w\{u(|PMV|) - \text{u}(|PMV| - 0.5)\} \tag{6.21}$$

Where,

w = weighting factor

6.6 Simulation results

6.6.1 Optimization using 2-D model

In Chapter 4, we explored the impact of thermal bridging effects on the performance of ventilated slab system by comparing the thermal and energy performance of the ventilated slab system obtained from 1-D to 2-D model. It was found that thermal bridging can affect heating and cooling energy consumption of the ventilated slab system depending on the insulation level at slab and wall joint. For example, 2-D model predicts approximately 14% of cooling energy consumption for 4 meter wide slabs due to thermal bridging when no insulation is placed at the slab and wall joint.

2-D model has an advantage that it can more accurately predict the energy consumption of the ventilated slab system compared to 1-D model. A disadvantage of 2-D model is that the computational effort noticeably increases compared with the 1-D model especially when it is applied to the optimization problem. Indeed, 2-D model requires enormous computational time to search for 3 optimal set-point schedule variables within a day (i.e. 1 optimal set-point temperature for each occupancy period in office building) through optimization process as shown in Figure 6.8. The result shows that computational effort proportionally increases for wider floor while 1-D model completes the optimization simulation in 3 hours regardless of the floor size. Indeed, the increase in the total number of nodes when utilizing 2-D modeling for the wider floor leads to significant increase in CPU time.

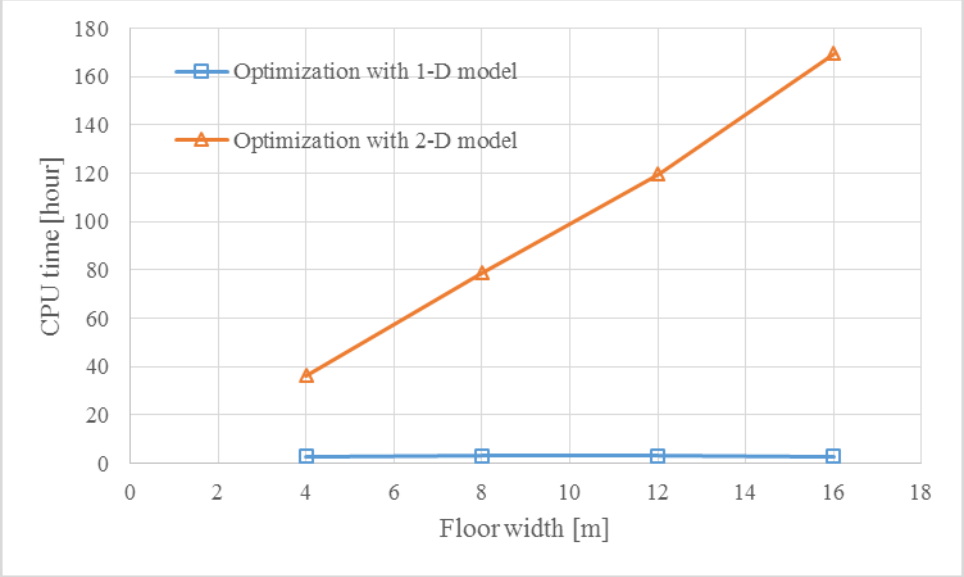

Figure 6.8: Computational time required for the optimization process of 1-D and 2-D model

For 16 meter wide slab, it takes 149 hours to obtain the optimum set-point schedule for one day. The required CPU time is absolutely unreasonable and unpractical to employ 2-D model for the optimization analysis.

In this section, we explored a method to convert 2-D model's optimization solution to the solution obtained from the optimization simulation carried out using 1-D model. Interestingly, it is observed that these percent differences of energy consumption between 1-D and 2-D model for various floor sizes and utility ratios remain the same after optimization process as shown in Figure 6.9. For these data, the R^2 value is 0.9711. This means that the correlation between 1-D and 2-D model can be applied to the optimization solution of 1-D model to estimate the optimization solution of 2-D model. Using the appropriate conversion factor, the optimization solutions obtained from 1-D model are expected to reflect those obtained using 2-D model.

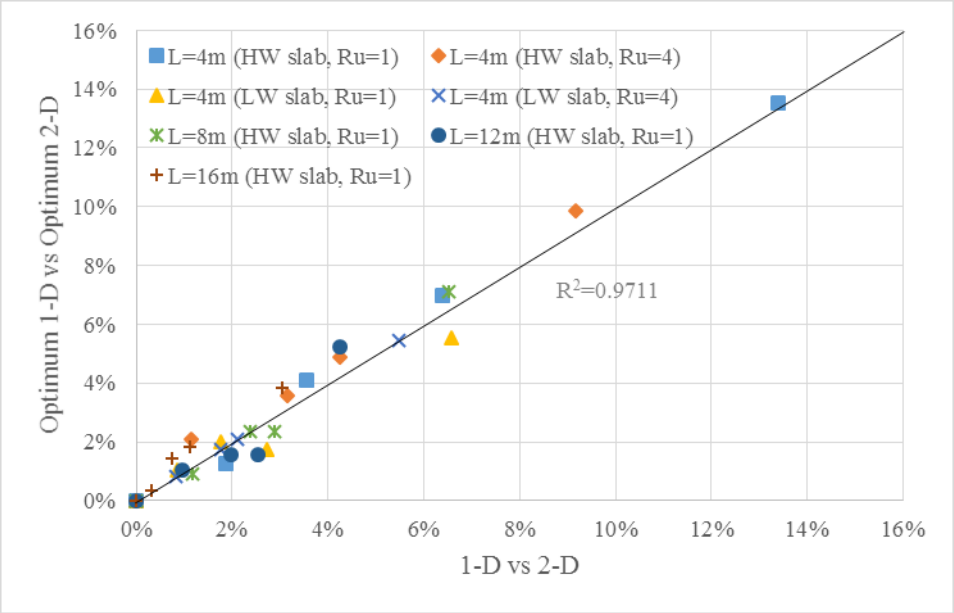

Figure 6.9: Percent difference of cooling energy use between 1-D and 2-D model after optimization process as a function of percent difference of cooling energy use between 1-D and 2-D model for various slab sizes and utility rates

We will take 0.25 meter thick slab as an example. Accordingly linear regression is applied to fit the percent cost difference between 1-D and 2-D model associated with the ratio of heat flows through walls to heat flows through slab as shown in Figure 6.12. The ratio of heat transfer rate

through exterior walls to heat transfer rate through a slab is defined by Y- to Δ-network transformation. Slab and wall joint can be schematized as Y-network in Figure 6.10. By a reduction from Y- to Δ-network, the temperature in the middle of the network is not required to calculate heat flows between each node. It is proved that the same heat flow is entering the three nodes (i.e.T_1,T_2, and T_3) using the Y- to Δ-network reduction (Hagentoft, 2001).

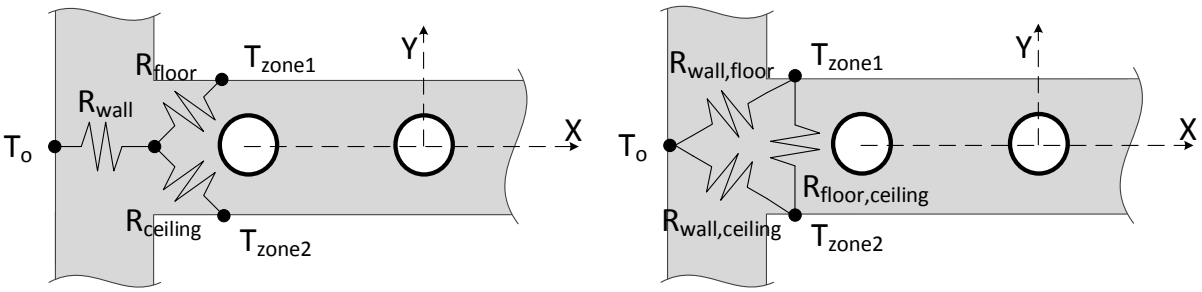

Figure 6.10: Reduction from Y- to Δ-network

The transformation shown in Figure 6.10 is summarized using the following formulas:

$$R_{wall,floor} = \frac{R_{wall}R_{floor} + R_{wall}R_{ceiling} + R_{floor}R_{ceiling}}{R_{ceiling}} \tag{6.22}$$

$$R_{wall,ceiling} = \frac{R_{wall}R_{floor} + R_{wall}R_{ceiling} + R_{floor}R_{ceiling}}{R_{floor}} \tag{6.23}$$

$$R_{floor,ceiling} = \frac{R_{wall}R_{floor} + R_{wall}R_{ceiling} + R_{floor}R_{ceiling}}{R_{wall}} \tag{6.24}$$

Where, R_{wall} is the thermal resistance of exterior wall, R_{floor} is upper half of the thermal resistances of the slab, $R_{ceiling}$ is lower half of the thermal resistances of the slab.

The Δ-network shown in Figure 6.10 can be redrawn to produce an equivalent thermal network in parallel as shown in Figure 6.11.

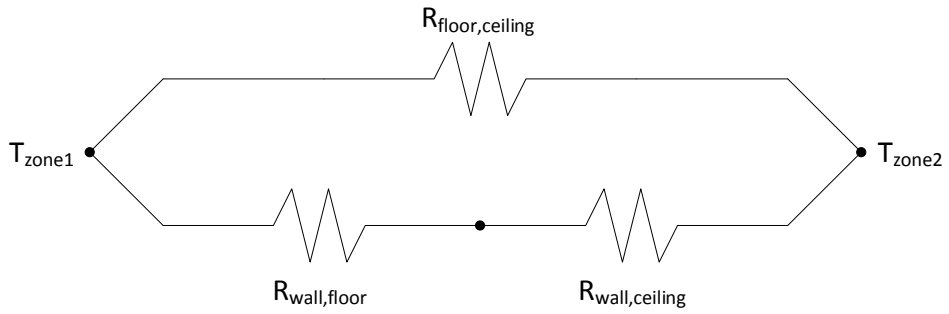

Figure 6.11: Parallel thermal network

The total heat flow $\dot{Q}_{total}$ from zone 1 node to zone 2 node is made up of the heat flow in the two parallel paths, $\dot{Q}_{total} = \dot{Q}_{wall,floor} + \dot{Q}_{wall,ceiling} + \dot{Q}_{floor,ceiling}$. Thus, the equivalent UA can be defined as follows:

$$UA_{eq} = \left(\frac{1}{R_{wall,floor} + R_{wall,ceiling}}\right) A_e + \frac{1}{R_{floor,ceiling}} A_s \tag{6.25}$$

Where,

A_e = area of slab edge (i.e. slab and wall joint)

A_s = area of slab surface

Rearranging Eq. (6.25) gives:

$$UA_{eq} = \frac{1}{R_{floor,ceiling}} A_s \left(1 + \frac{\frac{1}{R_{wall,floor} + R_{wall,ceiling}} A_e}{\frac{1}{R_{floor,ceiling}} A_s}\right) \tag{6.26}$$

The heat transfer factors (the ratio of heat transfer rate through exterior walls to heat transfer rate through a slab) can be expressed as follows:

$$f_{s,w} = \frac{\left(\frac{1}{R_{wall,floor} + R_{wall,ceiling}}\right) A_e}{\left(\frac{1}{R_{floor,ceiling}}\right) A_s} \tag{6.27}$$

Figure 6.12 shows the linear regression applied to fit the percent difference between 1-D and 2-D model associated with the heat transfer factors. R square value of the linear regression model is greater than 0.90 which indicated a quite good fit. The linear regression correlation will be used as 1-D model optimal solution correction factor to convert 1-D optimal solution to 2-D optimal solution.

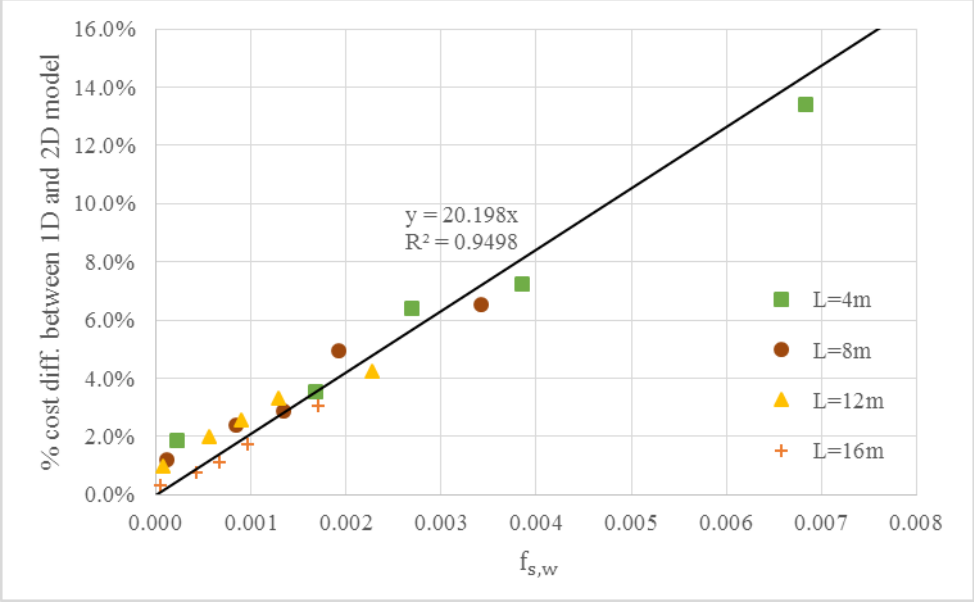

Figure 6.12: Percent cost difference between 1-D and 2-D numerical model as a function of ratio of heat transfer rate through exterior walls to heat transfer rate through a slab

Figure 6.13 and Figure 6.14 show that the optimization solution obtained from 1-D model can effectively be converted to the optimization solution obtained from 2-D model by applying the correction factors to the 1-D model. Coefficient of variation (CV) for 1-D model is lowered below 0.01 with the correction factors as shown in Figure 6.13. Figure 6.14 demonstrates good accuracy of using the 1-D optimal solution with correction as the optimal solution obtained from 2-D model. In general, performing the optimization using 1-D model with the appropriate correction provides

an adequate estimate for the optimal solution associated with the 2-D model analysis.

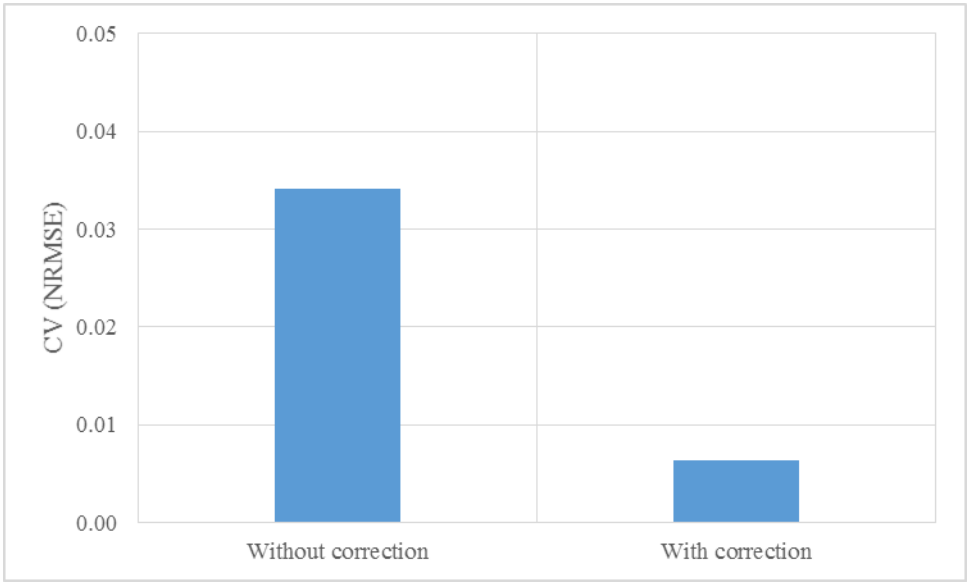

Figure 6.13: Comparison of coefficient of variation (CV) for 1-D model with/without correction

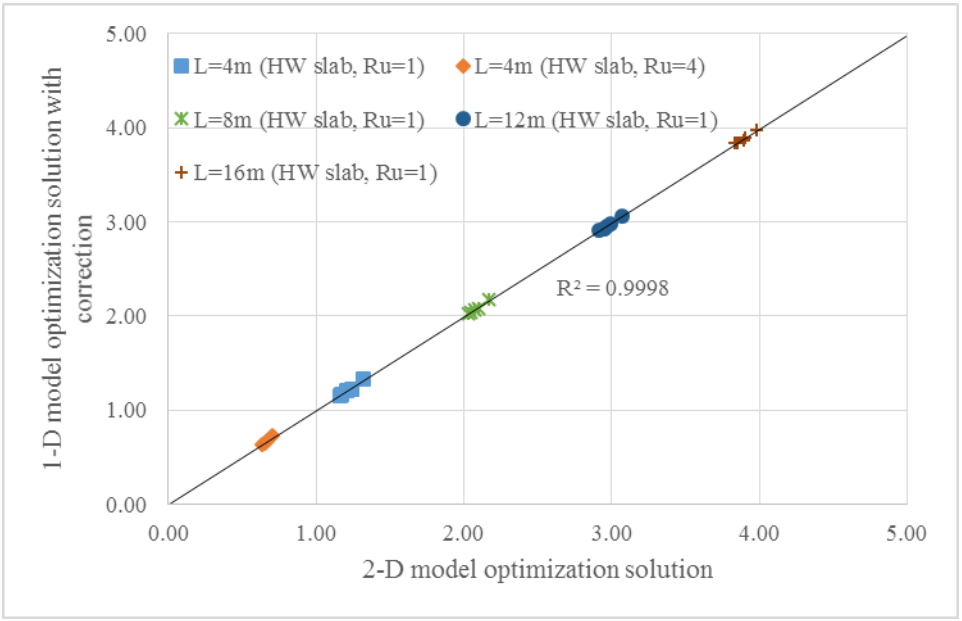

Figure 6.14: Comparison of optimization solution obtained from 1-D model with correction and 2-D model

6.6.2 Global optimization toolbox verification

The optimal set-point temperature schedule and energy use obtained from Matlab Global Optimization Toolbox are verified against the brute-force simulation results using all possible set-point schedule combinations. Specifically, Genetic algorithms from Global Optimization Toolbox is considered. Global Optimization Toolbox is set up to select integer variables within the constrained set-point temperatures (i.e. $23°C \leq T_{set} \leq 27°\text{C}$). Figure 6.15 present the penalized energy use with 6 hour interval set-point temperature schedule. It is found that optimal penalized energy use and set-point temperature schedule obtained from Global Optimization Toolbox are identical to minimum values found from entire simulation.

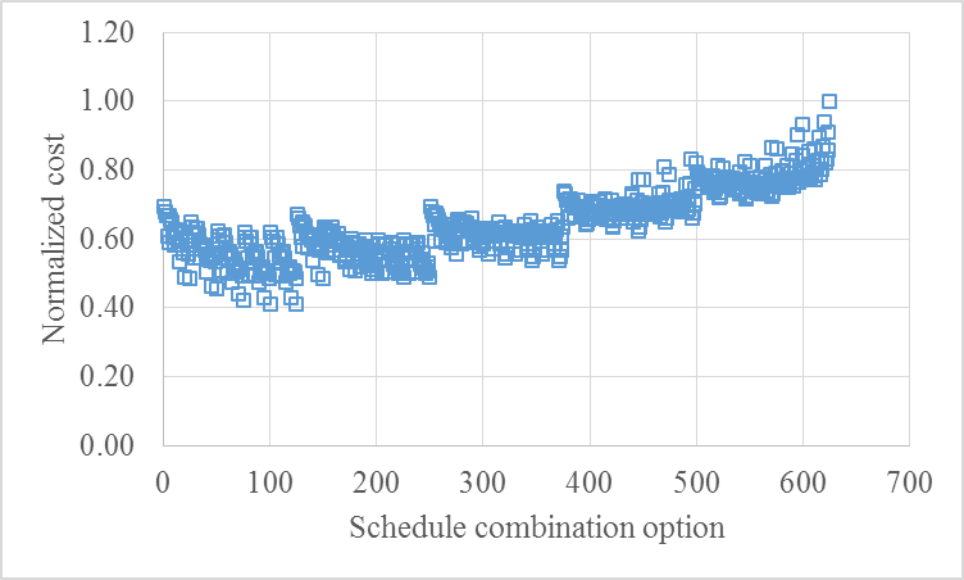

Figure 6.15: Energy cost as a function of 6hr interval set-point temperature schedule combination obtained from brute-force simulation

Table 6.2: Comparison of the optimal solution obtained from Matlab global optimization toolbox with brute-force simulation

	Normalized energy cost	Daily set-point temperature schedule
Brute-force simulation	0.41	1 AM to 6 AM: 23°C 7 AM to 12 PM: 26°C 1 PM to 6 PM: 27°C 7 PM to 12 AM: 27°C
Matlab Global Optimization Toolbox	0.41	1 AM to 6 AM: 23°C 7 AM to 12 PM: 26°C 1 PM to 6 PM: 27°C 7 PM to 12 AM: 27°C

6.7 Sensitivity analysis for the office building

Two different types of the cost penalty function have been considered and evaluated: exponential penalty function and step penalty function. Exponential penalty function is able to penalize the energy cost based on the degree of PMV violation. Step penalty function penalizes the energy cost using a constant value. Figure 6.16 depicts two different penalty functions with two levels of weighting factors. The cost penalty is imposed to the energy cost only when it violates the PMV constraint of thermal comfort zone which is between -0.5 and 0.5. We investigated the impact of cost penalty function type on the performance of optimization algorithm.

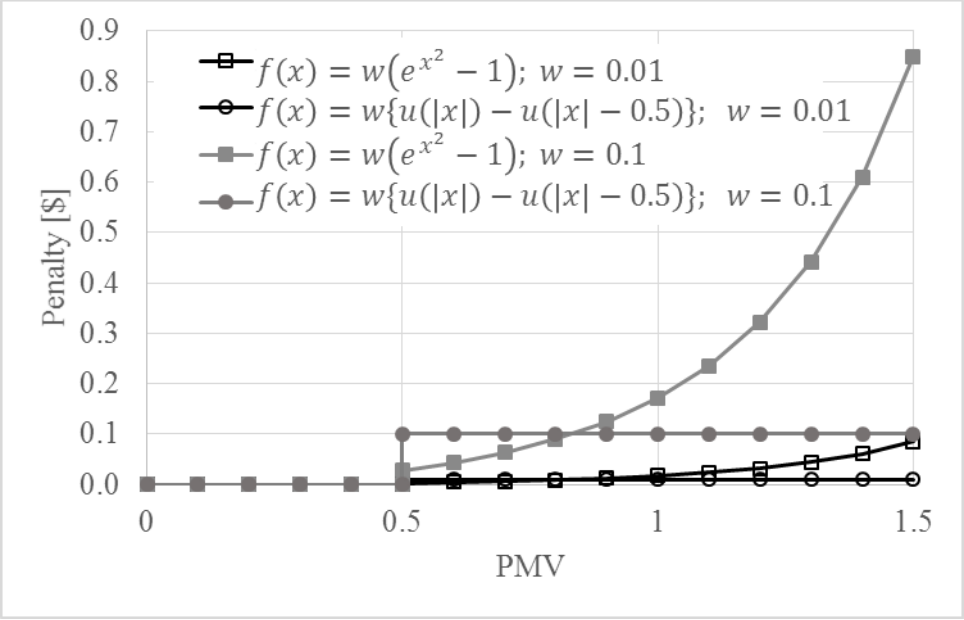

Figure 6.16: Exponential penalty function and step penalty function with two weighting factors

The total minimum energy cost and computational efforts obtained with two different cost penalty functions is shown in Figure 6.17. It is revealed that the selection of the cost penalty function has no impact on the performance of the optimization algorithm. The optimal solutions carried out with two different cost penalty functions are identical as shown in Figure 6.17. In the remainder of the analysis results presented in this chapter, the exponential cost penalty function is used.

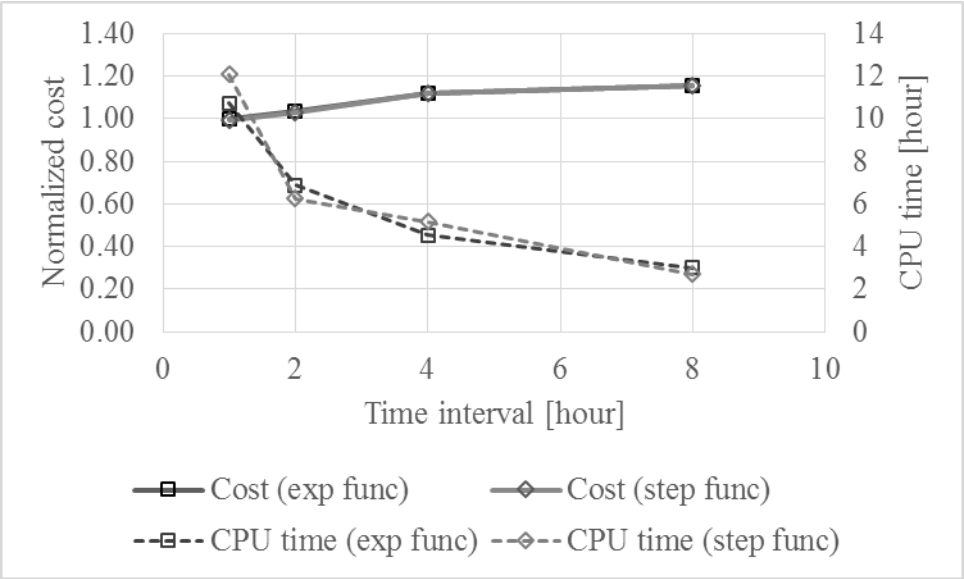

Figure 6.17: Cost and CPU time with two different penalty function (i.e. exponential function and step function) as a function of time interval

There are no rule of thumb for an appropriate population size for the evolutionary optimization algorithm such as particle swarm and genetic algorithm. However, the population size greatly affect the computational effort. The bigger the population size, the longer the CPU time. Thus, the population size for the evolutionary optimization algorithm should be properly determined. The proper population size cannot only provide accurate optimal solution but also reduce the computational effort. Figure 6.18 depicts the impact of population size on the performance of the genetic algorithm optimization technique. The population size is varied from 25 to 350 with 1 hour time interval of set-point schedule is considered for the analysis. Although the best swarm size highly depends on the nature of the objective function problem, the performance of GA is not sensitive to the population size as shown in Figure 6.18. Therefore, the population size of 100 is selected for the optimization analysis as Matlab Global Optimization Toolbox suggests for the GA.

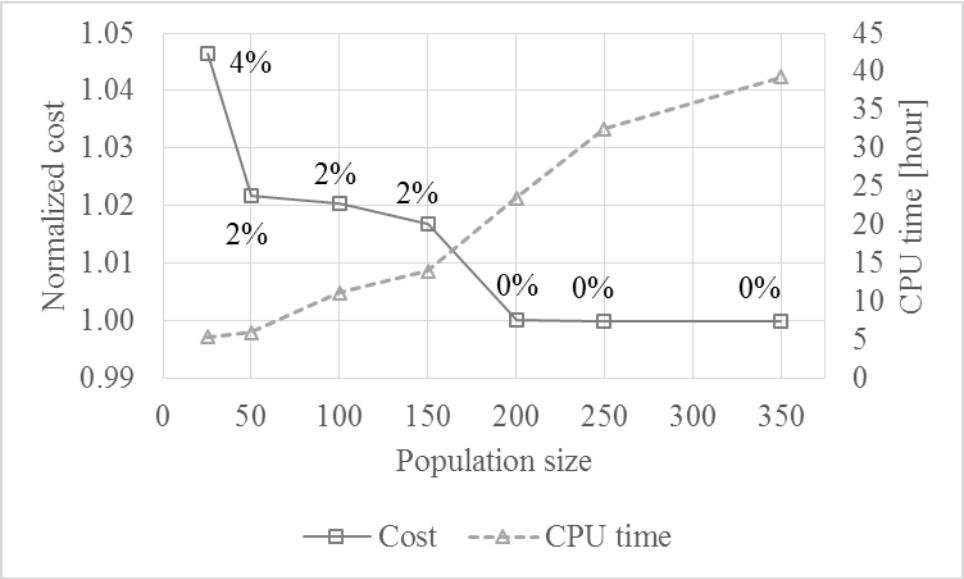

Figure 6.18: Cost and CPU time as a function of population size

We explored the impact of the weighting factor associated with the implementation of the exponential cost penalty function (which penalizes the total energy cost on the basis of thermal comfort) on the performance of optimization algorithm. A 2 hour interval optimal set-point schedule and a population size of 100 are chosen to investigate the impact of the weighting factor. The weighting factor is varied from 1 to 1000. It is found that low weighting factors leads to different optimal solution. The energy cost should be sufficiently penalized so that a reliable optimal solution is obtained and is capable in maintaining acceptable indoor thermal comfort. The impact of weighting factor greater than 10 on the performance of the genetic algorithm optimization algorithms is not substantial as shown in Figure 6.19.

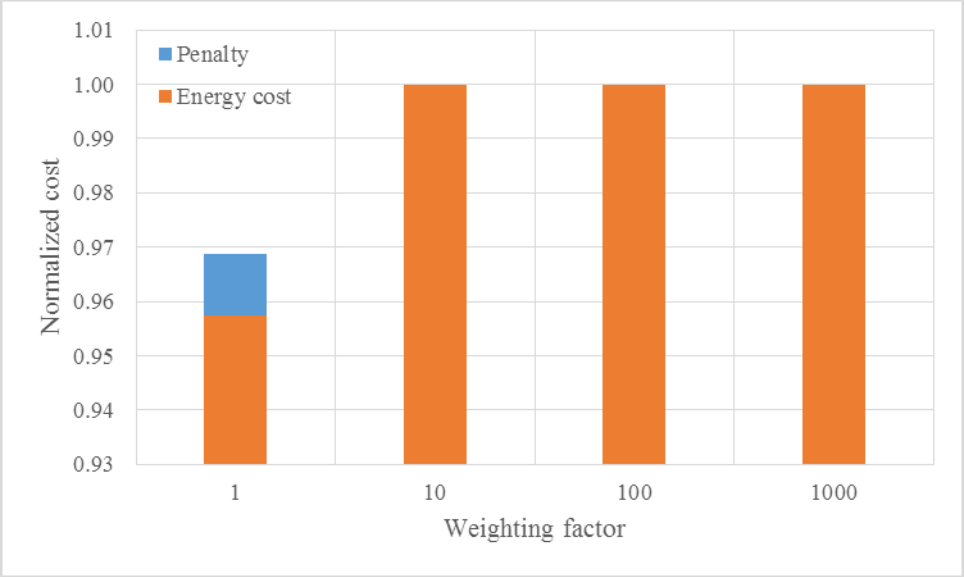

Figure 6.19: Cost as a function of weighting factor of penalty function

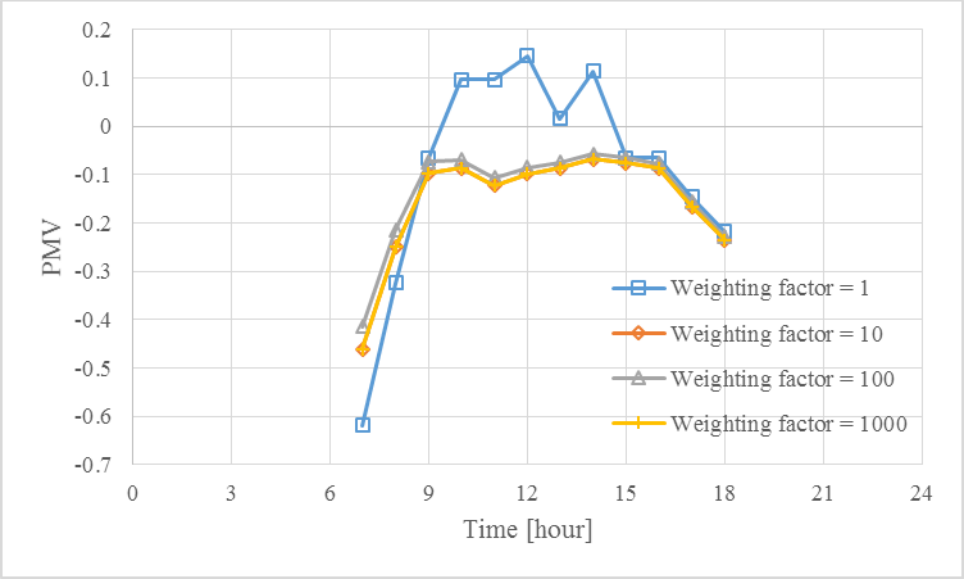

Figure 6.20: Variation of PMV for two different weighting factors

A series of sensitivity analysis of optimization simulation for an office building is carried out to analyze the impact of various design and cost parameters including building thermal mass, utility structure and floor area of the building on the savings potential for use of optimal operation mode of ventilated slab system. Although utility rates, on-to-off peak ratio, the length of peak period varies according to regions in the US, generic utility rate structure is applied to the simulation studies. The average electricity rates reported by U.S. Energy Information Administration (EIA) are assumed to be uniform with $0.10/kWh for energy charges and $10/kW for demand charges.

1. Optimal solution results compared to conventional control

A simplification is introduced to reduce the numerical complexity of the optimization problem. One global zone set-point temperature is determined for each combination of occupancy and utility rate period over a day. Using hourly time steps, the dimension of the solution space for one day is 24. The solution space for one day (24 hour horizon) can be reduced from 24 dimensions to 5 dimensions through a simplification approach. The utility rate structure has a strong incentive for peak-demand shifting with on-to-off peak ratio of 4. Specifically, it is assumed that during on-peak period the rates are $0.10/kWh and $10/kW, and that the rates are $0.025/kWh and $2.5/kW during off-peak period.

During the unoccupied period (i.e. 0 to 6 and 18 to 24), lower bound is set to 15°C and the upper bound is defined and 30°C.

During the occupied period, the lower and upper bounds are set to 20°C and 24°C, respectively. Figure 6.21 shows the best and mean fitness value for each generation searched by GA. Best fitness is the lowest fitness function (objective function) among all individuals in the population. Mean fitness is the average over all individuals in the population of the current generation.

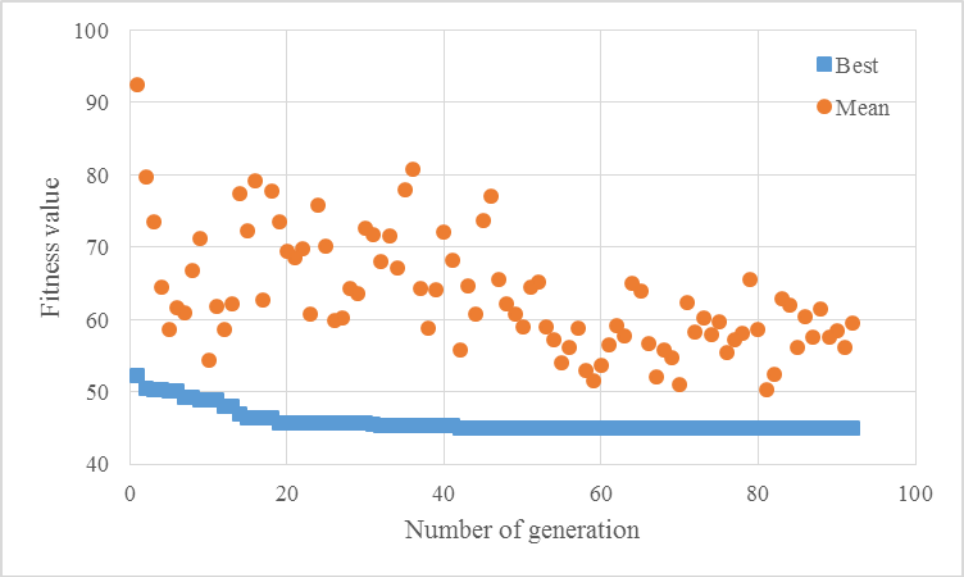

Figure 6.21: Fitness value for each generation of GA

Figure 6.22 shows the set-point temperature schedules obtained for conventional and optimal controls. The optimal controller of the ventilated slab system suggests precooling as shown in Figure 6.22. The set-point temperature is set to 20°C during the off-peak unoccupied period. The set-point temperature is slightly increased to 22.1°C for the off-peak occupied period. The zone air temperature remains at the upper comfort limit (24°C) during the on-peak occupied period. The zone air temperature floats freely as soon as the occupied period ends by returning high set-point temperature. Figure 6.23 shows the hourly zone air temperature using the conventional night setup control and the optimal control strategy. It is obviously shown that the optimal control can decrease the mean air temperature by 0.8°C. Figure 6.24 depicts that the cooling energy use is shifted to the off-peak period by the optimal controller. Figure 6.25 shows the hourly PMV profiles for both control options. A comparative analysis of the energy use and cost demonstrates the main benefit in precooling buildings as shown in Figure 6.26. The optimal controller leads to 8.5% of cooling energy cost reduction. However, Figure 6.27 shows that the total daily cooling energy use was

increased by 27% by adapting the precooling strategy. From a global energy conservation point of view, the energy cost and use should be carefully considered.

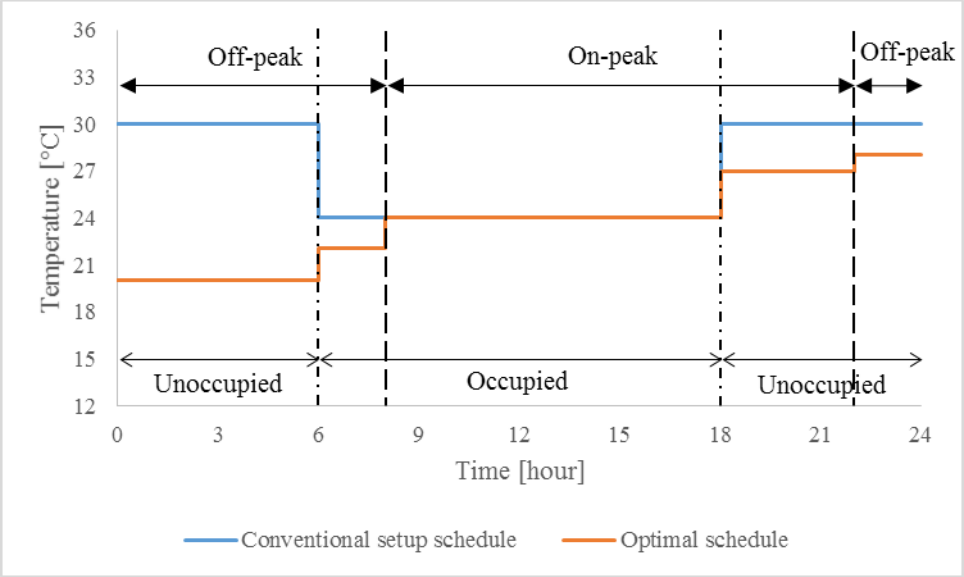

Figure 6.22: Set-point schedule of the ventilated slab system operation

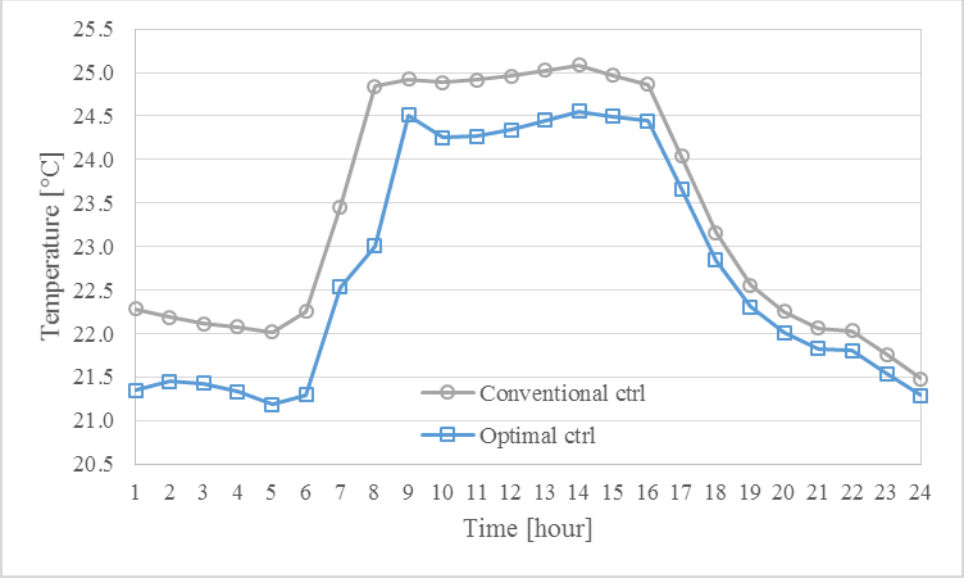

Figure 6.23: Hourly zone air temperature profiles

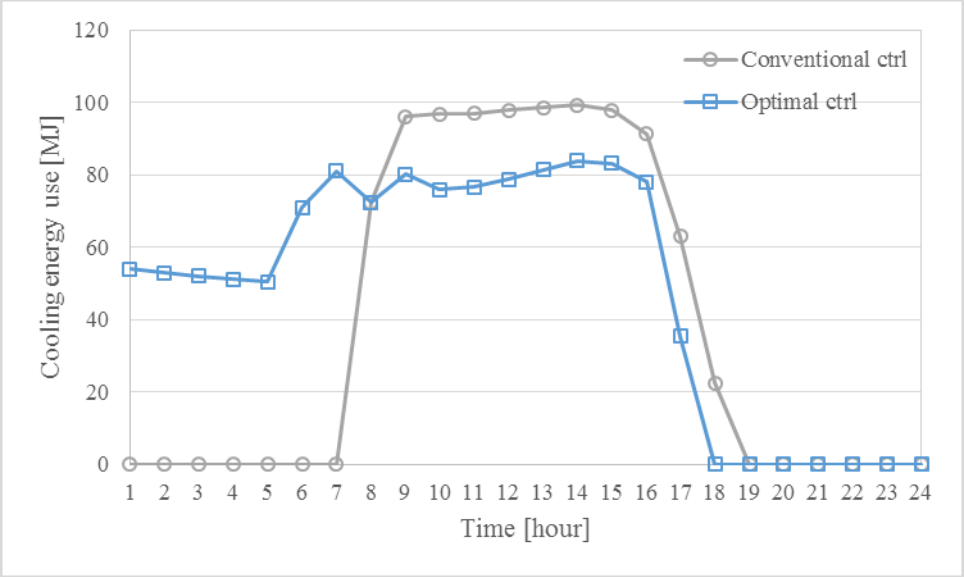

Figure 6.24: Hourly total cooling energy use profiles

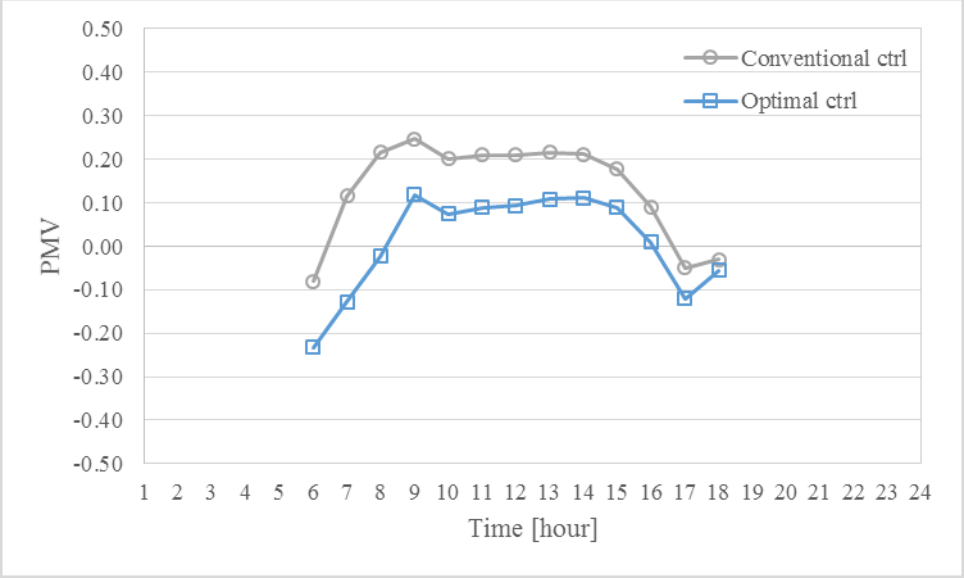

Figure 6.25: Hourly PMV profiles

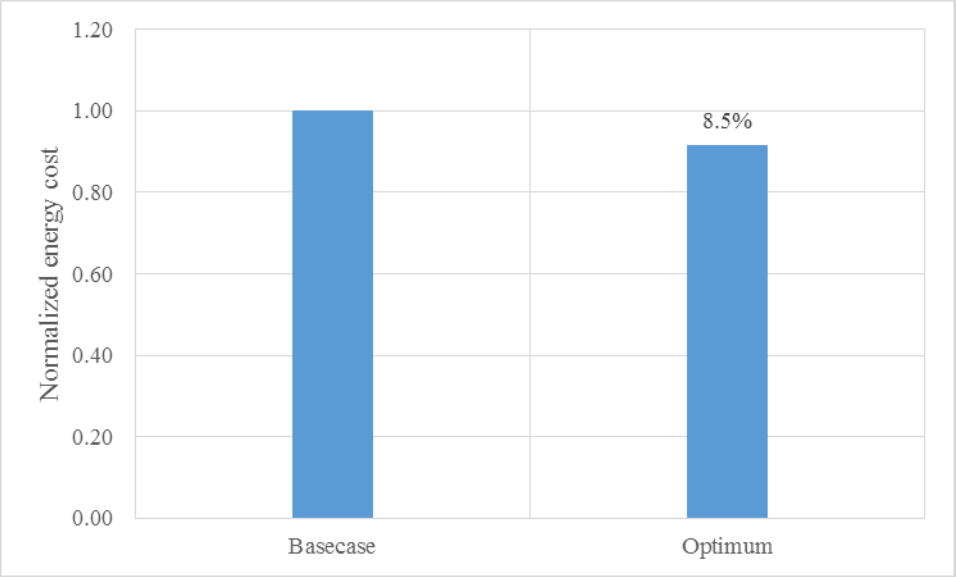

Figure 6.26: Comparison of normalized energy cost

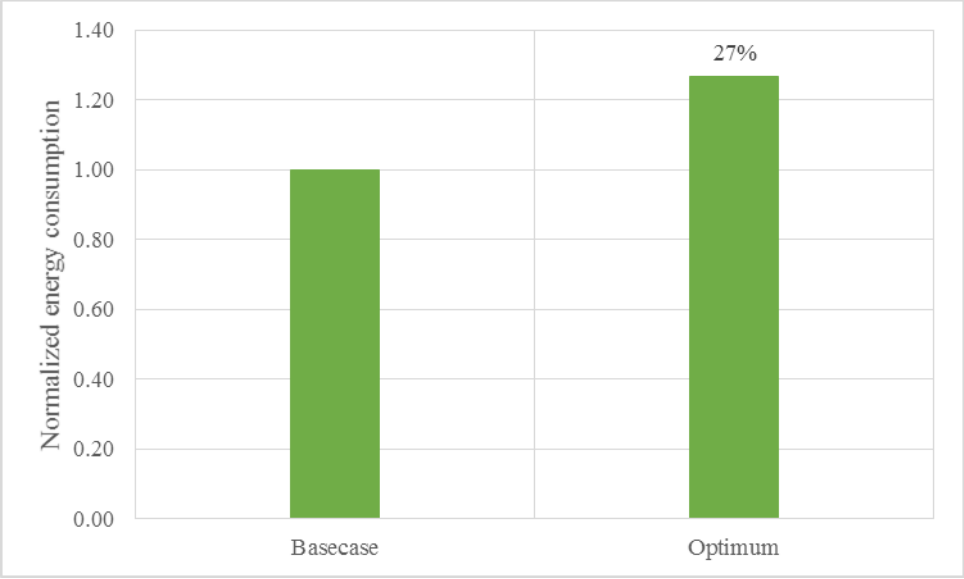

Figure 6.27: Comparison of normalized energy consumption

2. Impact of number of global zone set-point temperatures

In this section, the operating cost savings associated with each optimal control is explored. The control strategies are set up as follows:

- Basecase: 24°C for occupied period and 30°C for the unoccupied period (this represents the conventional setup schedule)
- 3 global zone set-point temperatures: One global but optimized zone set-point temperature for each occupancy period (occupied, unoccupied)
- 5 global zone set-point temperatures: One global and optimized zone set-point temperature for each combination of occupancy and utility rate periods over one day
- 12 global zone set-point temperatures: 2 hour basis optimal control
- 24 global zone set-point temperatures: Hourly basis optimal control

Note that the total operating cost (i.e., cost function) is the sum of energy charges, demand charges, and thermal comfort associated penalty cost. If the building is operated with a constant set-point temperature of 26°C which is relatively high set-point temperature, it will lead to the lowest energy cost consumption. However, this could also result in poor thermal comfort in the building and cost extra charge caused by thermal comfort penalty resulting in potential the highest total cost. For the analysis presented in this section, the building operated with a set-point temperature of 24°C during occupied period and 30°C during unoccupied period (in the case, no penalty cost associated with thermal comfort is generated) is considered as a basecase.

The total operation cost can be lowered by employing the optimal set-point schedule for 24 hour horizon. It is observed that more cost savings can be achieved by using finer set-point schedule discretization as shown in Figure 6.30. Figure 6.29 shows the hourly cooling energy use profiles for the different control strategies. The peak demand and energy use during on-peak period consistently reduced by a finer set-point schedule discretization. As expected, the most effective strategy is the hourly optimal control scheme reducing the total energy cost by 11.1% compared to the basecase.

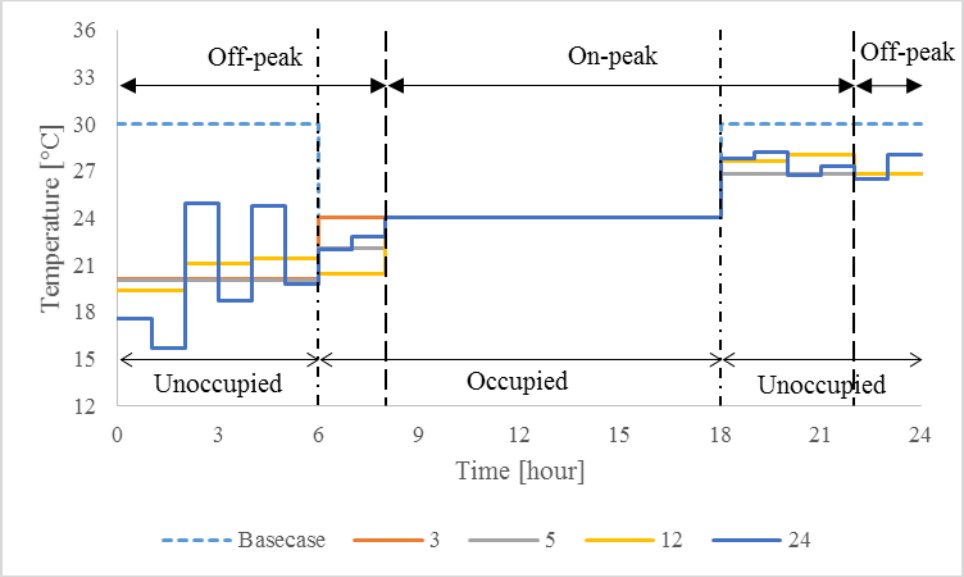

Figure 6.28: Set-point schedule of the ventilated slab system operation from GA

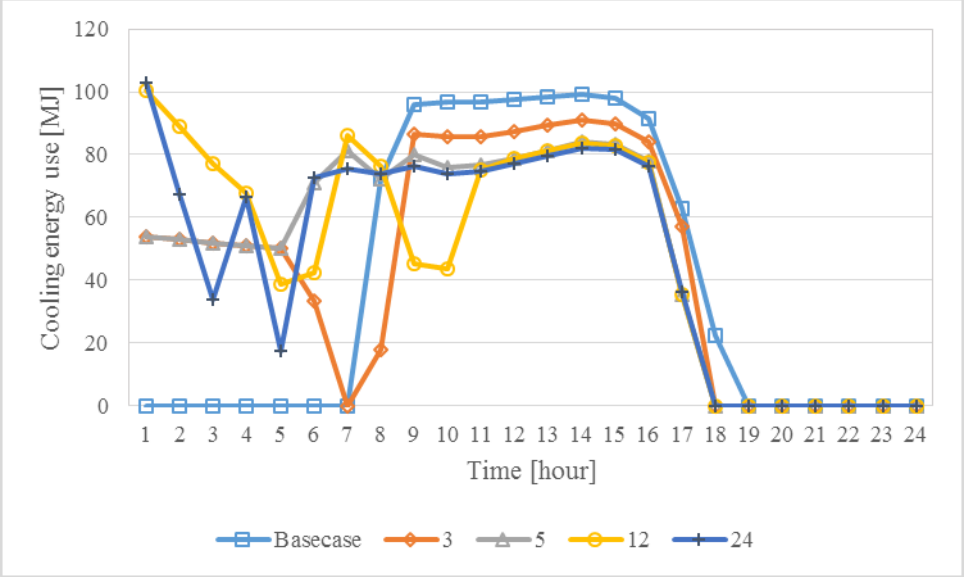

Figure 6.29: Hourly cooling energy use profiles

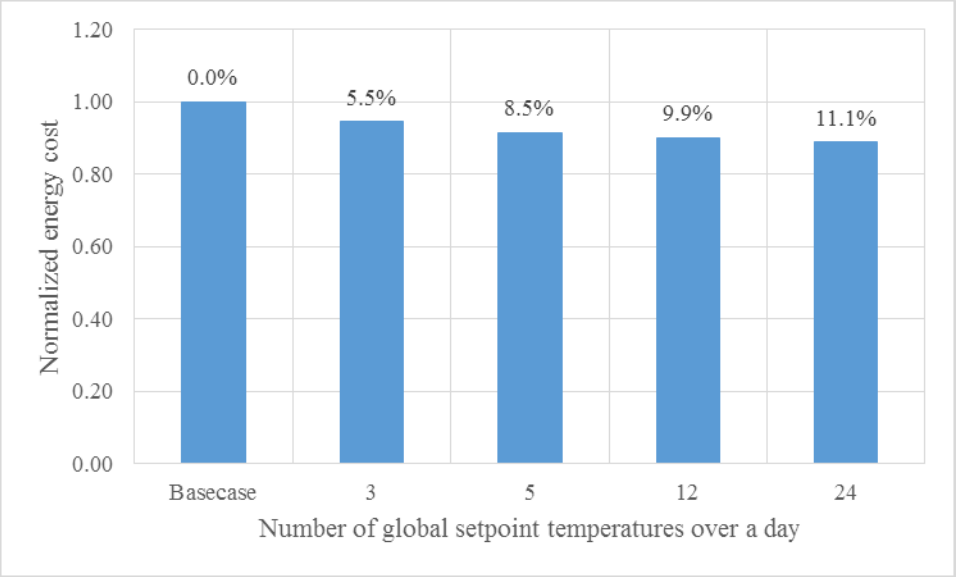

Figure 6.30: Comparison of savings potential of different control strategies

3. Impact of thickness of precast slab

For each thickness of the slab, the energy cost savings are estimated for all control strategies relative to the conventional control. Two strong utility rate structures are considered: $R_u = 4$ and $R_u = 10$. Figure 6.31 summarizes the impact of slab thickness for various control strategies. When there is strong incentive for demand shifting, precooling can save up to 19% for 0.25 meter thick slab as shown in Figure 6.31 (b).

These results are counterintuitive at first because the thickest slab is expected to offer the most savings. However, the slab thickness influences the level of slab thermal mass and also its time constant ($\tau = RC$). The main purpose of the heat sink (hollow core) inside the slab is to cool down its surfaces, but when the slab is too thick it is more difficult to transfer heat within the concrete to cool down the mass medium temperature as shown in Figure 6.32. Thus, the savings potential is more limited for buildings with thicker slab (i.e. 0.5 meter thick slab). The results are similar for all control strategies. A 0.25 meter thick slab offers the highest cost savings.

(a)

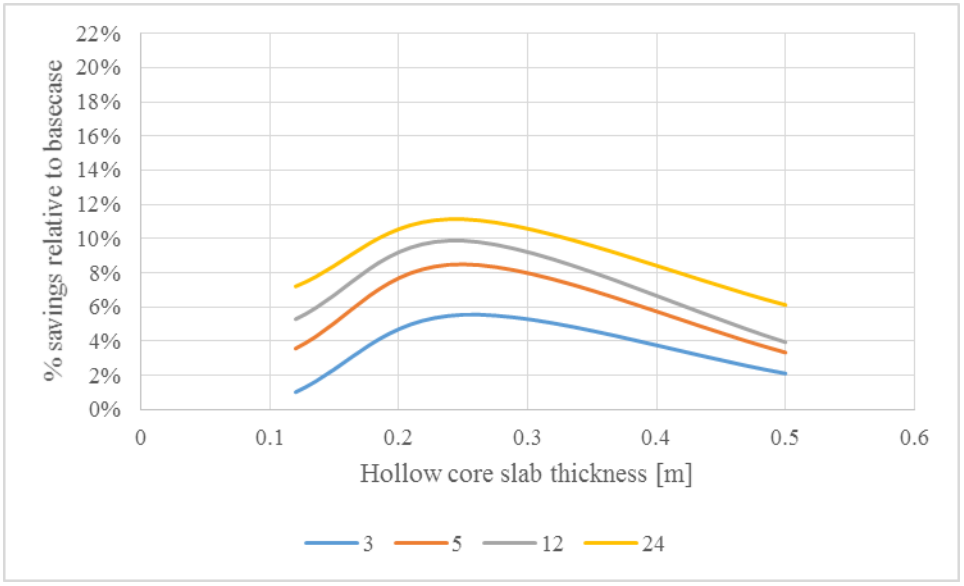

(b)

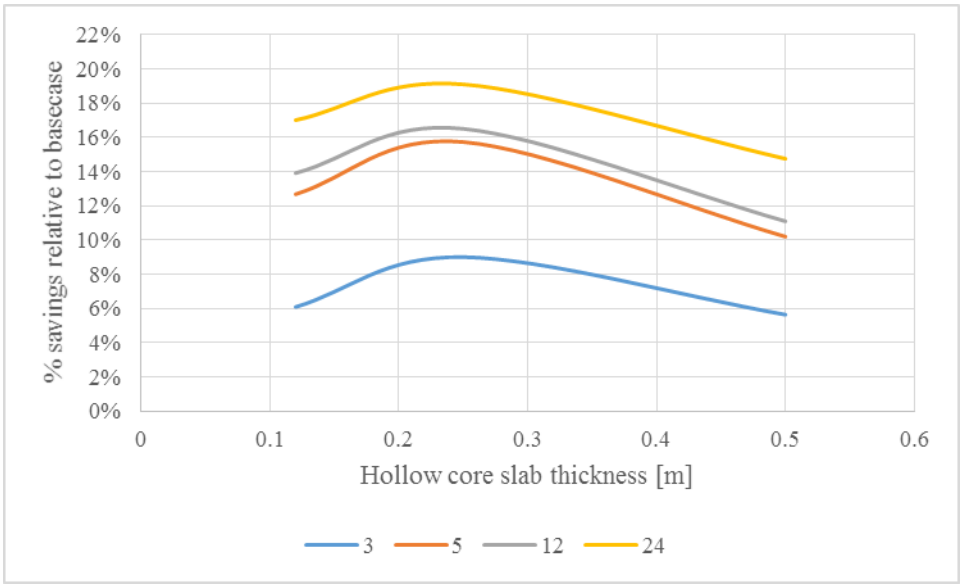

Figure 6.31: Percent energy cost savings of precooling vs. conventional control as a function of a hollow core slab thickness: (a) $R_u = 4$ and (b) $R_u = 10$

(a)

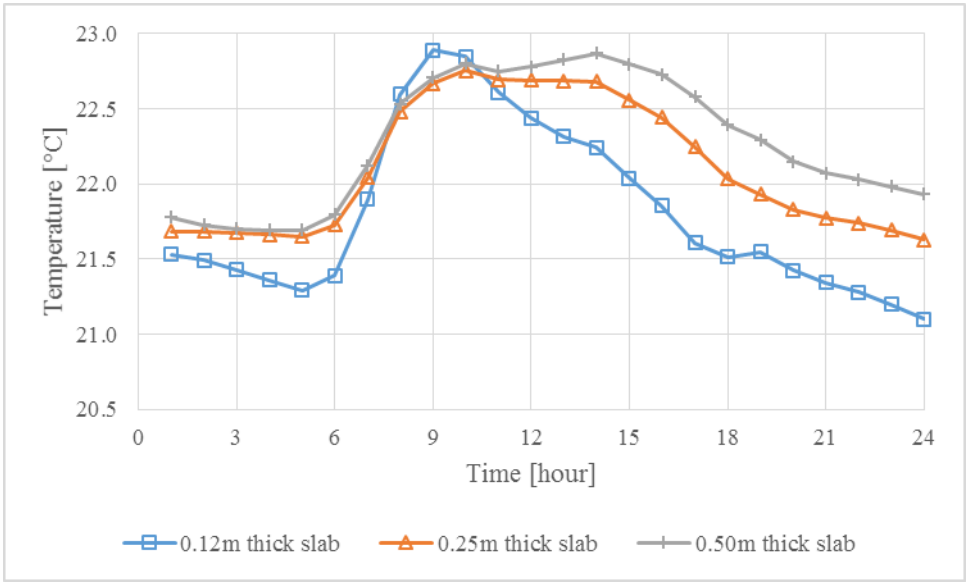

(b)

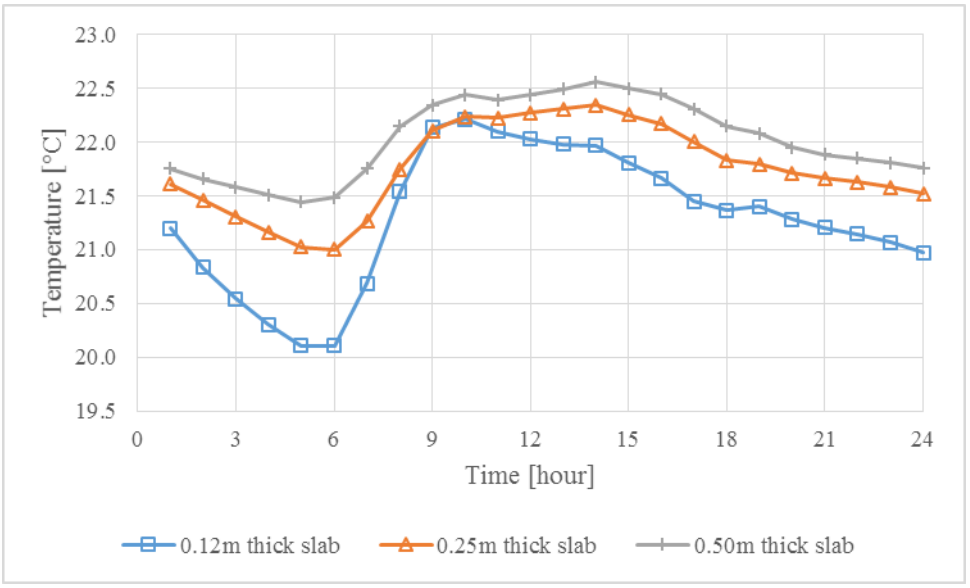

Figure 6.32: Comparison of ceiling/roof surface temperatures of different control strategies with various slab thickness: (a) conventional control and (b) precooling control

4. Impact of ratio of on-peak to off-peak charges

Figure 6.33 illustrates the effect of the ratio of on-peak to off-peak energy charges on the energy cost savings due to optimal precooling strategies. The results are presented for various thickness

of the slab: 0.12, 0.25, and 0.50 meter thick slab. The ratio of on-peak to off-peak is varied from 1 to 10, and it is applied to both energy and demand charges. For example, the ratio of 4 means that the energy charges and demand charges during the off-peak period are ¼ times smaller than those associated with the on-peak period.

If there are not sufficient levels of cost incentives to shift cooling load to the off-peak period (i.e. small ratio of on-peak to off-peak charges), there are no need for pre-cooling operation. Thus, energy cost savings relative to the basecase is 0 when the utility on-peak/off-peak ratio is 1 for all the slab thicknesses. Even a ratio of 2 is still too low to operate pre-cooling control strategy for 0.12 and 0.50 meter thick slabs. However and for a 0.25 meter thick slab, some energy cost savings start to be achieved through pre-cooling with a utility ratio of 2. To investigate the reason, the precooling set-point temperature, 21.4°C, obtained from the optimization simulation with 0.25 meter thick slab is virtually applied for 0.12 and 0.50 meter thick slab. It is observed that 0.12 meter thick slab does not require precooling because the ceiling surface temperature is already sufficiently low. Of course, precooling can lower the ceiling surface temperature but it requires much lower set-point temperature during the pre-cooling period. This would result in the increase of energy use compared to the conventional setup control strategy.

The same precooling strategy is not cost effective for the 0.50 meter thick slab. Indeed, the degree of ceiling temperature reduction achieved by precooling is found to be smaller compared to 0.25 meter thick slab as shown in Figure 6.34. As a result, precooling strategy could not effectively reduce peak and energy loads during the on-peak period as shown in Figure 6.35. A 0.50 meter thick slab may require much lower precooling set-point temperature to effectively decrease the ceiling surface temperature. However, lower pre-cooling set-point temperature requires more cooling energy consumption and utility ratio of 2 does not provides enough cost benefit to shift the building thermal load by precooling strategy.

As noted in Figure 6.30 Energy cost savings can be achieved by precooling strategy for all slab sizes when the utility on-peak/off-peak ratio is larger than 3.

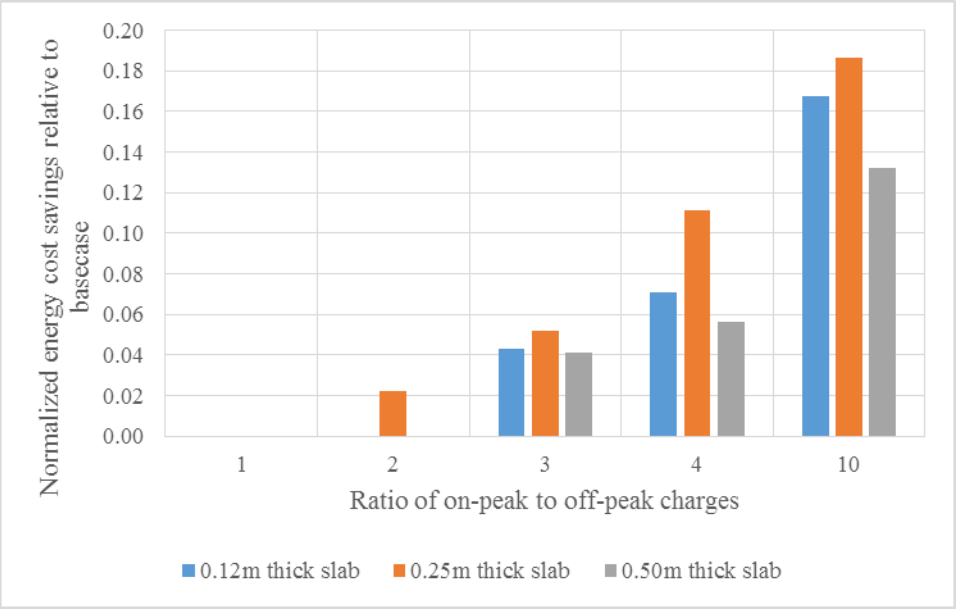

Figure 6.33: Comparison of savings potential of different utility structures with various slab thickness

(a)

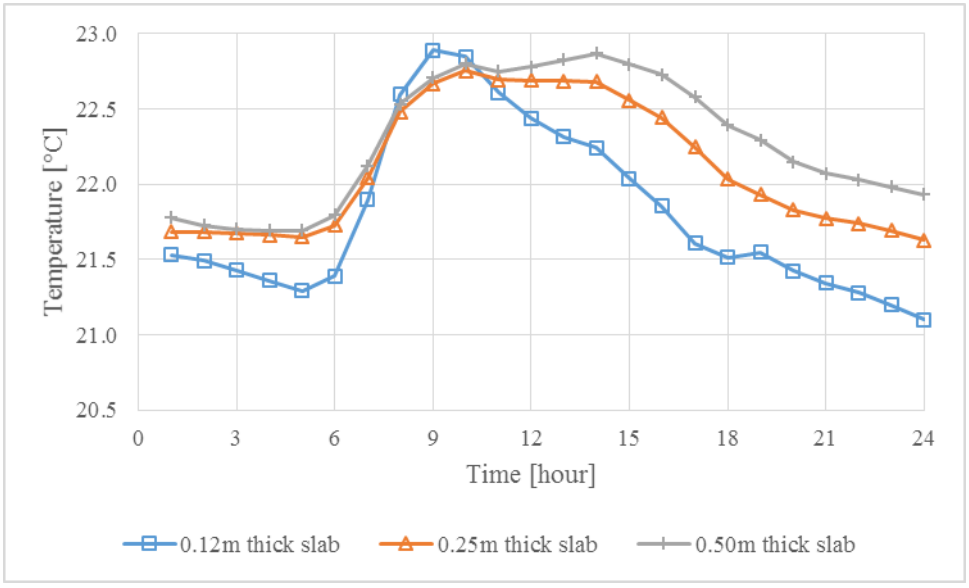

(b)

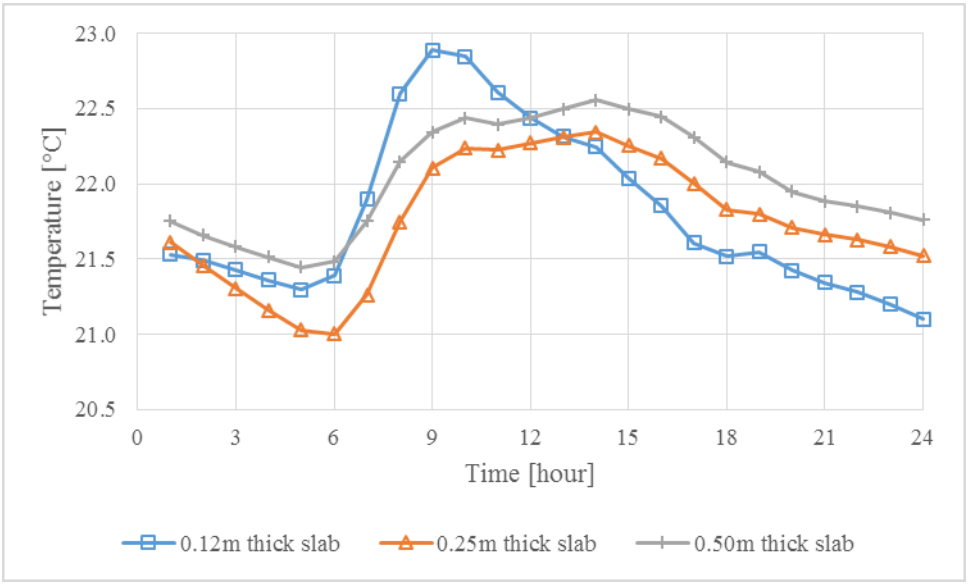

Figure 6.34: Comparison of ceiling/roof surface temperatures of different control strategies with various slab thickness: (a) conventional control and (b) forced precooling control (21.4°C)

(a)

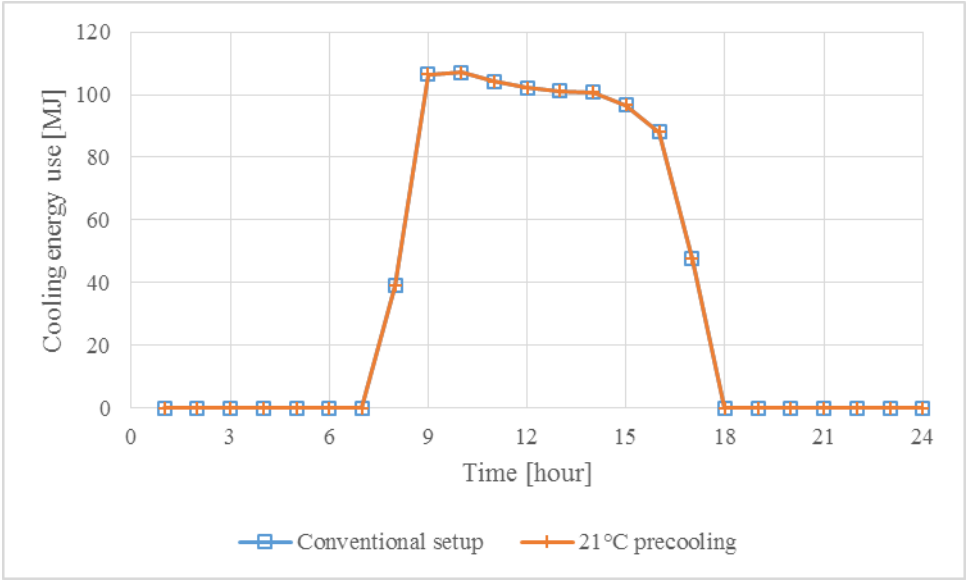
120
100
80
60
40
20
0
Cooling energy use [MJ]
0
3
6
9
12
15
18
21
24
Time [hour]
Conventional setup
21°C precooling

(b)

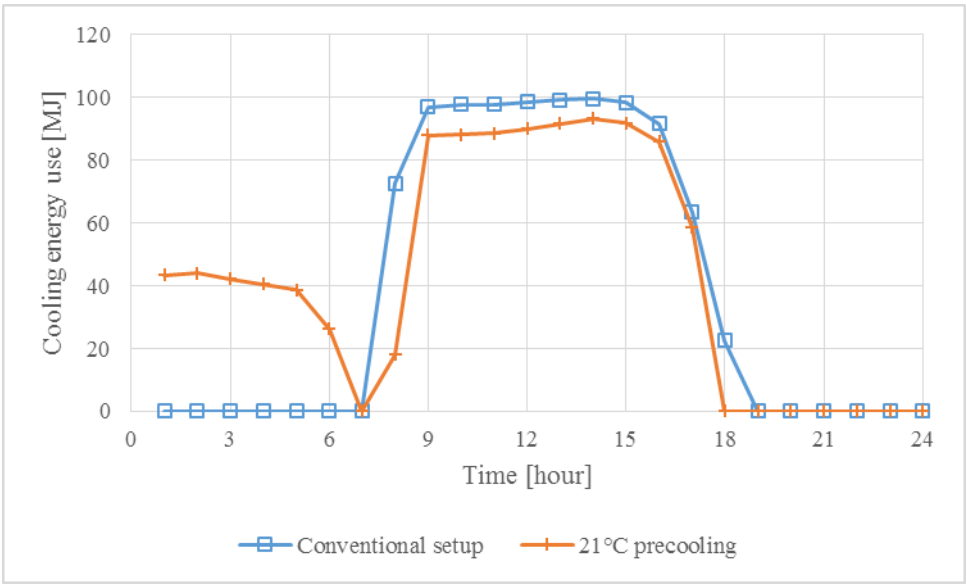
120
100
80
60
40
20
0
Cooling energy use [MJ]
0
3
6
9
12
15
18
21
24
Time [hour]
Conventional setup
21°C precooling

(c)

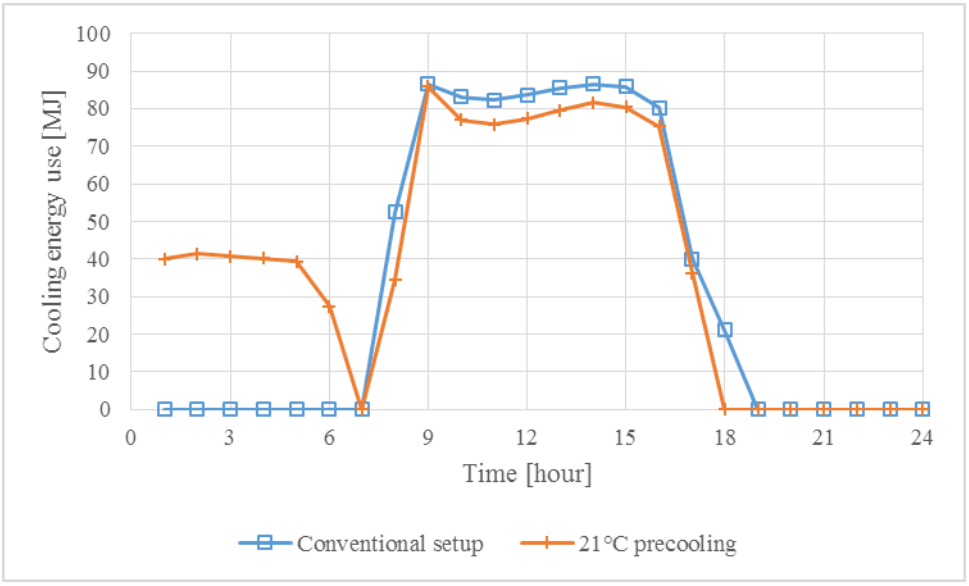

Figure 6.35: Comparison of hourly cooling energy use of different control strategies with various slab thickness: (a) 0.12m thick slab, (b) 0.25m thick slab, and (c) 0.50m thick slab

6.8 Summary and conclusions

The performance of select optimum control strategies of the hollow core ventilated slab is investigated in this chapter. For the analysis, Fanger's thermal comfort model is implemented in the simulation environment to calculate the predicted mean vote (PMV). The mean radiant temperature (MRT), estimated using the plane radiant method, is found to be one of the important variables needed to compute thermal comfort. The optimum control strategy is defined using a cost function that minimizes the energy cost with specific thermal comfort constraints. The optimal controls indicated that there is a good potential for achieving significant energy savings when ventilated slab to heat and cool commercial buildings.

Prior to establish the optimum controls, a simplified method to convert 2-D model to 1-D model for slab thermal analysis is developed. Indeed and while 2-D model can more accurately predict the energy consumption of the ventilated slab system compared to 1-D model, the computational effort for using 2-D modeling is significant when compared with the 1-D model especially for the optimization analysis. Using the conversion method, it is observed that the percent difference of energy consumption between 1-D and 2-D model for various floor sizes and utility ratios remains the same even after the optimization analysis. Specifically, it has been shown that the correlation between 1-D and 2-D model suitable before the optimization can be also applied to the optimization solution of 1-D model to estimate the optimization solution of 2-D model.

The results obtained from the Genetic algorithm of the Matlab Global Optimization toolbox are verified against brute-force simulation results. A series of sensitivity analyses for the optimum controls is performed to select proper type of cost penalty function, weighting factor for the cost penalty function, and the GA population size. Moreover, a series of parametric analyses using an

office building energy model is carried out to analyze the impact on the optimal solution of design and cost parameters including building thermal mass, utility structure, and floor area. Some of the main results of the parametric analyses are summarized:

- When compared to a conventional control strategy, the optimum control was found to always reduce energy costs throughout a 24-horizon while maintaining thermal comfort conditions within the acceptable range. Using hourly time step, the optimal control was able to reduce energy costs by 11.1% compared to the baseline control.

- The potential performance of the ventilated slab and any optimized control was found to depend on the thickness of the slab. A thick slab (i.e., 0.5 m) was found to require more energy to pre-cool and does not provide as much potential energy savings when a medium thick slab (i.e., 0.25 m) when optimal controls are utilized.

- It was found that sufficient cost incentive, through higher difference between on-peak to off-peak energy or demand charges, is needed in order for pre-cooling strategy can be effective in reducing energy costs for operating ventilated slabs.

CHAPTER 7: CONCLUSIONS AND FUTURE WORK

7.1 Summary and conclusions

The study presented in this thesis consists of a detailed thermal analysis of the hollow core ventilated slab system in multi-story building. In particular, the study investigated the thermal interactions between the ventilated slab system and the building indoor environment utilizing a newly developed comprehensive simulation environment that integrates an RC thermal network with FDM numerical model for the roof/floor slab. Several analyses have been carried out using the developed FDM numerical model as well as the integrated FDMRC simulation environment. Throughout the dissertation, the results of the analyses are provided and discussed. The main findings from the series of analyses conducted through the study summarized through this dissertation are briefly discussed in the following sections.

In Chapter 2, a numerical solution for a two-dimensional hollow core slabs heat transfer model is first developed. The predictions of the numerical solution for both the temperature distribution and heat flux along the slab surfaces are validated and analyzed. It is found that with the proper selection of the mesh size, a good agreement can be obtained between the numerical finite difference solution and the experimental data. Several parametric analyses are performed to determine the performance of ventilated slab systems under various design and operating conditions. In particular, the parametric analyses include the effects of convective coefficients inside the hollow cores, convective coefficients on the slab surfaces, supply air inlet temperatures, air mass flow rates, depths of the hollow cores, and core pitches. By varying the values of convective coefficient of the air that flows inside the hollow cores, it is found that a significant increase of average heat transfer rate along the slab surface can occur for the transition region from

laminar flow (Re<2300) to turbulent flow (Re>2300). For turbulent flow region, the average heat transfer rate slowly increases with diminishing returns as Reynolds number gets larger. The larger convective coefficient on the slab surface facilitates a heat transfer between a floor surface and zone air, but the effect gradually diminishes. It is observed that the average heat transfer rate along the slab surfaces more sensitively reacts to convective coefficient on the slab surface compared to convective coefficient inside the hollow cores. It is found that hollow core inlet air temperature greatly influences the performance of ventilated slab system. The average heat transfer rate on the upper surface of slab increases proportionally to the increase in supply air inlet temperature when heating is required. As the inlet air temperature increases, the average heat transfer rate on the slab surface rapidly decreases for cooling mode. As the air mass flow rate increases, slab heat transfer rate is increased, but the impact gradually reduces. When the air mass flow rate is larger than 1.0 kg/s, the total slab heat transfer rate is found to be not significantly affected by the mass flow rate in the heating mode. As the depth of embedded hollow core increases, the total slab heat transfer rate along the upper slab surface proportionally decreases, but the total slab heat transfer rate on lower slab surface increases. The effect of the depth of hollow core follows a diminishing return pattern with a gradually reduced impact. As the depth of embedded hollow core increases, the total slab heat transfer rates along the slab surfaces are found to be proportionally reduced. The effect of the depth of hollow core follows a diminishing return pattern with a gradually reduced impact. The contact area of heat source/sink has less impact on the heat transfer rates along the slab surfaces. As the contact area of core increases, the average heat transfer rates along the slab surfaces increases gradually until reaching asymptotic values. When the contact area is the same, the average heat transfer rate for the smaller core is slightly greater than when the core is large.

In Chapter 3, a three-dimensional numerical solution for a hollow core ventilated slab is developed. Using the developed solution, average values of heat transfer along the floor as a function of perimeter as well as of heat transfer per unit area as a function of A/P are evaluated and analyzed. It is observed that the heat flux could be fitted to the exponential curve with R^2 value greater than 0.99. In addition, when the heat source exist inside the floor the heat flux on the floor surface also lies on the exponential curve with R^2 greater than 0.99. The equivalent two-dimensional modeling approach for any three-dimensional floor is empirically verified by using curve fit analysis. In particular, it is verified that the A/P scaling correlation for two-dimensional model is effective to reflect the thermal behavior of the floor in three-dimensional floor model. Two-dimensional heat transfer from a rectangular slab corresponds to the three-dimensional, infinite aspect ratio case, there is an equivalent two-dimensional case for any three-dimensional rectangular floor.

In Chapter 4, a new simulation environment is developed for the ventilated slab systems in two-story buildings based on a two-dimensional numerical solution for roof/floor slab combined with an RC network model for the exterior walls and windows. The relationship between two- and three-dimensional models found in Chapter 3 is implemented into the new simulation environment. The predictions from the new simulation environment are validated with results obtained from EnergyPlus simulation for two-zone building located in Golden, CO and air-conditioned with a ventilated slab system. Then, the impact of thermal bridging effects on energy performance of a ventilated slab system is explored by comparing the thermal and energy performance of ventilated slab systems obtained from 1-D FDMRC to 2-D FDMRC. Two insulation placements are considered to evaluate the energy performance of a ventilated slab system: (a) insulation at inner surface and (b) insulation placed in the center of the wall.

It is found that 14% of heating energy consumption can be attributed to thermal bridging effects for the 16 meter wide uninsulated ventilated slabs in Golden, CO. Moreover, it is found that a ventilated slab system consumes 10% more cooling energy due to thermal bridging when no insulation is placed for the 16 meter wide slabs in Golden, CO. Moreover, it is observed that the relative percentage of energy losses increases as the width of the slab is reduced due to thermal bridge effect. When the insulation is placed in the center plane of the exterior wall, thermal bridging effect increases heating and cooling energy consumption of a 16 meter ventilated slab system by 9% and 8%, respectively. The relative percentage of energy losses due to thermal bridges is greatly increases as the width of the slab is reduced. However, the magnitude of the energy loss is smaller in comparison with the insulation placed at inner surface of the wall case. Moreover, the energy use obtained from 2-D FDMRC converges to energy use prediction of 1-D FDMRC much slower compared to the insulation placed at inner surface of the wall case because the heat losses still exist at the slab-wall joint.

For a representative winter period (Jan 15th to Jan 18th) and summer season (Aug 17th to 20th), it is observed that adding a slab edge insulation can significantly improve the energy efficiency of the ventilated slab system. Indeed, additional energy use caused by heat losses through wall-slab joint can be halved with R-5 vertical insulation relative to the case where the ventilated slab has no insulation. Furthermore, thermal bridging effects on the performance of the ventilated slab systems can be significant especially for small and un-insulated slabs, and should be considered in whole-building simulation analysis to assess the benefits of the ventilated systems compared to other more conventional air conditioning systems.

In Chapter 5, an effectiveness-NTU based method for the enthalpy heat exchanger model is developed to account for any potential loss or gain of moisture that may results due to water

condensation or evaporation. Such processes can occur when moist air flows through a heat exchanger. The developed enthalpy heat exchanger model is capable to compute the combined heat and mass released or absorbed from the air flowing inside the hollow cores. Two water condensation models are considered in the analysis conducted in this Chapter: simple and detailed calculation methods. It is found that the two methods provide the same results for water condensation and evaporation rates when forced convection is prevalent inside the hollow cores. However, the detailed model is found to be more accurate in estimating water condensation rate inside the hollow cores when the ventilated slab system is not operated (i.e. no forced air flow inside the hollow cores) as well as along the ceiling surface. It is shown that the calculation of water evaporation is essential to accurately assess the existence of condensate water inside a hollow core or along the ceiling surface. It is found that the simple and detailed calculation methods gave the same results for water condensation and evaporation rates since condensation is caused mainly by forced convection inside the hollow cores. Moreover and for the conditions used in the analysis performed in this Chapter, it was found that condensate water exists in hollow cores during less than 1.5 hour with very low risk of mold growth to occur inside hollow cores. In addition and for three typical hot and humid climates in the US (San Francisco, CA, Port Arthur, TX, and Miami, FL), it is observed that no water condensation is observed for an office building constructed with heavyweight precast concrete slabs. When the building is made up of lightweight ventilated slabs, it is noted that water condensation occurred only inside the hollow cores and only for Miami during just 2 hours for an entire year of analysis. Finally, it is observed that water condensation does not last more than 30 minutes and that the condensed water inside the hollow cores fully evaporates within 30 minutes. Thus, it is concluded that there is a very low probability of mold growth associated with ventilated slab systems.

In Chapter 6, the performance of optimum control strategies for the hollow core ventilated slab is investigated. In particular, Fanger's thermal comfort model is implemented in the simulation environment to estimate the predicted mean vote (PMV). In addition, the optimum control strategy is defined using a cost function that minimizes the energy cost with specific thermal comfort constraints. The results obtained using the optimal controls indicated that there is a good potential for achieving significant energy savings when ventilated slab to heat and cool commercial buildings. To expedite the optimization analysis, a simplified method to convert two-dimensional model to one-dimensional model for slab thermal analysis is developed. Using the conversion method, it is observed that the percent difference of energy consumption between one-dimensional and two-dimensional model for various floor sizes and utility ratios remains the same even after the optimization analysis. Specifically, it has been shown that the correlation between one-dimensional and two-dimensional model suitable before the optimization can be also applied to the optimization solution of one-dimensional model to estimate the optimization solution of two-dimensional model. As part of the analysis completed for Chapter 6, the results obtained from the Genetic algorithm of the Matlab Global Optimization toolbox are verified against brute-force simulation results. Moreover, a series of parametric analyses using an office building energy model is carried out to analyze the impact on the optimal solution of design and cost parameters including building thermal mass, utility structure, and floor area. Some of the main results of the parametric analyses are summarized below:

- When compared to a conventional control strategy, the optimum control was found to always reduce energy costs throughout a 24-horizon while maintaining thermal comfort conditions within the acceptable range. Using hourly time step, the optimal control was able to reduce energy costs by 11.1% compared to the baseline control.

- The potential performance of the ventilated slab and any optimized control was found to depend on the thickness of the slab. A thick slab (i.e., 0.5 m) was found to require more energy to pre-cool and does not provide as much potential energy savings when a medium thick slab (i.e., 0.25 m) when optimal controls are utilized.
- It was found that sufficient cost incentive, through higher difference between on-peak to off-peak energy or demand charges, is needed in order for pre-cooling strategy can be effective in reducing energy costs for operating ventilated slabs.

7.2 Future work

The study described in this dissertation has focused on the thermal analysis of the hollow core ventilated slabs. A number of modeling challenges have risen to extend the scope of this research work. Even though it is observed that percent differences of energy consumption between 1-D and 2-D model for various floor sizes (i.e. lengths and thickness) and utility ratios remain the same after optimization process. A linear correlation to account for various floor lengths has been developed but only one slab thickness is considered. Additional work is needed to develop regression correlations for slab floors with different thicknesses to convert 1-D to 2-D models.

Moreover, the integration of the developed simulation environment in EnergyPlus can be considered as part of the future work. However, the computational efforts associated with solving two-dimensional model within EnergyPlus would considerably increase. As an alternative to the full incorporation of two-dimensional hollow core ventilated slab model, the development of response factors suitable for modeling two- or three-dimensional heat transfer associated with core hollow slabs may reduce the runtime of EnergyPlus simulation.

Other recommendations for future development of the work described in this dissertation include

the following:

- Specific and details models for the mechanical equipment can be integrated in the simulation environment to accurately estimate the total electrical power consumptions associated with the zone conditioning.
- Weather prediction models should be implemented to apply the optimization controller to operate ventilated slab systems in actual buildings. The controller then would subject to the uncertainty of future boundary predictions. In case of non-deterministic model, closed-loop optimization (CLO) technique might provide more superior performance compared to consecutive time block optimization (CTBO) approach which is employed in this research.
- A life-cycle cost based analysis can be considered to compare between the costs effectiveness of various building and HVAC systems which actively utilize thermal mass as thermal storage systems (such as hollow core ventilated slabs and radiant slabs) and compared to the performance of conventional air-based HVAC systems.
- The implementation of other innovative building envelope systems can be combined with ventilated slab systems. Some of these systems include dynamic insulation materials (DIMs) and similar systems in which the thermal conductivities of wall assemblies are controllable and tunable, either due to applied electrical voltage to conducting polymers or other electrochromic materials (Park et al., 2015) as well as variable reflectivity coatings (VRCs) for building roofs (Park and Krarti, 2016).

The suggested work will lead to highly active and dynamic building envelope systems that would enhance the energy efficiency of the built environment under various weather conditions.

REFERENCE

Akander, J. (2000). *The ORC Method-Effective Modelling of Thermal Performance of Multilayer Building Components*. Kungl Tekniska Hogskolan.

Aldawi, F., Alam, F., Date, A., Alghamdi, M., & Aldhawi, F. (2013). A new house wall system for residential buildings. *Energy and Buildings*, *67*, 403–418. http://doi.org/10.1016/j.enbuild.2013.08.019

Allen, G., Kani, M., & Carpenter, S. (1984). Mechanically enchanced passive solar thermal storage. In *Proc. SESC1 '84, Calgary*.

Alshamrani, O. S., Galal, K., & Alkass, S. (2014). Integrated LCA–LEED sustainability assessment model for structure and envelope systems of school buildings. *Building and Environment*, *80*, 61–70. http://doi.org/10.1016/j.buildenv.2014.05.021

Andersson, J. (2001). *Multiobjective optimization in engineering design applications to fluid power systems*. LINKOPING STUDIES IN SCIENCE AND TECHNOLOGY.

Andersson, L. O., Bernander, K. G., Isfalt, E., & A.H., R. (1979). Storage of Heat and Coolth in Hollow-Core Slabs. Swedish Experience, and Application to Large, American-Style Buildings. In *2nd International Conference on Energy Use Management*. Los Angeles: Lawrence Berkeley National Laboratory.

Andresen, I., & Brandenuehl, M. J. (1992). HEAT STORAGE IN BUILDING THERMAL MASS : A PARAIVlETR C STUDY. *ASHRAE Transactions*, *8*(3), 910–918.

Arasteh, D., Kohler, C., & Griffith, B. (2009). *Modeling Windows in Energy Plus with Simple Performance Indices*.

Arnold, D. (1993). Within these walls. *Building Services Journal*, *15*(9), 28–9.

ASAConsulting. (2005). *Market Study: Thermal Energy Storage Air Conditioning Systems in*

Saudi Arabia.

ASAConsulting. (2006). Cool runnings. *MEP Middle East*. Retrieved from http://www.termodeck.com/Filer/pdf/cool_runnings_td_sep_2006_mep_middle_east_.pdf

ASHRAE. (2005). ASHRAE Handbook-Fundamentals. *ASHRAE Handbook-Fundamentals*.

Bahnfleth, W. P. (1989). *Three-Dimensional Modelling of Heat Transfer From Slab Floors*. Champaign, IL.

Balaras, C. A. (1996). The role of thermal mass on the cooling load of buildings. An overview of computational methods. *Energy and Buildings*, *24*(1), 1–10. http://doi.org/10.1016/0378-7788(95)00956-6

Balocco, C. (2002). A simple model to study ventilated facades energy performance. *Energy and Buildings*, *34*(5), 469–475. http://doi.org/10.1016/S0378-7788(01)00130-X

Barnaby, C. D., Nall, D. H., & Dean, E. D. (1980). Structural mass cooling in a commercial building using hollow core concrete plank. In *Proc. National Solar Conference*. Amherst, MA.

Barton, P., Beggs, C. B., & Sleigh, P. a. (2002). A theoretical study of the thermal performance of the TermoDeck hollow core slab system. *Applied Thermal Engineering*, *22*(13), 1485–1499. http://doi.org/10.1016/S1359-4311(02)00059-5

Baskin, E., & Ashrae, M. (2005). Evaluation of Hydronic Forced-Air and Radiant Siab Heating and Cooling Systems. *ASHRAE Transactions: Symposia*, 525–534.

Beaudin, M., Zareipour, H., & Schellenberg, A. (2012). Residential Energy Management Using a Moving Window Algorithm. In *2012 3rd IEEE PES Innovative Smart Grid Technologies Europe (ISGT Europe), Berlin* (pp. 1–8).

Becker, R. (1995). Computational Model for Analysis of Dynamic Thermal Performance of a Hybrid Slab-Collector System with Passive Discharge. *Solar Energy*, *55*(6), 419–433.

Beggs, C. B., & Moodley, K. (1997). *Facilities management of passively controlled buildings* (Vol. 15).

Blomberg, T. (1996). *Heat Conduction in Two and Three Dimensions-Computer Modelling of Building Physics Applications*.

Bolstad, W. M. (2004). *Introduction to Bayesian Statistics*. Hoboken, New Jersey: Wiley.

Borup, L., & Parkinson, A. (1992). Comparison of four non-derivative optimization methods on two problems containing heuristics and analytic knowledge. In *In Proceedings of the 18th Annual ASME Design Automation Conference* (pp. 137–143).

Box, M. J. (1965). A New Method of Constrained Optimization and a Comparison With Other Methods. *The Computer Journal*, *8*(1), 42–52. http://doi.org/10.1093/comjnl/8.1.42

Braham, G. D. (2000). Mechanical Ventilation and Fabric Thermal Storage. *Indoor and Built Environment*, *9*(2), 102–110. http://doi.org/10.1177/1420326X0000900206

Bratton, D., & Kennedy, J. (2007). Defining a Standard for Particle Swarm Optimization. *2007 IEEE Swarm Intelligence Symposium*, (Sis), 120–127. http://doi.org/10.1109/SIS.2007.368035

Braun, J., & Chaturvedi, N. (2002). An Inverse Gray-Box Model for Transient Building Load Prediction. *HVAC&R Research*, *8*(1), 73–99. http://doi.org/10.1080/10789669.2002.10391290

Braun, J. E. (n.d.). *Reducing Energy Costs and Peak Electrical Demand through Optimal Control of Building Thermal Storage*.

Braun, J. E. (2003). Load Control Using Building Thermal Mass. *Journal of Solar Energy Engineering*, *125*(3), 292. http://doi.org/10.1115/1.1592184

Braun, J. E., Montgomery, K. W., & Chaturvedi, N. (2013). Evaluating the Performance of Building Thermal Mass Control Strategies Evaluating the Performance of Building Thermal

Mass Control Strategies. *HVAC&R Research*, *7*(4), 37–41.

Breesch, H., Bossaer, a., & Janssens, a. (2005). Passive cooling in a low-energy office building. *Solar Energy*, *79*(6), 682–696. http://doi.org/10.1016/j.solener.2004.12.002

Burdick, A. (2011). Strategy Guideline : Accurate Heating and Cooling Load Calculations. DOE.

Byrne, S. J., & Ritschard, R. L. (n.d.). *A Parametric Analysis of Thermal Mass in Residential Buildings*.

CADDET. (1999). *Radiant Heating Panels Save Energy in Homes, Centre for the Analysis and Dissemination of Demonstrated Energy Technologies*.

Candanedo, J., & Athienitis, A. (2011). Predictive control of radiant floor heating and solar-source heat pump operation in a solar house. *HVAC&R Research*, *17*(3), 235–256. http://doi.org/10.1080/10789669.2011.568319

Cengel, Y. A., & Ghajar, A. J. (2001). *Fundamentals of thermal-fluid sciences*. New York: McGraw-Hill.

Chae, Y. T., & Strand, R. K. (2013). Modeling ventilated slab systems using a hollow core slab: Implementation in a whole building energy simulation program. *Energy and Buildings*, *57*, 165–175. http://doi.org/10.1016/j.enbuild.2012.10.036

Chen, Y., Athienitis, a. K., & Galal, K. (2010). Modeling, design and thermal performance of a BIPV/T system thermally coupled with a ventilated concrete slab in a low energy solar house: Part 1, BIPV/T system and house energy concept. *Solar Energy*, *84*(11), 1892–1907. http://doi.org/10.1016/j.solener.2010.06.013

Chen, Y., Athienitis, A., & Fazio, P. (2012). Modelling of High-performance Envelope and Façade Integrated Photovoltaic / Solar Thermal Systems for High-Latitude Applications. In *Proceedings of eSim 2012: The Canadian Conference on Building Simulation* (pp. 108–121). Montreal, Canada.

Chen, Y., & Athienitis, A. K. (2010). Thermal Performance and Charge Control Strategy of a Ventilated Concrete Slab (VCS). *ASHRAE Transactions*, *12*, 556–568.

Chen, Y., Athienitis, A. K., & Galal, K. E. (2006). Design and Simulation for a Solar House with Building Integrated Photovoltai-Thermal System and Thermal Storage.

Chen, Y., Athienitis, A. K., & Galal, K. E. (2013a). Frequency domain and finite difference modeling of ventilated concrete slabs and comparison with field measurements: Part 1, modeling methodology. *International Journal of Heat and Mass Transfer*, *66*, 948–956. http://doi.org/10.1016/j.ijheatmasstransfer.2013.05.076

Chen, Y., Athienitis, A. K., & Galal, K. E. (2013b). Frequency domain and finite difference modeling of ventilated concrete slabs and comparison with field measurements: Part 2. Application. *International Journal of Heat and Mass Transfer*, *66*, 957–966. http://doi.org/10.1016/j.ijheatmasstransfer.2013.07.086

Chen, Y., Galal, K. E., & Athienitis, A. K. (2014). Design and operation methodology for active building-integrated thermal energy storage systems. *Energy and Buildings*, *84*, 575–585. http://doi.org/10.1016/j.enbuild.2014.08.013

Cheng, H., Brandemuehl, M. J., Henze, G. P., Florita, A. R., & Felsmann, C. (2008). Evaluation of the Primary Factors Impacting the Optimal Control of Passive Thermal Storage. *ASHRAE Transactions*, *006*, 57–64.

Ciampi, M., Leccese, F., & Tuoni, G. (2003). Ventilated facades energy performance in summer cooling of buildings. *Solar Energy*, *75*(6), 491–502. http://doi.org/10.1016/j.solener.2003.09.010

Cohen, R., Bordass, W., & Leaman, A. (2007). Evaluations and Comparisons of the Achieved Energy and Environmental Performance of Two Library Buildings in England and Sweden. *ASHRAE Transactions*, *113*, 14–27.

Connor, a. M. (1999). Parameter Sizing for Fluid Power Circuits Using Taguchi Methods. *Journal of Engineering Design*, *10*(4), 377–390. http://doi.org/10.1080/095448299261263

Conroy, C., & Mumma, S. (2001). Ceiling radiant cooling panels as a viable distributed parallel sensible cooling technology integrated with dedicated outdoor air systems. *ASHRAE Transactions*, *107*, 578–585.

Corgnati, S. P., & Kindinis, A. (2007). Thermal mass activation by hollow core slab coupled with night ventilation to reduce summer cooling loads. *Building and Environment*, *42*(9), 3285–3297. http://doi.org/10.1016/j.buildenv.2006.08.018

Davies, M. G. (1982). Optimal RC networks for walls. *Applied Math. Modelling*, *6*(June), 403–404.

Delgado, J. M. P. Q., Barreira, E., Ramos, N. M. M., & Freitas, V. P. de. (2013). *Hygrothermal Numerical Simulation Tools Applied to Building Physics*. (A. Öchsner, H. Altenbach, & L. F. M. da Silva, Eds.). New York: Springer.

Déqué, F., Ollivier, F., & Roux, J. . (2001). Effect of 2D modelling of thermal bridges on the energy performance of buildings. *Energy and Buildings*, *33*(6), 583–587. http://doi.org/10.1016/S0378-7788(00)00128-6

Dewson, T., Day, B., & Irving, a. D. (1993). Least squares parameter estimation of a reduced order thermal model of an experimental building. *Building and Environment*, *28*(2), 127–137. http://doi.org/10.1016/0360-1323(93)90046-6

Diaz, N. F. (2009). *About the Use of Radiant Ceiling Simulation Models as Commissioning Tools*. University of Liege.

Djuric, N., & Novakovic, V. (2009). Review of possibilities and necessities for building lifetime commissioning. *Renewable and Sustainable Energy Reviews*, *13*(2), 486–492. http://doi.org/10.1016/j.rser.2007.11.007

DOE. (2011). *Buildings energy data book*. Retrieved from http://scholar.google.com/scholar?hl=en&btnG=Search&q=intitle:Buildings+Energy+Data+book#0

Dovrtel, K., & Medved, S. (2011). Weather-predicted control of building free cooling system. *Applied Energy*, *88*(9), 3088–3096. http://doi.org/10.1016/j.apenergy.2011.03.010

Ekrami, N., Kamel, R. S., & Fung, A. S. (2007). Effectiveness of a Ventilated Concrete Slab on an Air Source Heat Pump Performance in Cold Climate.

Engstrom, A., & Andersson, L.-O. (2005). Energy Storage in Concrete Slabs Reduce Energy Consumption and Peak Cooling Loads at no Increase in Capital Costs.

Evans, B. (1993). Underfloor heating and cooling. *Architects' Journal*, *198*(6), 40–1.

Evola, G., Margani, G., & Marletta, L. (2011). Energy and cost evaluation of thermal bridge correction in Mediterranean climate. *Energy and Buildings*, *43*(9), 2385–2393. http://doi.org/10.1016/j.enbuild.2011.05.028

Fanger, P. O. (1972). *Thermal Comfort*. New York: McGraw-Hill.

Fenwick, R., Bull, D., & Gardiner, D. (2010). *Assessment of hollow-core floors for Seismic performance*. Christchurch, New Zealand.

Field, J. (2001). Features-Main feature: School design-Top of the class Greenwich Millennium Village School could herald a new era in mixed-mode schools. *Building Services Journal*, *23*(2), 26–31.

Flores Larsen, S., Filippín, C., & Lesino, G. (2010). Transient simulation of a storage floor with a heating/cooling parallel pipe system. *Building Simulation*, *3*(2), 105–115. http://doi.org/10.1007/s12273-010-0307-6

Florides, G. ., Tassou, S. ., Kalogirou, S. ., & Wrobel, L. . (2002). Review of solar and low energy cooling technologies for buildings. *Renewable and Sustainable Energy Reviews*,

6(6), 557–572. http://doi.org/10.1016/S1364-0321(02)00016-3

Fuller, R. J., & Cheung, C. K. (2005). Performance of Ventilated Hollow Core Concrete Panel Systems in Australia. In *Proceedings of the 22nd Biennial Conference of the Concrete Institute of Australia* (pp. 1–6).

Fux, S. F., Benz, M. J., & Guzzella, L. (2011). Comparing Control-Oriented Thermal Models for a Passive Solar House. In *Proceedings of CISBAT 2011* (pp. 889–894). Lausanne, Switzerland.

Gandhidasan, P., & Ramamurthy, K. N. (1985). Thermal behaviour of hollow-cored concrete slabs. *Applied Energy*, *19*(1), 41–48. http://doi.org/10.1016/0306-2619(85)90038-8

Geetha, N. B., & Velraj, R. (2012). Passive cooling methods for energy efficient buildings with and without thermal energy storage – A review. *Energy Education Science and Technology Part A: Energy Science and Research*, *29*(2), 913–946.

Givoni, B. (1983). Convective nocturnal cooling. In *Proc. Second Int. Cong. Building Energy Management*. Ames, Iowa.

Givoni, B. (1984). Options and applications of passive cooling. *Energy and Buildings*, *7*.

Glover, F. (1989). Tabu Search - Part I. *ORSA Journal on Computing*, *1*(3), 190–206. http://doi.org/10.1287/ijoc.1.3.190

Godish, T., & Spengler, J. D. (1996). Relationships between ventilation and indoor air quality: a review. *Indoor Air*, *6*, 135–145.

Goldberg, D., & Holland, J. (1988). Genetic Algorithms and Machine Learning. *Machine Learning*, *3*, 95–99. http://doi.org/10.1023/A:1022602019183

Griego, D., Krarti, M., & Hernández-Guerrero, A. (2012). Optimization of energy efficiency and thermal comfort measures for residential buildings in Salamanca, Mexico. *Energy and Buildings*, *54*, 540–549. http://doi.org/10.1016/j.enbuild.2012.02.019

Guin, J. A. (1968). Modification of the complex method of constrained optimization. *The Computer Journal*, *10*(4), 416–417.

Gwerder, M., Lehmann, B., Tödtli, J., Dorer, V., & F., R. (2008). Control of thermally-activated building systems (TABS). *Applied Energy*, *85*(7), 565–581.

Haase, M., & Andresen, I. (2007). *Energy efficiency and comfort of concrete structures*. Trondheim, Norway.

Hagentoft, C. E. (2001). *Introduction to building physics*. Lund, Sweden: Studentlittleratur.

Hajela, P. (1999). Nongradient Methods in Multidisciplinary Design Optimization-Status and Potential. *Journal of Aircraft*, *36*(1), 255–265. http://doi.org/10.2514/2.2432

Hajiah, A., & Krarti, M. (2012a). Optimal control of building storage systems using both ice storage and thermal mass - Part I: Simulation environment. In *Energy Conversion and Management* (Vol. 64, pp. 499–508). http://doi.org/10.1016/j.enconman.2012.02.016

Hajiah, A., & Krarti, M. (2012b). Optimal controls of building storage systems using both ice storage and thermal mass - Part II: Parametric analysis. In *Energy Conversion and Management* (Vol. 64, pp. 509–515). http://doi.org/10.1016/j.enconman.2012.02.020

Hasnain, S. M. (1998a). Review on sustainable thermal energy storage technologies, Part I: heat storage materials and techniques. *Energy Conversion and Management*, *39*(11), 1127–1138. http://doi.org/10.1016/S0196-8904(98)00025-9

Hasnain, S. M. (1998b). Review on sustainable thermal energy storage technologies, Part II: cool thermal storage. *Energy Conversion and Management*, *39*(11), 1139–1153. http://doi.org/10.1016/S0196-8904(98)00024-7

Hassan, R., Cohanim, B., Weck, O. De, Venter, G., Associate, P., Systems, E., … Systems, E. (2004). A COMPARISON OF PARTICLE SWARM OPTIMIZATION AND THE GENETIC ALGORITHM. *American Institute of Aeronautics and Astronautics*, 1–13.

Henninger, R. H., & Witte, M. J. (2013). *EnergyPlus Testing with IEA BESTEST Mechanical Equipment & Control Strategies for a Chilled Water and a Hot Water System*. Washington, D.C.

Henze, G. P., Felsmann, C., Florita, A. R., Brandemuehl, M. J., Cheng, H., & Waters, C. E. (2008). Optimization of Building Thermal Mass Control in the Presence of Energy and Demand Charges. *ASHRAE Transactions*, *008*, 75–84.

Henze, G. P., Felsmann, C., & Knabe, G. (2004). Evaluation of optimal control for active and passive building thermal storage. *International Journal of Thermal Sciences*, *43*(2), 173–183. http://doi.org/10.1016/j.ijthermalsci.2003.06.001

Henze, G. P., & Krarti, M. (2003). *Predictive Optimal Control of Active and Passive Building Thermal Storage Inventory*.

Henze, G. P., Le, T. H., Florita, A. R., & Felsmann, C. (2007). Sensitivity Analysis of Optimal Building Thermal Mass Control. *Journal of Solar Energy Engineering*, *129*(4), 473. http://doi.org/10.1115/1.2770755

Henze, G. P., Pfafferott, J., Herkel, S., & Felsmann, C. (2007). Impact of adaptive comfort criteria and heat waves on optimal building thermal mass control. *Energy and Buildings*, *39*(2), 221–235. http://doi.org/10.1016/j.enbuild.2006.06.006

Hoffman, M. E., Gideon, M., Muller, K., & Katz, Y. (1984). Ventilation as a Means of Air-conditioning Power Saving in Reinforced Concrete Telephone-exchange Buildings-Analysis and Directions for Design. *Energy and Buildings*, *7*, 367–374.

Holland, J. H. (1975). *Adaptation in Natural and Artificial Systems*. *Ann Arbor MI University of Michigan Press* (Vol. Ann Arbor). http://doi.org/10.1137/1018105

Hottel, H. C., & Sarofim, A. F. (1967). *Radiative Transfer*. New York: McGraw-Hill.

Ihm, P., & Krarti, M. (2005). Optimal control strategies for heated radiant floor systems. In

ASHRAE Transactions (Vol. 111 PART 1, pp. 535–546).

Ihm, P., & Krarti, M. (2012). Design optimization of energy efficient residential buildings in Tunisia. *Building and Environment*, *58*, 81–90. http://doi.org/10.1016/j.buildenv.2012.06.012

Ihm, P., Nemri, A., & Krarti, M. (2009). Estimation of lighting energy savings from daylighting. *Building and Environment*, *44*, 509–514. http://doi.org/10.1016/j.buildenv.2008.04.016

Incropera, F. P., DeWitt, D. P., Bergman, T. L., & Lavine, A. S. (2007). *Fundamentals of Heat and Mass Transfer*. (F. P. Incropera & F. P. F. O. H. A. M. T. Incropera, Eds.)*Wiley* (Vol. 6th). John Wiley & Sons. http://doi.org/10.1016/j.applthermaleng.2011.03.022

Isanska-Cwiek, A. (2005). Experimental and CFD Research on the Thermal Performance of the Air Cooled Slab System. In *Ninth International IBPSA Conference* (pp. 443–450). Montreal, Canada.

Jansson, A. (1994). *Fluid Power System Design A Simulation Approach*. Linkoping University.

Kammerud, R., Ceballos, E., Curtis, B., Place, W., & Andersson, B. (1984). Ventilation cooling of residential buildings. *ASHRAE Transactions*, *90*(1B), 226–252.

Keeney, K., & Braun, J. (1996). A Simplified Method for Determining Optimal Cooling Control Strategies for Thermal Storage in Building Mass. *HVAC&R Research*, *2*(1), 59–78. http://doi.org/10.1080/10789669.1996.10391333

Kennett, S. (n.d.). Relocation, Relocation. *Building Services Journal*. Retrieved from http://www.termodeck.com/Filer/Building Services Journal - MET Office.pdf

Kennett, S. (2006). Surface treatment. *Building Services Journal*, *28*(12), 39–41.

Kintner-meyer, M., & Emery, A. F. (1995). Optimal control of an HVAC system using cold storage and building thermal capacitance. *Energy and Buildings*, *23*, 19–31.

Kirkpatrick, S. (1984). Optimization by simulated annealing: Quantitative studies. *Journal of*

Statistical Physics, *34*, 975–986. http://doi.org/10.1007/BF01009452

Krarti, M. (2003). An Overview of Artificial Intelligence-Based Methods for Building Energy Systems. *Journal of Solar Energy Engineering*. http://doi.org/10.1115/1.1592186

Krarti, M. (2008). Energy Efficient Systems and Strategies for Heating, Ventilating, and Air Conditioning (HVAC) of Buildings. *Journal of Green Building*. http://doi.org/10.3992/jgb.3.1.44

Kreith, F., Bohn, M., & Kirkpatrick, a. (1997). Principles of Heat Transfer. *Journal of Solar Energy Engineering*, *119*(2), 187. http://doi.org/10.1115/1.2887901

Krus, P., & Andersson, J. (2003). Optimizaing Optimization for Design Optimization. In *Proceedings of DETC'03 ASME 2003 Design Engineering Technical Conferences and Computers and Information in Engineering Conference* (pp. 1–10). Chicago, Illinois, USA.

Landau, L. D., & Lifshitz, E. M. (1987). *Fluid Mechanics*. (McGraw-Hill, Ed.)*Image Rochester NY* (Vol. 6). Pergamon Press. http://doi.org/10.1007/b138775

Laouadi, A. (2004a). Development of a radiant heating and cooling model for building energy simulation software. *Building and Environment*, *39*, 421–31.

Laouadi, A. (2004b). Development of a radiant heating and cooling model for building energy simulation software. *Building and Environment*, *39*(4), 421–431.

Lienhard, J. H. (2010). Heat Transfer. *Journal of Heat Transfer*, *82*(1), 198. http://doi.org/10.1115/1.3246887

Ma, P., Wang, L.-S., & Guo, N. (2013). Modeling of TABS-based thermally manageable buildings in Simulink. *Applied Energy*, *104*, 791–800. http://doi.org/10.1016/j.apenergy.2012.12.006

Marewo, G., & Henwood, D. (2006). A mathematical model for supplying air-cooling for a building using a packed bed. *Building Services*, *1*, 11–26.

Marinakis, V., Doukas, H., Karakosta, C., & Psarras, J. (2013). An integrated system for buildings' energy-efficient automation: Application in the tertiary sector. *Applied Energy*, *101*, 6–14. http://doi.org/10.1016/j.apenergy.2012.05.032

Mavromatidis, L. E., Bykalyuk, A., El Mankibi, M., Michel, P., & Santamouris, M. (2012). Numerical estimation of air gaps' influence on the insulating performance of multilayer thermal insulation. *Building and Environment*, *49*, 227–237. http://doi.org/10.1016/j.buildenv.2011.09.029

Mcgowan, A. G., & Desjarlais, A. O. (1997). Investigation of common thermal bridges in walls. *ASHRAE Transactions*, *103*, 509–517.

McQuiston, F. C., & Parker, J. D. (1982). *Heating, ventilating, and air conditioning: analysis and design*.

Mendell, M. J. (1993). Non-specific symptoms in office workers: a review and summary of the epidemiologic literature. *Indoor Air*, *3*, 227–236.

Menzies, D., & Bourbeau, J. (1997). Building related illnesses. *N. Eng. J. Med.*, *337*, 1524–1531.

Monette, M. (1984). Use of a composite concrete and steel floor system as a combination air storage medium/plenum for enhanced passive solar utilization. In *Proc. SESCI '84, Calgary*.

Mongeau, M., Karsenty, H., Rouzé, V., & Hiriart-Urruty, J. B. (2000). Comparison of public-domain software for black box global optimization. *Optimization Methods and Software*, *13*(3), 203–226. http://doi.org/10.1080/10556780008805783

Morgan, S., & Krarti, M. (2010). Field Testing of Optimal Controls of Passive and Active Thermal Storage. *ASHRAE Transactions*, *116*, 134–147.

Morris, F. B., Braun, J. E., & Treado, S. J. (1994). Experimental and simulated performance of optimal control of buliding thermal storage. *ASHRAE Transactions*, *100*(1), 402–414.

Mun, J., & Krarti, M. (2011). An ice rink floor thermal model suitable for whole-building energy simulation analysis. *Building and Environment*, *46*, 1087–1093. http://doi.org/10.1016/j.buildenv.2010.11.008

Nielsen, L. S. (2012). Building Intergrated System Design for Sustainable Heating and Cooling. *REHVA Journal*, 24–27.

Noguchi, M., Athienitis, A., Ayoub, J., & Berneche, B. (2008). Net Zero Energy Homes of the Future : A Case Study of the ÉcoTerra House in Canada. In *Renewable Energy Congress*. Glasgow, Scotland.

Omer, A. M. (2008a). Green energies and the environment. *Renewable and Sustainable Energy Reviews*, *12*(7), 1789–1821. http://doi.org/10.1016/j.rser.2006.05.009

Omer, A. M. (2008b). Renewable building energy systems and passive human comfort solutions. *Renewable and Sustainable Energy Reviews*, *12*(6), 1562–1587. http://doi.org/10.1016/j.rser.2006.07.010

Patankar, S. (1980). Numerical heat transfer and fluid flow. *Series in Coputational Methods in Mechanics and Thermal Sciences*.

Petersen, S., & Svendsen, S. (2011). Method for simulating predictive control of building systems operation in the early stages of building design. *Applied Energy*, *88*(12), 4597–4606. http://doi.org/10.1016/j.apenergy.2011.05.053

Pomianowski, M., Heiselberg, P., Jensen, R. L., & Johra, H. (2011). Numerical Analysis of Heat Storage and Heat Conductivity in the Concrete Hollow Core Deck Element. In *Proceeding of Building Simulation* (pp. 14–16). Sydney.

Rechenberg, I. (1973). *Evolution Strategy: Optimization of Technical systems by means of biological evolution*. Fromman-Holzboog, Stuttgart.

Ren, M. J. (1997). *Optimal Predictive Control of Thermal Storage in Hollow Core Ventilated*

Slab Systems. Loughborough University.

Ren, M. J., & Wright, J. A. (1970). *Predictive Optimal Control of Fabric Thermal Storage Systems*.

Ren, M. J., & Wright, J. A. (1998). A Ventilated Slab Thermal Storage System Model. *Building and Environment*, *1323*(97), 42–52.

Rijksen, D. O., Wisse, C. J., & van Schijndel, a. W. M. (2010). Reducing peak requirements for cooling by using thermally activated building systems. *Energy and Buildings*, *42*(3), 298–304. http://doi.org/10.1016/j.enbuild.2009.09.007

Rinaldi, N. (2009). *Thermal Mass, Night Cooling and Hollow Core Ventilation System as Energy Saving Strategies in Buildings*. KTH.

Rosenfeld, a., & Hafemeister, D. (1985). Energy conservation in large buildings. In *Proceedings of AIP Conference* (Vol. 135, pp. 148–168). Aip. http://doi.org/10.1063/1.35453

Russell, M. ., & Surendran, P. . (2001). Influence of active heat sinks on fabric thermal storage in building mass. *Applied Energy*, *70*(1), 17–33. http://doi.org/10.1016/S0306-2619(01)00023-X

Sanjuan, C., Suárez, M. J., González, M., Pistono, J., & Blanco, E. (2011). Energy performance of an open-joint ventilated façade compared with a conventional sealed cavity façade. *Solar Energy*, *85*(9), 1851–1863. http://doi.org/10.1016/j.solener.2011.04.028

Scarpa, M., Grau, K., & Olesen, B. W. (2009). Development and Validation of a Versatile Method for the Calculation of Heat Transfer in Water-Based Radiant Systems. In *Eleventh International IBPSA Conference* (pp. 688–695). Glasgow, Scotland: Building Simulation.

Schmidt, D. (2002). Approach for Modelling of Hybrid Heating and Cooling Components with Optimised RC Networks. *Nordic Journal of Building Physics*, *3*.

Schmidt, D. (2004). *Methodology for the Modelling of Thermally Activated Building Components in Low Exergy Design*. Kungliga Tekniska Hogskolan.

Seem, J. E. (1987). *Modeling of Heat Transfer in Buildings*. University of Wisconsin-Madison.

Seppänen, O. A., Fisk, W. J., & Mendell, M. J. (1999). Association of ventilation rates and CO2 concentrations with health and other responses in commercial and institutional buildings. *Indoor Air*, *9*, 226–252.

Sharp, T., & Ridge, O. (1995). Energy Benchmarking In Commercial Office Buildings.

Shaviv, E. (1989). The influence of the thermal mass on the thermal performance of buildings in summer and winter. *Science and Technology at the Service of Architecture*, 470–2.

Shaw, M. R., Treadaway, K. W., & Willis, S. T. P. (1994). Effective use of building mass. *Renewable Energy*, *5*, 1028–1038.

Shi, Y., & Eberhart, R. C. (1999). Empirical study of particle swarm optimization. *Proceedings of the 1999 Congress on Evolutionary Computation-CEC99*, 1945–1950. http://doi.org/10.1109/CEC.1999.785511

Simonson, C. J. (1998). *Heat and Moisture Transfer in Energy Wheels*. University of Saskatchewan.

Široký, J., Oldewurtel, F., Cigler, J., & Prívara, S. (2011). Experimental analysis of model predictive control for an energy efficient building heating system. *Applied Energy*, *88*(9), 3079–3087. http://doi.org/10.1016/j.apenergy.2011.03.009

Song, Y., Akashi, Y., & Yee, J.-J. (2008). A development of easy-to-use tool for fault detection and diagnosis in building air-conditioning systems. *Energy and Buildings*, *40*(2), 71–82. http://doi.org/10.1016/j.enbuild.2007.01.011

Sormunen, P., Laine, T., Laine, J., & Saari, M. (2007). The Active Utilisation of Thermal Mass of Hollow-Core Slabs. In *Proceedings of Clima 2007 WellBeing Indoors*.

Sourbron, M., Khaldi, F., Baelmans, M., & Helsen, L. (n.d.). *Validation of a thermally activated hollow core slab RC-model with measurements and FEM simulations* (Vol. 1).

Spendley, W. G. R. F. R., Hext, G. R., & Himsworth, F. R. (1962). Sequential application of simplex designs in optimisation and evolutionary operation. *Technometrics*, *4*(4), 441–461.

Standeven, M., Cohen, R., Bordass, B., & Leaman, A. (1998). PROBE 14: Elizabeth fry building. *Building Services Journal*, *20*, 37–42.

Stefano, S., Fred, B., Brad, T., & Julian, R. (2012). *Temperature stratification and air change effectiveness in a high cooling load office with two heat source heights in a combined chilled ceiling and displacement ventilation system*. *UC Berkeley*. Retrieved from https://escholarship.org/uc/item/58m8302p

Stetui, C. (1998). *Radiant Cooling in US Office Buildings: Towards Eliminating the Perception Climate Imposed Barriers*.

Stoecker, W. F. (1968). *Principles for air conditioning practice*. Industrial Press.

Strand, R. K., & Baumgartner, K. T. (2005). Modeling radiant heating and cooling systems: integration with a whole-building simulation program. *Energy and Buildings*, *37*(4), 389–397. http://doi.org/10.1016/j.enbuild.2004.07.009

Strang, G. (2006). *The Heat Equation and Convection-Diffusion*. MIT OpenCourseWare.

Sundell, J., Levin, H., Nazaroff, W. W., Cain, W. S., Fisk, W. J., Grimsrud, D. T., & Samet, J. M. (2011). Ventilation rates and health: multidisciplinary review of the scientific literature. *Indoor Air*, *21*(3), 191–204.

Tabares-Velasco, P. C., Christensen, C., Bianchi, M., & Booten, C. (2012). *Verification and Validation of EnergyPlus Conduction Finite Difference and Phase Change Material Models for Opaque Wall Assemblies*. Retrieved from papers3://publication/uuid/A97519FD-3B09-4348-958E-D0183A707A54

Taylor, B. J., Cawthorne, D. a., & Imbabi, M. S. (1996). Analytical investigation of the steady-state behaviour of dynamic and diffusive building envelopes. *Building and Environment*, *31*(6), 519–525. http://doi.org/10.1016/0360-1323(96)00022-4

Taylor, B. J., & Imbabit, M. S. (1997). The Effect of Air Film Thermal Resistance on the Behaviour of Dynamic Insulation. *Building and Environment*, *32*(5), 397–404.

Theodosiou, T. G., & Papadopoulos, a. M. (2008). The impact of thermal bridges on the energy demand of buildings with double brick wall constructions. *Energy and Buildings*, *40*(11), 2083–2089. http://doi.org/10.1016/j.enbuild.2008.06.006

Tuhus-Dubrow, D., & Krarti, M. (2010). Genetic-algorithm based approach to optimize building envelope design for residential buildings. *Building and Environment*, *45*, 1574–1581. http://doi.org/10.1016/j.buildenv.2010.01.005

Turner, C. H., & Tovey, N. K. (2006). Case Study on the Energy Performance of the Zuckerman Institute for Connective Environmental Research (ZICER) Building. *ASHRAE Transactions*, *112*, 320–329.

UIUC, & LBNL. (2013). EnergyPlus Engineering Reference: the reference to EnergyPlus calculations. US Department of Energy.

Underwood, C. P. (2004). *Modelling Methods for Energy in Buildings*. (C. P. Underwood & F. W. H. Yik, Eds.). Oxford, UK: Blackwell Publishing Ltd. http://doi.org/10.1002/9780470758533

Walton, G. N. (1983). *Thermal Analysis Research Program Reference Manual*.

Wang, S., & Xu, X. (2006). Parameter estimation of internal thermal mass of building dynamic models using genetic algorithm. *Energy Conversion and Management*, *47*(13-14), 1927–1941. http://doi.org/10.1016/j.enconman.2005.09.011

Wargocki, P., Sundell, J., Bischof, W., Brundrett, G., Fanger, P. O., Gyntelberg, F., … Wouters,

P. (2002). Ventilation and health in non-industrial indoor environments: report from a European Multidisciplinary Scientific Consensus Meeting (EUROVEN). *Indoor Air*, *12*, 113–128.

Watson, R. D., & K.S., C. (2002). *Radiant Heating & Cooling Handbook*. New York: McGraw-Hill.

Weber, T., & Jóhannesson, G. (2005). An optimized RC-network for thermally activated building components. *Building and Environment*, *40*(1), 1–14. http://doi.org/10.1016/j.buildenv.2004.04.012

Weber, T., Jóhannesson, G., Koschenz, M., Lehmann, B., & Baumgartner, T. (2005). Validation of a FEM-program (frequency-domain) and a simplified RC-model (time-domain) for thermally activated building component systems (TABS) using measurement data. *Energy and Buildings*, *37*(7), 707–724. http://doi.org/10.1016/j.enbuild.2004.10.005

Wilcox, S., & Marion, W. (2008). *Users Manual for TMY3 Data Sets*.

Willis, S., & Wilkins, J. (1993). Mass appeal.pdf. *Building Services*, *15*(1), 25–7.

Winwood, R., Benstead, R., & Edwards, R. (1997a). Advanced fabric energy storage I: Review. *Building Services Engineering Research and Technology*, *18*(1), 1–6. http://doi.org/10.1177/014362449701800101

Winwood, R., Benstead, R., & Edwards, R. (1997b). Advanced fabric energy storage II: Computational fluid dynamics modelling. *Building Services Engineering Research and Technology*, *18*(1), 7–16. http://doi.org/10.1177/014362449701800102

Winwood, R., Benstead, R., & Edwards, R. (1997c). Advanced fabric energy storage III: Theoretical analysis and whole-building simulation. *Building Services Engineering Research and Technology*, *18*(1), 17–24. http://doi.org/10.1177/014362449701800103

Winwood, R., Benstead, R., & Edwards, R. (1997d). Advanced fabric energy storage IV:

Experimental monitoring. *Building Services Engineering Research and Technology*, *18*(1), 25–30. http://doi.org/10.1177/014362449701800104

Winwood, R., Benstead, R., Edwards, R., & Letherman, K. M. (1994). Building fabric thermal storage: Use of computational fluid dynamics for modelling. *Building Services Engineering Research and Technology*, *15*(3), 171–178. http://doi.org/10.1177/014362449401500308

Wright, J. a., Loosemore, H. a., & Farmani, R. (2002). Optimization of building thermal design and control by multi-criterion genetic algorithm. *Energy and Buildings*, *34*(9), 959–972. http://doi.org/10.1016/S0378-7788(02)00071-3

Wright, J., Farmani, R., & Engineering, B. (2001). The Simultaneous Optimization of Building Fabric Construction, HVAC System Size, and the Plant Control Strategy. In *Seventh International IBPSA Conference* (pp. 865–872).

Xu, P., Haves, P., Piette, M. A., Braun, J., & Hope, L. ten. (2004). Peak Demand Reduction from Pre-Cooling with Zone Temperature Reset in an Office Building. In *Proceedings of ACEEE 2004 Summer Study on Energy Efficiency in Buildings*. Pacific Grove, CA: Lawrence Berkeley National Laboratory.

Xu, X., Yu, J., Wang, S., & Wang, J. (2014). Research and application of active hollow core slabs in building systems for utilizing low energy sources. *Applied Energy*, *116*, 424–435. http://doi.org/10.1016/j.apenergy.2013.09.064

Yazdanian, M., & Klems, J. H. (1994). Measurement of the Exterior Convective Film Coefficient for Windows in Low-Rise Buildings. *ASHRAE Transactions*, *100*.

Zaheer-uddin, M., & Cho, S. H. (1999). An Experimental Study of Multiple Parameter Switching Control for Radiant Floor Heating Systems. *International Journal of Energy Research*, *24*, 433–444.

Zhai, H., Dai, Y. J., Wu, J. Y., & Wang, R. Z. (2009). Energy and exergy analyses on a novel

hybrid solar heating, cooling and power generation system for remote areas. *Applied Energy*, *86*(9), 1395–1404.

Zhai, Z., Johnson, M. H., & Krarti, M. (2011). Assessment of natural and hybrid ventilation models in whole-building energy simulations. *Energy and Buildings*, *43*, 2251–2261. http://doi.org/10.1016/j.enbuild.2011.06.026

Zhang, L. Z., & Niu, J. L. (2002). Effectiveness Correlations for Heat and Moisture Transfer Processes in an Enthalpy Exchanger With Membrane Cores. *Journal of Heat Transfer*, *124*(5), 922. http://doi.org/10.1115/1.1469524

Zhang, Z. L., & Wachenfeldt, B. J. (2009). Numerical study on the heat storing capacity of concrete walls with air cavities. *Energy and Buildings*, *41*(7), 769–773. http://doi.org/10.1016/j.enbuild.2009.02.012

Zmeureanu, R., & Fazio, P. (1988). Thermal performance of a hollow core concrete floor system for passive cooling. *Building and Environment*, *23*(3), 243–252. http://doi.org/10.1016/0360-1323(88)90009-1

Zukowski, M. (2005). Heat transfer and pressure drop characteristics of the underfloor air distribution system. *Energy and Buildings*, *37*(8), 890–896. http://doi.org/10.1016/j.enbuild.2004.11.012

Zukowski, M. (2006). Modeling and designing heating and ventilation system with underfloor air distribution. *Energy and Buildings*, *38*(6), 600–609. http://doi.org/10.1016/j.enbuild.2005.08.015

APPENDIX A

LEED Building Energy Model

Krarti and Park (2012) assessed the energy performance of the hollow core ventilated slab system that is proposed for the 3-story office building located in Kochi, India. The climate of Kochi is very hot and humid. Two energy models, LEED baseline model and proposed design model with the ventilated slab system, of 3-story office building is created by using EnergyPlus. Fig A.1 is 3-D view of the office building. The gross floor area of the building is 174.2 m^2, and each floor has one thermal zone. The peak lighting power density is 10.38 W/m^2. The building is occupied from 9 a.m. to 7 p.m. and the peak occupancy density is 21.5 m^2/person. The HVAC systems operate during occupied period. Heating and cooling set-point temperatures are 20°C and 24°C, respectively and set-back/set-up temperature is applied from 8 p.m. to 8 a.m., non-occupied hours.

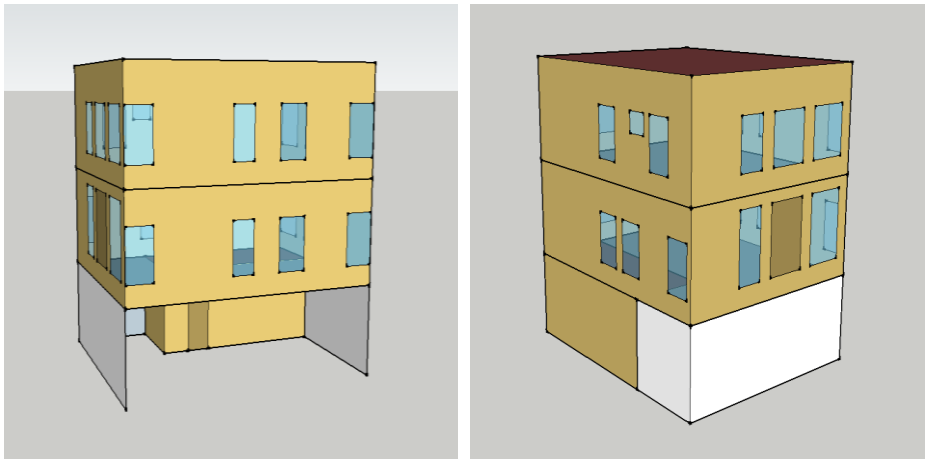

Fig A.1: 3-D view of 3-story office building model in Kochi, India

The building energy models with two HVAC alternatives are considered as follow:

- The LEED baseline building energy model is created in accordance with ASHRAE standard 90.1-2007 Appendix G for small office building. Packaged rooftop air conditioner with direct expansion cooling coil and furnace (System 3) is chosen for the LEED baseline building energy model.

- Proposed building energy model include the hollow core ventilated slab system. Specifically, the ceilings of the ground floor and the first floor are built with hollow core slabs to meet air conditioning requirements using rooftop units. The air inlet temperature to the hollow core slab is controlled from 10℃ to 15℃ based on the room condition. Nighttime precooling control strategy is not considered because the outdoor air temperature is not cool enough to utilize.

One of the major advantages of the ventilated slab is its ability of using the thermal storage capacity of the slab to cool the building. However, the same thermal mass of the slab leads to larger swing of the indoor air temperatures within various thermal zones of the building. Fig A.2 (a) presents the hourly variations of the outdoor dry bulb temperature and the mean air temperature temperatures within the second floor of the office building during two summer days (July 20th and July 21st) for the three building energy models. The higher temperature swing associated with the ventilated slab system can be maintained using appropriate control strategies to be within an acceptable thermal comfort ranges. ASHRAE standard 90.1 recommends to have discomfort hours per year less than 300 hours (i.e., hours where the indoor temperature is outside the throttling range). Tbl A.1 summarizes the number of hours of discomfort as predicted by Energyplus building energy models. The proposed design model equipped with ventilated slab system maintains the inside surface temperature of ceiling 1-2℃ lower compared to the LEED baseline model as shown in Fig A.2 (b). The lower inside surface temperatures of the proposed design model lead to the reduction of cooling energy consumption during the occupied period as shown in Fig A.3.

(a)

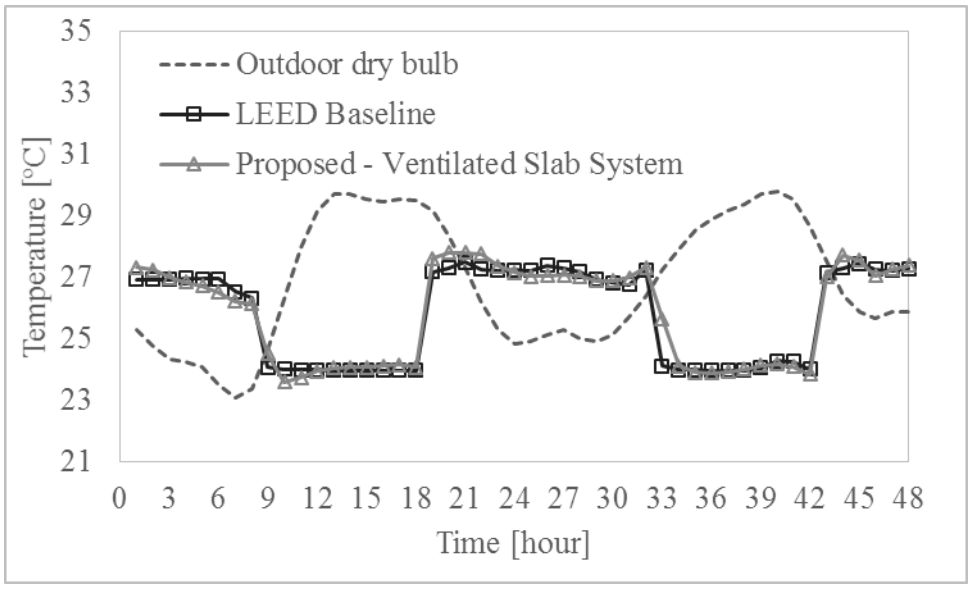

(b)

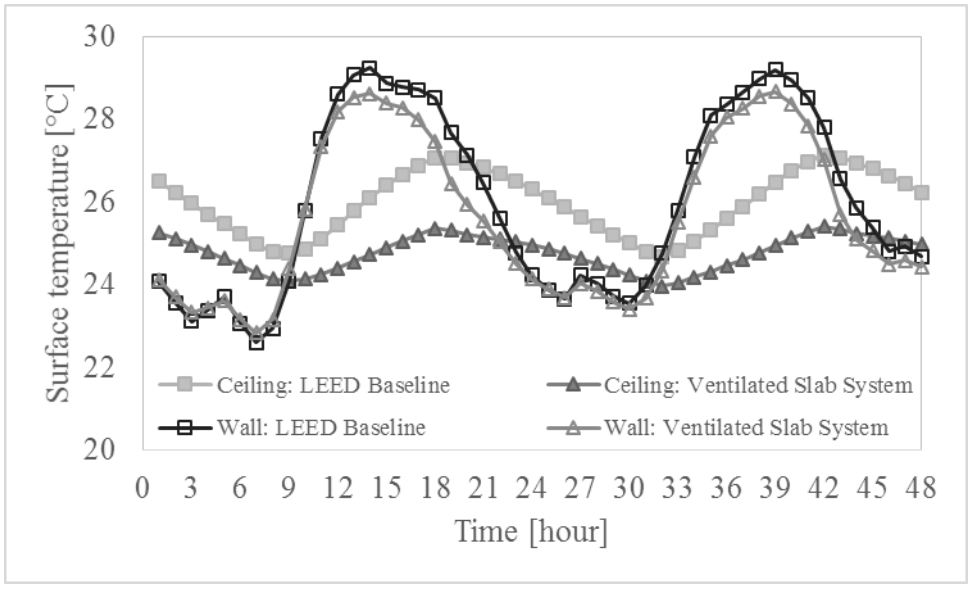

Fig A.2: (a) Hourly outdoor air dry-bulb temperature and zone mean air temperature profiles and (b) wall and ceiling inside surface temperatures obtained from LEED baseline energy model and proposed design energy model on July 20th and July 21st in Kochi, India

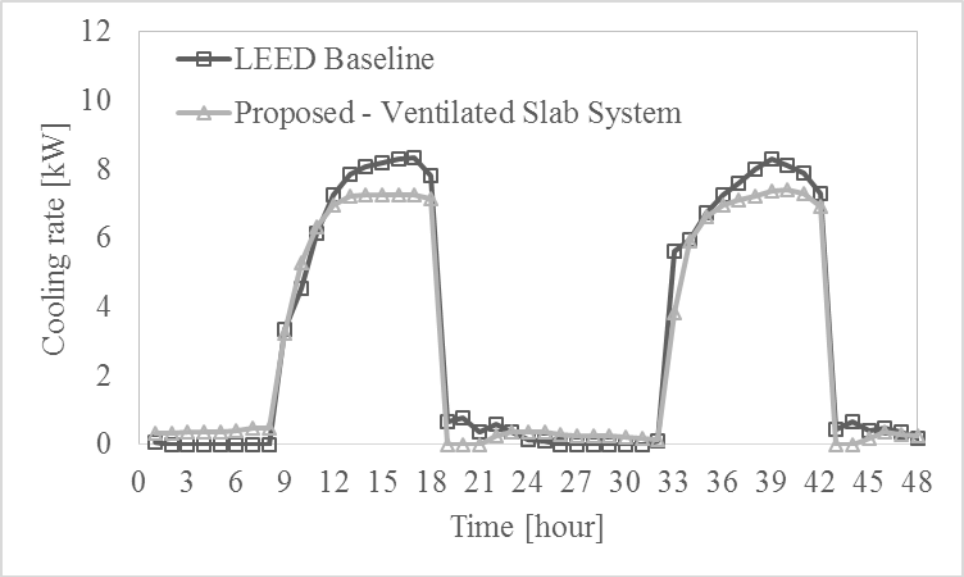

Fig A.3: Hourly cooling rate predicted by LEED baseline and proposed design energy model on July 20th and July 21st in Kochi, India

Tbl A.1: Time set-point not met during occupied period obtained from LEED baseline energy model and proposed design energy model

	LEED baseline	Ventilated slab system
Time set-point not met during occupied	126	178

Fig A.4 and Tbl A.2 compares the annual end uses of 3-story office building with HVAC alternatives. As indicated in results, the proposed building energy model with the ventilated slab system consumes 19% less energy compared to the LEED baseline model (Krarti and Park, 2012).

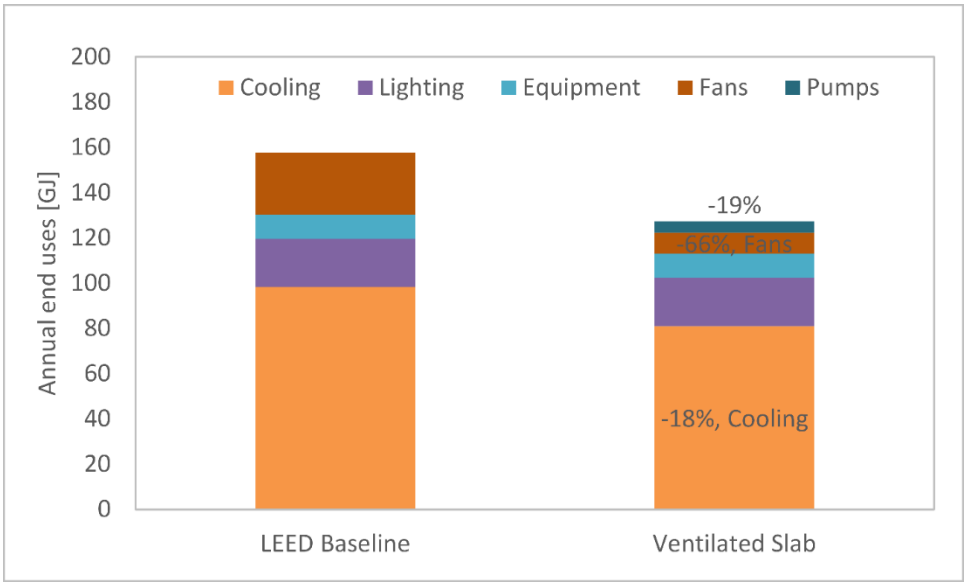

Fig A.4: Annual total energy consumption of HVAC alternative relative to a code-compliant building for 3-story office building in Kochi, India

Tbl A.2: Comparison of the annual total end uses for the three building energy models; LEED baseline and the hollow core ventilated slab

	LEED Baseline (Rooftop)	Proposed Design Model (Ventilated slab)	% Saving
Cooling (GJ)	98.32	80.96	(18%)
Lighting (GJ)	21.31	21.31	0%
Equipment (GJ)	10.69	10.69	0%
Fans/Pumps (GJ)	27.34	14.38	(66%)
Total End Uses (GJ)	157.66	127.34	(19%)

Comparison between radiant slab system and ventilated slab system

The top story of a prototypical office building is considered in this comparative analysis with a total conditioned floor area of 486 m^2. The height of the floor is 3-m resulting in a total conditioned volume of 1458 m^3. The building window-to-wall ratio is set to 15% for all orientations. The office building is occupied from 6 am to 7 pm.

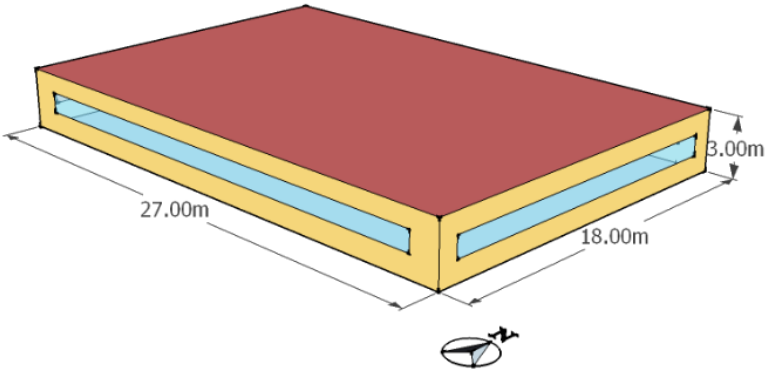

Fig A.5: Isometric view of the building model

Tbl A.3 shows the thermal characteristics of the exterior roof, floor, and walls for the office building. The total thermal mass is estimated to be approximately 1,134 kg/m^2 of conditioned floor area. Thus, the building is considered to have heavy weight construction and large thermal mass capacitance.

Tbl A.3: Thermal characteristics of building envelope constructions

Construction name	U-value [W/m^2-K]	Capacitance [kJ/m^2-K]
Roof	0.19	445
Floor	0.55	377
Exterior wall	0.49	266

Room air heating set point temperature is 19˚C and cooling set point temperature is 26˚C during occupied period. For the radiant slab system, the supply hot water temperature is set to 55˚C and the cool water temperature is set to 15˚C. The supply hot air temperature for the ventilated slab is varied between 30 to 35˚C and supply cool air temperature ranges from 10 to 15˚C. The comparative analysis is conducted using TMY3 weather data for Golden, CO for specific period representatives of winter and summer conditions.

Fig A.6 shows the total source energy use of both hydronic radiant and ventilated slab systems for representative summer season from June to August. The cooling energy use is decreased by 18% when ventilated slab is used instead of hydronic radiant system to cool the office building. While, the ventilated slab system need to use fan energy to supply cooled air to the hollow core slabs, it requires 40% less pump energy use compared to hydronic radiant slab system. As a result, the total source cooling energy use by the ventilated slab system is reduced by 12% compared to that obtained by the hydronic radiant system.

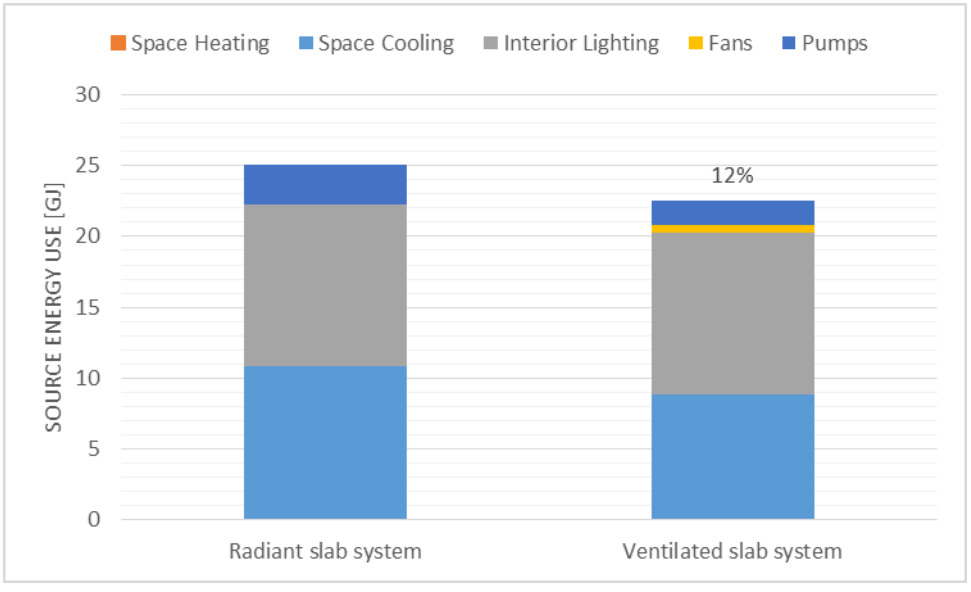

Fig A.6: Source energy use of hydronic radiant slab and that of the ventilated slab for an office building in cooling operation

Similarly, Fig A.7 shows the comparative analysis of the total source energy use between the ventilated slab and the hydronic radiant slab systems in representative heating period from December to February. The heating energy use is decreased by 26% when the ventilated slab is considered instead of the radiant slab system. Pump energy use for the ventilated slab system is 33% less than that of the hydronic radiant slab system. The total source heating energy use of the ventilated slab system is15% lower than that achieved by the hydronic radiant slab system.

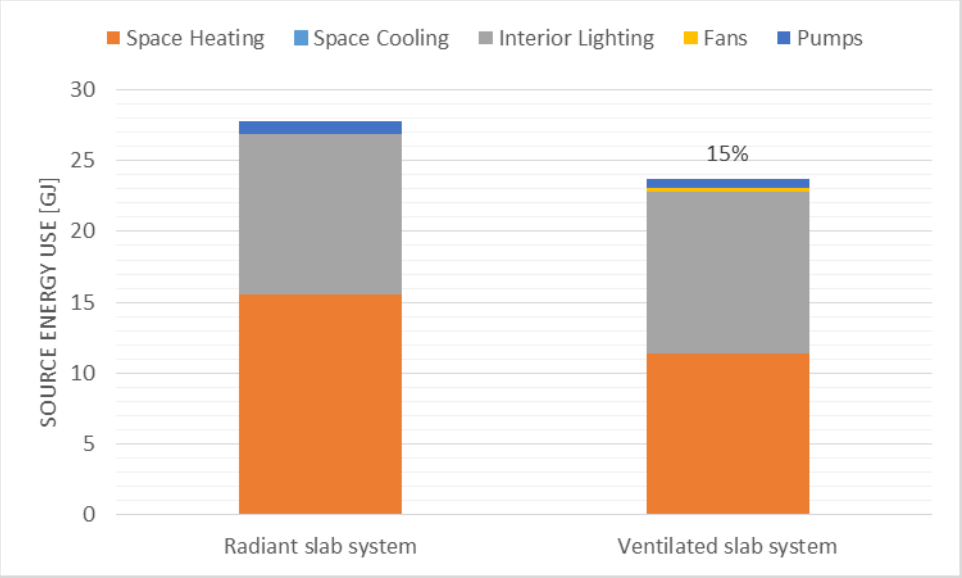

Fig A.7: Source energy use of hydronic radiant slab and that of the ventilated slab for an office building in heating operation

Parametric Studies on the Critical Parameters Associated with the Performance of Ventilated Slab System using 1-D, 2-D and 3-D Models

The findings from a series of parametric studies on the critical parameters associated with the performance of ventilated slab system using 1-D, 2-D and 3-D models are shown in Fig A.8 to Fig A.13. Specifically, several parametric analyses are performed to compare the performance of ventilated slab systems under various design and operating conditions by using 1-D, 2-D, and 3-D slab models. The parametric analyses include the effect of convective coefficient inside the hollow cores, convective coefficient on the slab surface, supply air inlet temperature, air mass flow rate, depth of the hollow cores, and core pitch. Some of the main observations from the parametric results illustrated in Fig A.8 to Fig A.13 are itemized:

i. For convective coefficient of the air that travels inside the hollow cores, significant increase of average heat transfer rate along the slab surface is evident when a transition occurs from laminar flow (Re<2300) to turbulent flow (Re>2300). For turbulent flow region, the average heat transfer rate slowly increases with diminishing returns as Reynolds number becomes larger.

ii. The larger convective coefficient on the slab surface facilitates heat exchange between the floor surface and zone air, but this effect gradually diminishes. It is observed that the average heat transfer rate along the slab surface is more sensitive to the convective coefficient on the slab surface compared to the convective coefficient inside the hollow cores.

iii. Hollow core inlet air temperature can greatly influence the performance of the ventilated slab system. The average heat transfer rate on the upper surface of slab increases proportionally to the increase in supply air inlet temperature when heating is required. As

the inlet air temperature increases, the average heat transfer rate on the slab surface rapidly decreases for cooling mode.

iv. As the air mass flow rate increases, slab heat transfer rate is increased, but the impact gradually reduces. When the air mass flow rate is larger than 1.0 kg/s, the total slab heat transfer rate is found to be not significantly affected by the mass flow rate in the heating mode.

v. As the depth of embedded hollow core increases, the total slab heat transfer rate along the upper slab surface proportionally decreases, but the total slab heat transfer rate on lower slab surface increases. The effect of the depth of hollow core follows a diminishing return pattern with a gradually reduced impact.

vi. As the depth of embedded hollow core increases, the total slab heat transfer rates along the slab surfaces are found to be proportionally reduced. The effect of the depth of hollow core follows a diminishing return pattern with a gradually reduced impact.

vii. The contact area of heat source/sink has less impact on the heat transfer rate along the slab surfaces. As the contact area of core increases, the average heat transfer rates along the slab surfaces increases gradually until reaching specific asymptotic values. When the contact area is kept the same, the average heat transfer rate for the smaller core is slightly greater than when the core is large.

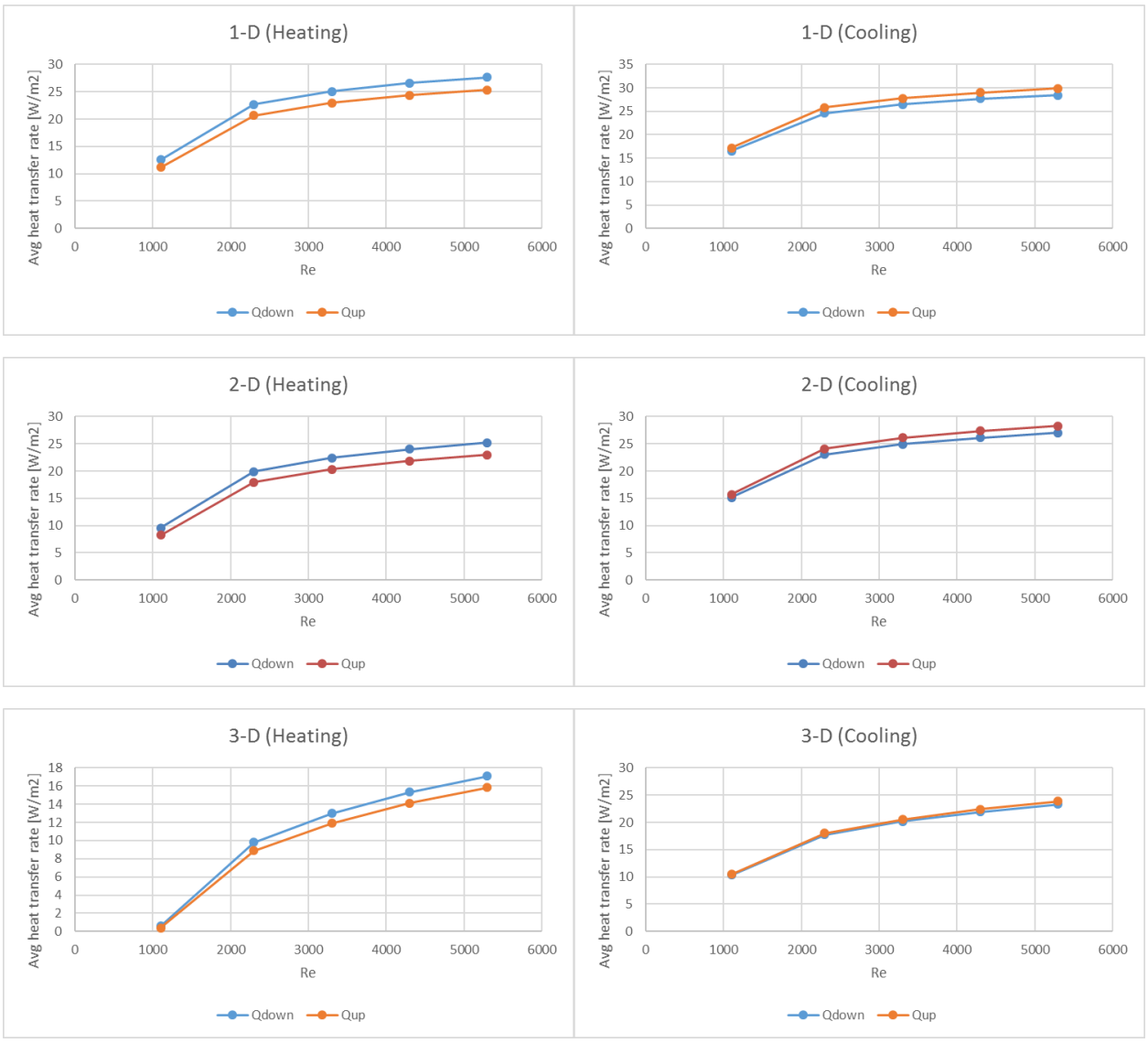

Fig A.8: Average heat transfer rate along the slab surface with no insulation as a function of convective coefficient inside a hollow core

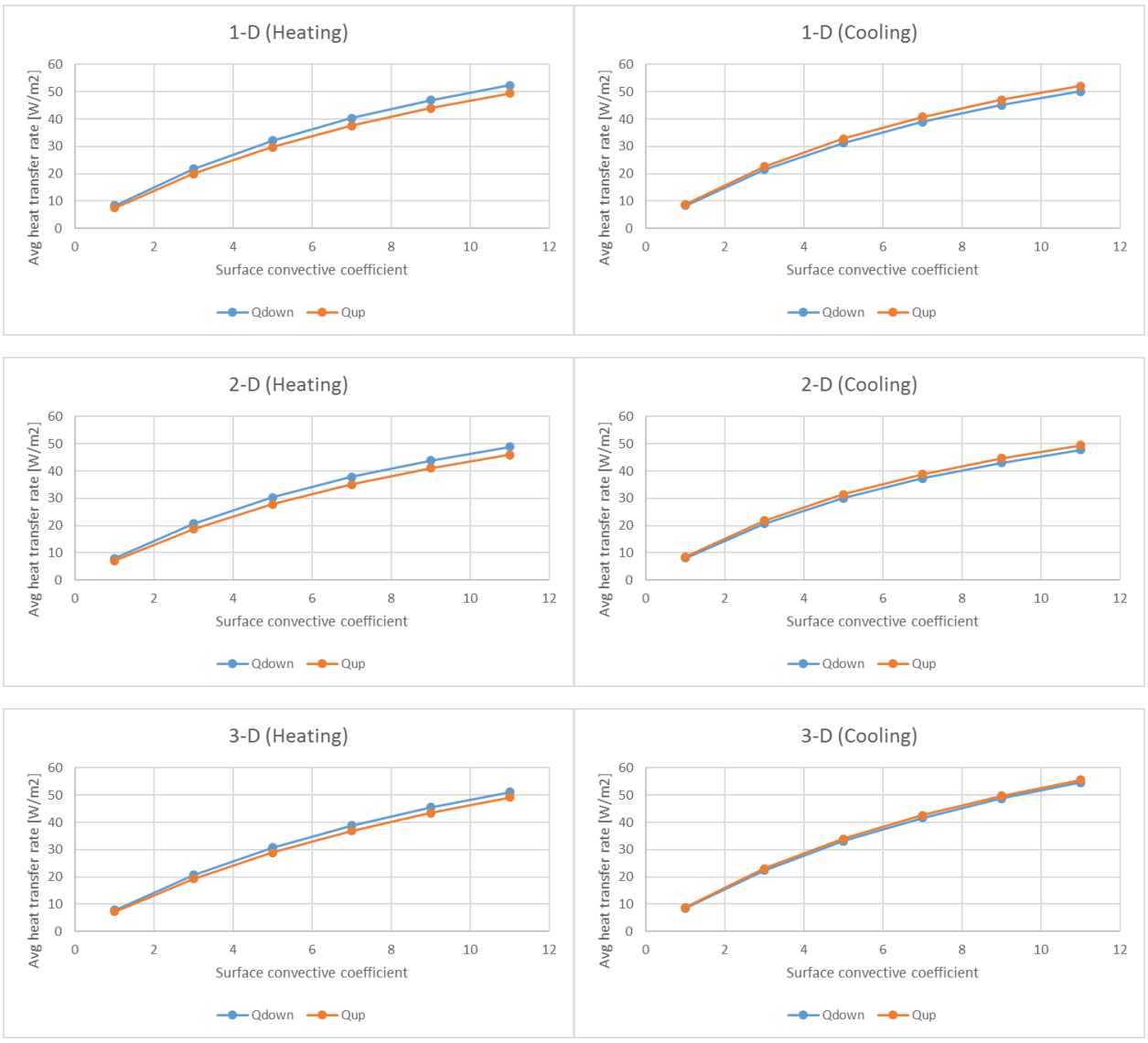

Fig A.9: Average heat transfer rate along the slab surface with no insulation as a function of convective coefficient on a floor surface

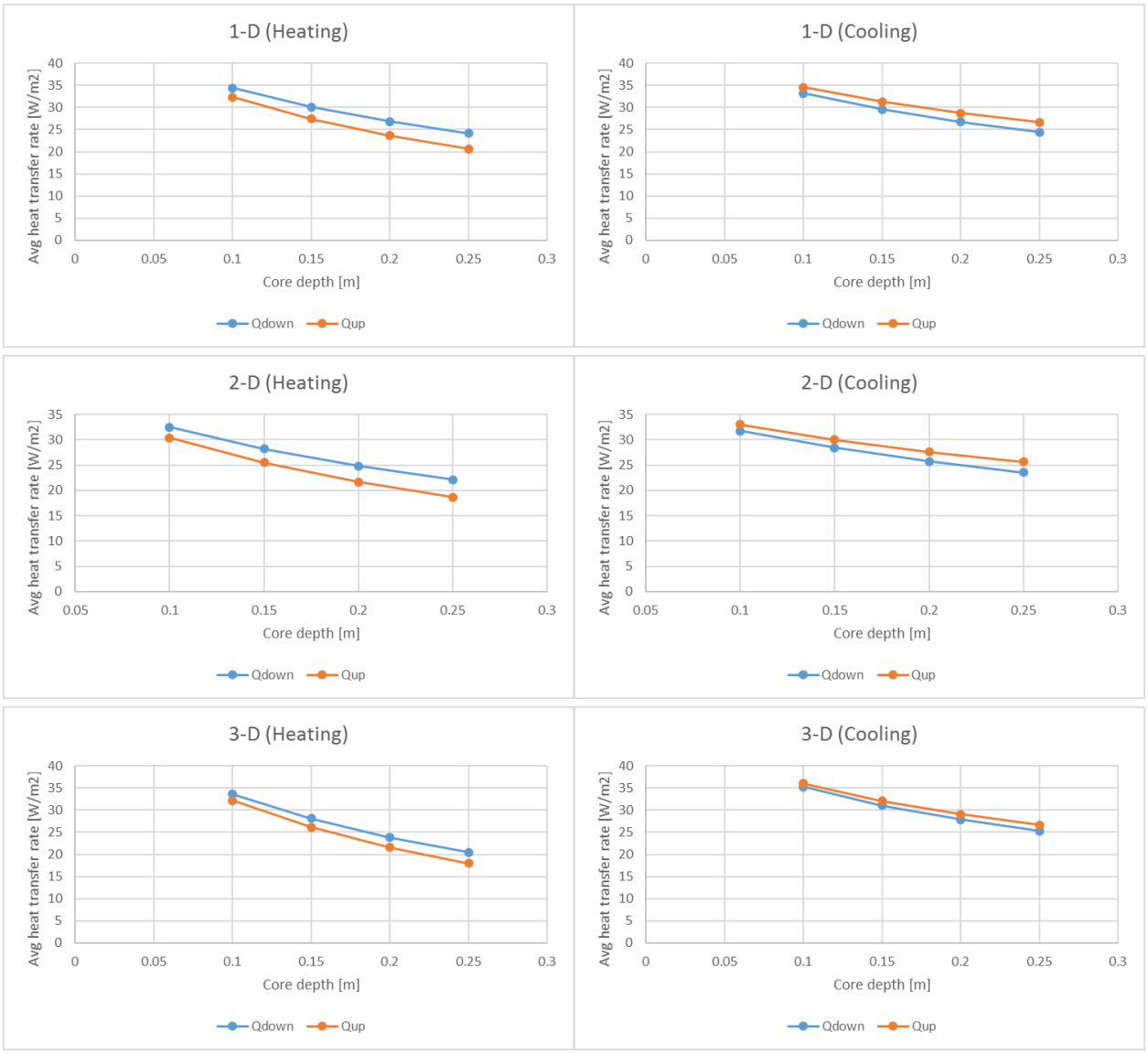

Fig A.10: Average heat transfer rate along the slab surface with no insulation as a function of the depth of hollow cores

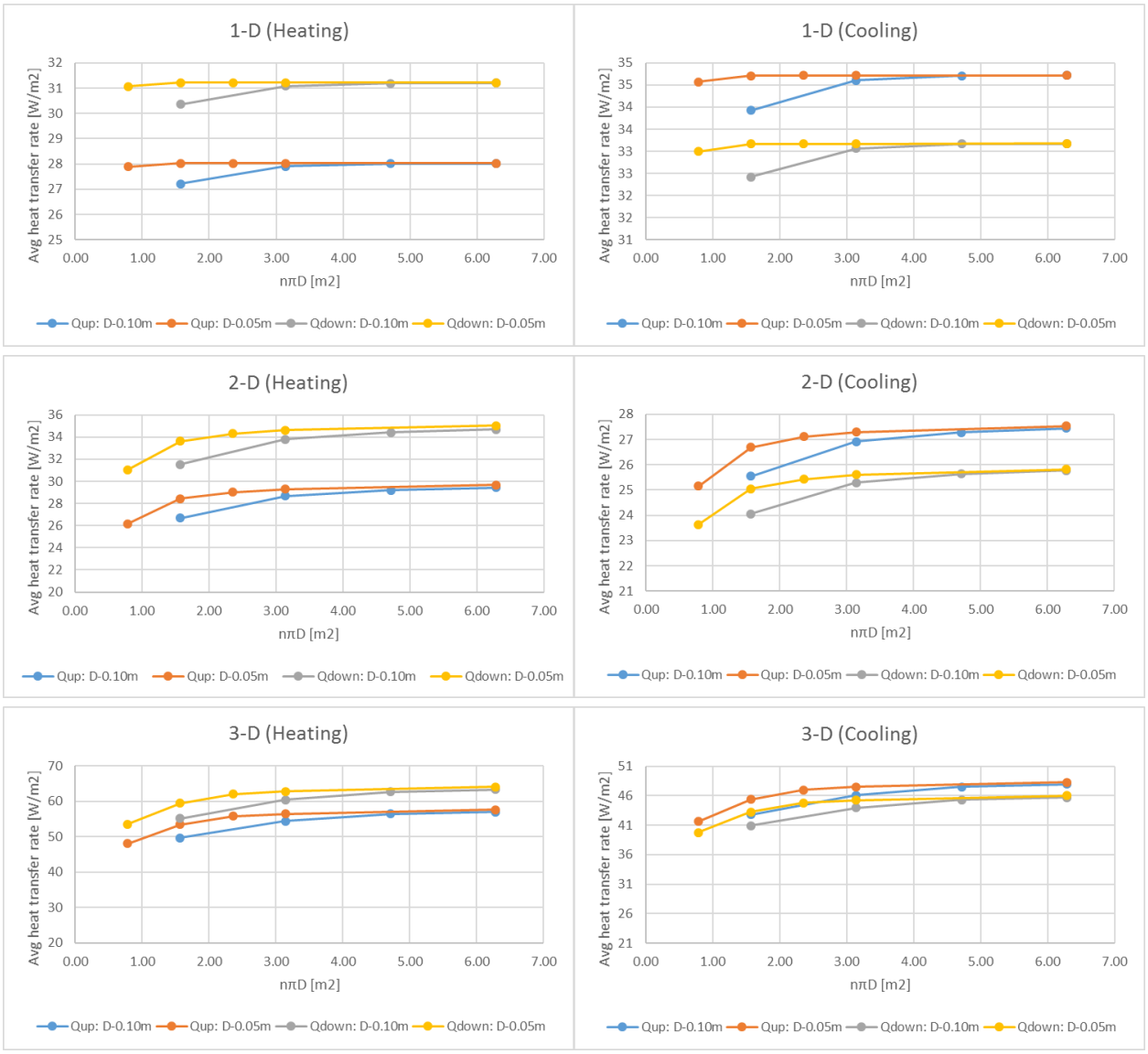

Fig A.11: Average heat transfer rate along the slab surface with no insulation as a function of hollow cores contact area embedded in a fixed concrete slab thickness for two core diameters

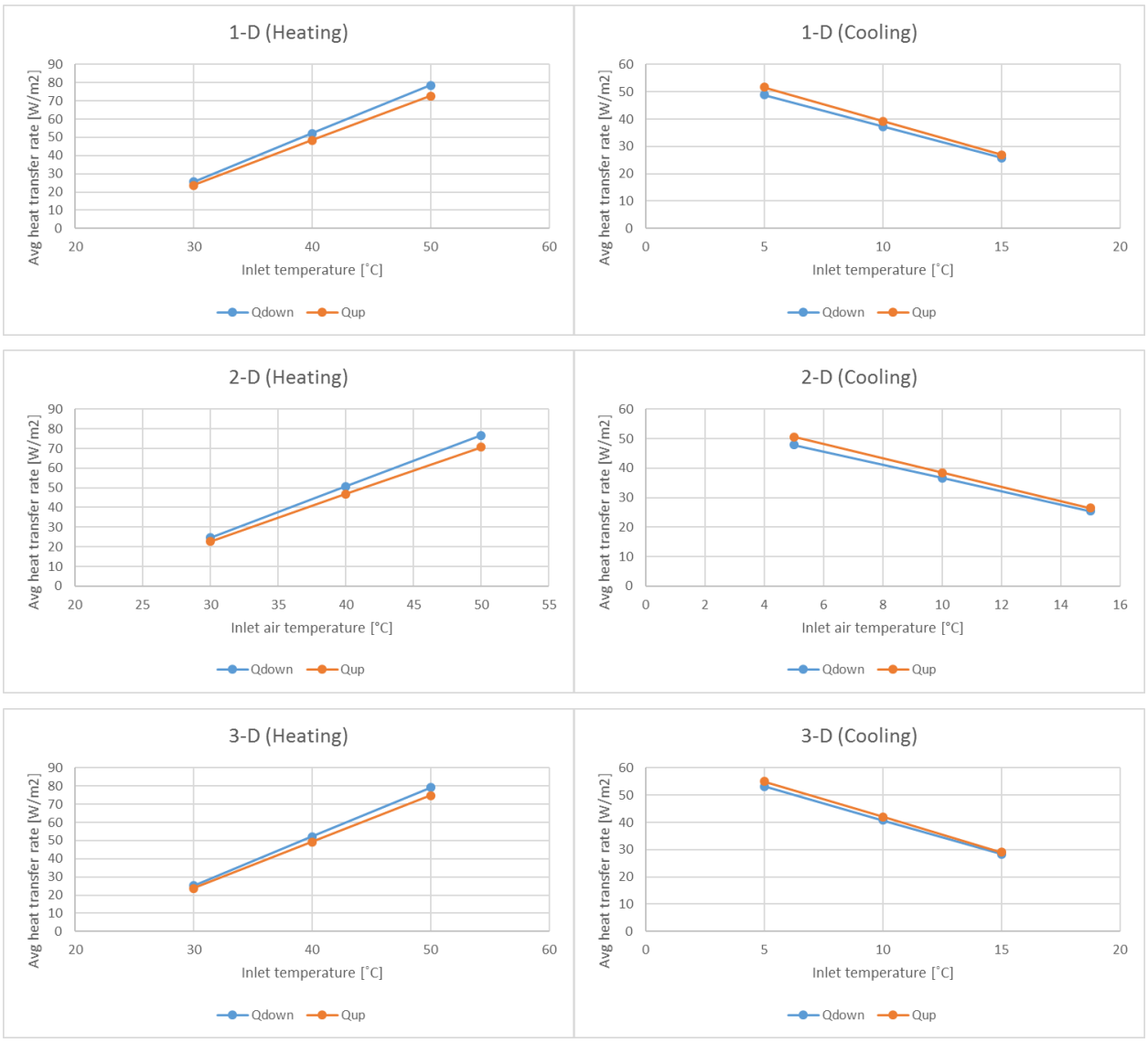

Fig A.12: Average heat transfer rate along the slab surface with no insulation as a function of air inlet temperature

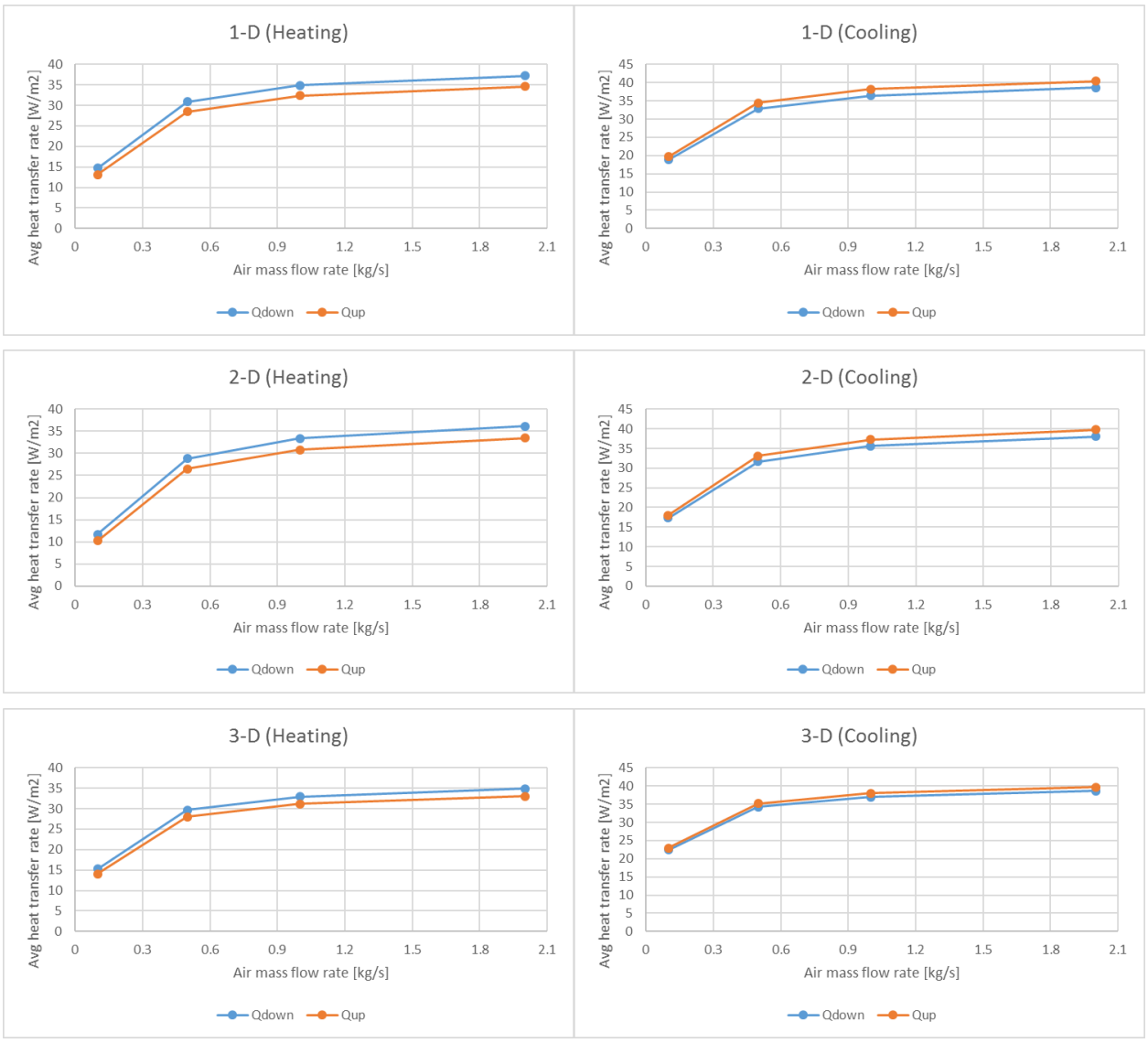

Fig A.13: Average heat transfer rate along the slab surface with no insulation as a function of air mass flow rate

Optimal Control Strategy for 1600m^2 Building

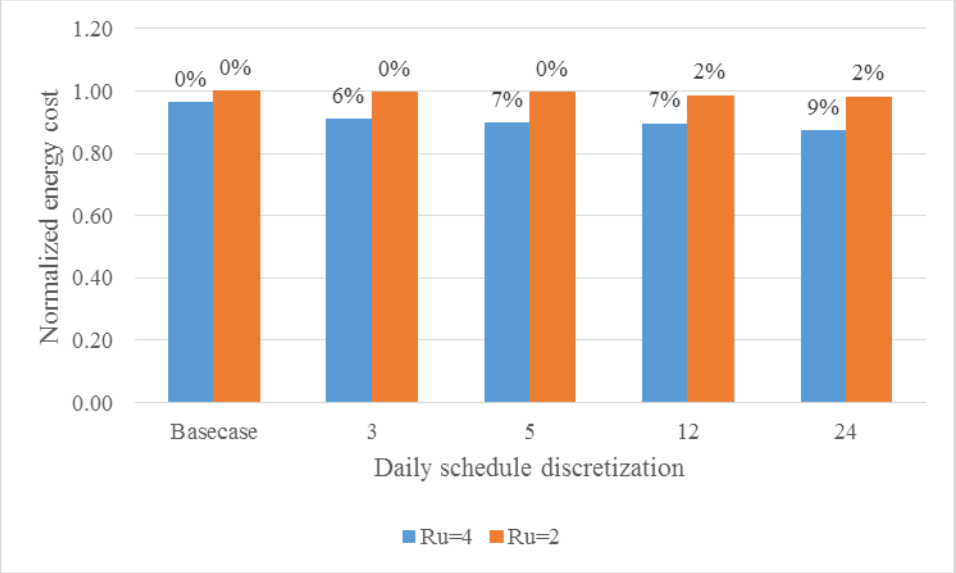

Fig A.14: Comparison of savings potential of different control strategies

(a)

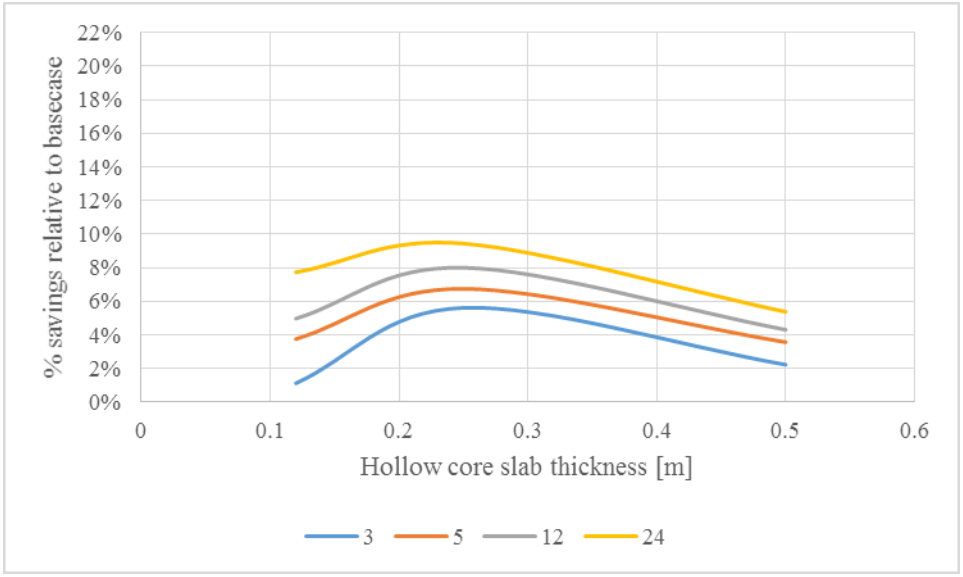

(b)

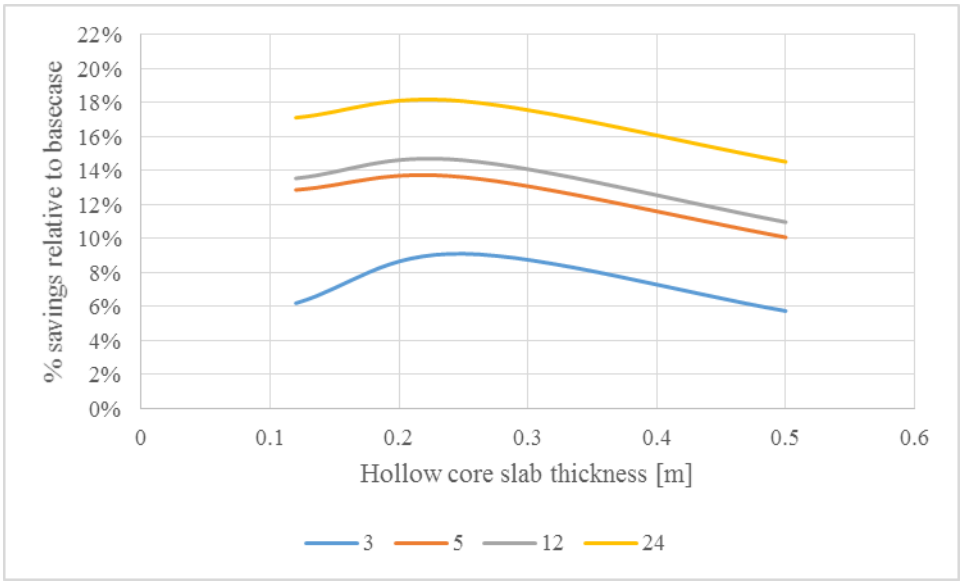

Fig A.15: Percent energy cost savings of precooling vs. conventional control as a function of a hollow core slab thickness: (a) $R_u = 4$ and (b) $R_u = 10$

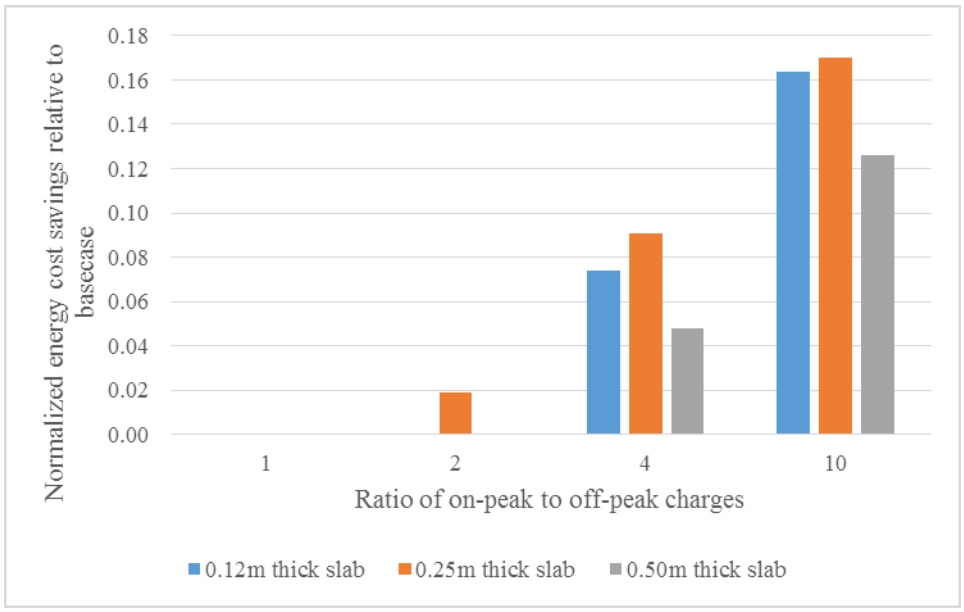

Fig A.16: Comparison of savings potential of different utility structures with various slab thickness

Optimal Control Strategy for 7680m^2 Building

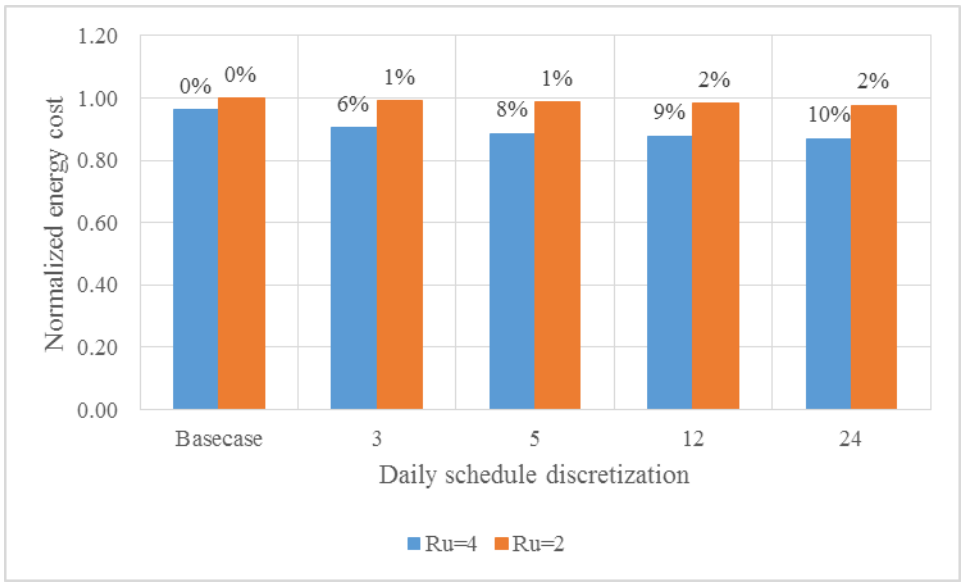

Fig A.17: Comparison of savings potential of different control strategies

(a)

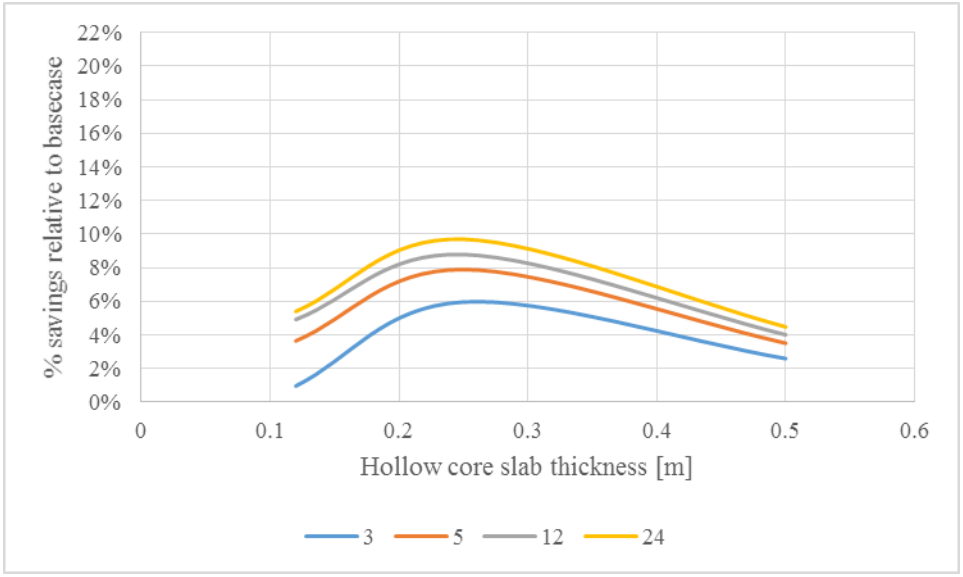

(b)

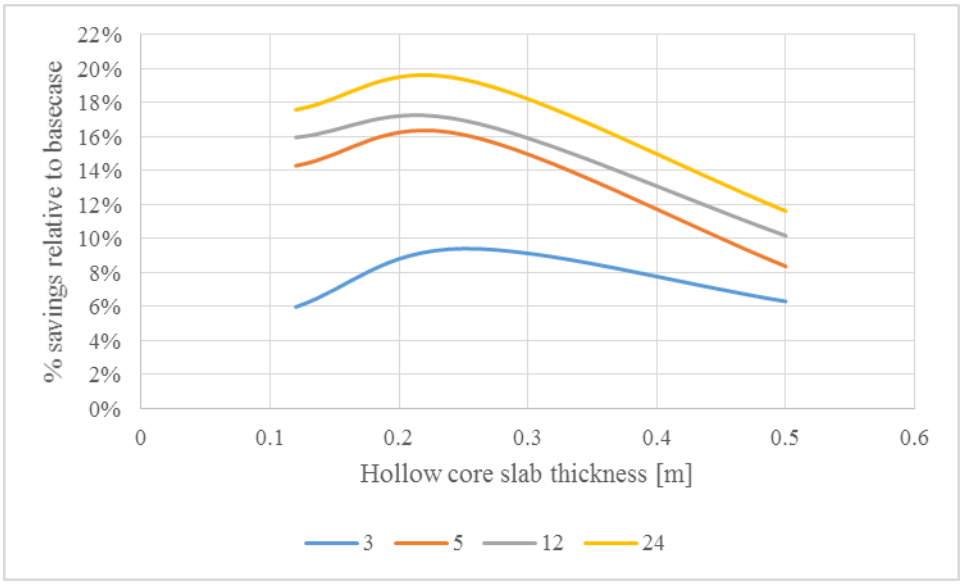

Fig A.18: Percent energy cost savings of precooling vs. conventional control as a function of a hollow core slab thickness: (a) $R_u = 4$ and (b) $R_u = 10$

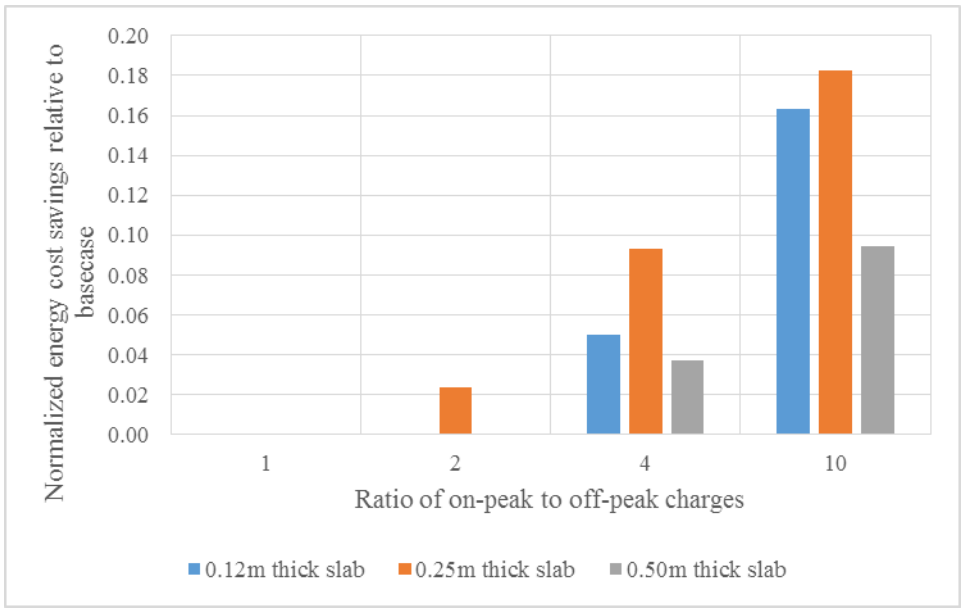

Fig A.19: Comparison of savings potential of different utility structures with various slab thickness